IMAGING THE DEVELOPMENT OF A BONE–TO–BONE LIGAMENT CONSTRUCT

by

ALISTAIR L. BANNERMAN

A thesis submitted to
The University of Birmingham
for the degree of
DOCTOR OF PHILOSOPHY

School of Chemical Engineering
College of Engineering and Physical Sciences
The University of Birmingham
September 2015

Abstract

Ligament injuries are commonplace, with poor native healing leaving injury sites exposed to instability and further damage. A number of surgical methods have been established for reconstruction using a range of materials, but these have a high failure rate and a number of undesirable side-effects. Much recent work has been focused on the development of tissue engineered ligament grafts. One of the major challenges for this is the formation of an effective ligament-bone interface. In native tissue a multi-phase interface enables smooth transfer of forces between the mechanically mismatched bone and ligament tissue, however this has proved hard to replicate. Previous work has developed a bone-bone ligament construct model intended to emulate the native interface through formation of a mineralised region by soluble cement anchors. Development and optimisation of the model has seen an increasing mechanical strength, but the mechanisms involved are poorly understood. This study investigates the development of the ligament construct through the use of multiple complimentary imaging techniques to provide information on the biological, chemical, and topological development of the construct as it forms from initially homogeneous and separate materials to a complex non-homogeneous system.

ACKNOWLEDGEMENTS

A number of people and organisations have provided help and support to me during the completion of this work. I would like to thank:

My supervisors Prof. Liam M. Grover, Prof. Paula Mendes, and Dr. Hamid Dehghani for their guidance, support and extensive knowledge in the area. Dr. Jennifer Z. Paxton for her invaluable advice and expertise on the ligament constructs and cell culture. Dr. Richard L. Williams for useful discussion and XRD data collection. Alexandra Iordachescu for providing further data and images of the mineralised sinews after my departure from the laboratory.

Dr. Pola Goldberg-Oppenheimer for the collection of TEM and SAD images for the mineralised sinews. Dr. James Bowen for assistance with the AFM and mechanical loading plenary tests. Prof. Peter Winlove, Dr. James Bell, and Dr. Eleanor Martin from the physics department in Exeter university for their helpful discussion and acquisition of two photon and second harmonic generation images of the constructs.

The staff and student members of Trailab and the PSIBS doctoral training centre at the University of Birmingham for their support. In particular Alan M. Race for useful discussion and computational assistance.

The EPSRC for funding this project through the PSIBS doctoral training centre (grant code: EP/F50053X/1). Additionally The confocal Raman microscope used extensively

in this research were obtained through Birmingham Science City: Innovative Uses for Advanced Materials in the Modern World (West Midlands Centre for Advanced Materials Project 2), with support from Advantage West Midlands and part funded by the European Regional Development Fund.

My family for their support, and providing a roof and coffee during the writing of this thesis.

Finally my examiners Dr. Pola Goldberg-Oppenheimer and Dr. Melissa Mather for their thorough and rapid analysis of this work.

CONTENTS

LIST OF FIGURES

LIST OF TABLES

ACRONYMS

2D-FFT two dimensional fast Fourier transform.

3D three dimensional.

A.U. arbitrary units.

ACL anterior cruciate ligament.

ACP amorphous calcium phosphate.

AFM atomic force microscopy.

BBLC bone-to-bone ligament construct.

BPTB bone patella tendon bone.

BSE backscattered electron.

CaP calcium phosphate.

CARS coherent anti-Stokes Raman spectroscopy.

CCD charged-coupled device.

CRM confocal Raman microscopy.

CT computed tomography.

CTF chick tendon fibroblast.

DAPI 4',6-diamidino-2-phenylindole.

DCPD dicalcium phosphate dihydrate.

DMEM Dulbecco's modified eagle's medium.

ECM extracellular matrix.

EDS energy dispersive x-ray spectroscopy.

EM electron microscopy.

FBS foetal bovine serum.

FFT fast Fourier transform.

FFTRS fast Fourier transform radial sweep.

FWHM full width half maximum.

HA hydroxyapatite.

HO heterotopic ossification.

IR infra-red.

L/T ligaments and tendons.

LCVR liquid to cement volume ratio.

MRI magnetic resonance imaging.

MSC mesenchymal stem cell.

NMR nuclear magnetic resonance.

OCP octacalcium phosphate.

OCT optical coherence tomography.

PBS phosphate buffered saline.

PCA principal component analysis.

PCL posterior cruciate ligament.

SAD selected area diffraction.

SBF simulated body fluid.

sDMEM supplemented Dulbecco's modified eagle's medium.

SEM scanning electron microscopy.

SERS surface enhanced Raman spectroscopy.

SHG second harmonic generation.

SNR signal-to-noise ratio.

SRS stimulated Raman spectroscopy.

TCP tricalcium phosphate.

TEM transmission electron microscopy.

TP two photon.

UV ultraviolet.

XRD x-ray diffraction.

CHAPTER 1

INTRODUCTION

1.1 Ligaments and Tendons

Ligaments and tendons (L/T) are dense connective tissue that connect bone-to-bone, and bone-to-muscle respectively. Ligaments play an important role in the biomechanical stabilisation and limitation of movement in the musculoskeletal system, and tendons transmit muscle generated force to bone [1]. Due to the nature and importance of their role in the musculoskeletal system, a high rate of injury due to sporting or occupational causes is associated with a number of L/T; notably the rotator cuff tendon [2, 3], Achilles tendon [4], the anterior cruciate ligament (ACL) [5, 6] and the extensor carpi radialis brevis [7]. These injuries can dramatically effect the lifestyle of patients and put a large financial burden on the economy through medical costs [8]. Due to its relevance to this project, the ACL will be the major focus of this chapter.

1.1.1 Anatomy and physiology

L/T have a largely similar structure, composed of a hierarchy of layered parallel fibre bundles (Fig. 1.1). At the lowest level collagen fibrils are formed by non-covalent crosslinking between collagen helices, these bundles of collagen fibrils are bound by an internal endotenon, a thin connective tissue sheath with cell alignment perpendicular to the collagen's

line of force, to form collagen fibres. The presence of the endotenon sheath allows fibres to slide relative to each other, increasing their capacity for deformation without mechanical failure. Groups of collagen fibres are bound into primary fibre bundles grouped together by another layer of internal endotenon. Groups of primary fibres form secondary fibres, or fascicles, which are again grouped by an external endotenon. The tertiary fibre bundles are composed of fascicles bound together by the external endotenon. The ligament proper is composed of a collection of tertiary fibres bound by a connective layer of tissue, the epitenon. It has been observed that when in a state of relaxation a sinusoidal crimp pattern is taken by collagen fibres [9]. L/T are largely avascular, requiring 7.5 times less oxygen than skeletal muscle due to their passive nature [10]. As a result of this nutrients are largely supplied through diffusion in the synovial fluid, instead of perfusion from blood vessels [11].

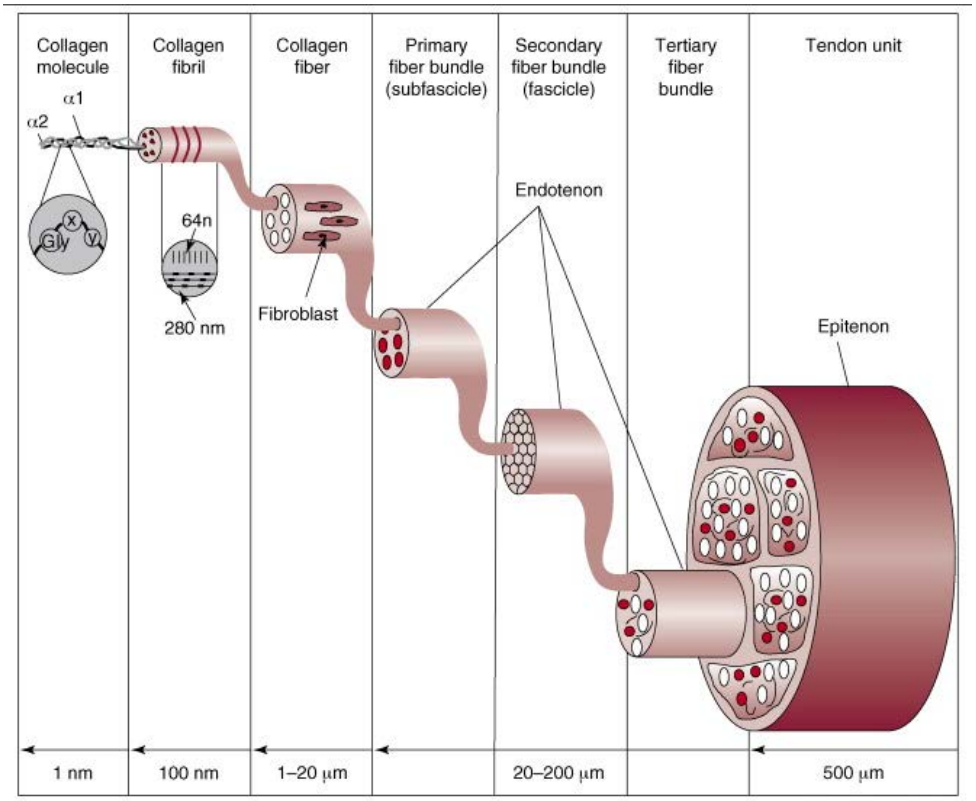

Figure 1.1: Anatomical structure of collagen bundles in L/T. Reproduced from Liu *et al.* 2008 [12] with permission.

The cellular population of L/T is largely composed of fibroblasts which are arrayed in longitudinal rows between collagen fibres. Fibroblasts produce the collagen and other extracellular matrix (ECM) components of the L/T [13], and regulate growth factors involved in maintenance and repair [14]. Other cells are present: notably fibrocartilage cells at attachment sites [1], and myofibroblasts reported at sites of ligament healing [15]. Mature L/T have a low cell density, whilst developing ones have a much higher level with the enthesis acting as the cell source [16].

The ECM biochemical composition of L/T is dominated by collagen which accounts for 70-80% of the dry weight and provides the main tensile strength [1]. Collagen is complemented by elastin, a viscoelastic fibre which is believed to be responsible for allowing input energy free long-range deformation and subsequent passive recoil [17]. The quantity of elastin is highly variable depending on location with the dry weight varying from 2% in tendons, to 5% in the ACL, to 47% in the ligament of the spine [18]. The ground substance (defined here as the ECM excluding fibre, or the extrafribillar matrix) contains proteoglycans which have a negative charge and account for the attraction of water that gives the ACL its 60-80% wet weight quantity of water [1]. The quantity and ordering of proteoglycans varies between each L/T in the body, and will effect how collagen fibres glide past each other, determining the viscoelasticity of the tissue [1].

The biomechanical properties of the ligament are dependent on the strain rate applied. Fig. 1.2 shows the stress/strain response to loading at the midsubstance. When undergoing tensile loading, the ligament stress/strain has three regions. Initially there is minimal stress change with strain in the toe region, as the collagen crimps are straightened out. This is followed by the linear region where stress and strain are directly proportional. Finally the failure region where there is a decline in stress when strain is applied.

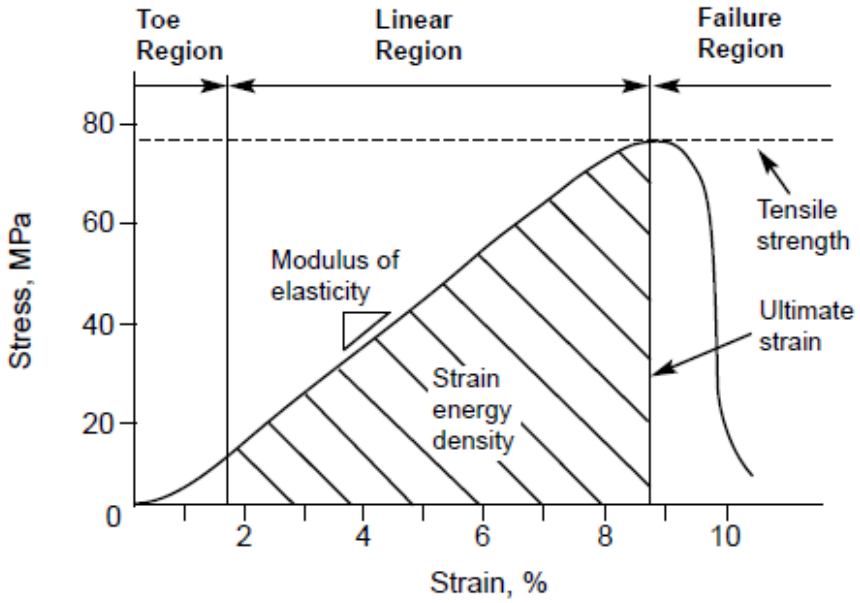

Figure 1.2: Mechanical properties of L/T undergoing tensile load. Illustrating the three regions of behaviour. For context approximate maximum ACL stress and strain have been reported at 38MPa and 44 respectively [19]. Reproduced from Woo *et al.* 2000 [20] with permission.

The enthesis

The enthesis (also referred to as the insertion site, osteotendinous junction, and osteoligamentous junction) is the attachment site of the soft tissue to bone [21]. Stress concentrations can build up here due to impedance mismatch between the two materials, making the enthesis one of the most important aspects for the biomechanical function of the L/T. Overuse injuries as a result of work or lifestyle are common [21]. The attachment and composition of the enthesis is divided into two types which develop as a result of the cellular process involved during formation (Fig. 1.3); fibrous and fibrocartilaginous [21].

The fibrous enthesis (Fig. 1.3a) is an direct attachment composed of two distinct zones; bone and ligament. The fibrous interface forms as a result of intramembranous ossification, with collagen bundles (known as Sharpeys or perforating fibres) being cemented into the lamellar bone [22]. The fibrocartilaginous enthesis (Fig. 1.3b) is a more complex multilayer tissue consisting of four distinct zones; bone, mineralised fibrocartilage, fibro-

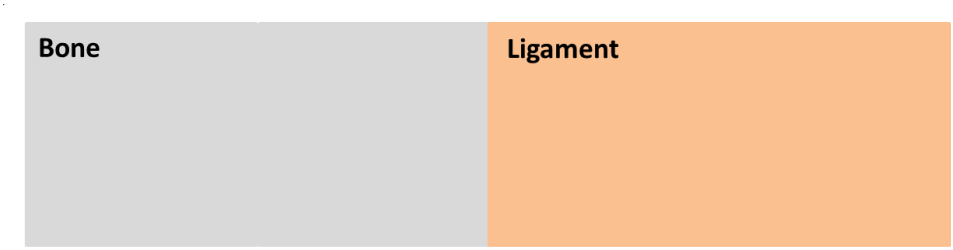

(a)

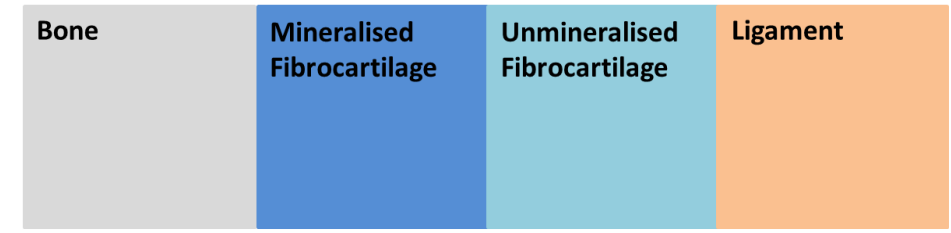

(b)

Figure 1.3: Schematic of the zones present in the fibrous and fibrocartilaginous enthesis. Showing (a) the two zone structure of the fibrous enthesis, and (b) the four zone structure of the fibrocartilaginous enthesis.

cartilage, and mature L/T. Each region has a unique ECM organisation and content, the boundary between each region is often hard to define, with the exception of the transition from cartilaginous to calcified fibrocartilage which is demarcated by a tidemark. The heterogenity is postulated to minimise stress concentrations, allowing for a smooth transfer and dissipation of forces [23] reducing the chance of mechanical impedence mismatch and injury. The thickness of the mineralised fibrocartiliage is thought to be proportional to the ultimate strength of the L/T [21].

1.2 The anterior cruciate ligament

The ACL is located in the knee, connecting the femur and the tibia (Fig. 1.4). It functions as one of the major stabilising components of the knee joint: resisting anterior

tibial translation and restraining internal rotation. The ACL has a complex anatomy and physiological function. The insertion site at the tibia is wider and stronger than at the femur [24]. It has a broad and flat shape when the joint is extended and twisted during flexion. It is split into two bundles the anteromedial bundle, and the posterior lateral bundle which are not isometric and undergo different structural changes during knee flexion; as one tightens the other loosens and vice versa. The ACL also works with the posterior cruciate ligament (PCL); winding around each other as the knee joint is flexed, and unwinding as the joint is extended [24]. Load required for daily activities has been estimated at 454N for descending stairs [25].

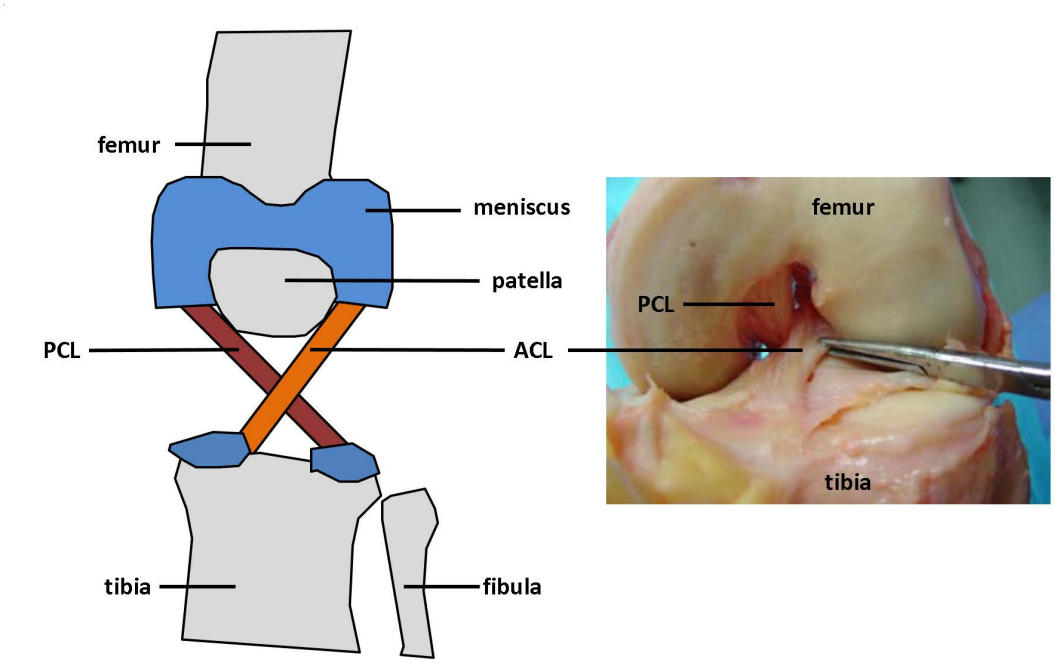

Figure 1.4: Anatomical position of the ACL inside the left knee joint. Photographic image modified from Zantop *et al.* [26] with permission.

Histologically the ACL is split into three regions; the proximal, middle, and distal [27]. The proximal section contains a high density of round fibroblast cells. The middle is composed of high density collagen fibres, with spindle and fusiform shaped fibroblasts. The distal consists of ovoid fibroblasts and a decreased collagen bundle density [27]. The structure and content of the ACL is largely similar to the general ligament properties

described in the previous section. Biochemically the ACL is compromised largely of type I collagen alligned parallel to the longitudonal axis, with type II collagen associated with fibrocartilidge present at the insertion sides, and small quantities of type IV and VI collagen.

As with many other ligaments the ACL has poor vascularisation. The middle genicular artery provides a small quantity of blood to the ACL [27], with a network of periligamentous vessels ensheathing the ligament. However the supply of blood is nonisometric with the distal part receiving less than the others. This low and unevenly distributed level of blood supply is thought to be one of the major factors in the inability of the ACL to fully repair [27].

1.2.1 Injury

Full or partial tearing of the ACL are among the most common muscoskeletal injuries in the developed world, with 100,000-200-000 reconstructions per year in the United States being commonly cited [28, 29]. Healing and recovery of ACL injuries is complex with the ligament generally showing poor self-repair. The major reasons given for this are the lack of blood supply [27], and the harsh environment. Recent work has suggested that intrinsic self repair of the ACL is possible with reattached ligaments showing that signs of spontaneous healing process can occur, but only under limited conditions [30].

An injured ACL will create an instability in the knee, with a knock-on effect as increased strain on other components leads to further damage. There is also evidence that a nonfunctional ACL can lead to oseteoarthristus in the long term [31]. Quality of life can suffer with many jobs and cultures requiring the ability to kneel in day-to-day tasks. Following injury and reconstruction many do not return to preinjury levels of activity [32].

Injury of other ligaments and tendons is also common with the rotator cuff in particular

being notable for a frequency of injury, with poor natural healing and low success rate for clinical reconstructions [2].

1.2.2 Reconstruction

As a result of the high incidence rate and long term issues associated with ACL tears, there are a number of established reconstruction methods with continuing research into new and more advanced techniques.

Current reconstruction methods

Autografts, which take donor tissue from the patient themselves and translate it as a graft to the ACL site, are the most commonly performed. By using the patients own tissue autografts minimise the chance of infection and/or immune rejection of the donor graft. However donor site morbidity is a problem with extensive physiotherapy required before and after the surgery to strengthen the tissue, and the patient likely to suffer from pain [5]. Typically the donor tissue is taken from the hamstring tendon, or the patellar tendon. The bone patella tendon bone (BPTB) graft is taken with a section of bone at both ends to aid osteointergration when inserted into the bone tunnel [5]. Alternatively autologous hamstring reconstruction lacks the bone to encourage osteointergration but has a lower level of donor site morbidity [33]. Despite much research into the area and a number of comparative literature reviews [6, 34, 35], opinion and evidence is still divided on the best choice of graft [36, 37], and conditions (single or double bundle, bone tunnel dimensions and placement, fixation device, and whether keep or remove the original stump [38]) to encourage effective healing and restore biomechanical properties, with the method used often coming down to the surgeons personal preference and experience.

Alternatively allograft and xenograft, where the donor tissue is taken from cadavers or another species respectively, remove the issue of donor site morbidity. However they are

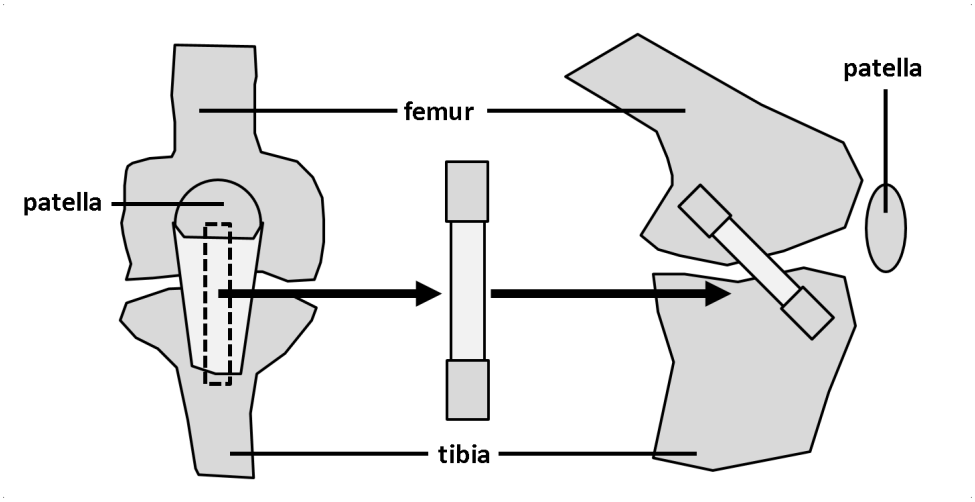

Figure 1.5: Use of autograft ACL replacement with a Bone-patellar tendon-bone (BPTB) graft.

susceptible to disease, immune rejection, and have been shown to exhibit slower biological integration [5]. These techniques require the decellularisation of the original tissue to allow the patients cells to be seeded, and prevent immune system responses [39]. Sterilisation of tissues has been performed either chemically or via ionising radiation. Chemical based methods using ethylene oxide often produce insufficient penetration to effectively sterilise the tissue [40]. Radiation initially proved problematic with gamma ray radiation damaging the tissue and reducing the biomechanical properties of the tendon. Recent work using lower radiation dose with gamma [41] and electron [42] radiation has shown that damage to mechanical properties is preventable. But these are still dependent on finding suitable donor tissue and encouraging effective biological integration.

Synthetic polymer replacements were developed as an off the shelf-option for high mechanical strength grafts that could be easily stored and sterilised, allowing the patients tendinous tissue to be preserved and minimising the risk of disease [43, 44]. A number of polymers including carbon fibres, Gore-Tex and Dacron have been used as materials [44]. These grafts have high a initial mechanical strength, but in clinical studies have been found to quickly deteriorate, resulting in pain and ultimately a high failure rate [44]. The Leeds-Keo formed of polyethylene terephthalate in a braided pattern designed to support

tissue ingrowth showed the most promising initial results [45]. However high instability and rupture rate combined with the fact it acts more as a load bearing prosthesis than a true graft have limited the success [46].

After the graft has been inserted there is a high failure rate associated with the primary surgery due to technical, biological or mechanical factors. Technical failures caused by nonanatomical graft placement and failure to consider other associated ligamentous injuries at the time of primary reconstruction, are the most reported cause [47], with 52% of 90 failures attributed to surgical technical errors in a review by Carson *et al.* 2004 [48]. Issues with bone tunnel widening have been related to a mixture of biological and mechanical [49]. During the initial postoperative period the attachment interface is the weakest part, with failures later mostly occurring in the midsubstance after 6-12 weeks [47].

One of the major factors in the success of a ligament graft is the successful attachment of the ligament to bone. Both the strength and structure of the attachment play an important role. As discussed in section 1.1.1, a strong attachment is required to prevent pull out of the soft tissue, and a graded interface like the fibrocartilaginous enthesis is needed to prevent impedance mismatching and stress concentrations building up. The attachment is prone to failure post surgery with 10% rate reported [50, 51]. With auto/allo grafts the connection is seen as the weak point and main limiter to initial physical rehabilitation [52, 53, 54]. One of the main advantages of the BPTB graft is faster and stronger integration as only hard to hard tissue bonding is required, with the enthesis maintained. Hamstring grafts have been found to fail to reproduce the fibrocartilginous enthesis with disorganised fibrovascular tissue forming in the bone tunnel rather than the bone-ligament functional enthesis [55, 56].

Due to the high failure rate revision surgeries for patients who require the replacement

or repair of a primary graft have been developed [47, 57]. The procedure - depending on the reasons for failure - is often complex requiring 2 stages; first repairing the bone tunnel with a graft material (typically harvested from the iliac crest, see section 1.3.3) and allowing that to heal, before performing a new ACL graft [47]. In addition to the inherent risk factors associated with multiple surgical operations and the issues from the bone donor site [58, 59], this process also requires a time period of 4-6 months to allow the bone graft to heal before the ligament graft can be performed, during which time the knee is liable to be unstable and can suffer progressive cartilage and meniscus damage [57].

1.2.3 Tissue engineered solutions

Due to the shortcomings of the established techniques discussed in the previous section there has been interest in developing a tissue engineered solution for replacement ACL grafts. Tissue engineering, which uses the patient's own cells to produce replacement organs and tissue, has emerged in recent decades as a field with great potential for changing the face of medicine [60]. Cells taken from the patient are cultured and expanded, seeded into a specially designed porous biomaterial scaffold, which once adapted by the cells can be implanted into the patient as a graft (Fig. 1.6). Such a method removes the need for donor sites, with minimal risk of infection or rejection by the body. Ideally implanted tissue engineered grafts will eventually be degraded and resorbed by the body leaving a fully integrated replacement composed entirely of native tissue.

Tissue engineered constructs need to recreate the micro-environment *in vitro* that the cells would experience *in vivo*. Engineered L/T need to provide mechanical strength to match that of the native tissues needs, in addition to supporting cellular proliferation and the formation of native like biological tissue. A number of variables are involved including the cell type(s) used, scaffold biomaterials and design, growth factors, and bioreactor conditions are important in determining the mechanical properties and biological viability

of the engineered product.

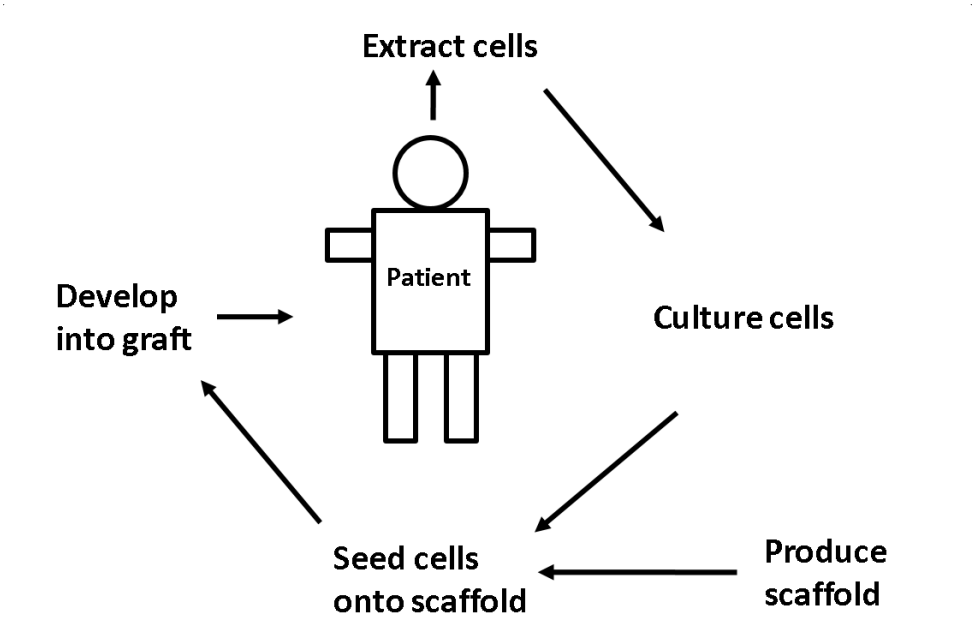

Figure 1.6: Tissue engineering method. Showing the process whereby cells are harvested from the patient, seeded into a specially designed scaffold, and allowed to culture until they are ready to undergo implantation to replace the original tissue.

The scaffold provides the necessary framework for cells to develop into the desired tissue [61], and so needs to encourage cell migration and proliferation, provide sufficient mechanical strength for post implant function, whilst degrading at a rate matched to biological proliferation. A multitude of biomaterials both synthetic and natural have been investigated for scaffolds. Collagen type I being the main composite of L/T has been a popular and an obvious option [62], however the mechanical weakness of reconstituted collagen type I has limited its success, leading to interest in other materials such as silk [63], and fibrin [64]. One of the major areas of interest has been using electrospun fibres to provide robust mechanical properties and highly aligned scaffolds to be produced [65, 66, 67]. Poly(L-lactide) fibres braided to form a porous structure have been shown to be effective in promoting cell in growth [68]. In addition to fibres that have been aligned there has also been work into producing self–crimping fibres that could be applied

to [69, 70]. The repurposing of decellularised tissues has been investigated by Wang *et al.* [71]. Increasingly multiphasic scaffolds designed to include regions representing bone-ligament-bone [72], and bone-interface-ligament-interface-bone [73] are being investigated.

The cell type used is important, the type of cells used and their source will determine their behaviour. Mesenchymal stem cell (MSC) have shown great promise but have shown potential for ectopic bone formation. Monoculture and co-culture have been used with one or more of osteoblast, tenocytes, mesenchymal and/or fibroblasts [74, 75, 76]. One of the major biological considerations is the use of growth factors. Growth factors are substances, typically proteins, that play a key role in cellular activity and the regulation of cellular processes. Growth factors can be added or encouraged to increase the up-regulation of L/T proteins and other components. Use of growth factors has shown increased mechanical strength, with enhanced proliferation of cells and expression of collagen type 1 and 3, and fibronectin [77]. However the types and quantity to use is hard to determine due to the complex nature and require considerable optimisation.

Bioreactors are used to provide a favourable environment for, and guide development of biological grafts by controlling conditions such as temperature, physiochemical environment, and external stimuli [78]. The use of bioreactors designed to apply forced to simulate the native environment as closely as possible for L/T can include functions such as periodic loading [79, 80]. Bioreactors can also be designed to aid monitoring of samples during development, with inbuilt chemical feedback and imaging [81, 82].

A major oversight in the development of tissue engineered solutions has been regarding the fixation of the construct to the bone. Much of the early work has focused on the formation/design of the intra-articular sinew and producing the desired biological and mechanical properties. Failure to form a strong attachment will create a risk of pullout for the graft. Attention has been increasingly given to the issue of attachment over the

last decade. A number of options simply coat the area that will be inserted into the bone tunnel with hydroxyapatite (HA) to encourage osteointegration [83]. More complex methods have been proposed using a multi phase scaffold to provide regions of differing properties through gradients in properties of the materials used [71, 72, 84]. The Lu group in particular has developed a triphasic scaffold system consisting of specially designed separate regions to recreate the multiple regions of the enthesis [85, 86, 87, 88]. A more detailed review on interfacial tissue engineering can be found by Paxton *et al.* 2012 [89] and by Qu *et al.* 2014 [90].

Whilst no true tissue engineered solutions have yet seen commercial human application success has been reported for engineered sinews used in animal models. Ma *et al.* 2011 [91] reported the implant of a bone-ligament-bone construct into a sheep as an ACL graft, with native like structure and strength observed after 6 months.

1.3 Bone to bone ligament construct

As discussed in the previous section, there is a need to produce a ligament graft that is able to effectively attach to and integrate with the bone, whilst allowing the smooth transfer of load across the attachment region. This thesis investigates the bone-to-bone ligament construct (BBLC) developed as a collaboration between the Grover group at the University of Birmingham, and the Baar group at the University of California, Davies (formally University of Dundee) [64, 92, 93, 94, 95, 96, 97, 98].

The BBLC mimics the BPTB graft (section 1.2.2) by depending only on hard/hard tissue bonding when implanted, with the intention of forming the hard/soft tissue attachment enthesis during the time being developed *in vitro*. The construct consists of a fibrin gel soft tissue sinew, held between two brushite cement anchors (Fig 1.7).

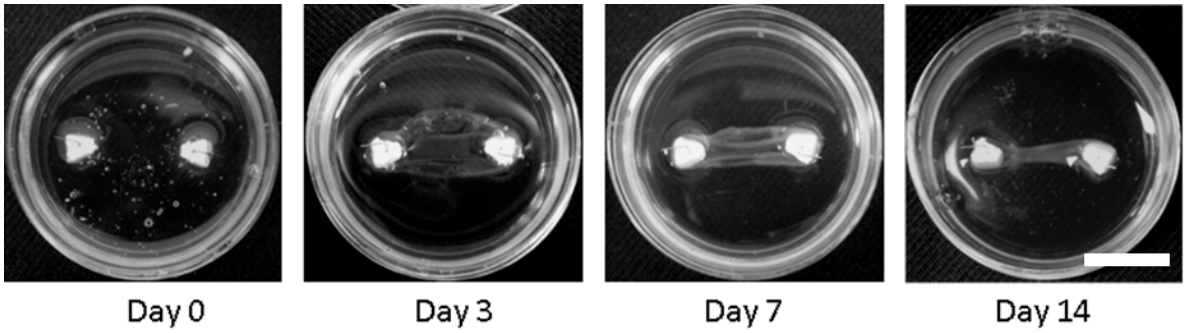

Figure 1.7: Photograph series of the bone-bone ligament construct during the first 7 days as it contracts to form the final ligament shape. Scale bar 10mm.

1.3.1 Formation

The construct is formed by pinning a pair of anchors into a well plate. A solution of thrombin is added and evenly distributed over the plate, fibrinogen is added and the fibrinogen/thrombin solution is allowed to set into a fibrin gel. The polyermised fibrin gel is seeded with chick tendon fibroblast (CTF) cells. Over time in culture the cells will migrate inside the fibrin matrix, rearrange and digest the fibres, causing the fibrin gel to contract. As the gel contracts it will be arrested by the anchors and become pulled into a taut ligament like structure. The initial contraction to the ligament shape takes about 1 week with the construct becoming mature at about 6 weeks [94].

The cell media/thrombin solution is supplemented with aminohexanoic acid and aprotinin as means of preventing protein degradation, and slowing the fibrinolysis - degradation of the fibrin matrix - by inhibiting proteolytic enzymes such as plasmin [99, 100].

1.3.2 Fibrin sinew

The soft tissue scaffold in the ligament construct is initially composed of a fibrin matrix seeded with CTF cells. Fibrin is a fibreous bipolymer protein that forms a 3D branching network when fibrinogen glycoproteins are cleaved by thrombin enzymes. Fibrin networks play an important role in the body by providing the first solid scaffold at wound

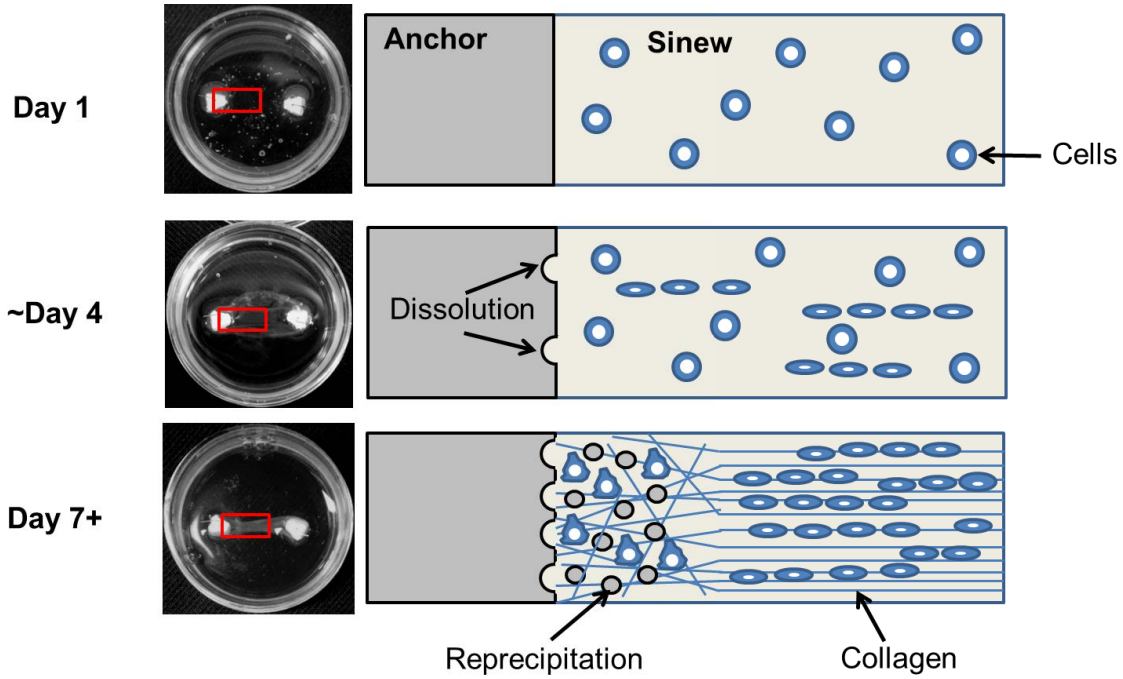

Figure 1.8: Theorised interface formation of the bone to bone ligament construct. Illustrating the expected changes in the composition and organisation; from the separate starting materials, during the first week of development, and when matured in the final form.

sites. Platelets will bind to and organise the fibrin [101], neutrophils and macrophages attach themselves to remove dead tissue and infectious agents [102], and fibroblasts anchor themselves to the fibrin first, when entering the wound site to reform the tissue [103]. Fibrinogen is produced naturally in the body and is an abundant component of blood plasma. Providing an accessible material, with minimal risk of infection or immune rejection when implanted [104].

Fibrin gels are assembled by a rapid modified polycondensation reaction between fibrinogen glycoproteins and thrombin enzymes. Fibrinogen is a 45nm long glycoprotein that is composed of three pairs of polypeptide chains [105]. Polymerisation is initiated by thrombin enzymes cleaving fibrinopeptides from the middle of the fibrinogen, producing a fibrin monomer [105]. The cleaving process exposes knobs at the middle of the monomer which are complimentary to holes found at both ends. As a result of interactions between the knobs and holes protofibrils of staggered fibrin monomers form. As more monomers

combine with the formed oligomers, they form two stranded protofibrils which aggregate into fibres [106]. Fibres branch trifunctionally to produce a three dimensional (3D) network [107]. The properties of the network such as fibre thickness, extent of branching and pore size can vary to a great extent depending on the polymerisation conditions [108].

When formed without guidance, the fibrin scaffold will consist of a highly disordered 3D fibre network [106]. Controlled patterning of fibrin has been demonstrated using flow forces, high magnetic field [109], and electrospinning [110]. When seeded the fibroblasts will migrate inside the fibrin and begin to reorder the fibrin fibres causing contraction. Over time the cells will begin to digest the fibrin fibres and deposit a new ECM.

As a cell scaffold fibrin has a number of desirable traits; it is able to adhere cells and growth factors [111], and has a high cell seeding density with an even distribution of cells [112]. It is also versatile in its delivery being usable as a moulded hydrogel, injected glue, or microbead [113]. As a result of the advantages and versatile nature fibrin has been investigated for use as a cell scaffold in cardiac, artery, muscle and neural tissues [99, 114].

1.3.3 Calcium phosphate cement anchors

Calcium phosphate (CaP) cements are a range of CaP based minerals with differing chemical compositions and activities [115]. CaP cements are formed when a powder and liquid phase are mixed and left to set. The resulting reaction will form a structure consisting of two of more phases; the product produced from the reactant, and any of the remaining reactant material. CaP cements have been investigated as bone graft materials with a number of commercial systems available. Cements can be delivered as a highly designed geometric structure [116] or, in the case of hydraulic cements, directly injected as a self setting cement [117]. They have also seen widespread use as coating for orthopaedic implants such as hip-replacements to encourage bone integration [118]. The porosity, pore size, pore connectivity, crystal structure, osteoinduction rate and other factors which in-

fluence the biological behaviour of the cement will depend on the conditions and materials used during the reaction [119, 120, 121].

Nomenclature in the area of calcium phosphates as they are used here is often confusing; the terms cement and ceramic commonly overlap in their use, and the definitions of each are often vague and ambiguous. Cements have been defined as a material capable of uniting fragments to form a solid whole [122], or a powdered material that if allowed to react with a suitable liquid phase will set to form a solid structure [123]. Ceramics are sometimes defined as being heat treated, but often fall under the same definition as cements. Henceforth materials that fall under one or both will be referred to as cements in this thesis.

As a bone graft material the use of a CaP cement will allow attachment of the anchor to bone tunnels drilled into the femur and tibia. Complications arising from an inability to form a strong attachment of the anchors to the bone tunnels could result in total failure of the graft (further information on this and investigation of chemical changes as a result in ageing in media are covered in Chapter 4). In addition to the attachment of the construct to bone tunnels, it is also thought that due to the sparingly soluble nature of the CaPs used, that the cement in contact with the sinew will undergo dissolution, with reprecipitation of mineralised particles into the soft tissue. This build-up of mineralisation will theoretically allow the formation of a graded interface, similar to that seen in the native enthesis (Chapter 3 investigates the ability of the BBLC system to mineralise the soft tissue around the anchor).

Development of CaP cements as bone grafts in biomaterials

Due to the limits of autograft and allograft bone materials, CaP cements have been increasingly investigated as potential graft materials [124]. In addition to cements there has

been interest in metallic and polymer based graft materials, or a combination of several types [120], however this work will focus only on the CaP based biomaterials. An ideal bone-graft material needs to be resorbable, mechanically strong, and osteoinductive; allowing the graft to be broken down and replaced by new bone without compromising the mechanical stability of the region [120].

The biological and chemical functionality of the CaP cement in an *in vivo* system is highly complex with a number of factors determining the biomaterial behaviour with regard to the resorbtion, and rate of osteoinduction [119, 120]. Surface architecture is known to play an important role, having been shown that it can be used to control osteoblast resorption [121], both macro (over 50μm) and micro (under 10μm) pores have been shown to be important [125]. The media that the cement is in plays a large role with a number of factors including the refreshment rate of the media, liquid to cement volume [126, 127], and media composition [126, 127] effecting the rate of dissolution.

The first studies began with tricalcium phosphate (TCP) ($Ca_3(PO_4)_2$) being injected into an animal model in 1920 [128]. Subsequently following the work of Brown and Chow [129], sintered HA ($Ca_5(PO_4)_3OH$) was the main focus during the 1980s due to its chemical similarity to natural bone mineral [130], and ability to set at a neutral pH [131]. However whilst it is superficially similar, native apatite has a nano-crystalline structure [132] whereas heat treated HA is micro-crystalline, this difference in crystal structure means that the specific surface area of the manufactured cement is much lower increasing the time required for it to be broken. Additionally bone is only 60-70% HA with the remainder composed of collagen matrix and other proteins which provide its unique ability to resist fracture [133]. These differences mean that HA functions differently on the biological and chemical level to bone. As a result HA is highly stable with a low resorbtion rate requiring time frames in the order of years for total resorbtion depending on the sample size and conditions [134]. Due to the mechanical mismatch between HA

and bone this has been known to cause complications years after implanting [134].

As a result of this there has been increasing research into other more soluble CaP phases (also known as salts, but will be referred to as phases in this thesis) as alternative materials. These include; octacalcium phosphate (OCP) ($Ca_8H_2(PO_4)_6 \cdot 5\,H_2O$), biphasic calcium phosphate (a mixture of TCP and HA), monetite ($Ca(HPO_4)$), and brushite ($CaHPO_4 \cdot 2\,H_2O$) among others [120].

Brushite, also known as dicalcium phosphate dihydrate (DCPD), is a metastable CaP cement that is stable over a pH range of 2-6 [135], and is known to undergo dissolution under *in vitro* conditions [126, 127]. The brushite CaP cement as a choice of anchor material is to serve two purposes; functioning as a bone graft material allowing effective integration to bone, and to encourage mineralisation of the bone/ligament interface. They are metastable under physiological conditions, so are resorbed by a mixture of cell controlled resorbtion and dissolution. This means that brushite will be resorbed at a significantly higher rate than HA *in vivo*. Additives can be added to reduce the setting time, control degradation and act as a slow release therapeutic drug.

Phase changes in CaP cements

One of the most important factors is the phase of the cement. In addition to dissolution, brushite can also undergo hydrolysis transforming it into a more stable phase. Such as for the transformation of brushite to calcium deficient HA in the presence of Ca ions, shown in equation 1.1 [136].

$$6\,CaHPO_4 \cdot 2\,H_20 + (4-x)CaCl_2 + (2-x)H_20 \rightarrow Ca_{10-x}(HPO_4)x(PO_4)_{6-x}(OH)_{2-x} + (8-2x)HCL + 12\,H_2O \quad (1.1)$$

Each phase has different dissolution and biochemical properties (Table. 1.1), with the stability of a phase at any given pH determined by the solubility isotherms (Fig. 1.9). In the knee joint the mean pH is 7.4 [137]. From this it can be seen that brushite, having a much higher stability than HA or OCP, is likely to undergo hydrolysis and produce unpredictable or varied results as solubility defines resorbtion rate. Given the much higher stability of HA over brushite, if a brushite implant is converted via hydrolysis to HA the time required for resorbtion will likely be dramatically increased and the benefit of using the brushite cement for osteointegration and interface formation lost.

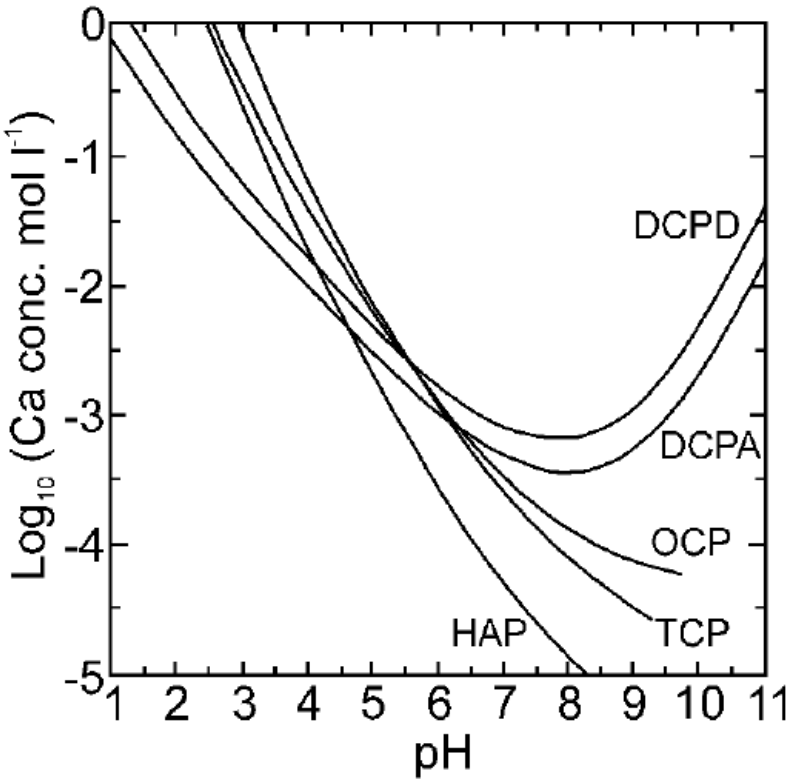

Figure 1.9: Solubility isotherms of calcium in different CaP phases plotted against pH. Reproduced from Borkiewicz *et al.* [138] with permission.

There has been extensive work performed looking at the supplementation of brushite cements to encourage faster dissolution and/or prevent hydrolysis and the formation of HA. Brushite modified with pyrophosphates [127, 139] and magnesium ions [140] has been shown to prevent apatite formation. The succcesful implementation of these systems has

produced varied results, cements that have resisted transformation *in vitro* have failed to do so under *in vivo* conditions. The addition of newberryite, a magnesium based orthopohpshate, for instance prevented transformation *in vitro* [141], but did not do so under *in vivo* implantation [142]. More work is required to understand the mechanisms involved and better control CaP behaviour.

Table 1.1: Calcium phosphate phase properties. Data from Dorozhkin 2012 [115].

CaP molar ratio	Phase	Formula	Solubility at 25°C -log(K_s)	Solubility at 25°C g/l	pH stablity range
1	Brushite	$CaHPO_4 \cdot 2\,H_2O$	6.59	0.088	2.0-6.0
1.33	OCP	$Ca_8(HPO_4)_2(PO_4)_4 \cdot 5\,H_2O$	96.6	0.081	5.5-7.0
1.5	β-TCP	$Ca_3(PO_4)_2$	28.9	0.0005	
1.67	HA	$Ca_{10}(PO_4)_6(OH)_2$	11.6	0.0003	9.5-12

1.3.4 BBLC development and progress

The development and optimisation of the ligament construct as a whole and a number of independent factors has been previously reported in a number of papers by Paxton *et al.* [64, 93, 94, 95], and the thesis of Dr. Jennifer Z. Paxton [92] and Uchena N. Wudebwe [96]. As mentioned earlier the construct forms via the contraction of a fibrin gel into a taut ligament body. It takes approximately 1 week for the sinew to contract, 2 weeks for it to form a single tubular structure, and 6 weeks for the mature ligament to form [94]. During this time the construct has been shown to undergo significant macro and biochemical changes.

During the contraction process, constructs become more opaque and white in appearance as they develop. Structurally the sinew has been observed to fold over on itself during contraction, creating a layered structure as shown using optical coherence tomography (OCT). The addition of ascorbic acid and proline has been shown to encourage the deposition of collagen, with up to 16% collagen content reported in supplemented constructs after 5 weeks as opposed to 6% in control samples, consisting mostly of type I but with type XII also present at the centre of the sinew [94], up to 50 % collagen content has been found in nonpublished data. The quantity added has been shown to have a large effect with the contraction of the sinew increasing to a more taut structure with a smaller cross sectional area with the addition of the supplements [94]. The reason behind this has been theorised as possibly due to increased cross linking between the denser collagen fibrils, or the increased cell number as a result of supplementation digesting the matrix at a higher rate [64].

Initially a poly(ethylene glycol) diacrylate hydrogel with HA incorporated into it was used to encourage attachment [143] before moving on to brushite anchors as reported in later work. The choice, composition, and shape of anchor material has been investigated [93]. Imaging about the edge region between the anchor and soft tissue has shown there is an interface between the two materials [64], but has been unable to clearly show any mixing

of the materials or mineralisation.

The mechanical properties of the construct are fundamental to the successful implementation. The mechanical properties have been improved through optimisation, but are still relatively poor, being several orders of magnitude below the level required for the demands of *in vivo* application [64, 93, 94]. In addition to constructs formed under static conditions constructs have been matured whilst undergoing periodic cyclic loading in a bioreactor [95]. Constructs that underwent periodic loading showed that the applied load upregulates the ERK 1/2 pathway enhancing the rate of matrix deposition. Wrapping of multiple sinews around each here has been investigated as a means of increasing the mechanical strength [97], with successful bonding of cells between the separate constructs observed under optical microscopy.

The 6 weeks required for formation of a mature construct is prohibitive from a clinical point of view. As a result of the need to provide a faster solution recent work has investigated a move toward preprepared constructs through the decellularisation, dehydration and storage of matured sinews [98]. It has been successfully shown that the sinews can be subsequently rehydrated and populated with an autologous cell population. The study also found that the mechanical properties of the construct increased as a result of the process with a 2.6 fold increase in maximum load and 8 fold increase in ultimate tensile strength reported. Reasons for the increase in the load bearing properties were given as a reduction in the fluid volume and cross sectional area of the sinew allowing a higher level of interaction between the polymer chains increasing the sinew stiffness.

1.3.5 Need for further work

The formation of the construct is a highly dynamic process. In such a complex system it is important to understand the changes that are occurring in each section of the construct (cement anchor, hard/soft tissue interface, sinew body). The loading bearing ability of

the sinew is the main issue that needs to be resolved, to improve this a comprehensive understanding of each element in the system will be required. The intended formation of the mineralised interface, shown in Fig. 1.8, is lacking evidence. Additionally the microstructure of the sinew is poorly documented during the development with only large scale changes understood.

1.4 Application of imaging techniques

With the development of tissue engineered constructs there is an important need to monitor their formation and responses to stimulation as *in vitro* test samples or before and after *in vivo* implantation. A range of imaging techniques exist that are able to provide information about one or more of the topography, composition and mechanical properties. This allows a large complimentary picture to be built up through the combination of multiple techniques. Information analysed from imaging data will be important to understand the fundamental mechanisms driving the formation and properties of the constructs, and optimise future designs. This section provides a brief overview of the main imaging techniques used in the presented work, with regard to the relevant instrument specifications and functionality. Imaging techniques were used to look at the sample morphology (confocal microscopy, nonlinear microscopy, electron microscopy, cellular structure and organisation (confocal microscopy, nonlinear microscopy), chemical and biochemical distribution (confocal Raman), large scale morphology and mineral distribution (Micro-CT, optical microscopy, electron microscopy), and mechanical variations (atomic force microscopy). An overview of each technique is shown in Table. 1.2, note that the information presented is for the instruments and techniques used in this work.

Those wishing to learn more about each technique can find relevant reviews and books covering each modality in greater depth; confocal scanning microscopy [144], nonlinear microscopy [145], electron microscopy [146], confocal Raman microscopy [147], micro-CT [148, 149], and AFM [150].

Table 1.2: Overview of imaging techniques used in the experimental work. Data from Bannerman 2013[151].

	Confocal	**Nonlinear**	**EM**	**CRM**	**Micro-CT**	**AFM**
Type	Optical	Optical	Electron beam	Optical	X-ray	Scanning probe
Soft tissue	Yes	No	Yes	Yes	No/Yes	Yes
Hard tissue	No	No	Yes	Yes	Yes	Yes
Resolution limit	200nm	400nm	nm	200nm	μm	nm
Image scale	μm/mm	μm/mm	nm/μm	μm/mm	μm/mm	nm/μm
Preparation	Flat surface Staining	None	Splutter coating Thin layer (TEM)	Flat surface flat surface	None	Flat surface
Destructive	No	No	Yes	No	No	No
Advantages	Single plane 3D stacks	Label free 3D stacks mm penetration	High resolution Elemental mapping crystal structure (TEM)	Chemical mapping Chemical mapping	3D reconstruction	Mechanical properties High resolution
Disadvantages	Low penetration Label photobleaching	Instrument availability	Preparation and imaging is highly destructive	Weak signal	Soft tissue information is limited	Surface only Needs very smooth surface

1.4.1 Confocal laser scanning microscopy

Since the initial work of Robert Hooke [152] and the early pioneers of lenses in the 1600s the application of optical microscopy to biological samples has become widespread with a number of different modalities and methods providing a wealth of information [153, 154].

One of the most popular techniques to emerge in recent years for biological purposes is confocal microscopy. The principle is very similar to that of a standard wide field microscope (Fig. 1.10). The key difference is the use of a pinhole before the detector enables out of focus light to be blocked, effectively limiting the light that is collected to a single diffraction limited volume - the Airy disk. The size of the disk is given by a Gaussian determined by the optics of the system [155]. An image is produced by raster scanning the excitation laser across the sample with a pixel collected at each point. Providing sharp images over a single plane, and allows stacks to be built showing a three dimensional volume by changing the focal plane with respect to the sample. The depth to which sufficient signal can be obtained will limit the range for 3D stacks and be dependent on the scattering properties of the sample; skin can only be penetrated to approximately $10\mu m$ at 488nm due to opaque high scattering structure, whereas the much more transparent corneal epithelium can be penetrated to approximately $200\mu m$ [156]. Under ideal conditions a resolution down to the diffraction limit of the system (potentially in the order of 200nm) can be obtained.

Samples can be labelled with fluorescent probes that attach to a specific biological component. These fluorophores are excited over a discrete spectral range and emit light at a well defined lower energy range, allowing the use of a carefully chosen excitation laser and detection filter to capture images showing only a single fluorophore. By using multiple stains with spectrally separated excitation wavelengths, the excitation laser wavelength and detector filter can be switched and multiple images acquired at each location of different components which can be combined into a composite providing a more detailed image.

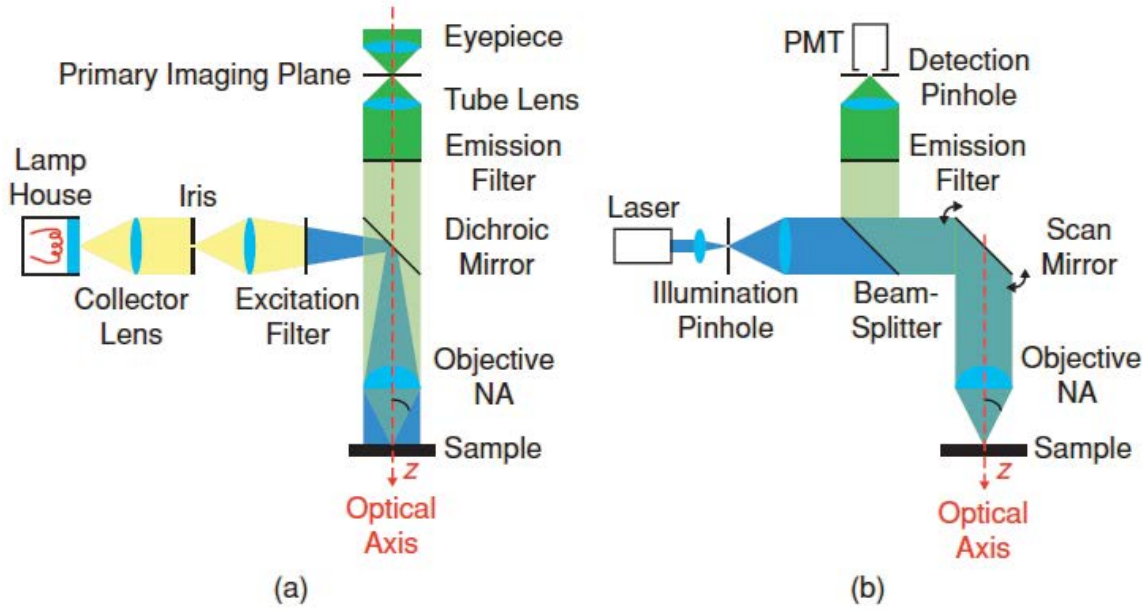

Figure 1.10: Schematics for (a) widefield and (b) confocal microscopes. Modified from Vonesch *et al.* 2006 [144] with permission.

In this study the fluorophores 4',6-diamidino-2-phenylindole (DAPI) [157] and phalloidin [158] which attach to the cell DNA and actin respectively. The life time of fluorescent probes is limited by an effect known as photobleaching. When excited, chemicals are more reactive, and so the fluorophore can become locked in the excited state and signal is lost.

1.4.2 Nonlinear microscopy

Nonlinear microscopy is a subset of optical microscopy that has emerged as a powerful technique in the last few decades. The nonlinear description refers to the nonlinear increase in the signal obtained with increase in incident beam intensity. Due to the nonlinear nature of the excitation interactions produce signal only in focal volume producing a confocal-like image. The longer wavelengths used reduce the chance of photobleaching and phototoxicity to samples. However this can be offset by the high density of photons required to produce sufficient two photon absorption rates [145]. Two photon (TP) and second harmonic generation (SHG) are nonlinear multiphoton microscopy imaging techniques:

Two photon autofluorescence is the absorption of two incident photons near simultaneously, resulting in the emission of . TP excited fluorescence is able to detect biological structures such as cell bodies and elastin depending on the sample and wavelengths used [145, 159]. The endogenous cellular signal is provided by autofluoresence in the cell, for fibroblasts the cellular components nicotinamide adenine dinucleotide, and flavin adenine dinucleotide excite in the TP range and provide signal giving an idea of cell parameter and structure [160, 161].

Second harmonic generation is the process by which photons of the same frequency are combined together upon interacting with a noncentrosymmetric material, producing a single frequency doubled photon [162]. SHG microscopy therefore uses the difference in emitted SHG light at each spatial location to provide contrast in images. In biological samples collagen is able to emit SHG light, allowing collagen to be observed independently and without the need for staining or other complex or destructive preparation. Individual collagen fibres can be resolved, mature and developing collagen fibrils differentiated [162], and the effect of strain on the collagen in the tissues studied by application of a mechanical load [163, 164].

Due to the signal generation from the sample no addition preparation such as staining is required, and the penetration depth reduces the need to section samples.In addition to the basic TP autofluoresence and SHG signals, the technique can be combined with stains such as DAPI to show cell nuclei, or other imaging modes, such as coherent anti-Stokes Raman spectroscopy (CARS) tuned to detect lipids, allowing cell bodies to be visually localised alongside multiple ECM components [159].

1.4.3 Electron microscopy

Electron microscopy (EM) is an imaging method that uses a high voltage electron beam to produce signals that provide topological and compositional information on samples [146]. An electron gun fires a beam of electrons at relativistic energies that are focused via condensers and electromagnetic lenses onto the sample. Due to the small wavelength of the high energy electrons a much higher resolution can be obtained than with optical techniques, making EM highly attractive for the study of cells, ECM and mineralised particles. However invasive preparation and harsh imaging conditions prohibit live sample imaging and are often destructive to the sample [146]. The two main types of electron microscopy are scanning electron microscopy (SEM) and transmission electron microscopy (TEM).

In SEM the electron beam is scanned across the surface of the sample, with the signal gathered from electrons and/or x-rays that are emitted up from the sample. SEM can achieve resolutions down to the nm and produce images covering areas from submicron to mm [146]. The most common signal type used for imaging is secondary electrons ejected from atoms in the sample which allow high depth of field images to be produced. Backscattered incident X-rays produced by Compton scattering in the incident electron beam provide elemental information on the elemental composition of the sample [146]. A conductive sample holder and sputtering with a thin coating of a conductive material are required to prevent the build up of electrons, unless an atmospheric chamber is used in which case the sensitivity is reduced [146].

TEM uses the scattering of electrons passing through the sample as signal to produce an image, and allows an even greater resolution that SEM, potentially down to the angstrom level [165]. For electrons to be transmitted the sample must be very thin, typically 100nm or less [165] making preparation highly destructive to the sample. In addition to images, diffraction patterns can be produced which can be used to determine the

crystalline structure of the sample [165].

1.4.4 Confocal Raman microscopy

The Raman effect is the inelastic scattering of light due to the interaction of an incident photon with the vibrational modes present in molecules [166]. A laser with highly coherent photons is shone onto the sample, light is scattered back either elastically or inelastically. The majority of the returned light will be elastically scattered (also known as Rayleigh scattering), with only a very small number of photons - typically less than 1x10^6 scattering photons - undergoing Raman scattering [147]. The quantity will depend on the materials and excitation wavelength, but relative intensity ratio for Rayleigh to Raman is often greater than 10^9 [167]. Raman scattered light is typically measured in wavenumber units (cm^{-1}). In this study the wavenumber axis will be presented negative-to-positive.

The Raman effect (more properly but less commonly known as the Smekal-Raman effect) was predicted by Adolf Smekal in 1923 [168], and shown by Sir Chandrasekhara Venkata Raman in 1928 [169]. However due to the low sensitivity of the technique substantial efforts were required to collect data at the required signal-to-noise ratio (SNR), making the technique less appealing than IR until the widespread appearance of lasers and development of high quantum efficiency charged-coupled device (CCD) photo detectors in the 1960s. Advances in recent years with the introduction of low temperature CCDs to reduce dark noise, a range of applicable laser wavelengths from ultraviolet (UV) 244nm to infra-red (IR) 1060nm, and spectrograph gratings allowing whole spectra to be recorded at once through 1000 or more channels have made Raman scattering increasingly practical and commonplace [147]. The laser wavelength and system set-up used will often be determined by the sample. Raman scattering intensity is inversely proportional to the wavelength λ, in the form λ^{-4}. However biological samples are often highly fluorescent and vulnerable to heat damage under low wavelength lasers. So red or NIR wavelengths such as 785nm are often used in these cases [147].

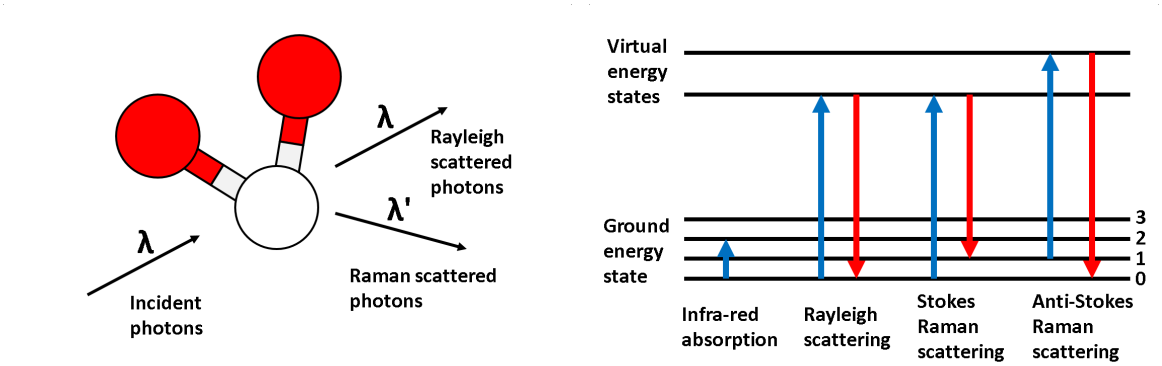

(a) (b)

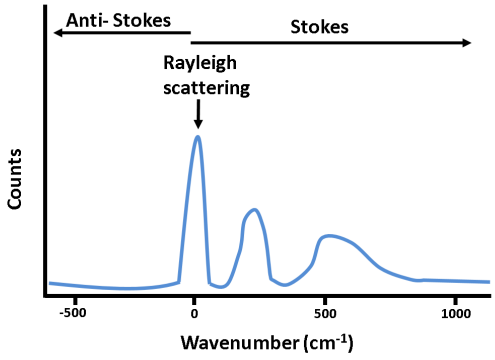

(c)

Figure 1.11: Principles of Raman spectroscopy. (a) Raman scattering off a molecule. (b) Photon absorption and emission in different mechanisms. (c) Example Raman spectroscopy spectrum showing the different regions (note that the Rayleigh peak is often removed by use of filters).

By recording the energy shift in the scattered light a spectrum can be produced. The presence, and location of peaks (also known as Raman bands) in the spectrum provides information on the chemical bonds present. The intensity, shape, full width half maximum (FWHM), and spectral shift of peaks present in the spectrum can provide a further wealth of information on the current state and environment of the sample such as the phase [170], crystallinity [171] and polymorphism [172]. A number of peaks have been identified and assigned for organic and inorganic compounds [173, 174, 175]. The nature of Raman scattering means that samples do not require staining and acquisition of multiple

analytes (multiplexing) can be performed. Generally the data will require pre and post processing before effective analysis can be performed [147]. Cosmic ray removal, baseline correction, smoothing, deconvolution and peak separation are commonly performed [147].

Raman spectroscopy is very similar to IR spectroscopy which also provides information on the vibrational modes of chemical bonds, and the two are often used to provide complimentary data on samples [176, 177]. The selection rules for each determine the presence and strength of bonds that are detected. IR focused on the absorption/transmission of wavelengths due to interacting with molecular bonds, as a result of the difference IR shows symmetric and Raman shows asymmetric bonds. Raman has the advantage of the signal not being blocked by water like in IR.

Due to the high level of information that can be obtained with non-destructive and non-disruptive means, Raman spectroscopy is becoming increasingly popular as a tool for investigating the composition of tissues [3, 178, 179, 180], monitoring wound healing [181], and other biomedical areas such as scaffold development in tissue engineering [182, 183, 184, 185, 186].

Confocal Raman microscopy (CRM) is the combination of Raman spectroscopy with a confocal imaging system (as discussed in the previous section) using the confocal optics system to guide the scattered light to the detector, which allows a spectrum to be obtained at discrete points. A map can be acquired by collecting a spectrum at each grid of points over the sample. This allows hyperspectral imaging maps to be produced showing the distribution of a particular species or variations between multiple species based on the ratio in peak heights. In addition to the precise mapping the confocal system provides a smaller detection volume, reducing the quantity of fluorescence [147]. However the inherently weak nature of the Raman effect limits the quality of mapping resolution and/or spectral integration time, to avoid sample damage and unreasonably long mapping times.

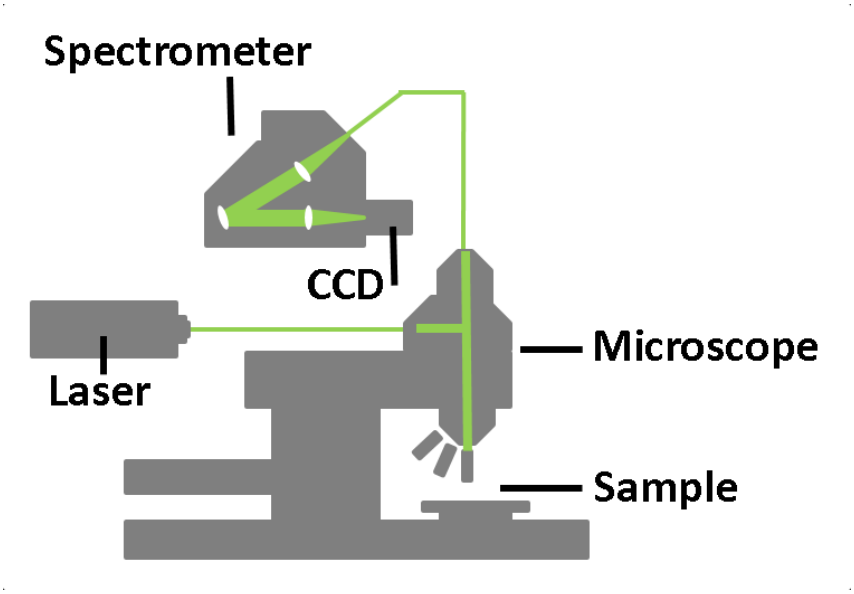

Figure 1.12: Confocal Raman Microscope upright instrument layout. Based on schematic from Dieing 2011 [147].

Line and global acquisition methods can reduce this by an order of magnitude but are less sensitive due to higher laser diffusion inside the sample [166]. Additionally the limited depth penetration of confocal microscopy is further reduced by the weak signal from Raman scattering, with refraction being shown to further limit and effect depth sensitivity [187, 188].

In addition to standard spontaneous Raman scattering a number of enhanced signal techniques have been developed in recent decades [189], these are not used in this study but are mentioned in the discussion. Surface enhanced Raman spectroscopy (SERS) exploits a plasma-resonance effect exciting the surface of a local nanoparticle or substrate that causes a high scattering cross section, creating a 10^6 or greater increase in the Raman signal [190]. SERS methods can interfere with the sample, shifting or changing the bands present in the spectrum. Coherent Raman scattering techniques uses two synchronised lasers to focus excitation on a single band. CARS [191] and stimulated Raman spectroscopy (SRS) [192] are the two main variations. Both provide a signal several orders of magnitude higher than spontaneous Raman, allowing for video rate capture [193, 194],

but are limited by the requirement of specific tuning and the complex nature limiting the number of instruments and their availability.

1.4.5 Micro-CT

The three-dimensional information provided by optical techniques in thick opaque samples is very limited. X-ray based techniques are able to non-destructively provide information on complete samples without the need for physical or chemical preparation. Micro computed tomography is an off-shoot of standard computed tomography (CT). Developed as a result of the need for high resolution tomographic imaging of small samples, typically in the order of a cm in diameter. Standard absorption based micro-CT provides information on morphology with contrast given by difference in X-ray attenuation at each location. A resolution down to $5\mu m$ with corresponding voxel volumes of $1\text{x}10^{-7}$ cubic mm can be achieved.

X-rays beams passing through a material are attenuated based on the density and electron configuration at each point, and the incident X-ray energy. The type of attenuation in the range used by micro-CT instruments is dependent on the X-ray energy with the photoelectric effect dominating below 25keV, and Compton scattering being dominant at higher energies [148]. By passing X-rays through a sample and detecting their intensity, X-ray radiography produces a shadow image showing the internal structure, purely in two-dimensions with depth information lost. CT methods collect a number of shadow images around the sample and use them to reconstruct the volume. The most commonly used technique in micro-CT is cone beam, which projects a magnified shadow image of the sample onto a detector array. X-ray projection images are acquired of the sample which is rotated about it's vertical axis between the X-ray source and detector [148]. The use of a cone beam allows the entire volume to be acquired at each angle, minimising the number of exposures required. An inverse Radon transform can be applied, to produce a three-dimensional reconstruction of the attenuation of each point in the volume through

filtered back projection.

Soft tissue contrast is often very poor with micro-CT even at low energy levels due to the low electron density of the tissue. Iodine and metal based stains can be used to increase contrast, with Metscher [195, 196] showing whole animal staining, and Jeffery *et al.* 2011 showing iodine providing contrast for individual muscle fibres [197]. Only the attenuation of the material at each volume is provided so no specific chemical or biological information beyond that which can be deduced from the morphology. Dual energy [198, 199] Phase contrast [200, 201, 202], fluorescence [203] and spectral would provide such information,but is still in early developmental stages [204]. In addition to the limitations of the information, artifacts and misleading results can be present in micro-CT. Ring artifacts occur as a result of differences in pixel sensitivity across the CCD detector, and beam hardening [205]. The use of beam filters and instrument calibration combined with algorithms have been developed to correct for these during or after reconstruction [206]. Whilst the method is nondestructive, exposure to ionising radiation can damage samples, especially by the dose applied to live cells. The absorbed dose is dependent on the exposure time and X-ray beam properties. No live imaging is done in this study so the chance of damage is minimal and of no real concern.

The ability to non-destructively produce three-dimensional information on scaffolds has made micro-CT a popular modality in tissue engineering for looking at hard and soft tissue scaffolds and their development [207, 208]. One particular application of interest is the use of micro-CT as an effective means of studying mineralisation of soft tissue scaffolds [209].

1.4.6 Atomic force microscopy

Atomic force microscopy (AFM) is a high resolution scanning probe technique that can provide images of the topology and mechanical properties of samples [150], first devel-

oped by Binnig in 1986 [210] it has become an important technique for analysing material properties at the nano and micro scales. The principle behind the method is that a laser illuminated cantilever with a sharp point is moved across the sample, as the cantilever interacts with the sample the laser spot is deflected up or down. By measuring the deflection on a photodiode array the level of deflection can be determined. An image is built up by changing the x-y location of the probe and producing a colour map of the reading at each point as it is scanned across the sample.

As the probe is not limited by a diffraction limit a higher resolution than SEM and optical techniques can be achieved [150]. Additionally forces down to the nN level on the sample can be achieved [211], allowing highly sensitive measurements with minimal damage to delicate materials like soft tissues. Scans can be performed in fluid or ambient air requiring no sample preparation or treatment required beyond a reasonable flat surface. However an uneven or rough sample is liable to produce artifacts by distorting the cantilever movement, along with other sources of error such as thermal drift from changes in the ambient temperature [150]. Scans are typically limited to an area at most a few hundred microns across, making it impractical for large sample analysis.

Mechanical properties of the sample such as hardness and stiffness can be calculated and mapped from the acquired data. Measurement of mechanical properties [212], for fragile soft tissue samples this is ideal with minimal risk of disruption from the probe. Indentation can be performed by measuring indent caused by AFM tip and calculating the elastic or Young's modulus [212]. Significantly analysis of soft tissues has been presented by Zhu *et al* [212]. Such a technique for mapping mechanical properties with high sensitivity and minimal sample disruption, is theoretically ideal for application to measuring the mechanical gradient between the hard and soft tissues in the BBLC.

1.5 Research aims

The aim of the work presented in this thesis is to investigate the development of the ligament construct and the suitability of the system for *in vivo* implantation with a focus on the use of imaging techniques. Specifically:

- Develop methods for imaging the biological, chemical and topological development of the BBLC. To allow a comprehensive investigation of the system and the underlying mechanisms involved.
- Elucidate the mineralisation mechanism at the interface. Specifically how exposure to heated cell media effects the dissolution and chemical state of the CaP cement anchors as a result of *in vitro* ageing.
- Investigate the biological formation of the system, with regard to how seeded cells react to, and reorganise the soft tissue gel.
- Investigate biomineralisation of the sinew.

The work is divided into chapters as detailed below and illustrated in Fig. 1.13.

- Chapter 3 investigates the formation of a mineralised interface between the hard and soft tissues as a result of culture under *in vitro* conditions.
- Chapter 4 investigates the biological development of the ligament sinew, focusing on the changes in cellular and ECM structure and orientation as the construct contracted and the mature ligament formed.
- Chapter 5 investigates chemical changes in the calcium phosphate phase in the brushite anchors as a result of time spent under *in vitro* conditions.
- Chapter 6 investigates the induced mineralisation of the soft tissue sinew to create a biomineralisation model using the BBLC.

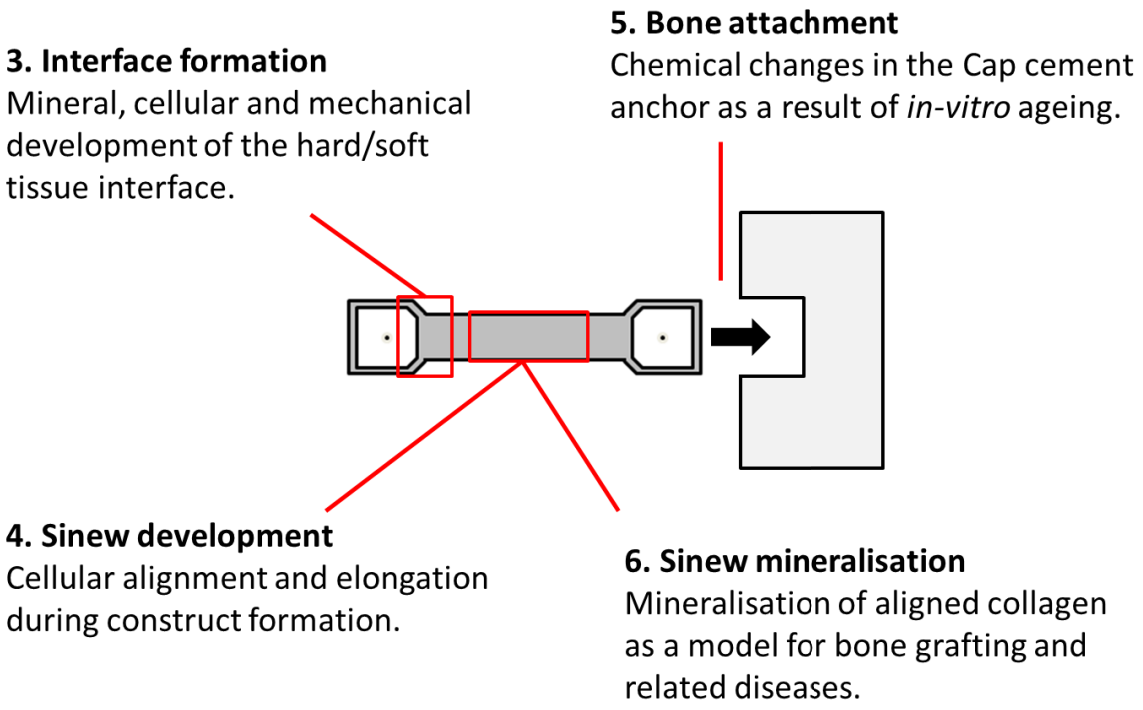

Figure 1.13: Overview of the focus of each results chapter presented in this study.

CHAPTER 2

METHODS

2.1 Phosphate buffered saline solution

Two phosphate buffered saline (PBS) tablets (Sigma-Aldrich, UK) were dissolved in 400mL of distilled water to yield 0.01 M phosphate buffer, 0.0027 M potassium chloride and 0.137 M sodium chloride. Alternatively, 4 PBS-Dulbecco A tablets (OXOID, UK) were dissolved in 400mL of distilled water.

2.2 Autoclaving

PBS and distilled water solutions were sterilised by autoclaving at 115°C for 15 minutes.

2.3 Cell preparation and culture

Cell work was performed under sterile conditions in a laminar flow hood (BSB, Gelair Inc Biomedicals, Germany) with all materials and tools sterilised before use and/or sprayed with 70% ethanol before being entered into the hood.

2.3.1 CTF cells

Cells were prepared as described in [94]. Embryonic chick tendon fibroblasts were isolated from the flexor tendons of 13.5 day old chick embryos by a 1.5 hr digestion in the collagenase type-II solution (in serum, and antibiotic-free DMEM) at 37°C. After digestion, the solution was passed through a 100mm cell strainer (BD Biosciences, UK) to remove any insoluble material. The cell solution was spun at 2500 rpm for 3 minutes. The obtained cell pellet was suspended in DMEM supplemented with 10% FBS and 1% P/S (Invitrogen, UK). Cells were frozen at -196°C in 1mL vials of CTF cells in a 10% dimethyl sulfoxide 30% foetal bovine serum (FBS) and 60% DMEM solution.

2.3.2 Cell thawing

A 1mL vial of CTF cells stored in liquid nitrogen at -196°C was thawed in a waterbath (JB Aqua 12, Grant Instruments, UK) kept at 37°C. The 1mL cell suspension was transferred to a 50mL centrifuge tube, with 9mL of supplemented Dulbecco's modified eagle's medium (sDMEM) was added. The 10mL cell suspension was pipetted up and down in succession to separate cells before centrifuging (MSE Mistral 2000, UK) for 3 minutes at 1000rpm. The supernatant was aspirated and the cells were resuspended in 10mL of fresh sDMEM. The cell suspension was then transferred to a T-75cm^2 flask for expansion in a humidity controlled incubator (InCusaFe MCO-15AC, Sanya, Japan) at 5% CO_2 and 37°C.

2.3.3 Cell culture

Cells in T-75cm^2 flasks were cultured until they reached -70% confluency and were then passaged into T-175cm^2 flasks. The sDMEM growth medium was changed every 2 to 3 days. Cells between passages 2-5 were used for BBLC or split before reaching confluency.

2.3.4 Cell dissociation from flasks

Spent sDMEM medium was aspirated and the cells were washed in PBS. 1mL of TrypLE Select 1X solution (Invitrogen, UK) was added to a T-75cm^2 flask and incubated for 1-5 minutes at 37°C. To aid cell detachment from the flask, the flasks were tapped gently to assist the dissociation process. TrypLE was deactivated by adding 9mL of sDMEM. Where T-175cm^2 flasks were used, 2mL of TrypLE was added, which was deactivated using 8mL of sDMEM.

2.3.5 Cell counting

A drop taken from the cell suspension was loaded onto a haemocytometer, and cells distributed in the 5 square grids were counted. The sum of the combined squares was multiplied by 2000 to give the cell count in 1mL of the sDMEM cell suspension. Which was then multiplied by the total volume of the cell suspension solution. For each suspension two counts were taken and the average used.

2.4 BBLC materials and production

2.4.1 Brushite anchors

Orthophosphoric acid (H_3PO_4) (Fisher, UK) was supplied as 85% w/v in water, a concentration of 15.2M. To prepare 100mL of 3.5M acid, 77mL of distilled water was added to 23.03mL orthophosphoric acid to obtain 3.5M orthophosphoric acid. 96mg of citric acid (Sigma-Aldrich, UK), and 96mg of sodium pyrophosphate (Sigma-Aldrich, UK), were added to the acid, to obtain 50mM citric acid and 50mM sodium pyrophosphate in 3.5M orthophosphoric acid.

Brushite anchors were manufactured by mixing β-TCP with 3.5M orthophosphoric acid

supplemented with 200mM citric acid and 200mM sodium pyrophosphate, in a 3.75 g/mL ratio. The solid and liquid phases were mixed in a plastic weighing boat with a spatula on a vibrating stage, then transferred into a custom designed trapezium mold (3mm back, 1mm front, 3mm length, 3mm depth, total volume of 18 cubic mm), had a stainless steel pin inserted through the centre and was left to dry overnight.

2.4.2 Sylgard prepared well plates

SYLGARD polymer solution was prepared by mixing the SYLGARD base to catalyst at a ratio of 10:1 (SYLGARD 184 Silicone Elastomer Kit, Dow Chemical Company, USA). Approximately 1.5mL of the polymer solution was added to 35mm diameter well-plates. The polymer filled plates were left on a flat surface to polymerise at room temperature for 7 to 14 days.

2.4.3 Thrombin

1% w/v BSA in F12K was prepared by adding 1mg BSA powder (Sigma-Aldrich, UK) per mL of Ham's F12K (Kaighn's) medium (Invitrogen UK). 5mL of the BSA/F12K medium was added to each 1000 Units thrombin (UT) vial (Calbiochem, UK or Enzyme Research Laboratories, UK) resulting in a stock of 200UT/mL. Solutions of 200UT/mL were transferred into Bijou tubes and frozen at -20°C. When needed the prepared thrombin was removed from the freezer and defrosted at room temperature.

2.4.4 Fibrinogen

Fibrinogen solutions were prepared by dissolving 20mg of fibrinogen (Sigma-Aldrich, UK) per mL of Ham's F12K (Kaighn's) medium (Invitrogen, UK) in a waterbath at 37°C for a period of 4 hours. The 20mg/mL fibrinogen solution was gently shaken every hour to ensure dissolution of the fibrinogen powder. Thereafter, the fibrinogen was sterile filtered using $0.22\mu m$ syringe filters. Alternatively, fibrinogen was sterilised sterile filter, frozen at

-20°C. When needed the prepared fibrinogen was removed from the freezer and defrosted at room temperature.

2.4.5 Ascorbic acid and proline solutions

L-ascorbic acid 2-phophate sesquimagnesium salt hydrate (Sigma-Aldrich, UK) was dissolved in phosphate buffer saline by dissolving 0.869g in 12mL of PBS. The final solution had a concentration of 250mM and was syringe filtered to sterilise.

50mM L-Proline solutions were prepared by dissolving 69mg of L-Proline (Sigma-Aldrich, UK) in 12mL of PBS. The solutions were then sterilised by syringe filtering.

2.4.6 Construct production

Ligament constructs were produced using the methodology described by Paxton *et al.* 2010 [64]. Pairs of anchors were pinned pointing toward each other 10mm apart in a SYLGARD (Dow Chemical Company, USA) coated 36mm well plate and sterilised in 70% ethanol for 20 mins. 500μL of thrombrin containing growth media (Dulbecco's modified eagle's medium (DMEM) (Sigma-Aldrich, UK) supplemented with 10% fetal bovine serum (Biosera, UK) and 1% penicillin/streptomycin (Sigma-Aldrich, UK) containing 2μL/mL thrombin (Calbiochem, UK), 2μL/mL 200mM aminohexanoic acid (Sigma-Aldrich, UK) and 50μL/mL aprotinin (10mg/mL; Roche, UK)) was added evenly and perturbed to cover each plate. 200μL of 20mg/mL fibrinogen (Sigma-Aldrich, UK) was added to each plate drop wise and left to polymerise for 1 hr at 37°C. Embryonic chick tendon fibroblast cells between passage 2 and 5 were seeded on top of the gel with a cell concentration of 100x10^3/mL. Constructs were aged in incubators at 37°C with a 5% CO_2 atmosphere. The cell media was changed every 2-3 days with 2mL of sDMEM, supplemented with 10% bovine serum, 1% penicillin/streptomycin, HEPES (Sigma-Aldrich, UK), L-glutamine (Sigma-Aldrich, UK). From day 7 onward 50μM ascorbic acid (Sigma-Aldrich, UK) and 50μM proline (Sigma-Aldrich, UK) were added to encourage collagen deposition. Plates

which developed a yellow hue indicating a change in pH due to a high level of brushite loss were discarded. Instances of fibrin sticking to the plate during contraction were dislodged using sterilised pipette tips.

2.4.7 Removal from media

For removal from culture, DMEM media was removed, constructs were washed with PBS (3x5mins), fixed in 4% formaldehyde overnight, washed in PBS (3x5mins). Samples were stored in PBS at 4°C to keep them hydrated until imaging.

2.5 Note on preparation and consistency of constructs

Preperation after removal from culture

The dynamic and fragile nature of the constructs made consistent preparation problematic. During the first 7-10 days the soft tissue is thin and highly flexible which presented significant problems in the handling of the sinews. Cryotoming samples to provide a flat surface was liable to distort or damage the interface and brushite anchor. When possible the steel pin was removed to reduce the limiting effect it had on the cryotoming process. Attempts to reduce the effect by setting the SYLGARD around the anchors or digging pits in plain SYLGARD proved ineffective with the anchors being coated in a thin layer or becoming to unstable.

Consistency

Due to the complex nature of the sinews and the number of materials used the ligament constructs were highly sensitive to changes in material batch and cell behaviour. With the cell viability, fibrin contraction rate, and cement anchor setting/dissolution among other factors being liable to vary widely based on the used materials. Attempts were made to ensure consistency with bulk batches of FBS and other highly materials acquired

to minimise the variations.

Additionally preparation techniques were liable to perturb the sample. Cryotoming - performed to expose the hard/soft interface or the inside of the sinew - was highly liable to disrupt the sample; tearing or stretching the soft tissue component of the sinew or fracturing the CaP anchor.

2.6 Computational analysis

Computational analysis of collected data was performed using a mixture of general (MATLAB (R2011a, Mathworks, USA), and ImageJ (v1.48, National Institute of Health, USA)) and instrument specific software (see below).

2.7 Main imaging modalities

2.7.1 Confocal Raman microscopy

Confocal Raman microscopy was performed using a Witec Alpha 300R (Witec, Germany) confocal Raman microscope, equipped with spectrograph (Acton SP2300, Pinceton Instruments, NJ USA) 1024 channel CCD cooled to -63°C, and 5x 0.1NA (E plan, Nikon, Japan), 20x 0.45NA (Plan Fluor, Nikon, Japan), and 100x 0.8NA (LMPlanFL, Olympus, Japan) atmospheric lenses. 785nm 300mW helium neon laser (Xtra single frequency laser, Toptica Photonics, Germany) with a 300g/mm spectrograph grating producing a mean spectral resolution of $3.23cm^{-1}$ over a range of $3088cm^{-1}$, with laser spot sizes of 5x - δ_{xy}4788nm δ_z78500nm, 20x - δ_{xy}1064nm δ_z3876nm, 100x - δ_{xy}598nm δ_z1226nm. Alternately a 514nm variable power 10-200mW (Model 277, Spectra-Physics,RI USA) with 600g/mm and 1800g/mm gratings providing mean spectral resolutions of $4.00cm^{-1}$ and $1.19cm^{-1}$ respectively over a range of $4096cm^{-1}$ and $1217cm^{-1}$, with laser spot sizes of

5x - $\delta_{xy}3.135\mu m$ $\delta_z 51.400\mu m$, 20x - $\delta_{xy}0.696\mu m$ $\delta_z 2.538\mu m$, 100x - $\delta_{xy}0.391\mu m$ $\delta_z 0.800\mu m$.

Acquired data were preprocessed with cosmic ray removal performed using the Witec Project software (v2.10, Witec, Germany). Baseline correction was performed in MATLAB using a least squares method proposed by Zhang *et al.* [213]. The system used a uint16 system for data collection from each CCD channel, allowing integer values between 0 and 65,536. In cases with a very weak signal in spectral areas of interest, or with a very high fluorescent impurity the maximum value was reached leaving a saturated region in the spectrum distorting the shape of the signal.

Single and line spectra were acquired at points and regions of interest. Spectrum are presented with the number of CCD counts/intensity given in arbitrary units (A.U.). Peak intensity and shape are presented as; vs - very strong, s - strong, m - medium, w - weak. The instrument was able to perform multiple accumulations at each point, reducing the SNR. Generally no difference in signal quality was seen in variations between high integration time - low accumulations, and low integration time - high accumulations.

Area mapping images were produced by either using the in-built Witec Control image mapping function or exporting the data in SPC format and reading it into MATLAB.

2.7.2 Confocal microscopy

Confocal microscopy was performed on a confocal microscope system (TCS SPE, Leica systems, Germany) 10x and 40x atmospheric lenses. 6 frame averaging was used for each image to minimise noise. Digital zoom was used for higher magnification images of regions of interest, but was generally used between 1x-1.5x.

Samples were imaged to observe the nuclei (stained with $10\mu L$ of 5mg/mL DAPI (Invitrogen, UK)), and actin (stained with $10\mu L$ of $6.6\mu M$ phalloidin (Invitrogen, UK)) in

cells, and general structure via reflectance. Using excitation wavelengths and spectral detection channels of: DAPI 410nm exciation 430-480nm detection range, phalloidin 532nm excitation 545-625nm detection range, reflectance 490nm excitation 470-520nm detection range. Laser intensity, and detector gain were adjusted to optimise the observed image and SNR based on the quality of the staining, the quantity of cells and background at that region, optical properties of the tissue at each stage of development, and effect of photobleaching. Penetration depths varied significantly with the composition of the sinew and its optical properties at each time point, up $30\mu m$ were typically obtainable.

Subsequent image processing was performed using MATLAB, imageJ, and ICY (v1.5.4.2 developed by de Chaumont *et al.* [214]).

2.7.3 Micro-CT

Micro-CT data was acquired using a benchtop micro-CT unit (SkyScan 1172. Bruker-microCT, Belgium). Samples were mounted on polystyrene bases and held vertically in 1.5mL eppendorf tubes for ligament constructs, or in the air for brushite cylinders. X-ray shadow images were acquired about 180° as the sample was rotated on its vertical axis. Magnification, voltage, current and other specific settings were varied between samples depending on the material size and properties.

Data was reconstructed from shadow images using Nrecon v1.6.9.4 with graphical processor unit acceleration using GPUReconServer v1.6.9.4 (Bruker-microCT, Belgium) with correction for beam hardening and ring artifacts applied during reconstruction. Cropping of excessive file sizes and basic thresholding and brightness/contrast changes were performed using ImageJ. For thresholding to remove the sinew and SYLGARD base; histograms of the pixel intensity for each dataset were used to determine the range for each component, with the ranges for non desired components set to 0. Saggital, transverse and coronal image sets produced from reconstructed data using DataViewer (v1.5.1.2, Bruker-microCT, Belgium).

2.7.4 Two photon and SHG microscopy

Constructs fixed in 4% formaldehyde were imaged at the Department of Physics at the University of Exeter using a custom confocal-like TP/SHG system as described by Mansfield *et al.* 2009 [159]. Imaging was performed using 60x immersion lens with a PBS meniscus used to maintain focus, with a 1020nm 200mW excitation laser. Image stacks were taken at the midpoint of the sinew to a depth of $80\mu m$ into the sample from the surface, either at the middle providing a top down view into the sinew, or at the edge providing a cross section. Image stacks were acquired as 512x512 pixel images giving a pixel size of $0.5\mu m$x$0.5\mu m$. Higher resolution individual 1024x1024 pixel images with averaging applied.

2.7.5 AFM

AFM was performed on the front of a day 15 interface immersed in PBS using a NanoWizard II AFM (JPK, UK) housed on a vibration isolation table in a closed chamber. Data were acquired by intermittent contact mode under ambient conditions, using rectangular pyramidal-tipped Si cantilevers (RTESP, Veeco, UK) with a nominal tip diameter of 50 nm. 100x100 pixel images were acquired from an area of 100x100 μm. Data was analysed, and height, slope and adhesion mappings were produced using JPK Data Processing software (v4.1.8, JPK, UK).

CHAPTER 3

INTERFACE MINERALISATION

The formation of a mineralised interface is essential to the intended function of the ligament model. The extent of the interface formation and its functional effects will depend on the quantity, size, and distribution of any mineralised particles deposited into the sinew. As discussed in section 1.3.3, the brushite CaP cement used for the BBLC anchor is expected to undergo fragmentation, and/or dissolution and reprecipitation whilst under *in vitro* physiological conditions.

3.1 Imaging of the hard soft tissue interface

With such a chemically and biologically complex environment as the enthesis and similar hard/soft junctions, no single imaging technique is able to provide a complete level of information. This requires the use of multiple complimentary methods to provide the full picture and enable a complete understanding of the structure and mechanics involved. The contrasting properties of materials in the hard/soft interface makes sample preparation difficult, with the preparation required for one technique liable to disrupt the results for another. A review on the imaging of biological hard/soft tissue interfaces by the author covers the topic in more depth (Bannerman *et al.* 2013 [151]).

Optical microscopy has been the most commonly applied imaging technique for study of

the interface in native and engineered tissue. Histology in particular has been the most commonplace method, and has a number of advantages in that it is able to show the cellular distribution and determine matrix components [215]. However it generally requires the fixation and/or freezing of samples, and the sectioning of tissues to thickness in the order of microns to allow light through. These preparation methods can damage and distort the sample making it unrepresentative of the true structure. More advanced optical techniques such as differential interference contrast [216], second harmonic generation [162], and polarised OCT [217] can non-destructively provide a high level of information, particularly with regard to isolating collagen content and structure, but are less commonly applied. Electron microscopy, generally SEM, allowing a much higher resolution than optical based techniques is usually combined with light micrographs to provide morphology and basic compositional information over multiple length scales from nano to mm [143, 178, 215, 218].

Other imaging techniques that can provide a greater level of information on the biochemical composition or three-dimensional structure are often under exploited. This is particularly important for engineered tissues where composition and properties need to be determined, by an ideally non-destructive means, for optimisation. Magnetic resonance imaging (MRI) and ultrasound are often used at the clinical level to evaluate macro scale enthesis disorders, such as arthritis [219]. There has been little use in research applications despite potential for closer enthesis examination with MRI ultra-short sequences [220, 221] and use of contrast agents, such as phosphate based ones that could be attached to the hard tissue [222, 223]. Ultrasound has been more used, with spectral options allowing quantification of mineralisation in hydrogels [224] and collagen detection [225]. Chemical microscopy (such as Raman and IR) is often used as a point method, either shown as single spectrum or with the spectra of a number of acquired points superimposed onto a light micrograph providing crude spatial information on the composition [3, 178, 226]. Chemical imaging has been very limited with IR being the only technique to have been

applied to chemical imaging of the enthesis, as reported by Spalazzi *et al.* 2013 [227]. Mechanical probe methods, which can provide important information on spatially localised mechanical properties, have also been largely overlooked. AFM and nanoindentation have been applied by Campbell *et al.* 2012 to the osteochondral interface [228], and to the periodontal ligament by Lin *at al.* [229]. X-ray based methods have been limited with the most notable example being the use of synchrotron imaging by showing the phase contrast of the osteochondral junction [201]. Despite the rise of micro-CT, its application to the study of micron scale mineralisation at the native interface has been limited or non-existent.

3.2 Chapter aim

The aim of this chapter was to investigate the mineralisation of the fibrin sinew soft tissue, via the breakdown of the brushite CaP cement anchors, as a result of ageing under *in vitro* conditions. Using a range of modalities: CRM, micro-CT, and AFM to provide information across the interface on the biochemical composition, morphological structure, and mechanical properties, respectively.

3.3 Methods and materials

3.3.1 Confocal Raman microscopy

Ligament constructs were frozen to -20°C and cyrotomed to the midpoint of the sinew depth at the interface with the anchor. Stainless steel pins were removed from the anchors if it was possible without damaging the sample, otherwise the protruding portion was removed with wire-cutters to minimise their disruption. A number of means to prepare and image the sample with minimal disruption were investigated; embedding the construct in agarose gel, setting SYLGARD around pinless anchors, and inserting pinless anchors into

sections cut from the SYLGARD with poor results.

CRM mapping was performed using CRM as described in Chapter 2, with a 785nm excitation laser, and 1s integration times. Mappings were acquired at the front and side of the anchor with 1s integration time and the area sizes and number of acquired spectral points varying from small interface area only scans over 1000x1000μm with 150x150points (approx 6.5 hrs), to 2000x6500μm with 200x200points (approx 11 hrs) covering the length of half the ligament construct. Individual spectra were acquired at multiple points of interest in the sinew and anchor with 20 accumulations of 3s integration times. Samples were immersed in deionised water to prevent dehydration during the scan. Data was pre-processed to remove cosmic rays using the instrument associated Witec Project software, exported in SPC format into MATLAB, baseline corrected using a least squares penalised method [213]. False colour image maps were produced by integrating over the sum of peaks of interest in MATLAB and/or Witec Project.

3.3.2 Micro-CT

Constructs were imaged either unprocessed, or stained with an iodine solution. In both cases the constructs were not the same samples as those used for Raman. Iodine staining was performed by dehydrating the sample in a graded series of ethanol baths (30% ethanol for 1hr, 50% ethanol for 1 hr, and 70% ethanol 1 hr) then leaving samples in 1% w/v iodine in 100% ethanol over night, finally washing and storing the sample in 70% ethanol until imaging. For both stained and unstained samples, constructs and their neighbouring region of SYLGARD were cut out from the well plate, then inserted into 2mL eppendorf tubes so that the sinew was parallel to the long axis of the tube and held firmly in place by the remaining SYLGARD base to prevent movement during scanning.

Scanning was performed in a micro-CT system with sample tubes held vertically. X-ray shadow images were taken 180° about the sample with an angular step size of 0.48°, X-

ray energy of 30kV for unstained or 40kV for iodine stained samples. Scans performed over whole or half construct lengths with pixel sizes of $8\mu m$ and $11\mu m$ respectively for all dimensions. Reconstruction was performed using NRecon software with correction for beam hardening and ring artifacts. Visualisation and cross sections were produced using DataViewer. Further processing was performed using ImageJ and MATLAB to enhance image contrast.

Quantification of the number and morphological properties of mineralised particles in the sinew was performed using MATLAB. Reconstructions were thresholded to remove voxels representing the sinew and SYLGARD base using pixel values determined from the distribution of intensity for each material in image pixel intensity histograms. Remaining particles outside of the anchor were labelled, with the number, volume distribution and size dispersion (standard deviation divided by the mean for all particles) calculated.

3.4 Results

3.4.1 Brushite anchor and construct formation

The conversion of β-TCP and orthophosphoric acid to brushite is given by:

$$Ca_3(PO_4)_2 + H_3PO_4 + 6H_2O \rightarrow 3CaHPO_4.2H_2O \tag{3.1}$$

Given this conversion, the liquid to powder ratio (3.75:1), and the orthophosphoric acid molarity (3.5M) a TCP to brushite conversion of 71% would be expected. Producing a multiphase CaP scaffold consisting of 71% brushite and 29% TCP. Constructs were formed as described by Paxton *et al.* 2010 [64]. After seeding with CTF cells, the fibrin sinew contracted to form the ligament body over a period of 7 days, as described in section 1.3. In a small number of samples mineralised particles were observable to the naked eye in the sinew body after 15 days in culture. Constructs removed from culture at set time

points were fixed in 4% formaldehyde and left in PBS at 4°C until analysed.

3.4.2 Confocal Raman microscopy

Fixed constructs were cryotomed to provide a flat surface suitable for confocal imaging and expose the hard/soft tissue interface. CRM was performed using a 785nm wavelength excitation laser, due to the destructiveness to the sample and high autofluorescence that blocked all signal with the 514nm laser. Poor wide-field quality due to low lamp intensity made comparison of Raman mapping to optical images impossible, and imaging of specific locations challenging. The hard/soft interface location was determined by change in spectrum as the quantity of brushite decreased at the edge of the anchor for purposes of setting up the mapping parameters.

Individual Raman spectra for the brushite anchors, and fibrin sinew were acquired (Fig. 3.1) and Raman band assignments of the bonds present in the were performed (Table 3.1) based on reports in the literature [230, 179]. TCP spectrum showed distinctive P-O stretching at 948cm^{-1} and v_1PO_4 stretching at 970cm^{-1}, additionally the spectrum was dominated by very strong peaks present at 1327cm^{-1} 1386cm^{-1} 1491cm^{-1} and 1656cm^{-1} determined to be associated with P=O phosphate stretching [231]. The mixed brushite/TCP cement anchor was dominated at every point by the 1300-1656cm^{-1} peaks observed in the TCP spectrum. The presence of brushite and relative quantity compared to TCP at each point was identified by the presence of P-O stretching at 878cm^{-1} and a v_1PO_4 peak shift to 985cm^{-1}. The spectrum of CTF cell seeded fibrin exhibited a strong autofluorescence peak at 130cm^{-1} with a high background exponentially tapering off to approximately 2500cm^{-1}.

CRM Imaging mapping was performed across the hard/soft tissue interface along the hard/soft interface of the anchors (Fig. 3.2). Mappings were taken at different time points in the development of the sinews (Fig. 3.2) however difficulties with the reliability

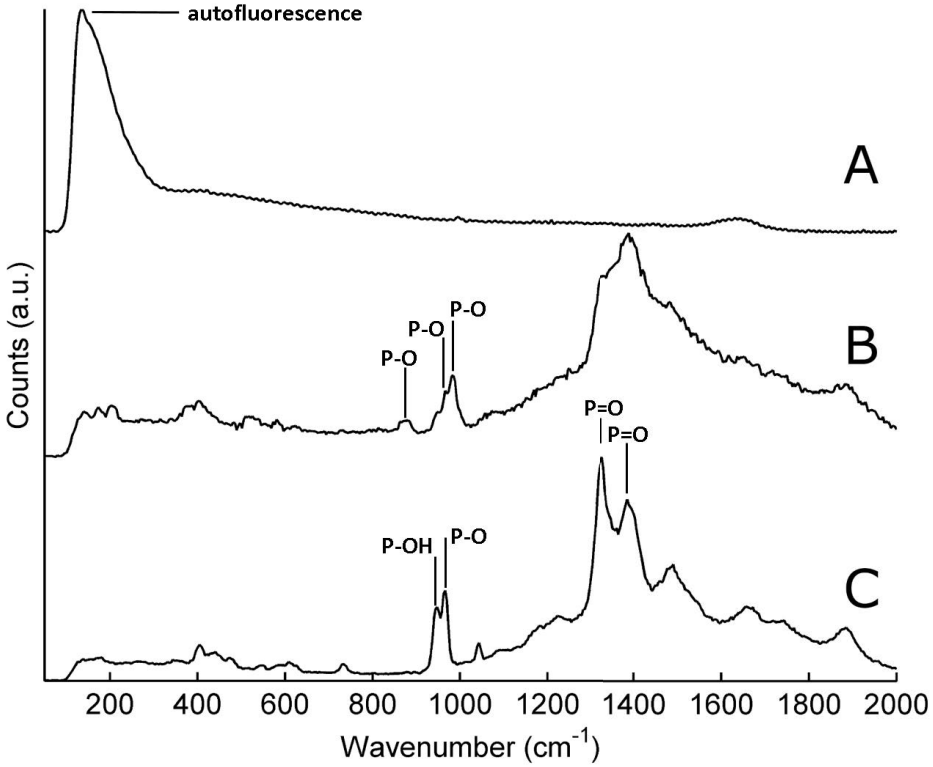

Figure 3.1: Raman spectra of BBLC components. (A) CTF cell seeded fibrin, (B) brushite/TCP cement inter-grain region, and (C) brushite/TCP cement grain region.

Table 3.1: Major Raman peaks present in the 800-1050cm^{-1} region of interest and their phase assignments based on the literature [230] for nonaged and aged brushite cement anchors.

Wavenumber (cm^{-1})	Vibrational mode	Phase assignment
878m	P-O stretching mode of PO_4 group	Brushite
948m	P-OH stretching mode of HPO_4^{2-}	TCP
960vs	P-O stretching mode of PO_4 group	OCP
970vs	P-O stretching mode of PO_4 group	TCP
985vs	P-O stretching mode of PO_4 group	Brushite
1010m	P-O stretching mode of HPO_4^{2-}	OCP
1327vs	P=O stretching	TCP
1386vs	P=O stretching	TCP

of the preparation process prevented acquisition of a complete time series over 30 days.

The spatial sampling was variable between images depending on the settings used as a

result of attempts to optimise the methodology. The spectral resolution was constant but the low sensitivity made accurate determination of CaP phases (notably the v_1PO_4 shifts) and biological components present difficult in some cases.

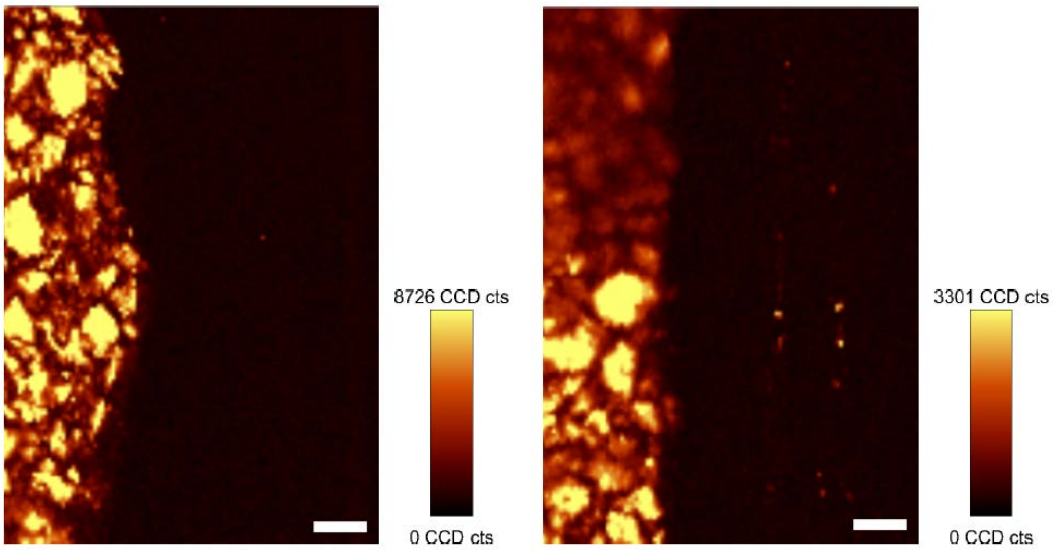

Figure 3.2: Raman mapping of the PO_4 group (950-990cm^{-1}) for all CaP phases showing the distribution of mineralised particles at the hard/soft tissue interface. Mappings show the interface at the front of the anchor (left side of the image) at (a) 10 days and (b) 14 days. Scale bar 100μm.

Mappings of the cement anchors show a granular structure, with brushite being dominant in the inter-grain region but both phases present in the grains and inter-grain region. Comparison of the front of the anchor for days 10 and 14 mapping of the v_1PO_4 phosphate for all CaP phases shows an increase in the number of mineralised particles in the soft tissue sinew (Fig. 3.2). Conversely mappings taken at day 31 shows a mineralised particle in the sinew when mapped over phosphate peaks (Fig. 3.3 (b)). However the sinew and it's structure was clearly evidenced when mapping over the autoflouresence peak (Fig. 3.3 (b)), and investigation of the spectra at multiple points showed the sinew in the anchor region to have a high phosphate content and the sinew further away to be composed of collagen with little to no mineral content when compared to the single

particle (Fig. 3.3 (c)) showing that development of the soft tissue was well advanced. The different image parameters used to collect the day 31 image provide a lower spatial sampling which will limit the sensitivity and may prevent smaller particles being observed in the image mappings.

Large area scans from the anchor along to the midpoint of the sinew were also able to show the separate components and the structure of the soft tissue clearly, but due to the lower sampling resolution no mineral particles were observed in the sinew (Fig. 3.4). The long 8+ hour mapping times also made the large are scans highly impractical with a low sample processing rate and high chance of damage to the sample during the long exposure time.

More detailed investigation of the spectrum at points in the anchor, sinew and of mineralised particles showed evidence of significant changes in the anchor composition during the BBLC development. In the case of mineralised particles observed in the sinew of the day 14 samples the particles and anchor were determined to be composed of brushite and TCP (Fig. 3.5), with no transformation OCP or HA evidenced. Spectra taken from the sinew near the anchor at day 31 showed high TCP content (Fig. 3.3) suggesting a high presence of mineralisation below the mapping resolution of the techniques used. Mapping of the most intense CaP phase based on the PO_4 peak in each location is shown in Fig. 3.6. Comparison of the CaP content of the anchor at day 10 (Fig. 3.6 (a)) and Day 31 (Fig. 3.6 (b)) suggests extensive removal of the brushite content near the edge of the anchor over time from the outside of the anchor, leaving a TCP cement with slowly advancing formation of by OCP. Such a reduction in the quantity of brushite without total replacement by OCP would explain the observed softer nature of the anchors at later time points. However due to the low spectral resolution of the spectrograph, as can be seen in the spectrum for each phase in Fig. 3.6 (c), the chance of cross talk between peaks reduces the reliability.

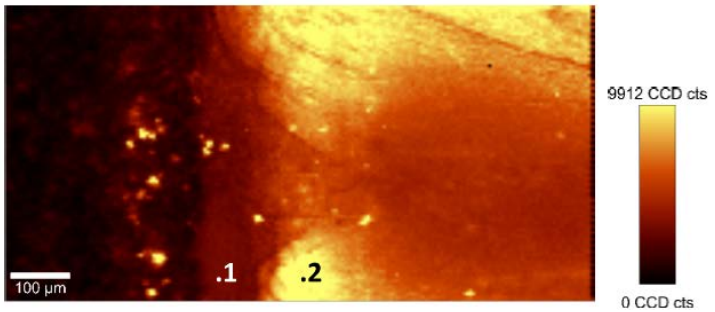

(a)

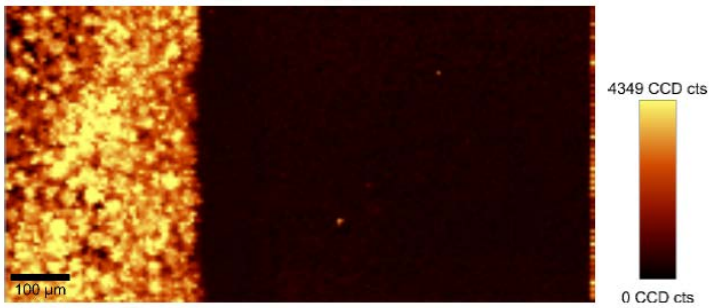

(b)

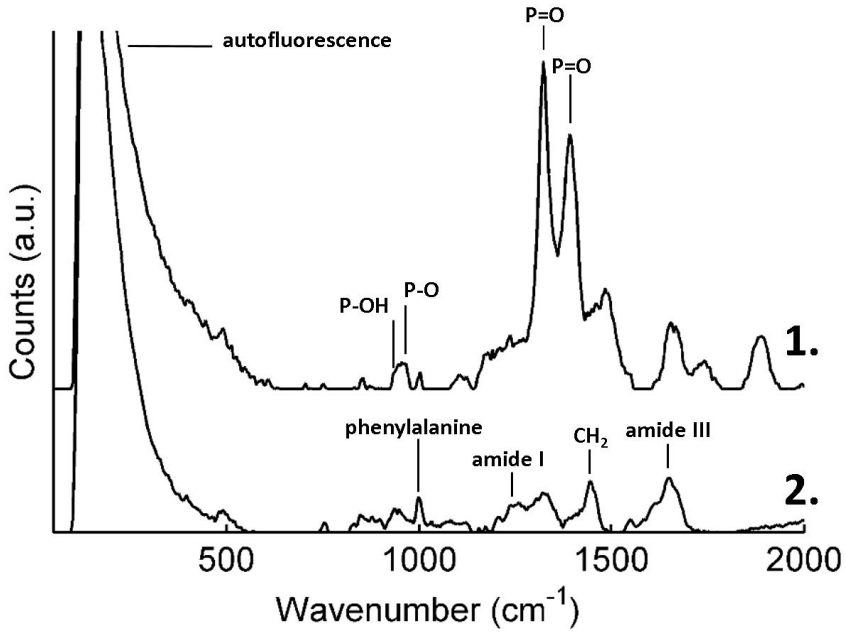

(c)

Figure 3.3: Raman mapping of the interface and sinew for a day 31 BBLC. Mappings show the interface at the front of the anchor (left side of the image) for (a) autofluorescence (90-115cm^{-1}), (b) v_1PO_4 for all CaP phases (950-990cm^{-1}), and (c) the spectrum from points 1. and 2. labelled in (a). Scale bar 100μm.

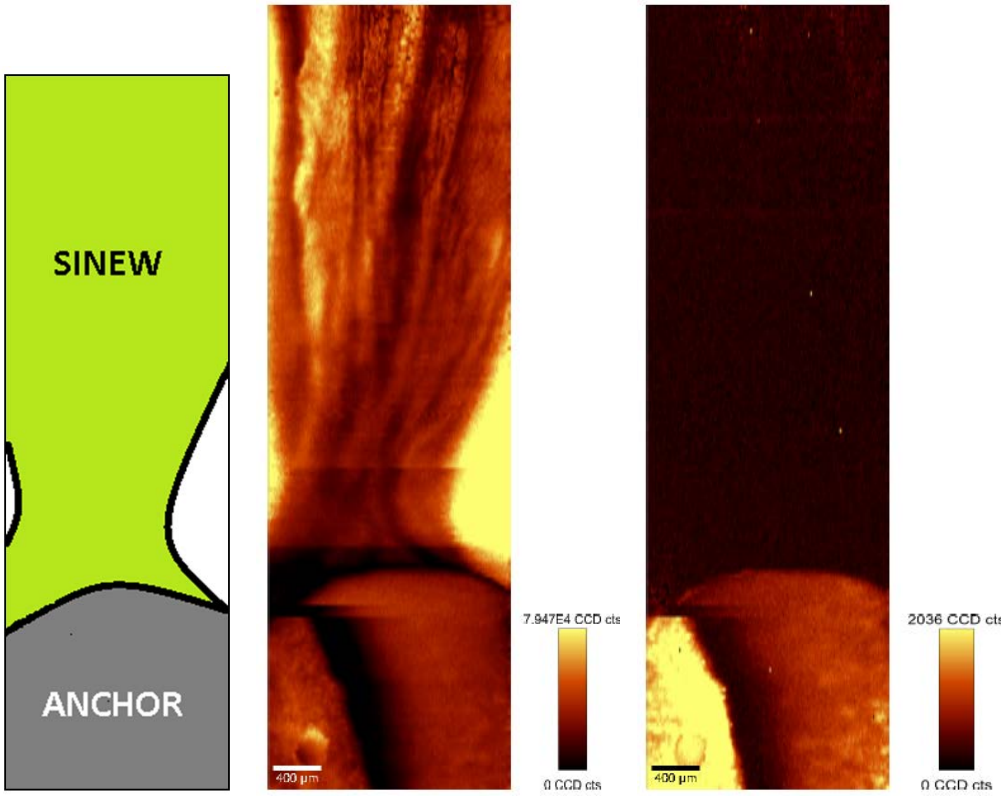

(a) (b) (c)

Figure 3.4: Raman mapping over the anchor and up to the sinew midpoint in a day 10 construct. (a) schematic labelling the regions present (b) Sum of all peaks showing the distribution of material (c) PO_4 group for all CaP bands (950-990cm^{-1}) showing the distribution of mineralised material. Scale bar 400μm.

The actual presence of collagen as the ECM deposited by the CTF cells is complicated to determine at early time points due to the weak nature of the signal for the soft tissue in comparison to the CaP cement, and the spectral overlap between the of the CaP and collagen peaks under Raman spectroscopy. The initial formation and early presence of collagen around the interface region is hard to determine. At day 31 spectra showing collagen associated peaks such as the 1000cm^{-1} phenylalanine and the 1655cm^{-1} amide type I [173] are observed in the sinew (Fig. 3.3c). The signal remains weak however and so information about collagen beyond its presence in the region could not be determined.

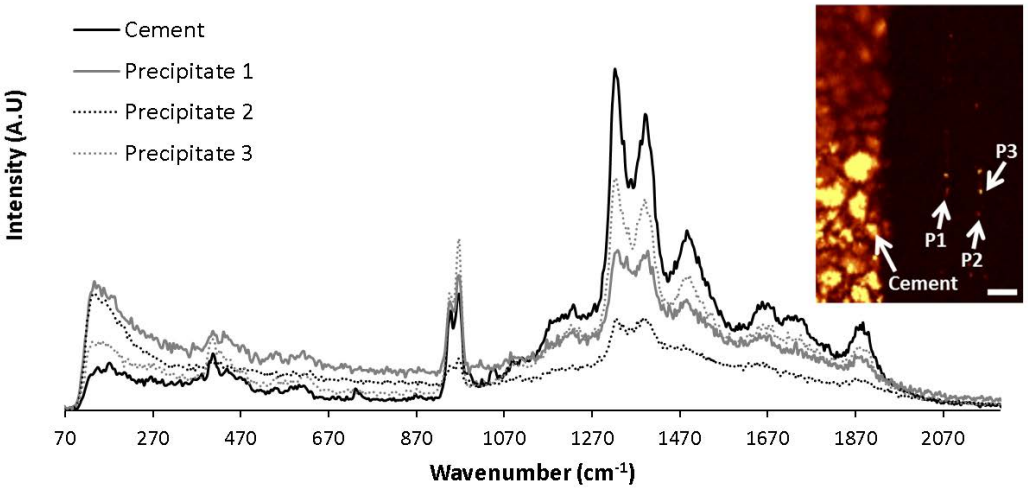

Figure 3.5: Raman spectral analysis of the day 14 PO_4 group (950-990cm^{-1}) mapping shown in Fig. 3.2. Scale bar 100μm.

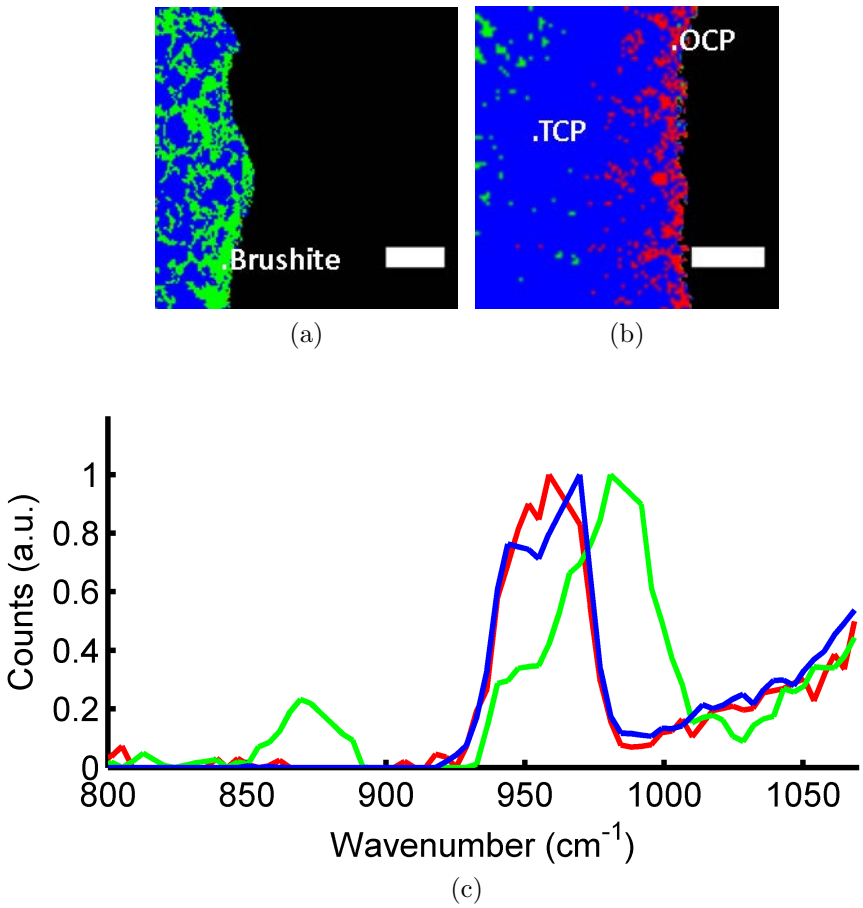

(a) (b)

(c)

Figure 3.6: Raman cluster mapping showing change in CaP anchor composition after (a) 10 and (b) 31 days *in vitro*. (c) Spectrum for each phase present in the day 31 sample showing the v_1PO_4 shift taken from the labelled points. Red - OCP, Green - brushite, Blue - TCP, Black - sinew. Scale bar - $200\mu m$.

3.4.3 Micro-CT

Three-dimensional reconstructs of constructs were produced using micro-CT on samples either without preparation, or stained with iodine. Micro-CT scans were used to produce 3D reconstructions of unprocessed sinews at days 11, 19 and 30. Scans were performed on ligaments held vertically in sealed eppendorf tubes in an air medium. Samples used for micro-CT scans were fixed in formaldehyde but otherwise not processed in any way that might damage of distort them. Samples were kept mounted on the SYLGARD base to provide support and maintain the structure of the sinew. X-ray shadow images (Fig. 3.7) acquired at 180° about the vertical axis of the sample. In these images the build up of mineralised particles along the length of the sinew were observed, with little to no internal details in the sinew structure other than the macro-structure apparent.

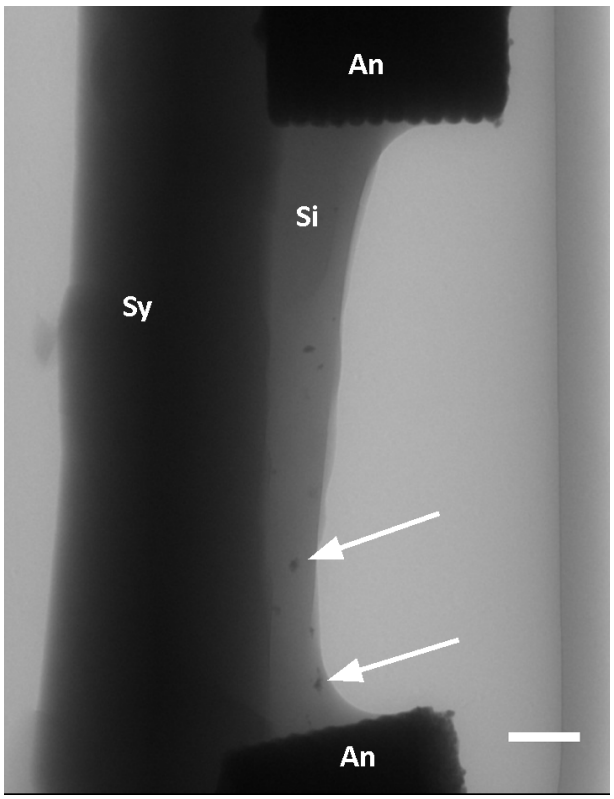

Figure 3.7: X-ray shadow image of day 19 construct. Mineralised particles are apparent in the soft tissue outside the anchor. An - anchor, Sy - SYLGARD, Si - sinew, arrows highlight mineral in sinew. Scale bar 1mm.

Three-dimensional reconstructions were produced of sinews and slices used to study the structure (Fig. 3.8, Fig. 3.9). Reconstructions showed high levels of contrast due to x-ray attenuation in the CaP anchors. The soft tissue sinew conversely produced a very weak signal contrast with the internal structure showing no specific structure, appearing essentially homogeneous. The SYLGARD base provided a higher level of attenuation and contrast than the sinew. The internal structure of the sinew and SYLGARD based was dominated by ring artifacts, even with high correction applied. Beam hardening artifacts were also present around pins and anchors.

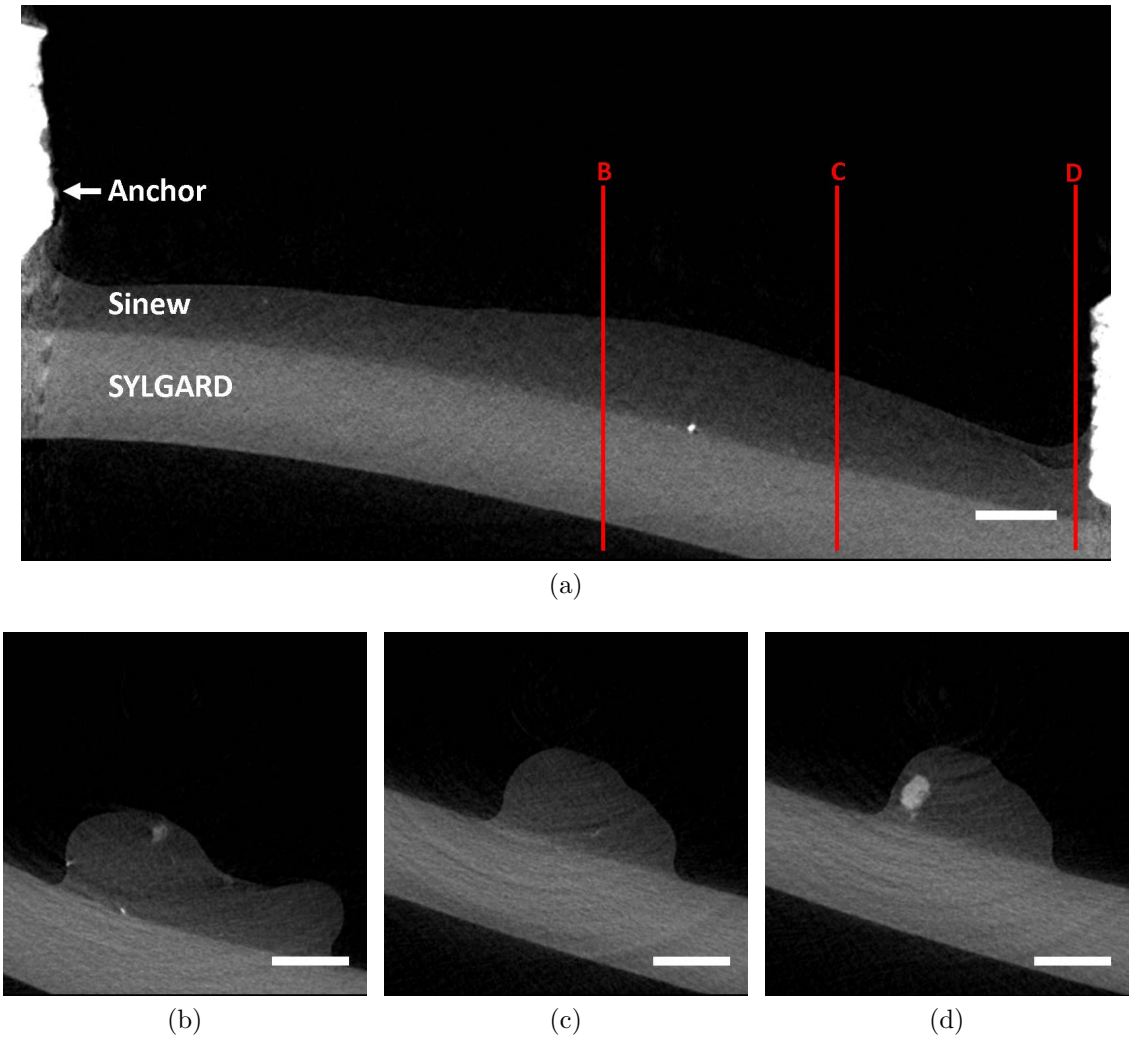

Figure 3.8: Slices of Micro-CT reconstructions for day 19 ligament constructions. Showing full length slices (a) the coronal and (b,c,d) transverse slices taken at the points labelled in (a). Scale bar 1mm.

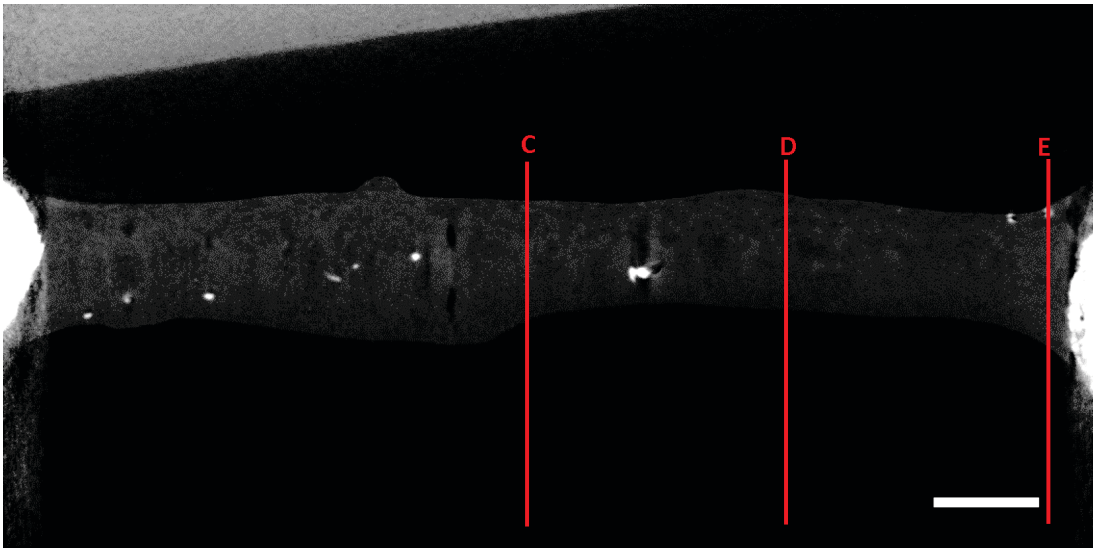

(a)

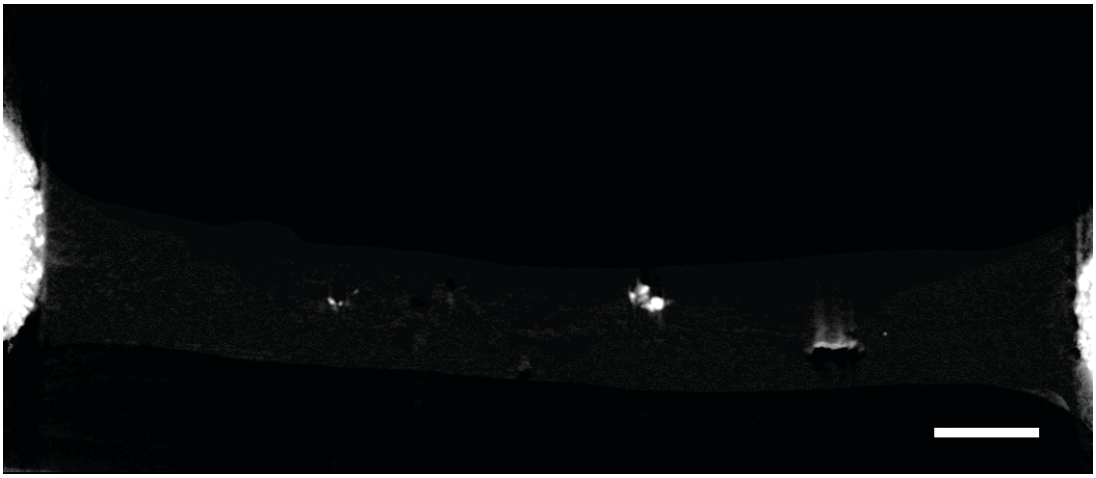

(b)

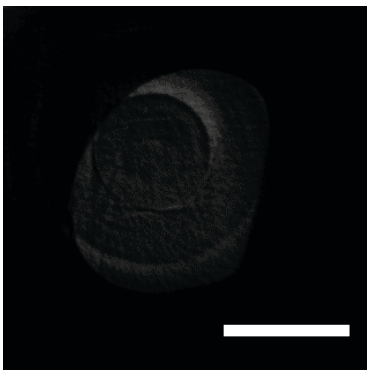

(c)

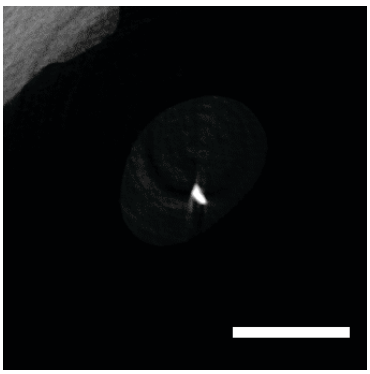

(d)

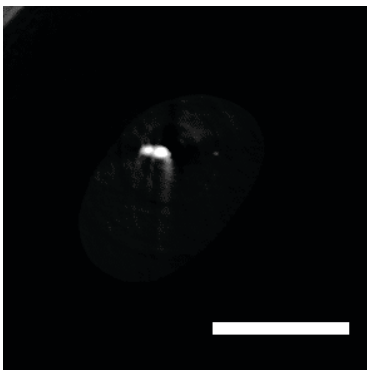

(e)

Figure 3.9: Slices of Micro-CT reconstructions for day 30 ligament constructions. Showing full length slices (a) the coronal, (b) sagittal, and (c,d,e) transverse slices taken at the points labelled in (a). Scale bar 1mm.

Slices taken from 3D reconstructions show mineral present in the sinew (Fig. 3.8, 3.9). Variations along the transverse slices are seen, possible as result of folding of the sinew, at day 19 (Fig. 3.8) but the sinew is essentially a uniform cylinder at day 30 (Fig. 3.9). Sagittal slices of the reconstruction taken at the interface between the hard and soft tissues (Fig. 3.10) show an apparent break down of the anchor material from a constant surface at day 19, to a broken and pitted one at day 30. Suggesting that the mineralised hard/soft tissue interface theorised in Chapter 1 is forming.

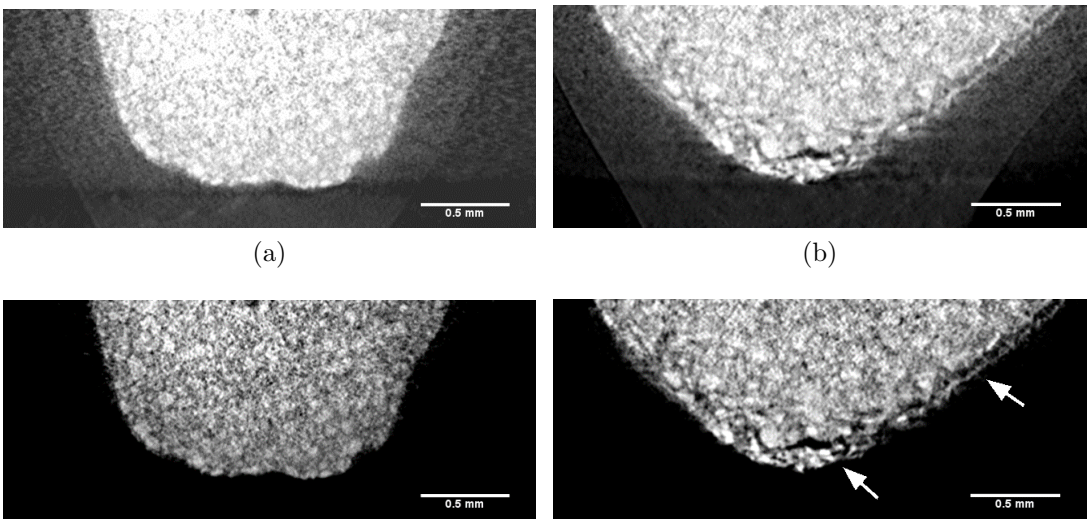

(a) (b)

(c) (d)

Figure 3.10: Micro-CT sagittal slices across the hard/soft interface. (a,c) Day 19 and (b,d) day 30 across the hard/soft interface. With (a,b) soft tissue included and (c,d) thresholded out to only show the mineralised components. Arrows in (d) highlight fractures in the anchor. Scale bar 0.5mm.

In addition to the distribution of mineralised particles at the interface, reconstructions were used to investigate mineralisation along the length of the sinew. Three dimensional reconstructions with the soft tissue removed by thresholding are shown in Fig. 3.11. A substantial quantity of mineralisation can be seen along the length of the sinew at each of the time points that were imaged. Quantification of the sinew mineralisation shown in Table. 3.2 was performed using MATLAB to determine the size and distribution of the mineralised particles by thresholding to remove the soft tissue and then labelling the

particles across the whole image-stack (with an upper size limit to exclude the anchors). The results line up with, and provide quantifiable values to the images shown in Fig. 3.11. Notably the upper size range of the mineralised particles are much larger than those observed under CRM in the previous section, likely as a result of the much larger volume investigated and nondestructive preparation method. Mineralised particles below the scan resolution will be missing or distorted in their representation so the distribution of submicron mineralisation is unknown.

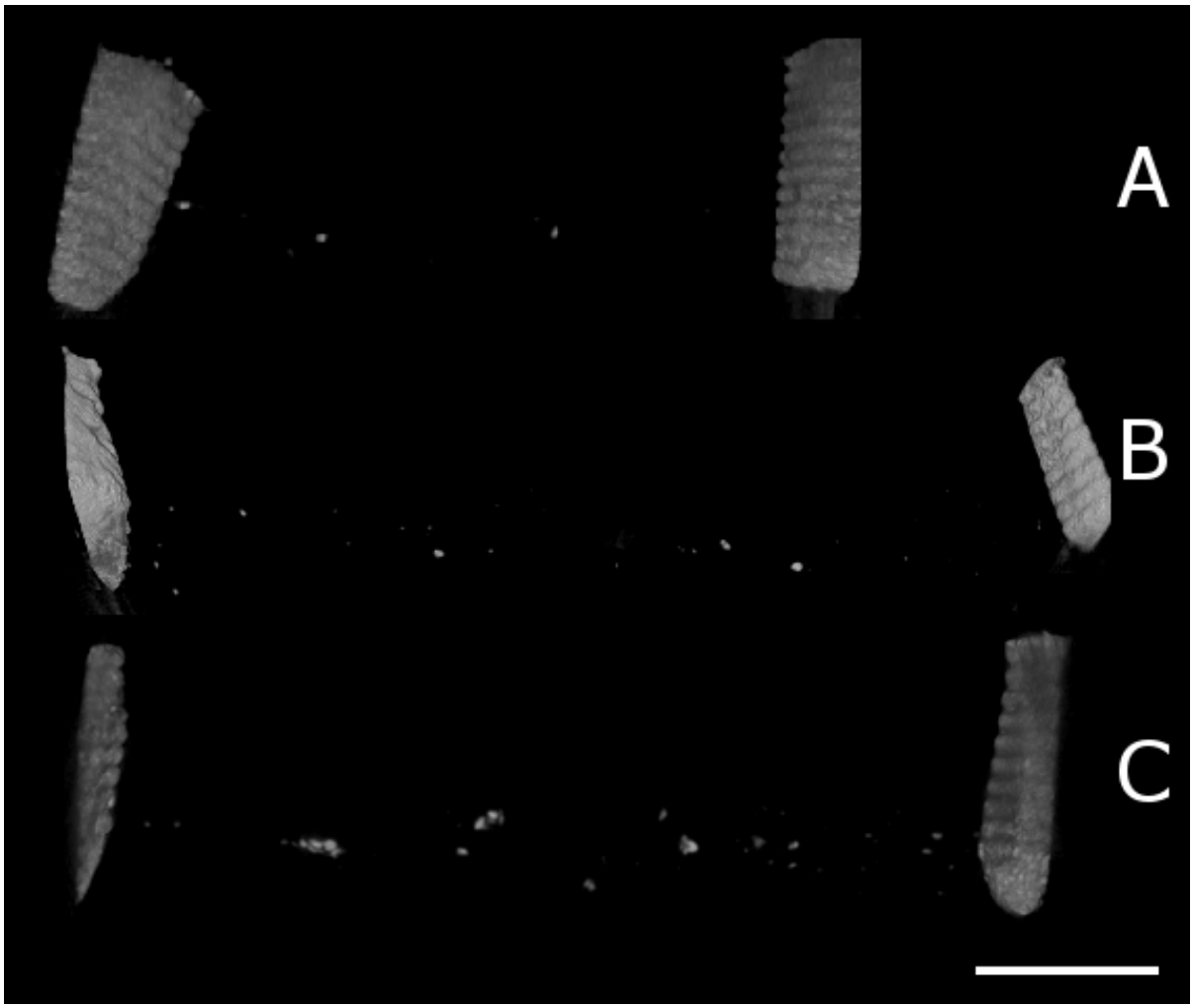

Figure 3.11: Thresholded micro-CT 3D reconstructions showing mineralisation along the sinew for day (a) 11, (b) 19 and (c) 30 constructs. Scale bar 1mm.

Table 3.2: Quantification of mineralised particles in Micro-CT reconstructions shown in Fig. 3.11. Particles measured over entire sinew volume.

Day	Number of particles	Max volume (μm^3)	Median volume and STD (μm^3)	Size dispersion
11	16	1.93x10^6	1.29x10^5, 5.84x10^5	1.44
19	24	1.63x10^6	8.01x10^4, 3.70x10^5	1.58
30	32	3.40x10^6	7.04x10^6, 7.16x10^5	2.18

Iodine stained BBLC

To produce a high signal and contrast in the soft tissue samples were dehydrated by an alcohol series and stained with an iodine based solution. Samples stained in iodine exhibited a significant increase in stiffness, becoming highly rigid as a result of the dehydration process, with a notably dark brown colour due to the absorbed iodine. X-ray shadow images show the much reduced volume of the sinew which had contracted away from the SYLGARD based (Fig. 3.12). The processing method is not expected to produce changes in the quantity and aggregation of mineralised particles, other than an apparent higher density.

Micro-CT reconstructions of these samples showed a much higher contrast sinew, with internal structure visible in addition to the mineralised particles. Slices taken along the saggital and transverse axis show the increased contrast of the sinew, with the stronger signal reducing the effect of ring artifacts (Fig. 3.13). A much higher density of the sinew is seen diverging away from the front of the anchor (Fig. 3.13 (B,C)). At the midpoint of the construct, differences in the sinew structure suggest that folding or aggregation of the sinew is observed as reported by Paxton *et al.* 2012 [94].

One of the effects of the dehydration process was the shrinkage of tissue causing it to pull away from the front interface with the brushite anchor in a number of places. Notably in these cases a large quantity of mineralised particles are observed in the sinew adjacent to the anchor region (Fig. 3.14, Fig. 3.13 (C)). It is uncertain if the folding pattern shown in the transverse slices is the actual state of the sinew or entirely/partly due to shrinking and deformation as a result of dehydration during the iodine staining process.

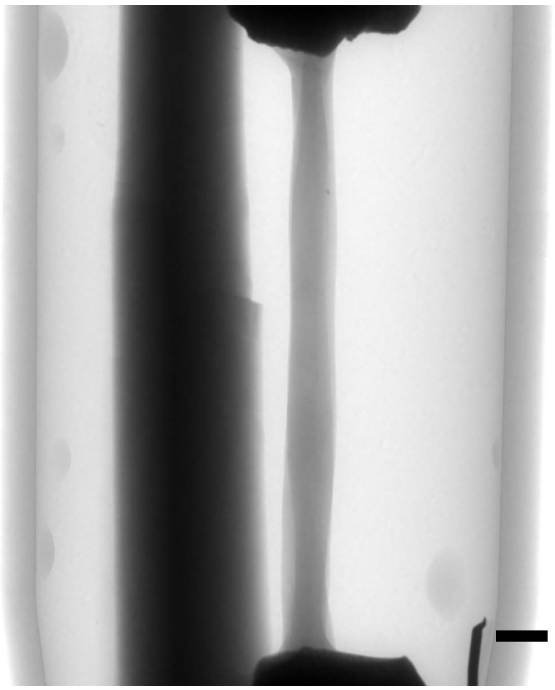

Figure 3.12: X-ray shadow image of a day 20 iodine stained construct. Scale bar 1mm.

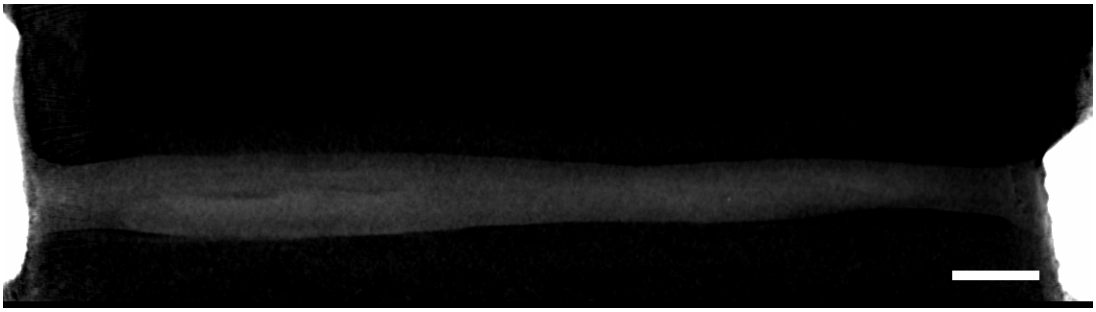

(a)

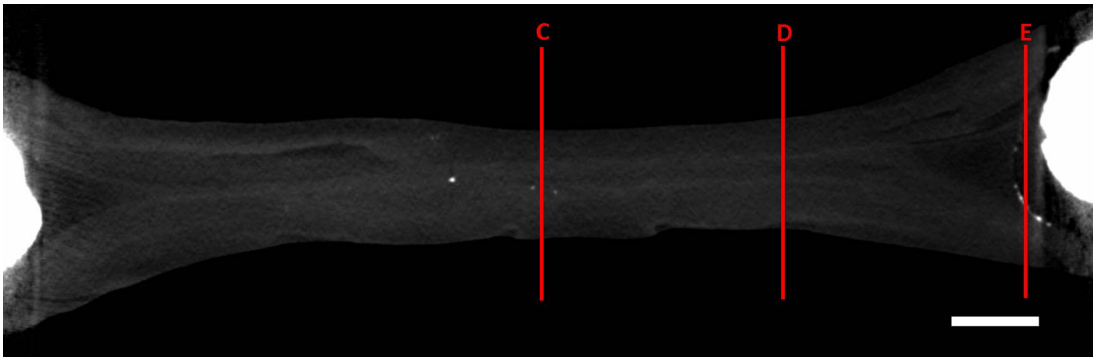

(b)

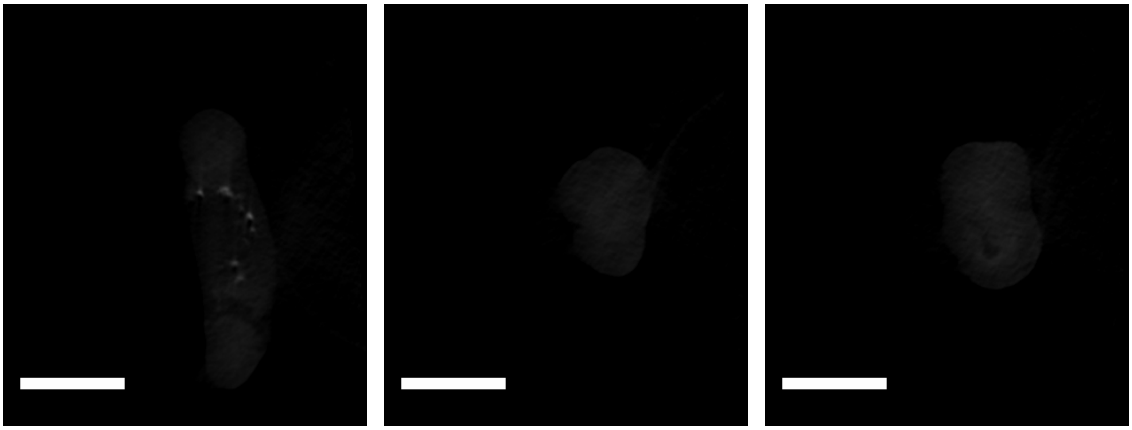

(c) (d) (e)

Figure 3.13: Slices of Micro-CT reconstructions for a day 20 iodine stained ligament constructions. Showing full length slices (a) the coronal and (b) saggital, and transverse slices (c,d,e) taken at the points labelled in (b). Scale bar 1mm.

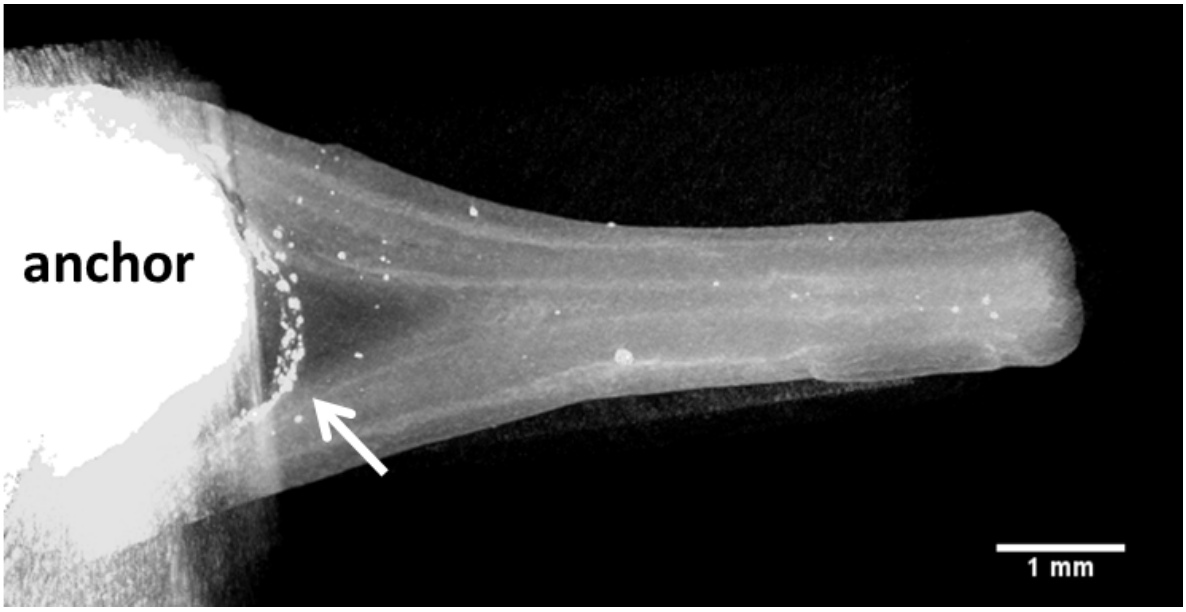

Figure 3.14: Three-dimensional reconstruction - shown in two-dimensions - of a day 20 iodine stained ligament construct. Arrow highlights dense region of mineralised particles in the soft tissue around the interface region. Image brightness has been increased to improve visual contrast of mineralised particles. Scale bar 1mm.

3.4.4 AFM

A preliminary experiment with AFM was performed on a day 15 interface in intermittent contact mode, to investigate the change in stiffness and other properties across the interface between the tissues. Produced images of the measured slope, height, and probe adhesion (Fig. 3.15) show a clearly defined interface was resolved. With the hard and soft tissues discernible and mineralised particles apparent in the soft tissue, similar to Raman mappings shown above. However there was insufficient sensitivity to collect data to accurately infer mechanical properties across the interface. This was further confounded by an inhomogeneous surface produced as a result of cutting artifacts required to expose the interface, which are visible as horizontal lines staggered across the mappings. A more highly polished surface is needed for further AFM mapping, with loss of interface integrity from preparation a problem for collecting and the reliability of data. During data collection there was additionally drift in intensity due to changes in environmental thermal conditions.

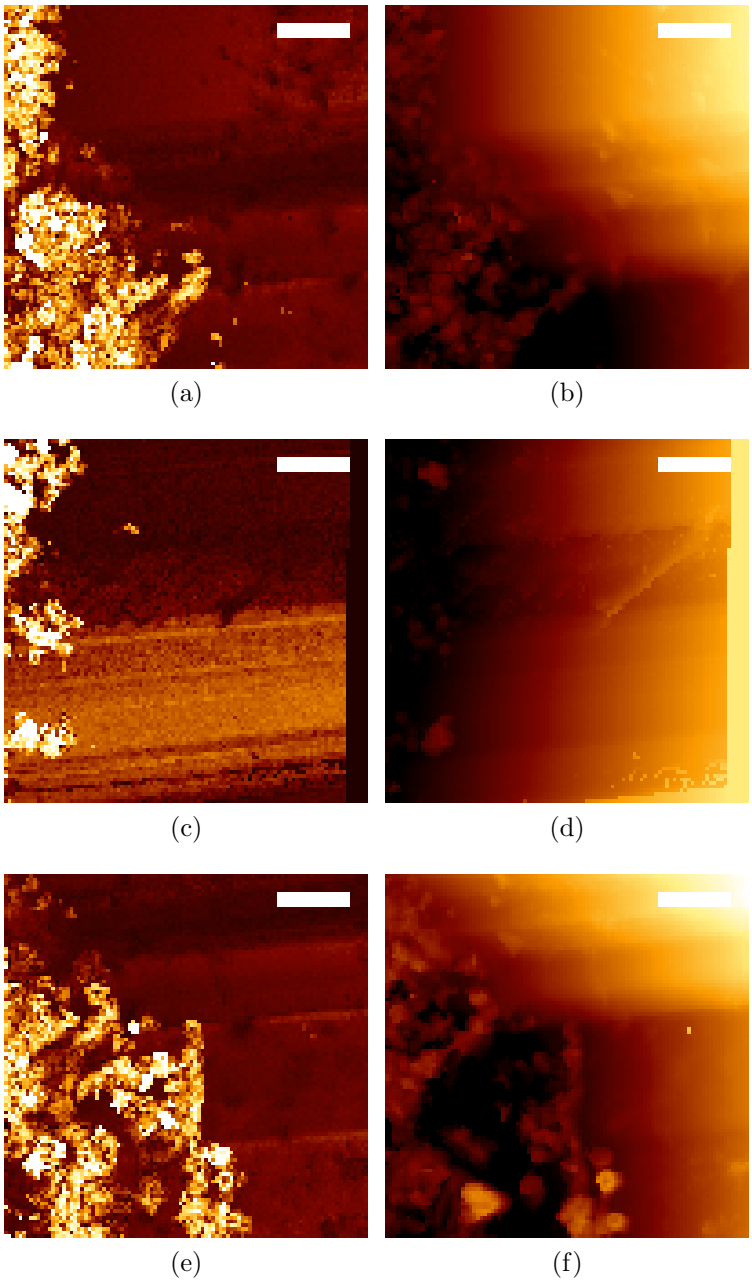

Figure 3.15: AFM mappings across the hard/soft tissue interface. Showing anchor on the left, and soft tissue on the right hand side of images. (a,c,e) Height and (b,d,f) phase. Scale bar 20μm. Colour scale is arbitrary between images with white-dark representing max-min.

3.5 Discussion

Transitions of force between materials with different properties in the L/T–bone attachment site is smoothed and dissipated by the graded enthesis to prevent damage and failure. In addition to the L/T–bone application focused on here, mineralisation of soft tissue also has potential application in a number of other areas. Graded interfaces are important in a number of biological applications including the bone–cartilage osteochondral junction [232], tooth–bone via the peridontal ligament [233], and attachments of similar materials such as the dentine–enamel interface in teeth [234] and narwhal tusks [235]. The general method used for reproducing this in biomaterials has been the designed combining of multiple materials or property gradients in a single material, the BBLC model is intended to form from separate materials with no direct guidance.

The work presented in this chapter (Fig 3.2, 3.10) has shown that as expected the brushite cement anchor underwent dissolution and fragmentation with time when aged *in vitro*. Creating a region of mixed hard/soft tissue from the breakdown of the anchor in contact with the soft tissue, and mineralisation observed in the sinew as both large micron–scale particles and a submicron background level in the sinew between particles as seen under CRM. This provides important evidence in support of the formation of a graded mineralised interface between the two tissues similar to the native enthesis. However the quantity of large mineralised particles observed along the length of the sinew was seen to increase with time. The extensive mineralisation is liable to produce complications that might have important ramifications for the mechanical and biological function of the mature ligament. With a likely excessive stiffness resulting from mineralisation potentially reducing their elastic properties and disrupting collagen formation. Though mechanical testing through tensile loading and AFM would be needed to determine this.

CRM only allowed a small sampling window over a single plane to be practically imaged. Whilst the confocal nature allows multiple planes to be imaged, the limited depth achiev-

able for confocal techniques in turbid media and the long acquisition time required for a single plane to be mapped makes collection of a detailed 3D image-stack with significant volume with respect to the total hard/soft tissue height impractical. In addition to the limited window offered by CRM, the destructive nature of the preparation process to access the interface makes it possible that mineralised elements seen in the sinew were a result of damage during preparation. Whilst the number of particles present is seen to increase over time was in part seen to increase here and in similar hydrogel/brushite systems [231]. Other factors such as the weakening of the anchor material making it more liable that the particles are the result of the preparation process. As a result of this micro-CT was performed to verify the mineralisation process and provide a means of fully quantifying the number and morphological properties of particles in the soft tissue.

Micro-CT reconstructions showing interface breakdown (Fig 3.10) and mineralised particles (Fig 3.11) in the sinew confirmed that the mineralised particles are present in the mature sinew and not (at least entirely) a result of the destructive CRM preperation. Reconstructions of the soft tissue sinew provided poor contrast due to the low attenuation, with no useful information beyond the structure boundaries. Iodine staining based on previous work by Metscher [195, 196] greatly increased the soft tissue contrast. Whilst the level of internal structure inside the sinew would be expected to be too small, and low in contrast for the iodine staining to show substantial information, the macrostructure was shown much more clear, in particular in the cross sections shown in Fig 3.13. The wavelike/crimping shape of the reconstructed cross sections is similar to the results of OCT reported on the developing sinews previously [94]. The morphology might also be due to shrinkage and distortion of the soft tissue as a result of the dehydration by the alcohol series. One of the most significant of the iodine results was the reconstruction shown in Fig. 3.14. In this case it appears that shrinking of the soft tissue resulted in it pulling away from the front of the anchor, leaving a distinct air–gap between the two materials, and revealing a dense layer of radio-attenuating mineralised particles in the

sinew.

The formation of a graded interface was the aim of this chapter and this has been achieved to an extent. A region of dense mineralised particles mixing with the soft tissue was observed. The presence of a smooth mechanical gradient remains uncertain as whilst the AFM was able to differentiate between the tissues, showing a mapping of the hard tissue similar to those produced using CRM, mechanical measurements and mapping were made unreliable by preparation artifacts.

Previous work performed using a similar system to determine the ability of brushite to mineralise a hydrogel has been reported by Koburger *et al.* 2014 [231]. In this study brushite/hydrogel disks were aged in PBS or simulated body fluid (SBF), and imaged via CRM mapping over the interface region between the two materials. Mappings over the v_1PO_4 phosphate peak for all CaP phases showed a deposition of mineralised particles in the hydrogel near the interface after exposure under *in vitro* conditions similar to the results presented in this chapter. Likewise analysis of the mineralised particles showed their composition matched that of the cement, with little compositional change, beyond evidence of a low quantity of OCP forming [231]. The quantity of mineralised particles was determined to be much higher in samples with static media, than those with media changed dynamically on a daily basis, as a result of saturation of ions in the static media. The increased complexity and dynamic nature of the BBLC system compared to the brushite/hydrogel disks, which used a different and acellular hydrogel, presented different biochemical conditions. The build up of particles is much smaller and highly variable in the BBLC, in part this will be due to the refreshment rate of the media and the known dissolution inhibition of the FBS proteins present in the sDMEM media [126].

The extension of large mineralised particles along the entire length of the sinew, as observed in the micro-CT reconstructions, complicates the matter with mineralisation clearly

occurring and influencing the ligament sinew well beyond the interface region. Collagen becomes progressively stiffer with mineralisation [236]. Whilst the presence of bonding between mineral and collagen is unknown the presence in such a large quantity will effect the stiffness and reduce the effectiveness of the sinew to act as a viscoelastic soft tissue. To reach a point up to 5mm away from the anchor itself the mineralised particles will have undergone reprecipitation from the media. Migration of large particles without a large driving force will be limited by the fibrin–gel pore size, which whilst not measured could not be on the order of the larger particles observed. Alternatively dissolved mineral ions in the sinew could be re-precipitated, as a result of media saturation, onto a suitable nucleation site which acted as a seed for further crystallisation. It is possible that particles were detached from the anchor during the construct preparation process and became caught in the contracting sinew. However the internalisation of the particles and increase with respect to time in culture makes this unlikely.

The mechanisms for the breakdown and dissolution of the CaP cement anchor are key to understanding and controlling the formation of the interface. The behaviour of cements is complex with the composition [115], architecture [121], and chemical and biological environment playing important roles. In an implanted graft, native osteoclast cells would be expected to assist in the breakdown and resorption of CaP cements [121], however the CTF cells present in the construct are not osteo–like in their properties and so would not be expected to be a factor. As such changes can be assumed to be as a result of dissolution and re-precipitation of soluble ions caused by immersion in unsaturated media.

Cement formation is a result of the reactant and acid reacting when mixed, leaving product and a residual quantity of reactant. A granular structure can be seen in the results from each imaging modality with Raman spectroscopy showing that the grains are TCP dominated, surrounded by an inter-grain region composed of brushite and TCP. Mineralisation across multiple length scales is observed in the sinew at later time points. A

background of the major TCP peaks can be observed in the sinew well away from the anchor and observed particles so that it would be outside the spot size to excite and collect from the anchor itself. The weaker v_1PO_4 peaks are harder to determine in these cases due to the weaker signal making the composition other than TCP less certain. Unpublished results obtained from TEM have shown a high build up of need-like mineralised crystals is present in the sinew and cells around the anchor at the nano-scale. These needles are expected to be HA based on their structure, however the ability to detect such small quantities of HA in the sinew is limited to higher resolution imaging techniques such as TEM. The dominance of the TCP peaks indicates that a large quantity of submicron TCP crystals are present in the sinew.

Phase changes as a result of ageing of the brushite samples are not expected in significant quantity due to the recorded inhibition of the hydrolysis of brushite in an environment with serum [127]. However the observation of brushite undergoing dissolution at later time points leaving a TCP dominated cement, with the formation of OCP at the outside of the anchor and in mineralised particles in the sinew. It has previously been reported that the rate of brushite dissolution increases with the refresh rate of the media as more saturation free media allows for the dissolution of ions [126]. However conversely for the re-precipitation, in this case in the form of OCP, the removal of Ca and P ion saturated media reduces the resources for recrystallisation and precipitation.

TCP is much less soluble than brushite, and so is not expected to undergo dissolution, despite this the presence of TCP was observed in particles and the background of the sinew. Based on the results shown it appears the dissolution of the brushite dominated intergrain-region might release locked up smaller particles of TCP and cause the TCP grains to fragment. Additionally TCP grain boundaries have been shown to be more soluble, so could cause fragmentation in TCP with cell media when not expected to be any at all [120]. The high quantity of mineralisation observed in the iodine stained sample

suggests fragmentation with mixing by the sinew around it.

In native tissue the crystallisation of minerals is a complex process controlled by biological mediation. Cyclic stretching of the sinews may be an important factor in the controlled extent of mineralisation, no work has been performed directly testing this development however.

Pathological crystallisation is common with the higher than normal saturation of the mineral in body fluids, quantity of crystallisation inducers/inhibitors and a lapse in the immune system leading to the formation of calcified deposits [237]. The deposition of large quantities of mineral in the ligament portion of the BBLC is particularly similar to results seen in clinical studies of the formative phase of calcific tendinopathy, a disease where calcified deposits build up in the L/T [238]. Calcific tendinopathy can occur in any L/T, with the most common being in the rotator tendon cuff [237]. The build up of calcification is thought to be due to either the degeneration of L/T fibres followed by development of calcium deposits [239], or a favourable environment permitting cell mediated calcification [238]. Calcifications generally are later reabsorbed, or in a smaller number of cases require surgery to remove [238]. Analysis of removed calcified deposits reported by Grases *et al.* 2014 found they were present in regions of collagen disarray and consisted of amorphous and poorly crystalline carbonated HA [237]. The same research also suggested that lower levels of the inhibitor phytate, and high levels of the regulator osteopontin.

The similarities in the two environments (particularly the particle's dense, well defined and homogeneous nature) suggest the possibility of using the findings from native systems to optimise the BBLC and use it as a model for calcific teninopathy. The cells present and differences in environment likely make mediation by cells in the BBLC unfeasible. More probable is the supersaturation of dissolved brushite in the media followed by seed-

ing onto a crystallisation inducers. The poorly developed and organised collagen at early time points in the formation of the BBLC may allow crystalline seeding, or other debris. In either case the presence of mineralised particles will be disruptive to the formation of the sinew and its desired biomechanics.

Given the high rate of brushite dissolution, this raises the issue of whether brushite and similar high solubility bone graft materials may present an increased risk for calcification of proximal soft tissues. A search of the literature found no evidence of this, however the only relatively recent introduction and low use of brushite may have prevented sufficient cases to be noted. The high refreshment rate of fluids and relative total volume when *in situ* compared to the *in vitro* experimental environment may prevent such an issue occurring.

A number of limitations were present in the work presented in this chapter. Consistency in the materials used, development *in vitro* and sample preparation. Attempts were made to ensure materials used were consistent and from the same batch. Preparation of interface in particular was problematic due to the differing material properties between the hard and soft tissues. The use of pins to hold the anchor in place further complicated this by weakening the anchor structure and providing a large fault line for total structural failure. Attempts to embed pinless anchors into the SYLGARD were unsuccessful.

Another main limitation in the work presented here is the resolution of each modality used was in the μm range. Crystals and particle sizes of mineralised components are far more often on the nano-scale. Work not published by other members of the group using TEM has shown extensive mineralisation of the cells and fibrin sinew about the anchor at the nm scale.

The work in this chapter has shown that mineralised particles, with chemical spectra matching those observed in the anchor, became distributed in the soft tissue. In part this

has suggested the formation of a mixed interface with a dense mineralised band around the anchor, however the micro-CT results showing large (micron or larger) mineralised particles along the length of the sinew and increasingly as a result of time *in vitro* suggests that the mineralisation is able to occur well beyond the interface. This total mineralisation could present a significant obstacle to the development of the ligament construct as the mineralised particles will disrupt the formation of aligned collagen in the soft tissue and a sufficiently high level of mineralisation along the soft tissue would greatly increase the stiffness, reducing both the effectiveness of the developed interface and the ability of the soft tissue to undergo tensile load without failure. Controlling the extent of the mineralisation may prove difficult due to the single unit nature of the construct which is formed in a open environment, making localised addition of growth factors to encourage the breakdown of mineralisation in only specific areas infeasible.

Given a sufficient supply of phosphates or similar minerals it might be expected that the entire sinew will eventually consist of mineralised collagen. Such a result would make it impractical as a ligament, but it could potentially be translated to use as a bone graft material or model of bone formation. Native cortical bone is composed of a hierarchical structure consisting of collagen fibrils bonded to HA. The medical applications of such a graft and a further investigation into the potential is presented in Chapter 6.

3.6 Future work

Future work on the development of the interface will need to focus on the optimisation of the design of the cement anchors, and the imaging techniques. Especially with regard to requiring minimal invasive sample preparation to reduce artifacts and the number of destroyed samples.

Optimisation of mineral release and resorption will be key for the CaP cement anchors

to produce a graded interface over a range in the order of several hundred microns with a strong attachment. The use of surface modification to control the size and release of mineralised particles along with factors such as porosity to encourage biological and soft tissue ingrowth may be required. The use of methods such as 3D printing would allow for such high precision design, with potential for the incorporation of biological materials such as collagen [240]. This would provide a significant advance over the current method of mixing the components by hand and leaving the solution to set as a whole, which is liable to produce inconsistent results. Considerable work could be performed looking at the composition and phases used in the anchor, in addition to the embedding of drug or growth factors into the cement for slow release and their effect on the soft tissue. Increasing the media refreshment rate, such as by a constant flow as found in closed bioreactors, may limit the saturation of mineral ions in the media and reduce or prevent substantial mineralisation in the sinew body. The addition of crystalisation inhibitors such as pyrophosphates to the media may reduce the build up of large mineralised particles [139, 241]. Biologically the co-culture of osteoblast cells on the anchors prior to, or after BBLC production may allow for better biological mediation of the mineral components in the system.

Imaging techniques to improve the quality and reliability of data obtained using the reported modalities, and extension to further modalities is required to elucidate the mechanisms and evolution of the interface region. One of the major limitations in this work was the weakness of the signal from Raman scattering, requiring long image scans for a single area. This was limiting both in the throughput of samples, and in the quality of data with risk of deformity from dehydration for exposed samples, or appearance of bubbles or changes in the volume of water present in hydrated imaging conditions. Whilst Raman is an inherently weak scattering effect there are techniques with significantly higher signals which have been developed that are able to produce video-rate images; CARS and SRS. Ideally a micro-tome combined with a CARS or SRS microscope, similar to those

reported before by Rosenthal *et al.* [242], would allow a rapid and detailed throughput of data and a 3D chemical map of the entire interface region to be built. However with large mineralised particles the cryotoming process may remove particles from the sample, leaving an empty hole in later layers and images. Extension of computational analysis with the applications of more advanced techniques such as Principal component analysis (PCA), to provide a deeper analysis of the spectral information may be key to understanding the mineralisation process. Additionally combined CRM and AFM is possible with commercial instruments available. The setup with an ideally prepared sample would allow detailed chemical and mechanical data to be collected simultaneously over the same region. Such information would be highly valuable in determining if there is a gradient in mineralisation and stiffness that is truly representative of the mechanical function of the native enthesis.

Further TEM of the interface to investigate mineralisation at the nanoscale is required, particularly with respect to mineral presence at different times and distances from the anchor. Nanoindentation has been applied alongside AFM, to the mechanical mapping of the osteochondral interface [228] such an application here would enable the mechanical gradient across the interface to be measured. An alternative to probe based mechanical mapping would be Brillouin imaging [243], which uses the detection of thermally excited phonons to determine mechanical properties. Combined with Raman it has be shown to produce mechanical and chemical mapping [244], providing a detailed level of information that would be invaluable for understanding the state of the BBLC system and helping to optimise it.

Ultimately for the system to be directly clinically translatable effective, non-invasive imaging and monitoring will be needed. As discussed at the start of this chapter (section 3.1) a number of modalities allow for this including: ultrasound, MRI, OCT, and CT with controlled doses. These would allow 3D reconstructions and data to be collected non-

invasively, but at the cost of reduced resolution compared to EM and standard optical microscopy. Knowing the state and organisation of collagen at the interface is important. With regard to mineralisation along the sinew, investigation of collagen structure and organisation around the mineralised deposits would be required to understand their structural effect. It is later shown in Chapter 6 that TP/SHG is able to produce three-dimensional stacks through the mineral component and the collagen organisation through the TP and SHG modes respectively.

CHAPTER 4

SINEW DEVELOPMENT

The soft tissue sinew body of the construct is another vital component in the effective tissue engineering of a viable ligament replacement graft. As discussed in section 1.1.1 the load bearing capabilities of ligaments are enabled by high levels of collagen and elastin which align along the axis of load providing tensile strength and viscoelastic properties respectively. For the ligament-construct to function as an effective replacement graft the digestion of fibrin and formation of a new ECM by the seeded fibroblast cells will need to take place. This chapter investigates the changes in cellular and extracellular content and organisation inside the sinew body as the construct develops and matures.

4.1 Alignment in tissue engineering

Due to the importance of cellular and ECM organisation in tissues there has been a large quantity of work performed investigating controlling the alignment of engineered scaffolds through scaffold design or external forces. Previous work has used topologically patterned surfaces, chemical signals, loading forces, and electric stimulation to induce the desired structural alignment [245].

The initial scaffold design, and subsequent growth and remodelling under *in vitro* conditions need to be monitored and optimised to ensure effective integration. The cells

present, matrix composition, and application of external stimuli will affect how the scaffold is remodelled and the growth factors or ECM that are secreted. Fibroblast cells are known to be load sensitive and will align along the axis of strain [246, 247]. They have been shown to continually reorganise existing collagen based matrices based on the load [248], with the remodelling and deposition of new collagen dependent on the cellular morphology [249] and environmental conditions [250].

Cells react to their environment and external stimuli, with the deposition and remodelling of the ECM [249]. Various means have been used to achieve this in two dimensions including the use of micropatterned surfaces [251], mechanical tensile forces [252, 253], or shear forces [254]. These have allowed effective study of the effect of specific conditions such as cell elongation [249]. However the physiological accuracy and application of two dimensional substrates is limited due to their unrepresentative nature making them unsuitable for biomedical applications. As a result an increasing number of studies are concentrating on inducing alignment in three dimensions, by the design of scaffolds to incorporate features such as electrospun fibres [67, 70] and the application of static or cyclic tensile loads [95, 255]. Much of the reported work has been performed on 2D surfaces. This allows easy control and observation of the cells and ECM but is not representative of a 3D system. Due to the limits of the 2D systems and need to develop effective tissue engineered scaffolds for *in vivo* there has been increasing interest in the development of 3D aligned scaffolds. Computational modelling of finite element systems has been increasingly used in recent years to predict strain and resulting matrix organisation [247, 256]. For further information on engineering alignment see a recent review by Li *et al.* 2013 [245].

As discussed in Chapter 1 there is an essential need to image tissue engineered constructs as they develop, to monitor their development and ensure successful optimisation [257]. A range of imaging techniques have been harnessed to provide information on tissue engineered constructs [257]. Of these light microscopy is the most widespread and easily

accessible allowing general reflectance/transmission, polarisation, or specific labelling of cellular structure; both *in vitro* and after removal from culture. Depending on the nature of the material, birefringence can be exploited by polarised light to provide further information on alignment, particularly with materials like collagen which have an intrinsic birefringence. Polarised light microscopy [258, 259], OCT [260], and SHG [164], along with the other modalities discussed in section 3.1 are able to provide information on the collagen structure in the imaging of engineered tissues. However microscopy images of complex cellular environments often require processing and analysis to gain the desired information. Manual quantification of microscope images is time-consuming and open to variations based on individual interpretation. As a result of this a number of automated or semi-automated computational quantification techniques have been developed in recent years for application in this area for the purpose of measuring cellular/fibre orientation and overall alignment [245]. These include elliptical fitting [261, 262], binary statistical [263], Radon transform [264], and fast Fourier transform radial sweep (FFTRS) [254, 265, 266, 267].

4.2 Chapter aim

The aim of this chapter was to investigate the biological formation and development of the soft tissue sinew body as the BBLC developed and matured. Using microscopy techniques to image the development and provide quantifiable measurements by computational processing.

4.3 Methods and materials

4.3.1 2D fibroblast culture

22x22mm glass cover-slips were sterilised by immersion in 70% ethanol followed by rinsing in PBS, and placed inside 33mm well plates. 1mL of DMEM (supplemented with 10% bovine serum, 1% penicillin/streptomycin, HEPES, L-glutamine) with CTF cells between passage 2 and 5 were added with a cell concentration of $100x10^3$/mL. Cells were aged in incubators at 37°C with a 5% CO_2 atmosphere. The cell media was replaced every 2-3 days with 2mL of sDMEM. At 14 days slides were removed from culture and prepared for imaging.

4.3.2 Fibrin only and SYLGARD sinews

In addition to the brushite anchors constructs were produced using SYLGARD anchors cut to the shape of the brushite anchors with stainless steel pins inserted through them, or with only stainless steel pins.

Fibrin only constructs were produced as above, with the exception of the exclusion of anchors, were produced and aged for 0 to 21 days.

4.3.3 Immunofluorescence staining

Constructs were removed from incubation at 3-4 day intervals from day 0 to day 18 and prepared for imaging using a whole mount method. Constructs were removed from culture, washed with PBS, set in 4% formaldehyde overnight, washed with PBS, cryotomed at -21°C (Starlet 2212, Bright Instruments, UK) to provide a smooth surface for imaging and allow penetration of the constructs inner structure, washed with PSB, permeablised in 0.5% triton-x (Fisher, UK) at 37°C for 4 hours, washed with PBS, stained with $10\mu L$ 5mg/mL DAPI (Invitrogen, UK) and $10\mu L$ phalloidin 6.6μM (Invitrogen, UK) in 2mL PBS for 4 hours at room temperature, washed in PBS to remove excess stain, and left to

dry overnight.

4.3.4 Confocal microscopy

Imaging was performed using a fluorescence confocal microscope (TCS SPE, Leica systems, Germany) with a 10x atmospheric objective lens. 410nm and 532nm laser excitation wavelengths were used for DAPI and phalloidin images respectively, with 3 frame averages used to produce each image. Images were acquired along the length of the sinew at each time point, and saved as 1024x1024 pixel uncompressed tif files with both stains overlaid.

4.3.5 Fast Fourier transform radial sweep

Images were selected to avoid ligament wall or external space outside of the sinew. MATLAB was used to apply computational processing. Images were converted to grey-scale, tapered around the edge using a Gaussian based function, and put through a high-pass filter, before being converted via a two dimensional fast Fourier transform (2D-FFT) to a frequency shifted power spectrum. Pixel intensity was summed along each angle from the centre of magnitude power spectrum images about 180 degrees in 1 degree increments. The image was rotated for each angle, with every increment taken from the default image. The first 10% of the pixels in each angle outward from the centre were discarded. Results were normalised against a theoretical maximum intensity for an ideal case of total alignment. A histogram of the intensity for each angle was output. Values for the angle of maximum intensity and orientation index defined by the number of steps away from the angle of maximum intensity until more then 50% of the total pixel intensity had been covered - were calculated.

4.3.6 Rat tendon

Tendon sections were taken from the tail of adult rats. Extracted sections were fixed in formaldehyde, cryotomed, permeablised in triton-x, stained with DAPI and imaged using

confocal microscopy as described for the constructs described above.

4.3.7 Raman Spectroscopy

Single point spectra were taken from the surface of the ligament midpoint in fixed day 7, 35 and 45 BBLCs. Raman spectroscopy was performed using a 785nm excitation wavelength, with 20 accumulations of 3s integration times acquired. Cosmic ray removal, and baseline correction performed on collected spectra.

4.4 Results

4.4.1 Cells cultured on cover-slips

Cells were grown under two-dimensional culture conditions to determine their behaviour under non-guided conditions. CTF cells cultured on plain glass cover slips in a 2D system were observed to quickly multiply and cover the slip to the point of confluence within 5 days. Confocal images of slides stained with DAPI and phalloidin at 14 and 21 days (Fig. 4.1) showed a high density of cells covering the surface of the slide with no overall alignment or orientation preference at either time point.

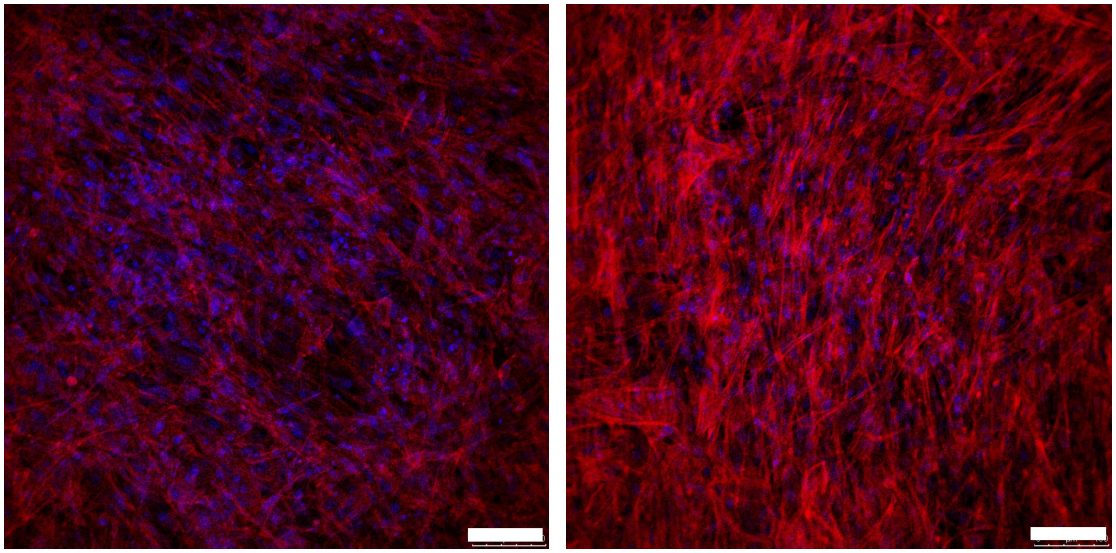

(a) (b)

Figure 4.1: Confocal images of CTF cells grown in two-dimensional culture conditions. Stained with DAPI (blue) and phalloidin (red) at (a) 14 and (b) 21 days. Scale bar $100\mu m$.

4.4.2 Fibrin contraction

Fibrin only scaffolds, identical to BBLCs without anchors to arrest the contracting sinew, were produced and allowed to contract under *in vitro* conditions for up to 21 days. To allow investigation of the behaviour of cells seeded into fibrin, without the driving forces induced by the anchors. Without the anchors in place to guide the morphology, the fibrin contracted into a singular spherical ball 2-3mm in width by day 7 and remained at that size for the remainder of the time course. Confocal imaging of the fibrin scaffolds (Fig. 4.2) showed changes in the cellular behaviour as the CTF cells adapted to, and changed the matrix. Initially at day 0, 4 hours after seeding, cells were seen to attach to the fibrin forming a thick layer of disorganised cells at the surface (Fig. 4.2a) with a much less dense quantity of disorganised cells to a limited depth into the scaffold (Fig. 4.2b). As the cells multiplied and migrated further into the contracting scaffold different cell behaviour was observed dependent on location. The thick outer wall of disorganised cells remained at all time points, with cells inside the scaffold body aligning together to form fibres of elongated cells connecting sections of outer wall (Fig. 4.2c, 4.2d).

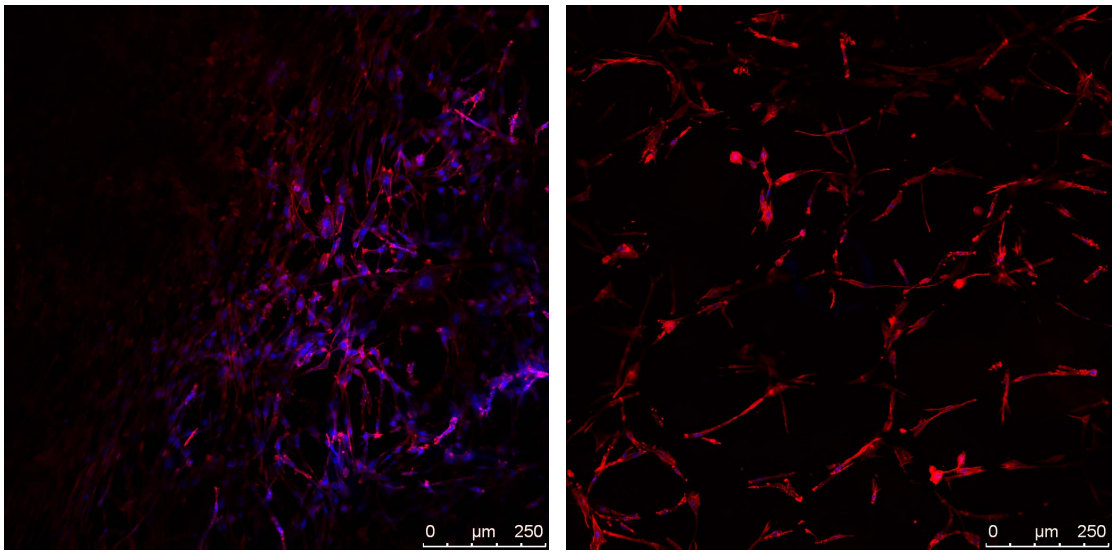

(a) (b)

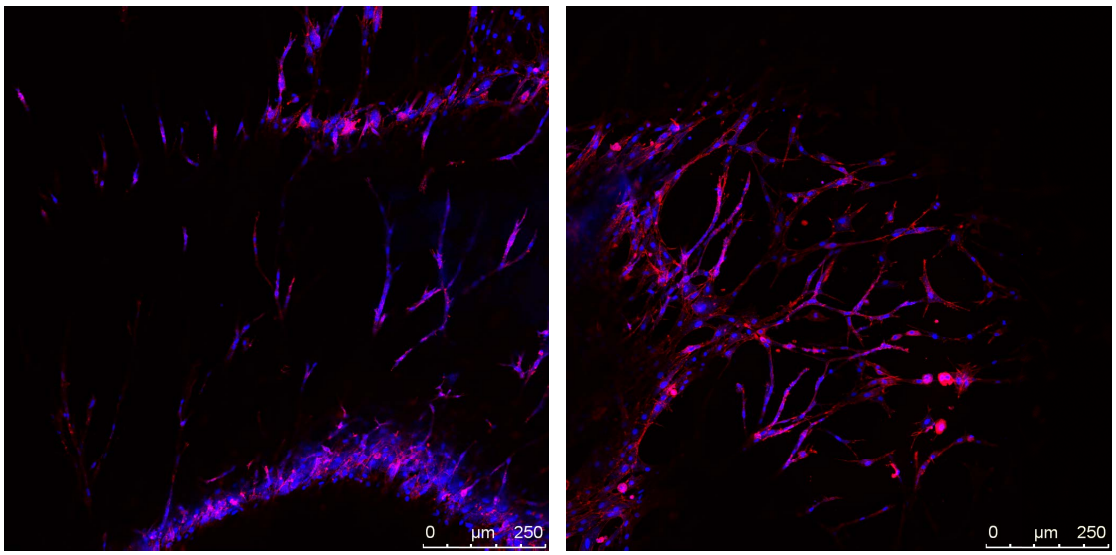

(c) (d)

Figure 4.2: Confocal images of stained CTF cells in fibrin undergoing contraction. Cells were stained with DAPI (blue) and phalloidin (red). Images show (a) the outside of the fibrin scaffold at day 0. (b) $40\mu m$ inside of the fibrin scaffold at day 0. (c) A cross section of the walls and inside of the fibrin scaffold at day 4. (d) Cell interaction at day 4.

4.4.3 Construct formation

Confocal microscopy performed on the midpoint of BBLC sinews at multiple points of development is shown in Fig. 4.3. As shown previously with the fibrin only constructs, a cell dense sheath was observed on the outside of the constructs at all time points with cellular migration into the fibrin gel matrix. In addition to the outer walls, thick inner walls were observed (Fig. 4.3b, 4.3d).

Significantly a high quantity of cellular elongation and alignment was apparent in the sinew body orientated along the axis of fibrin stretching, both in very high (Fig. 4.3a, 4.3d) and very low (Fig. 4.3c) cell density regions. The alignment of cells was generally observed to be highly linear, with large scale curvature around denser walls, but no evidence of a sinusoidal crimp like effect as seen in native tissues. A non-uniform structure was apparent in a number of cases. Typically the cell density inside the inter-wall region was much lower than that in the walls (Fig. 4.3b), further more the density and organisation of cells was seen to vary amongst regions at the same spatial point along the sinew with a highly aligned and elongated region or cells being separated (Fig. 4.3e). Gaps or distortions in the sinew as a result of tearing during preparation or disruption caused by the mineralised particles described in Chapter 3 were apparent (Fig. 4.3e).

Images obtained at the interface with the hard tissue showed cells behaving differently between the ligament body and when in proximity to the anchor. The interface at day 15 is shown in Fig. 4.4. A clear difference in cell shape and organisation is seen with cell in the ligament body exhibiting high elongation and alignment (as shown in Fig. 4.3), but becoming more stellate and less organised as they approach and reach the anchor. Notably a high level of alignment can be seen in cells looping around the outside of the anchor. Due to damage from the preparation process the tearing, distortion or total destruction of the interface region was a common problem.

To allow a better examination of cell behaviour around the anchor region, BBLCs were produced with SYLGARD anchors to prevent anchor/sinew bonding; allowing the non-destructive removal of the anchor without distorting the surrounding soft tissue region. Confocal imaging of contracted SYGLARD anchor constructs are shown in Fig. 4.5. Images taken at the interface region show highly aligned phalloidin stained cells diverging around the front of the anchor leaving a corridor of disorganised cells to the front of the anchor (Fig. 4.5 (a)). Fig. 4.5 (b) shows a stitched series of figures following around the interface to the side of the anchor showing the high alignment of cells in the lassoing arms.

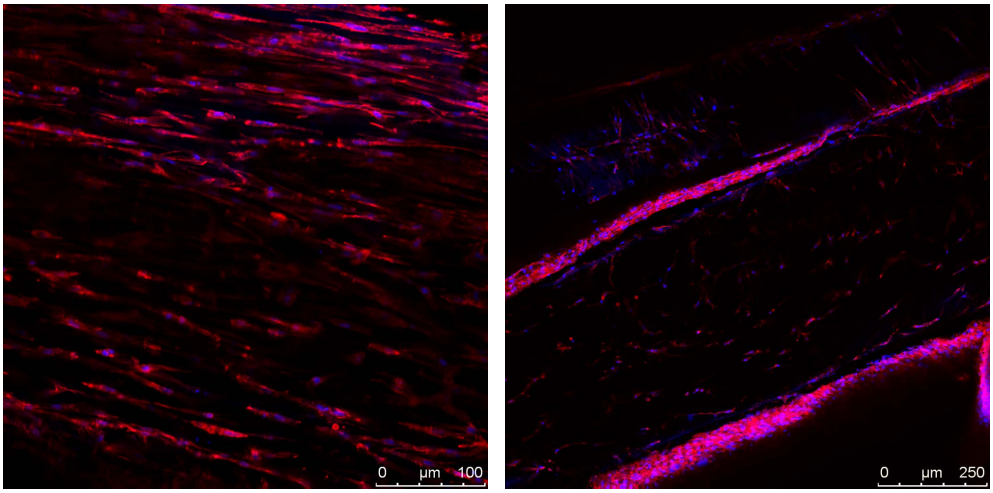

(a) (b)

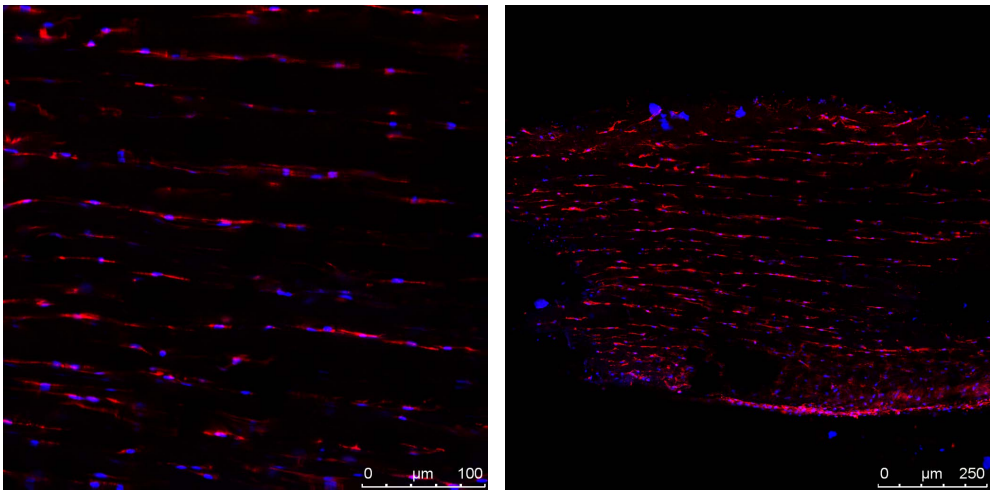

(c) (d)

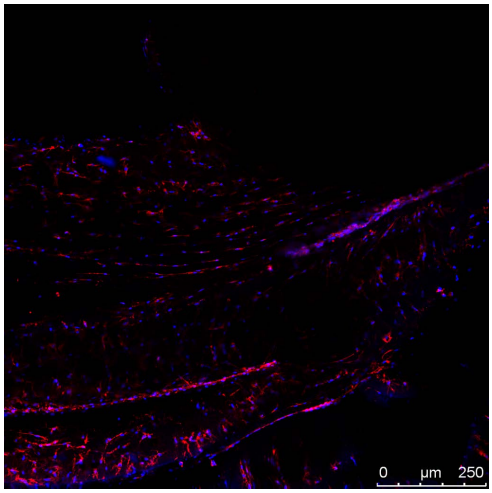

(e)

Figure 4.3: Confocal images of cells in contracted BBLCs. Stained with DAPI (blue) and phalloidin (red). Constructs at (a,b) 11 and (c-e) 18 days. Images are acquired with the long axis of the ligament going left-right.

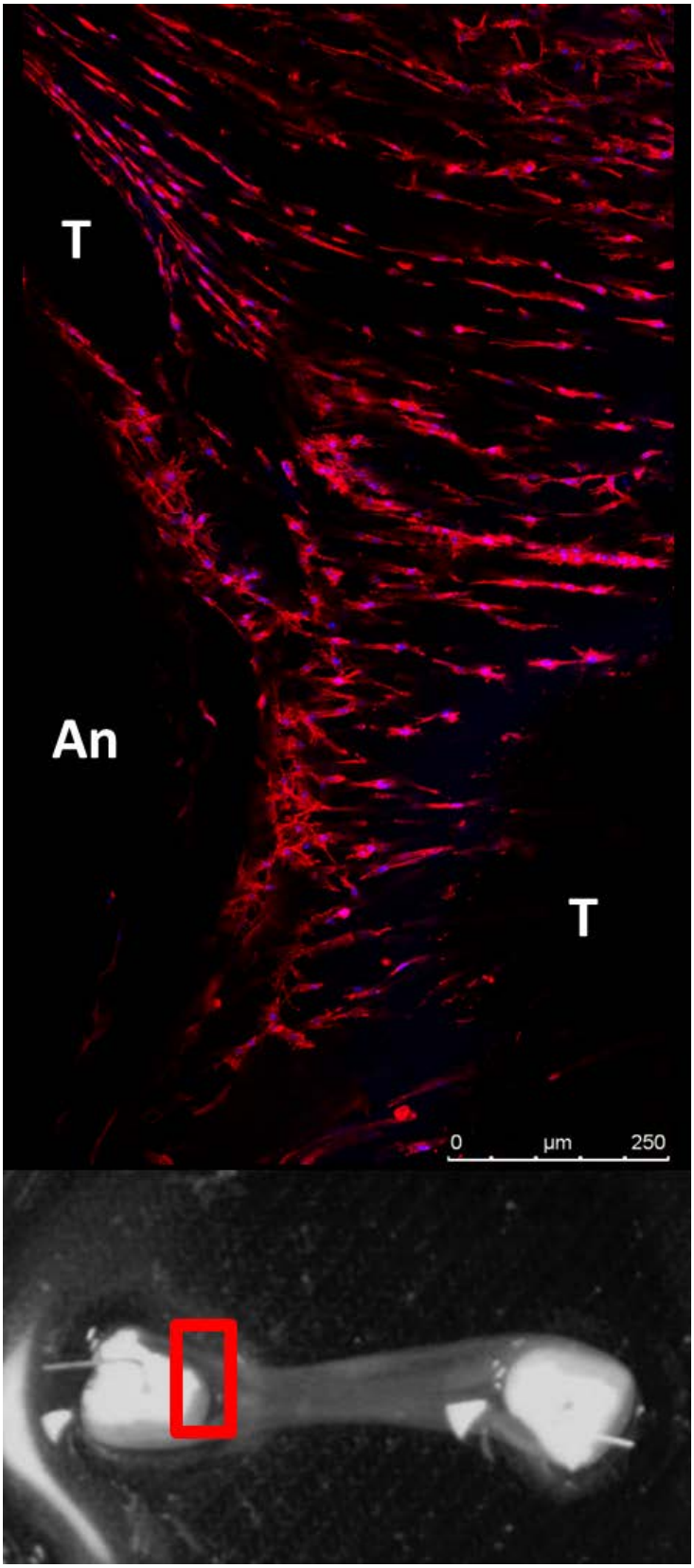

Figure 4.4: Confocal images of the day 15 anchor interface between the brushite anchor and soft tissue. Stained with DAPI (blue) and phalloidin (red). As shown in the photograph the brushite anchor (An) is on the lower left hand side, dark regions on the right are regions distorted by tears (T) in the soft tissue.

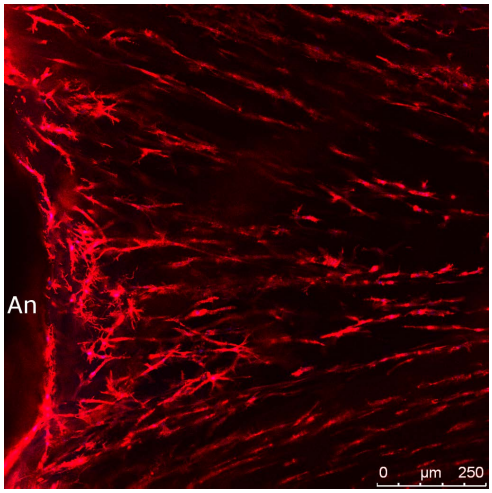

(a)

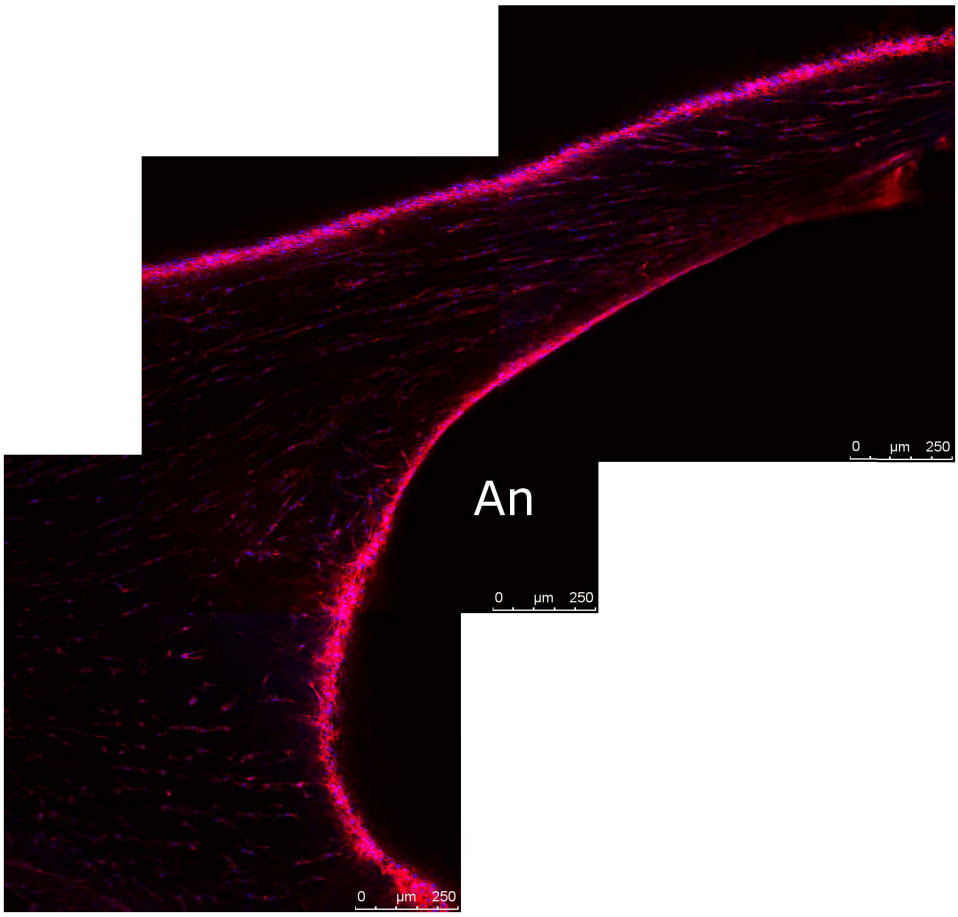

(b)

Figure 4.5: Confocal images of stained cells in BBLC produced with SYLGARD anchors. Stained with DAPI (blue) and phalloidin (red). (a) Cell organisation at the interface showing the divergence of aligned cells away from the front anchor/sinew interface and around the sides. (b) A series of sitched images taken at the interface and moving around the side of the anchor. An - anchor.

4.4.4 Computational analysis

Computational analysis of alignment in produced phantoms designed to mimic extreme examples of rounded vs elongated cells (Fig. 4.6) and imaged constructs (Fig. 4.7) was performed using FFTRS. By converting the image to K space by using a fast Fourier transform (FFT) a magnitude image can be produced (Fig. 4.7b) . By measuring the pixel intensity along each radial line a value for each angle giving a value for orientation can be produced and used to plot a histogram for each angle (Fig. 4.7c) [266]. Orientation index defined as - the number of steps away from the angle of maximum intensity until more than 50% of the total pixel intensity had been covered - was used to quantify each image as described by Sacks *et al.* 1997 [268]. Measured orientation index values of 47 for circles and 23 ovals for phantom images, and 25, and 18 for the day 0 and 18 BBLC sections respectively. Quantifiable results were obtainable, however the large variations in sinew structure and cell density made a more complete quantification along each construct and the whole time series impractical.

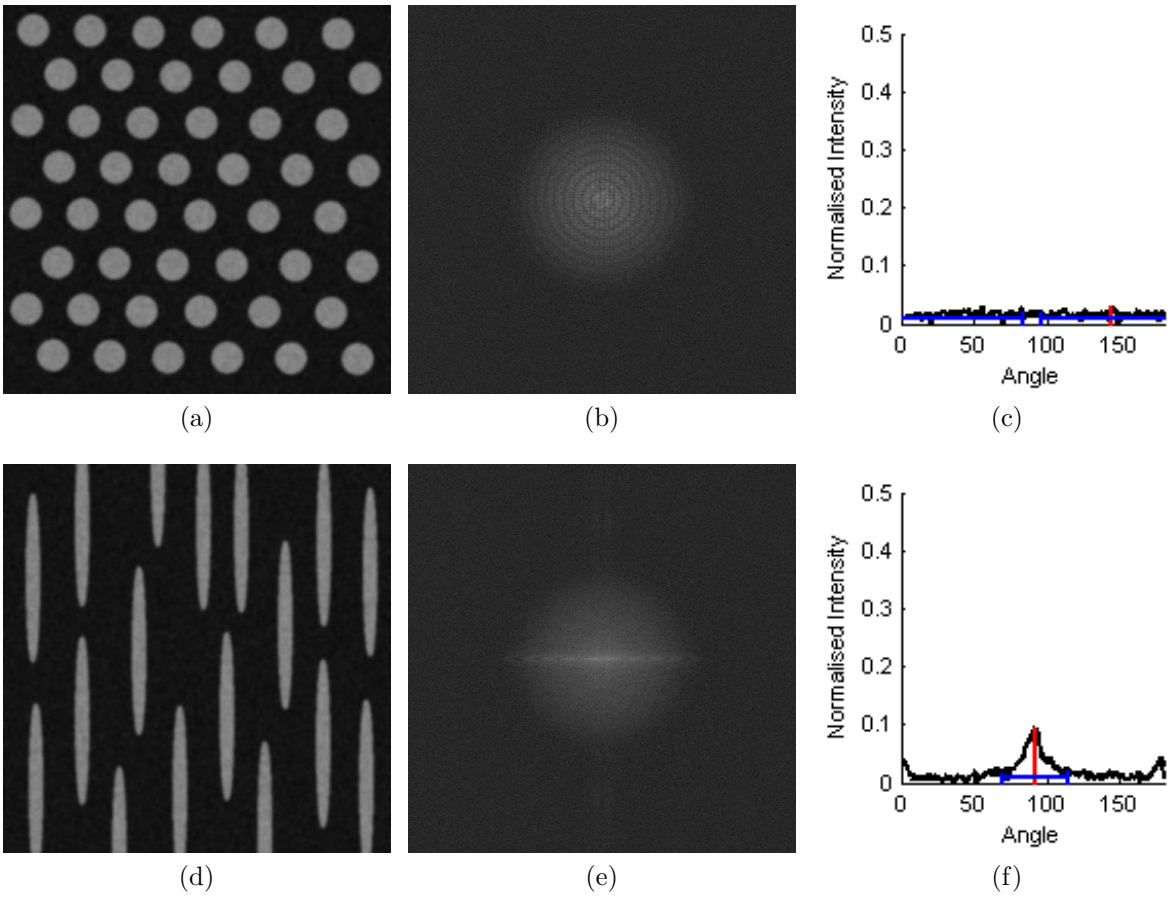

Figure 4.6: FFTRS of phantom images. Phantom images of (a) circles and (d) elongated ovals, with their respective (b,e) magnitude images, and (c,f) radial sweep histograms.

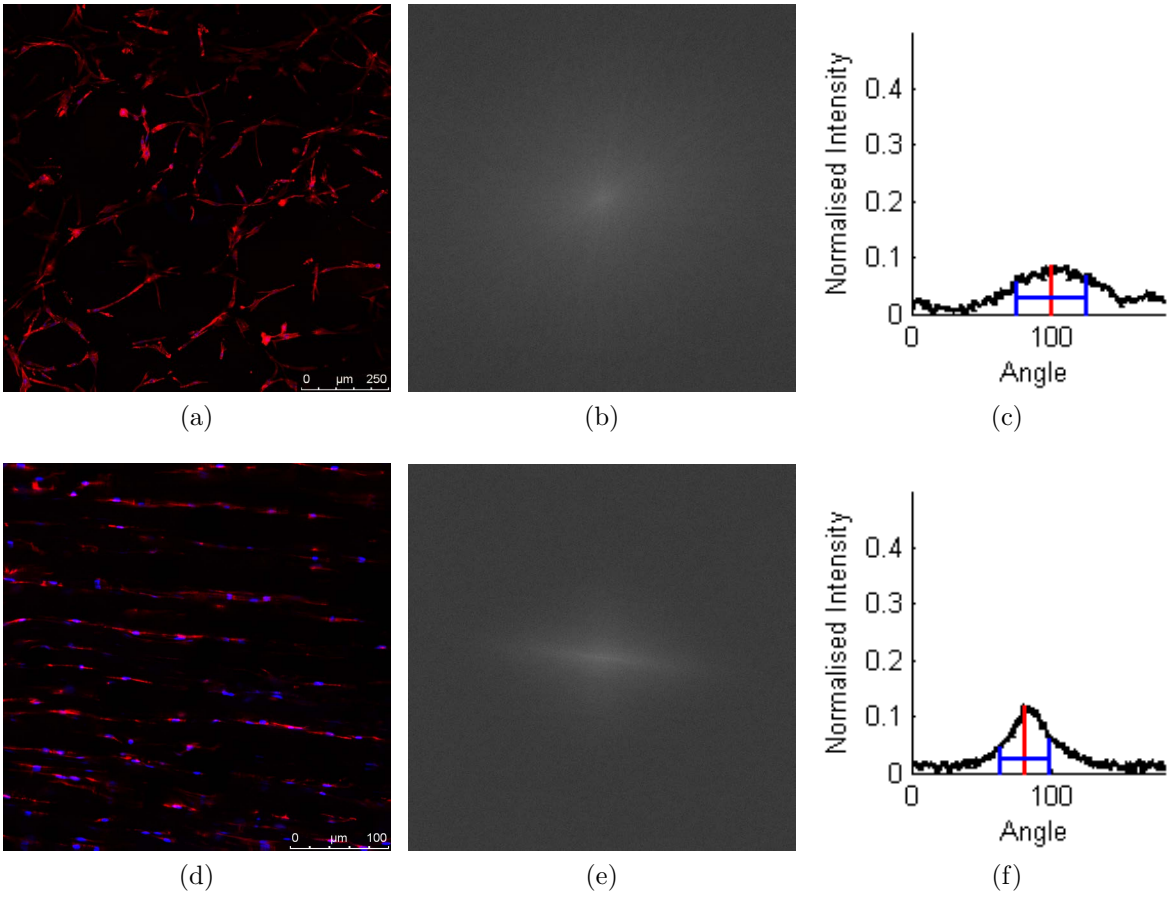

Figure 4.7: FFTRS of confocal microscopy images. Confocal microscopy images of (a) disorder day 0 cells and (d) elongated highly aligned cells, with their respective (b,e) magnitude images, and (c,f) radial sweep histograms.

4.4.5 Rat tendon

Rat tendon was imaged as a native tissue comparison for the BBLC cellular structure. Sections of rat tail tendon stained with DAPI were imaged under confocal microscopy (Fig. 4.8). Images were taken at multiple points in the tendon, with possible further variation due to preparation perturbations. As would be expected the images show a structure representative of the L/T anatomy described in section 1.1.1. Thick cell walls of the endotenon surrounding secondary fibre bundles, $250\mu m$ to greater than $500\mu m$ diameter were observed (unexpected given that others report much smaller sizes). The crimping of the collagen fibres can clearly be seen from the organisation of the cells which are known to be organised parallel to the collagen fibres. The amplitude and frequency of the crimping is seen to vary between images with a notable difference between the short sharp crimps seen in Fig. 4.8c and 4.8d, compared with the shallow longer crimps in Fig. 4.8a and 4.8b this is Likely due to the preparation of the tendon exerting a tensile force or allowing the fibres to relax. Interestingly the organisation of cell dense sheaths, separated by regions of less dense but highly aligned cells is similar to some of the structure seen in the BBLC sinew in the previous sections (despite the apparent lack of crimping).

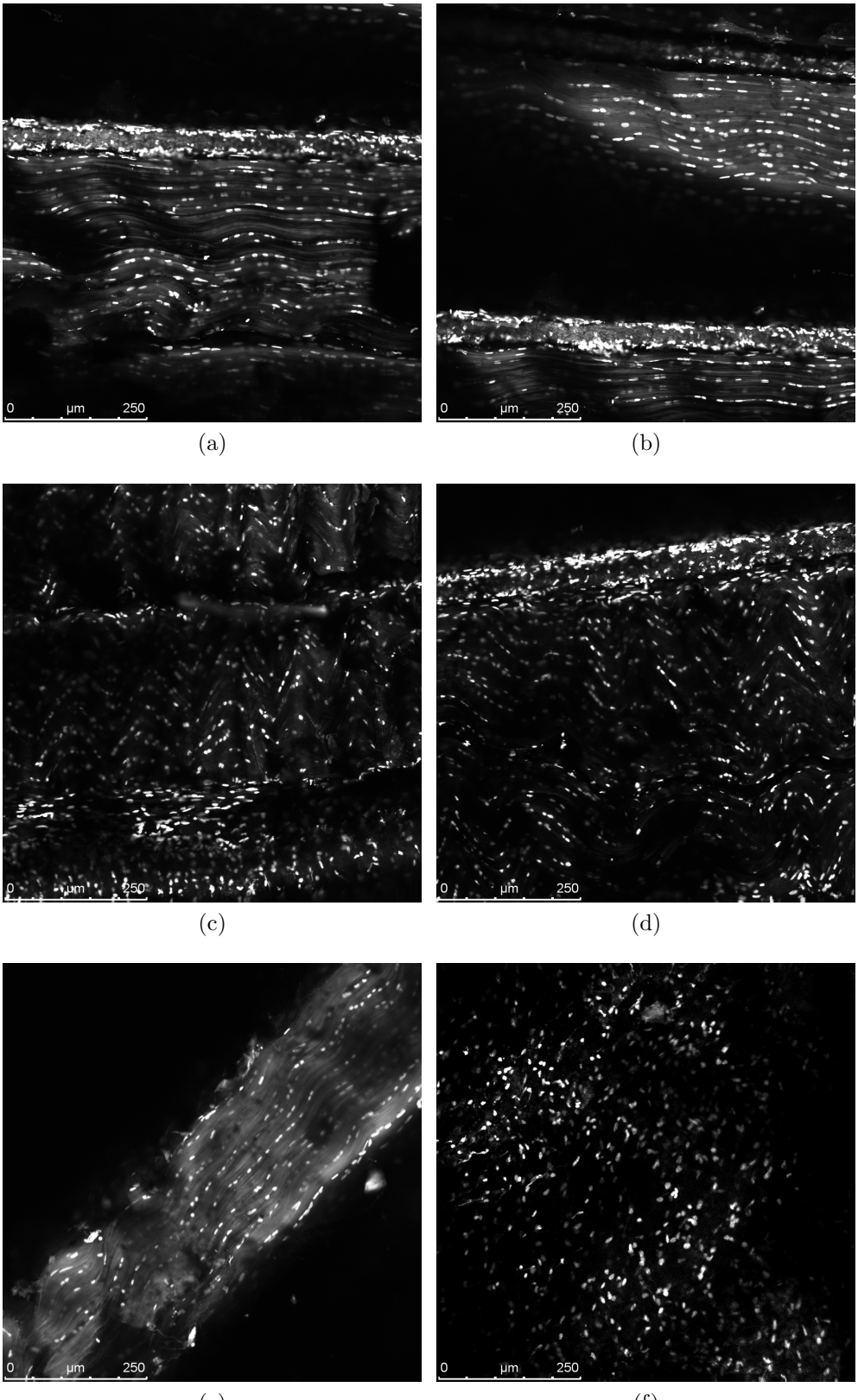

(a) (b)

(c) (d)

(e) (f)

Figure 4.8: Confocal microscopy of rat tail tendons stained with DAPI. Showing (a-e) the crimping structure of the cells between fibres inside secondary collagen bundles, and (f) the outer layer of the sheath surrounding the tendon.

4.4.6 Raman spectroscopy

Raman spectra were taken at the centre point in the sinew at multiple time points with a 785nm excitation laser (Fig. 4.9). Raman bands were assigned (Table. 4.1) based on previous reports in the literature [174, 269, 173]. Analysed spectra showed a clear presence of collagen content from day 7 onwards with the spectrum with dominance of strong peaks at the 1000cm^{-1} phenylalanine and 1655cm^{-1} amide I. The collagen associated signal was very weak compared to the background autofluorescence. Before day 7 only the auto-fluorescent aspect of the spectrum was apparent with the thin and highly transparent nature of the sinew making background signal from the polystyrene well plate a common interference (removed or not shown in presented results).

The Raman spectrum of fibrin and fibrinogen reported by Marx *et al.* 1979 using a 488nm excitation laser [270], show a highly similar spectral composition to that of collagen. The low level of signal, with no discernible peaks until the deposition of collagen is shown by biochemical assays [64], suggests that the Raman spectrum of collagen is what is observed in (Fig. 4.9). Assays for the specific collagen and fibrin content at each time point would be needed to confirm this though. While fibrin should be detectable under Raman spectroscopy it was not detected beyond the background noise in this study. The ratio and position of Raman peaks during the development suggest that the collagen composition remains consistent.

Table 4.1: Major Raman peaks found in the BBLC sinew.

Wavenumber (cm^{-1})	Vibrational mode	Assignment
750	Symmetric breathing of tryptophan	Tryptophan/DNA
850	Hydroxyproline	Collagen
936	Proline	Collagen
972	C-C backbone	Collagen
1003	Phenylalanine	Collagen
1243	Amide III	Collagen
1323	CH_2/CH_3 deformation	Collagen
1450	CH_2	Collagen
1655	Amide I	Collagen

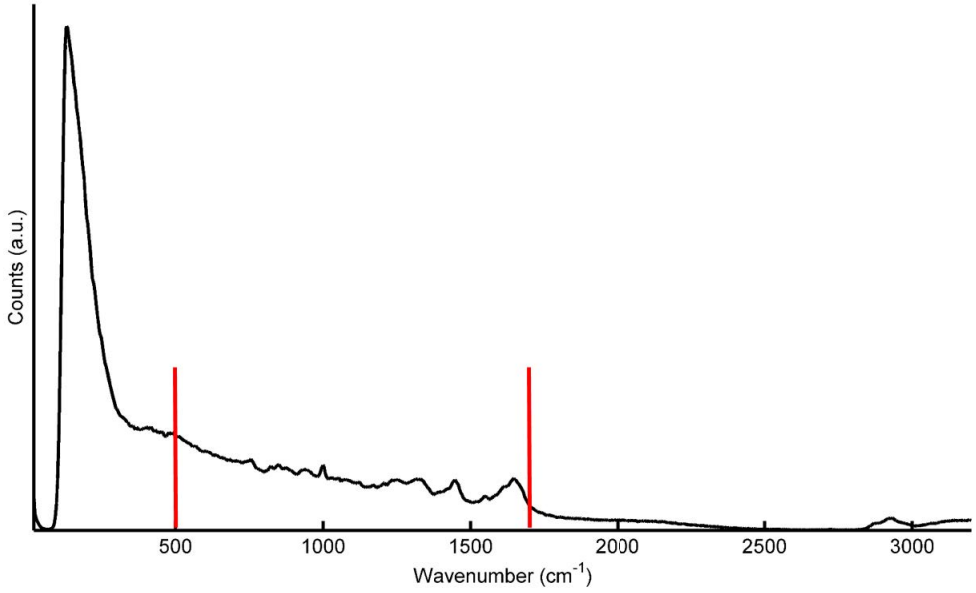

(a)

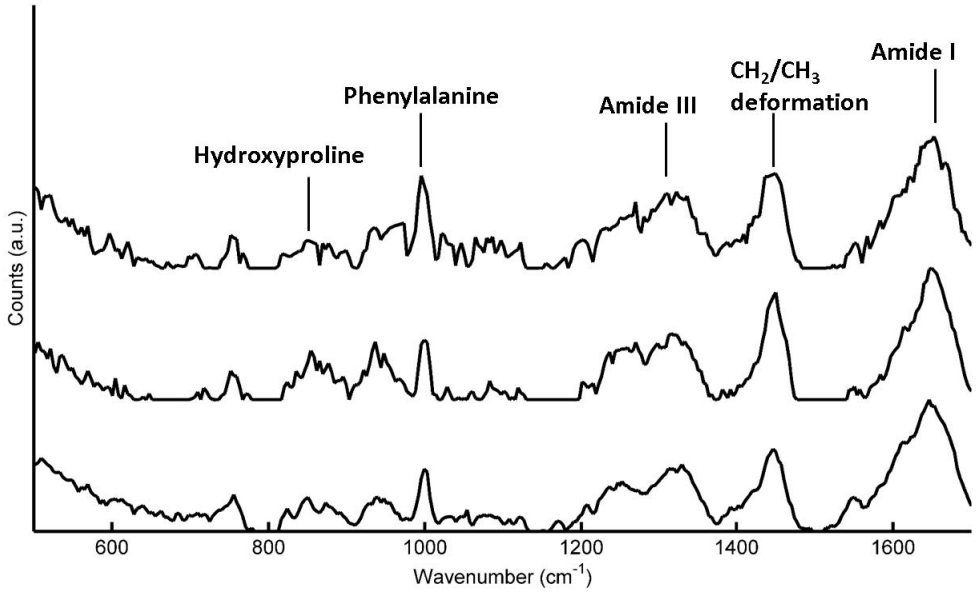

(b)

Figure 4.9: Raman spectra of BBLC sinew taken at multiple points during sinew development. (a) unprocessed Raman spectrum for day 7. (b) Background corrected Raman spectra of sinew taken at the midpoint of day 7, day 35 and day 45 samples. The red bands in part (a) show the position of the magnified region in part (b).

4.4.7 Two photon and SHG microscopy

As a means of simultaneously imaging the cellular and collagen structure of the BBLC, TP/SHG microscopy was performed on day 3, 7 and 45 BBLCs. Two photon and second harmonic generation image stacks were acquired simultaneously from the surface to about $80\mu m$ into sinews. Image stacks were taken at the surface at the midpoint of the sinew at the middle and edge showing the inside of the sinew (Fig. 4.10), and the cross section respectively. In each case a high level of autofluorescence is seen in the background of the TP images due to the fixation of the samples in formaldehyde.

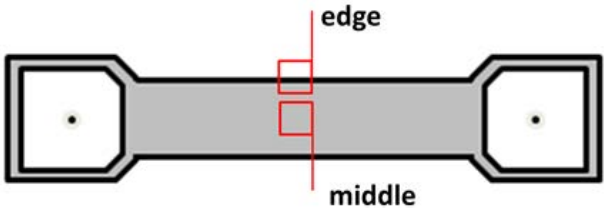

Figure 4.10: Schematic of regions TP/SHG image stacks were acquired in, and their designations.

Day 3 image stacks taken at the surface of the sinew are shown in Fig. 4.11. TP images showed a low density of cells organised into long strands as observed with the fluorescent stained cells under confocal microscopy previously (sections 4.4.2 and 4.4.3). SHG showed no evidence of collagen with only white noise evident in the collected images. Day 7 image stacks at the surface of the sinew (Fig. 4.12) more clearly showed the outer sheath of cells with alignment and interaction between cells. As with the day 3 sample the SHG images showed no collagen signal in the area imaged. A layer of thick particles were observed on the outside of the sinew, the lack of appearance of the particles in other samples and suggests that the structure observed was a contamination.

Stacks were taken at the surface (Fig. 4.13, with a higher resolution single frame shown in Fig. 4.14), and both edges (Fig. 4.15) of a day 45 sample. The mature structure showed significant change to the sinew structure in comparison to the earlier samples.

Most notably the SHG signal showing a very dense layer of collagen in the outer sheath along with the dense cell sheath. Inside the sinew the presence of continuous collagen fibres, with lengths in the order of 100s of microns, aligned along the axis of the sinew as seen under SHG indicates significant collagen organisation. In addition to the detection of collagen a much higher cell density both at the outside wall and inside of the sinew is observed compared to the younger samples, and a higher background fluorescence in the two photon images.

The outside of the sinews are shown in Fig. 4.15. From this it was seen that the collagen and cell density was highest at the outside of the sinew where it is in contact with the media. Matching the high cell density sheath shown with confocal imaging in section 4.4.3.

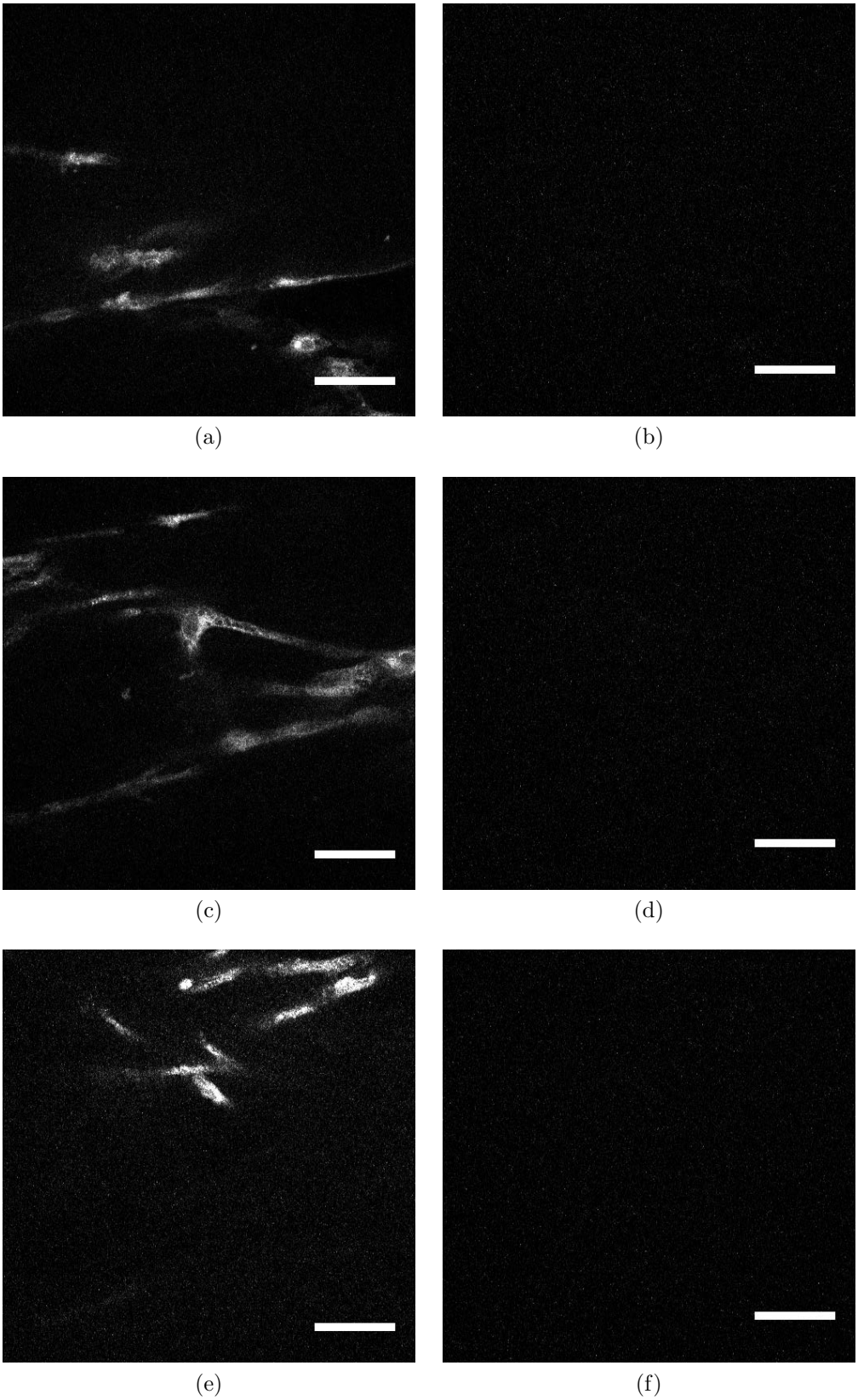

Figure 4.11: Two photon (a,c,e) and SHG (b,d,f) microscopy of the surface of a day 3 sinew. (a,b) At the sinew surface, (c,d) $30\mu m$ and (e,f) $60\mu m$ into the sample. Scale bar $50\mu m$.

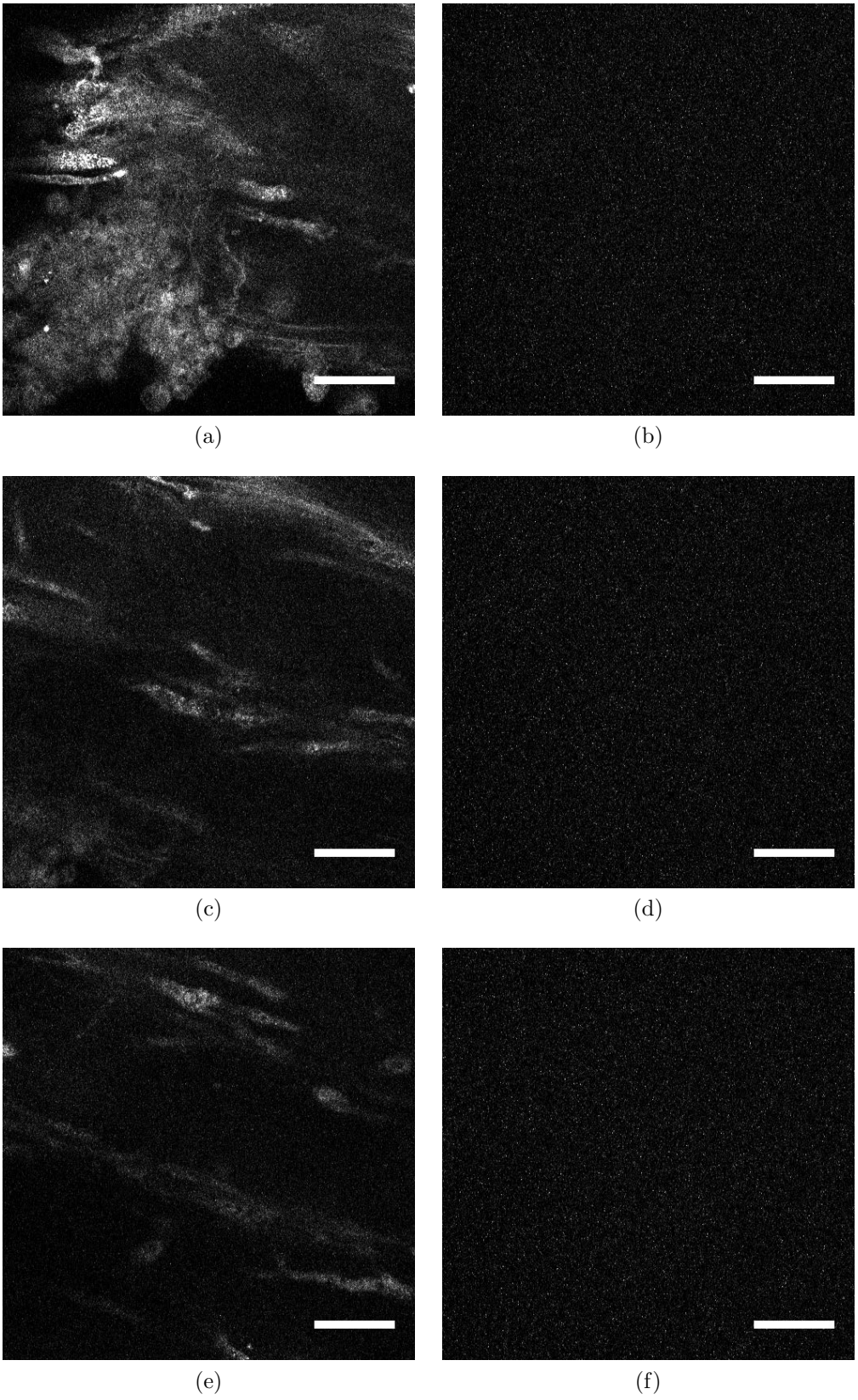

Figure 4.12: Two photon (a,c,e) and SHG (b,d,f) microscopy of the surface of a day 7 sinew. (a,b) At the sinew surface, (c,d) $30\mu m$ and (e,f) $60\mu m$ into the sample. Scale bar $50\mu m$.

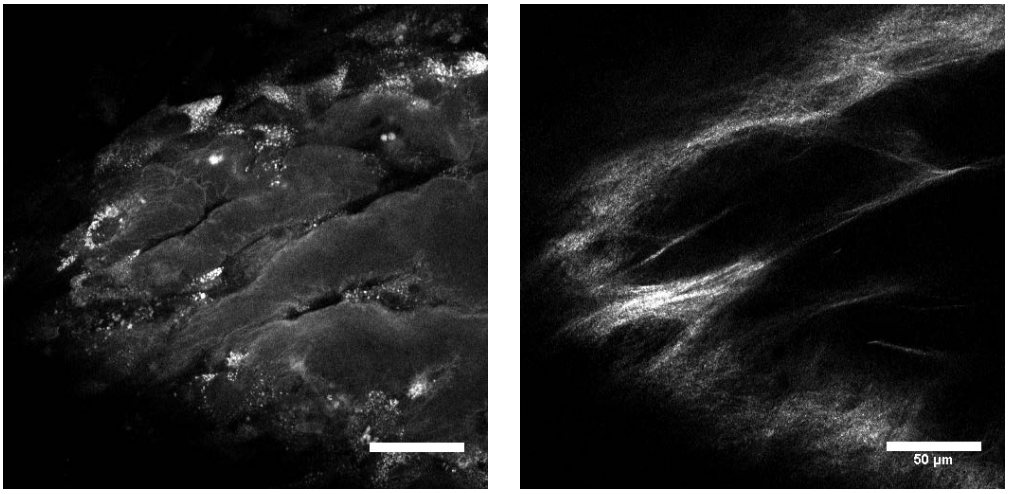

(a) (b)

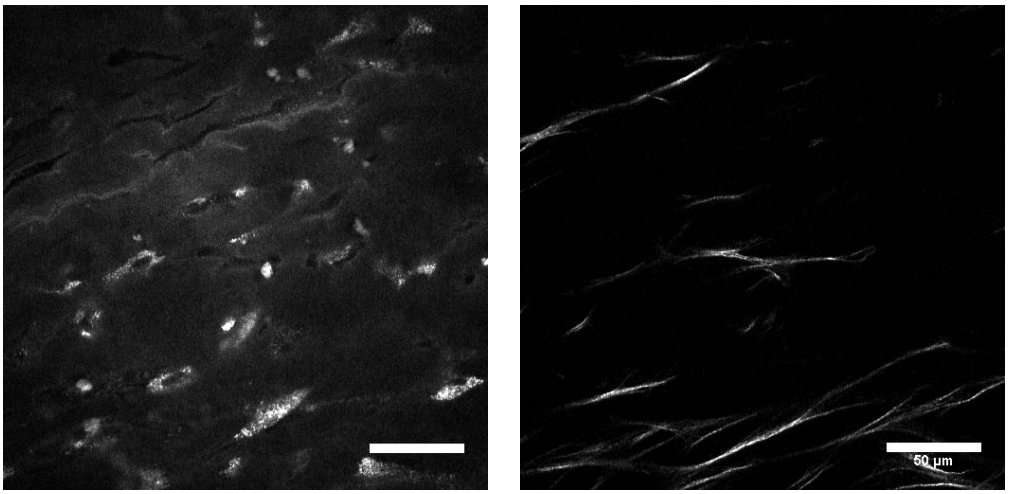

(c) (d)

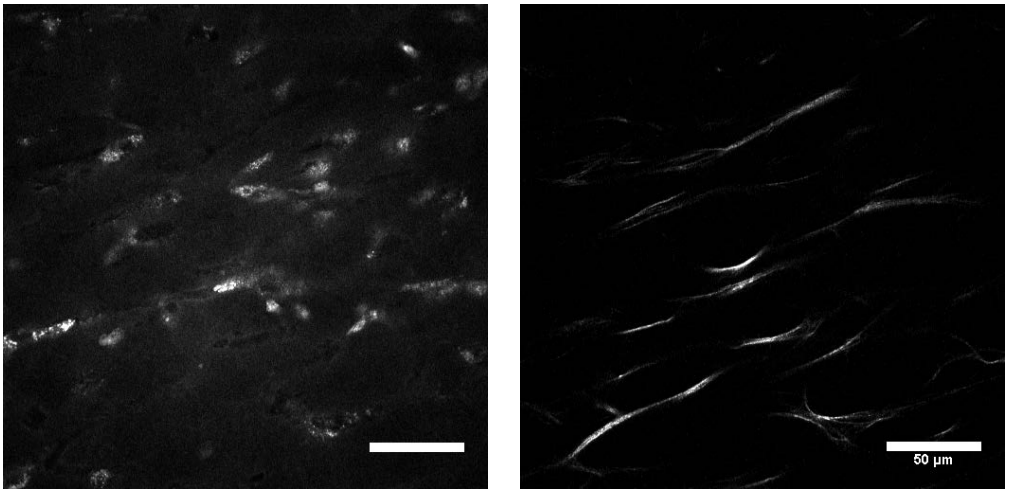

(e) (f)

Figure 4.13: Two photon (a,c,e) and SHG (b,d,f) microscopy of the surface of a day 45 sinew. (a,b) At the sinew surface, (c,d) $30\mu m$ and (e,f) $60\mu m$ into the sample. Scale bar $50\mu m$.

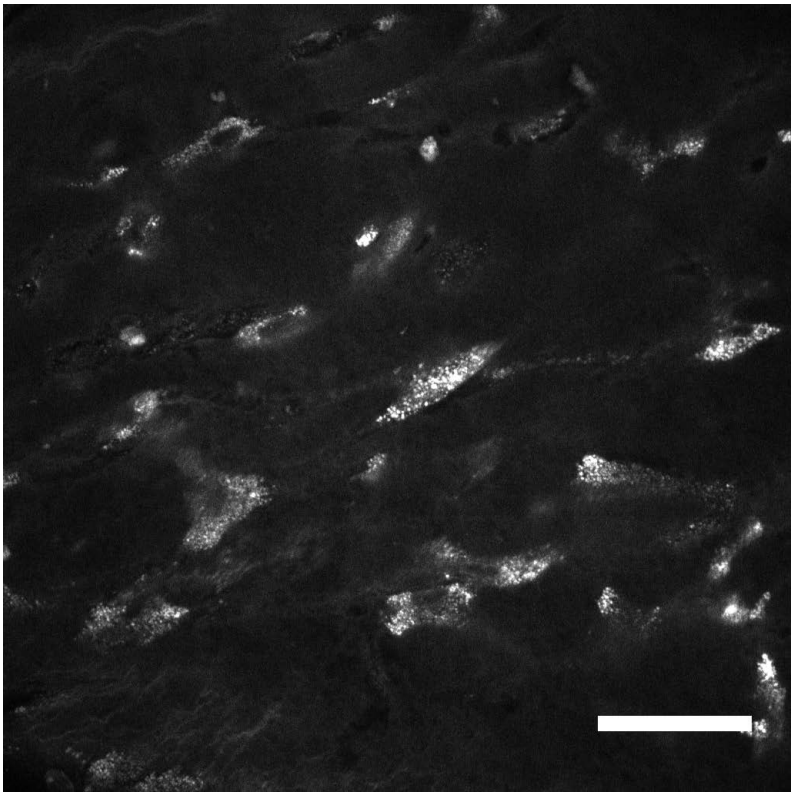

(a)

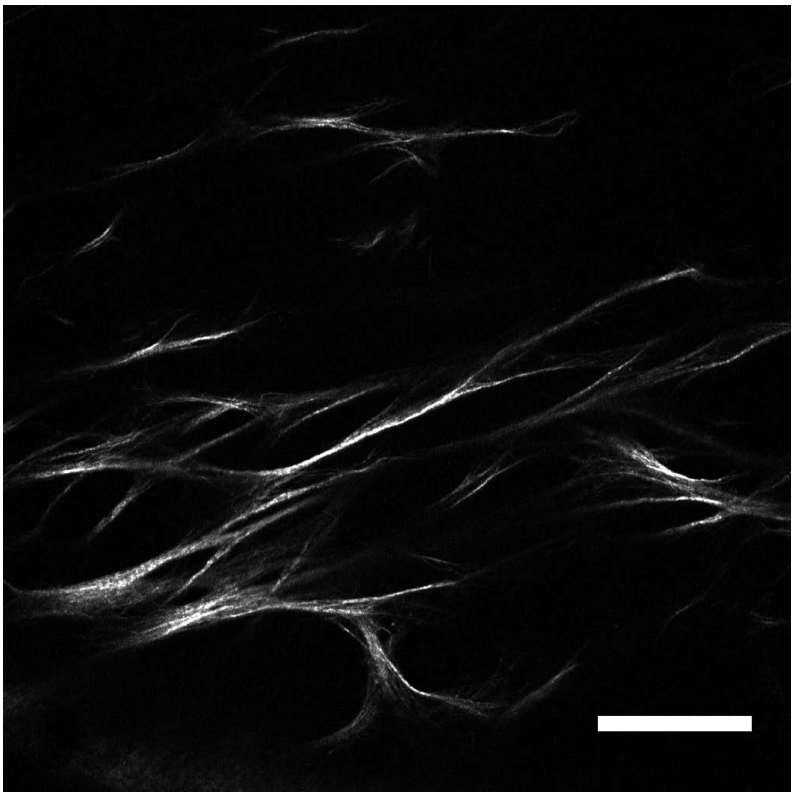

(b)

Figure 4.14: TP/SHG microscopy of day 45 sinew surface, obtained at a higher resolution with averaging applied. (a) TP and (b) SHG images. Scale bar 50μm.

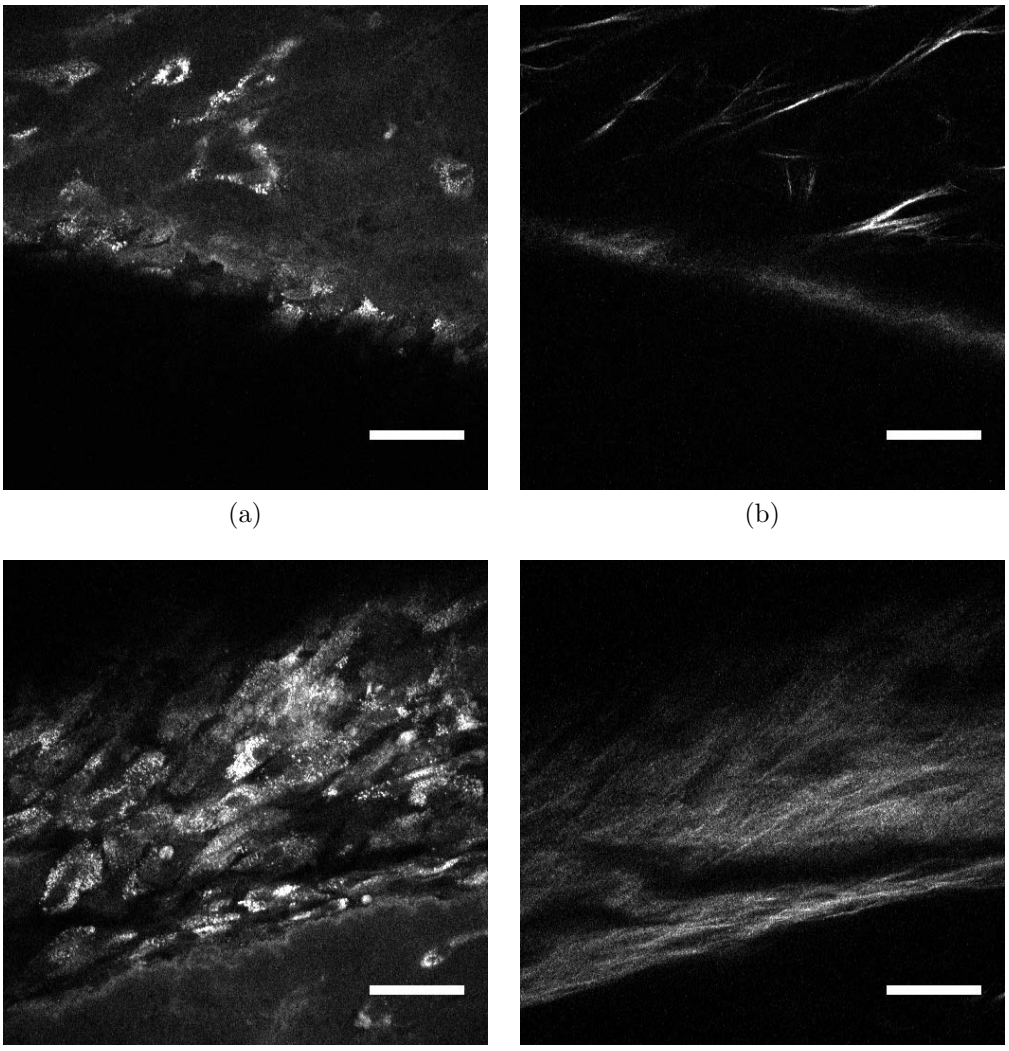

(a) (b)

(c) (d)

Figure 4.15: Two photon (a,c) and SHG (b,d) microscopy of the edges of a day 45 sinew. (a,b) At the sinew upper edge, (c,d) at the lower edge. Scale bar $50\mu m$.

4.5 Discussion

Alignment of cells and ECM plays a key role in the function of a number of tissues, and dictates how the cells interact with their environment [245, 271]. For L/T in particular, aligned collagen provides the tensile strength required to withstand the loading from the performance of day–to–day tasks [1] with the matrix morphology and mechanical load shown to influence cell behaviour [248, 251]. As such the formation of constructs with highly aligned collagen and cellular structure is essential for the successful development of tissue engineered solutions.

The results presented in this chapter show that the formation of the BBLC is a dynamic process. The soft tissue undergoes significant change at multiple scale levels during development. On the macro scale it starts as a thin flat fibrin sheet, which then contracts into a dense collagenous cylinder held taut between the anchors. During the contraction process high levels of cellular order were seen to emerge from initial total disorder of the seeded cells, as shown in Fig. 4.16. With the highest concentration of cells and collagen present at later time points forming a dense outer sheath. In addition to the cell dense outer-sheath, cell dense inner-walls were observed inside the sinew of contracted constructs, presumably as a result of the folding reported by Paxton *et al.* 2012 [94]. The results of the system using anchors to guide the formation are clearly much more complex and well ordered than those of cells cultured in a two-dimensional environment or unguided fibrin that were also investigated. However the cell density and alignment was heterogeneous across a given cross section, and the divergence of matrix and aligned cells around the interface are likely to be limiting factors in the mechanical properties of the sinew.

Computational quantification of alignment present at each point in time and location along the sinew was investigated using FFTRS. The FFTRS has been previously used in studies of fibre and cellular alignment [254, 272]. The ability to provide quantification without specific labelling and easy filtering of noise makes the use of FFTRS practical in

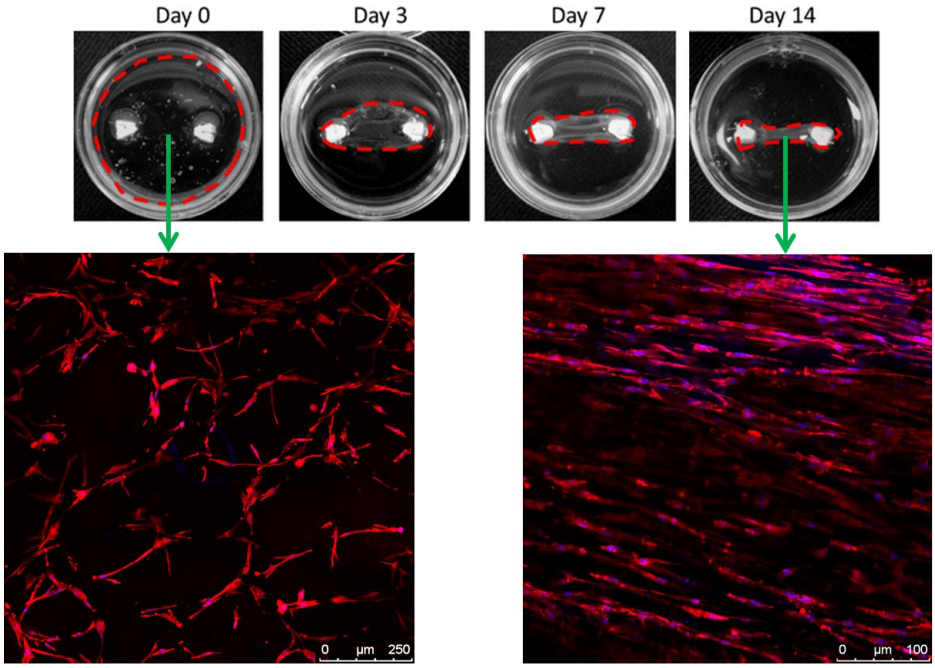

Figure 4.16: Overview of cellular changes in the BBLC during development.

complex environments such as seen in the BBLS. Values that matched the expectation of extreme examples and phantoms showed the method is applicable to relatively sparsely cellular systems, however variations in the sinew content and structure made complete systematic quantification for each spatial location and time point challenging.

The mechanics of the sinew contraction and subsequent re-organisation of cells and ECM are key to understanding the developing sinew.

The major factors in cellular organisation will be tensile load due to contraction, and contact guidance from the internal structure of the scaffold itself. A number of studies have investigated the cues and interplay between the two factors in fibroblast seeded scaffolds [273, 248, 274]. With the reported results suggesting a high ability to remodel cellular and collagen alignment in response to loading, even in cases with inert guidance patterning [274]. Initially the fibrin gel scaffold will be in a state of disorder when polymerised without any guiding factors [106]. So for seeded cells initially contact guidance from the fibrin gel matrix is likely to be the dominant factor, with cells showing generally isotropic organisation as they migrate into the unmodified fibrin during the first 5 days

after initiation. Fibroblasts once migrated into in a fibrin matrix will reorder the fibrin fibres causing contraction [275]. Once the fibrin contraction passes the anchors and the shape of the ligament-proper forms, a critical point will be achieved with tensile load becoming the dominant factor, causing cells to align along the axis of load as reported.

It was observed that in addition to the highly aligned regions of cells that there were also regions which showed low cellular alignment, and sections where high and low alignment regions were adjacent. The continued presence of regions of low alignment once the critical point had been reached suggests that the load across the sinew at a given cross section is not homogeneous, with some areas being exposed to much smaller tensile strain. This corresponds with physical [247, 255] and computational models [256] of collagen systems under tensile load showing an uneven load distribution. It has been shown previously that the thickness of the sinew is dependent on the quantity of supplements added [94], as such it is possible that control of supplementation combined with cyclic loading may encourage development of a uniformly developed sinew. Variations in regions of high/low alignment and cell density may be a result of the sinew contraction, and folding process that takes place during the contraction, creating differences in the exposure to mechanical load and the availability of fresh nutrients at each point in the sample. Indeed at every time point it was observed that the density of cells was much lower in the inner body of the sinew as compared to the sinew/media interface. This suggests that the environment inside the body of the sinew is less favourable for cellular growth and migration, with a lower replacement rate of media likely to be one of the major causes. This may mean that areas of high cellular density, and therefore high ECM deposition and remodelling, bearing the majority of the load are limited to the outer sections of the sinew.

Nutrient depletion and build up of metabolic waste as a result of high cell density around the outside of the sinew and poor internal diffusion is likely to be the reason for the low cell density observed inside the sinew. Mature L/T have a low cell density [1], but this might

lead to inhomogeneous ECM deposition [276]. Regions with lower cell density and/or mechanical load will be weaker with less capability to withstand and repair damage from loading forces. The acidic nature of brushite and the pH changes caused by dissolution of ions in the media might be expected to deter cells from the region. The quantity of cells seen around the anchor region suggests the high CaP cement and Ca/P ion saturation is not sufficiently toxic or disruptive to prevent cells living in, and organising the interface region. However investigation of the effect of cellular internalisation stained of CaP particles with fluorescent markers on MC3T3 cells, has shown potentially toxic consequences for cells as a result of aggregation beyond the cells ability to handle has been reported by Williams *et al.* [277, 278]. The work concerned the application of CaP as transfection reagents where large quantities of small particles not bound into a cement will be used, but the effect could still be problematic given the high number of nano sized needle like particles observed in the TEM images and strong sub-micron background shown under Raman spectroscopy as noted in Chapter 3. It is possible that function such as collagen deposition and organisation may be effected, but no data were able to support this either way.

One of the most notable variations in alignment across the sample was the interface region around the anchor. Cellular imaging has shown evidence of a lasso like effect, as the final structure formed in the soft tissue looped around the anchor rather than forming a close connection with the front of the anchor (Fig. 4.17) as would be desired. In addition to the microscopy imaging presented in this chapter, the iodine stained constructs reconstructed using micro-CT in Chapter 3 showed further evidence of this, with higher density soft tissue in Fig. 3.14 diverging around the anchor. Such a divergence poses a significant problem for the formation of a strong interface, with the tissue at the front of the anchor unprepared for load bearing. However this is complicated by the previous findings that the attachment strength is increased with the use of CaP based anchors, as opposed to more stable materials such as alumina [93], indicating that the mechanical properties are

likely a mix of sinew/anchor bonding, in addition to the simple lasso around the anchor.

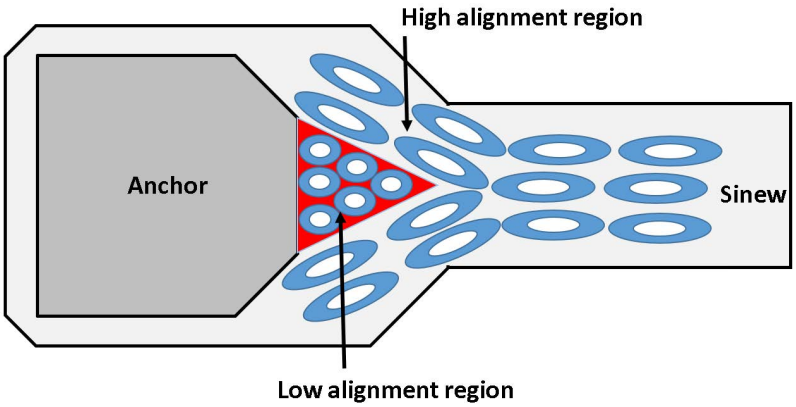

Figure 4.17: Schematic of areas of greatest cell/material density and alignment in developed constructs.

In addition to the cellular content, the ECM plays an important role in the tissue function. Collagen is key to the effective working of connective tissues, providing the tensile strength to prevent failure under load. The quantity and organisation of collagen are both important factors. Elastin provides the viscoelastic properties for passive relaxation. The presence of collagen from early time points in the sinew has been shown here via Raman spectroscopy and in previous work by assays [64]. The simultaneous detection of both components by the use of TP/SHG microscopy has been reported before [159]. In the TP/SHG microscopy presented in this study high fluorescence detected in the TP signal, as a result of fixation, prevented the observation of elastin fibres in the sinew. Raman spectroscopy detection of elastin presence and organisation has been demonstrated [279, 280], however was not observed in the results of this study. Leaving it uncertain if elastin is present in the sinews at any time point. The absence of a collagen SHG signal before day 45, despite the presence at the earlier time points as shown by other methods, suggests that the deposited collagen has not been organised at earlier time points. The collagen structure observed under SHG at day 45 is very different to that seen in native tissues, in terms of its morphology and relatively lower density. Investigation of the Raman signal for differences in the collagen spectra showed no apparent difference, although

the weak signal may have lead to minor peaks or shifts and morphological changes in the major ones being lost amongst the background noise. Fluorescent stains for collagen and procollagen [281] might allow for a better understanding of the state of collagen at earlier time points.

As noted in the previous chapter there were a number of complications and limitations arising as a result of the dynamic nature of the BBLC and techniques used.

The dynamic nature of the system makes consistent and effective sample preparation and comparison challenging as the morphology and properties of the materials changed between each time point. The level of structural information is limited by the depth penetration of the techniques available. The depth penetration of confocal microscopy is dependent on the scattering of the tissue. At day 0 when the fibrin is highly transparent with limited cell penetration this presents a minimal problem. However the mature construct has a thickness in the order of mm with a much more opaque composition and varying structural changes as a result of the folding reported previously, with cell sheets changing in Z height with respect to the imaging plane. Whilst the general structure has been imaged using micro-CT in the previous chapter and OCT previously [94], these provide limited information on the micro-structure at the cellular level where the density and alignment of cells provide important information on the cell viability and behaviour under load.

Another major limitation of this work was the static nature of the construct once it had contracted completely to the final form. For the properties of the native tissue to be replicated, the environmental conditions need to be applied to induce proper adaptation by the construct. Previous studies, including cases on the BBLC [95], have used bioreactors to induce a periodic cyclic load onto the sample [252, 282]. The reported results have varied with differences in materials and conditions, but a general agreement of higher

collagen deposition and growth factor expression is common [95] with higher cell count compared to static samples also has been recorded [283]. Studies of non-loaded native L/T have even shown negative effects, with loss in tenocyte elongation and increase in crimping after only 4 weeks [284].

The results shown in this chapter have shown the formation of highly aligned collagenous sinew from initially disordered and through a dynamic self-assembling process to one with a complex structure showing differences in cellular organisation between the ligament body and anchor region. However variations in the biological structure inside the construct, divergence of alignment away from the interface, and purely linear alignment will limit the potential effectiveness under mechanical load.

4.6 Further work

As with the previous section regarding the interface formation, further work on the ligament body will need to focus on the optimisation of the sinew, and the imaging techniques used to allow a better understanding of the development and composition at each stage.

Optimisation of the sinew to produce a graft with native tissue like properties is essential. Therefore further optimisation of the sinew itself is required through design of the scaffold itself and the addition of physical driving factors *in vitro*. With regard to the design, the dynamic nature of the fibrin scaffold limits the ability to add physical modifications such as micropatterning in the sinew to guide formation. One potential idea is use of biodegradable nanofibres attached into anchors, either set into the cement or attached by a biologically friendly glue. Such a system would ideally guide contraction and encourage more direct cellular development and organisation about the interface, rather than diverging away. Of particular interest is the development of methods to form crimping sinusoidal nanofibres [70], such a morphology would theoretically encourage the forma-

tion of a sinusoidal patterning in the cellular and extracellular structure with the ability to withstand higher loads by recreating the toe region, characteristic of the stress-strain relation for native L/T. Computational methods such as finite element modelling, based on data from imaging results, may be needed to quantify the expected load at each point in the sinew, particularly with regard to the anchor region.

As discussed earlier cyclic loading replicates the mechanical environment of developing connective tissues and has been shown to be an important factor in the development of native and engineered tissues [79]. The requirement of a motorised bioreactor with a controlled environment however limits the throughput of samples.

The current work was performed on fibroblast cells extracted from chicken embryos seeded onto bovine fibrin in FBS. It has been shown that foetal and adult cells from the same species exhibit different behaviour [285]. So for clinical application it will need to be verified that results can be reproduced with human adult tissue. Whilst successful decellularisation and storage of the BBLC has been reported [98], how reseeded cells migrate into and adapt to the emptied scaffold, and whether subsequent mechanical loading to prepare them is unknown. Alternatively other options for the BBLC include the development as a thin sheet of aligned cells that could be wrapped around injured native L/T tissue to encourage repair.

Further imaging is required to build up a more complete image of the current sinew formation and assist in future optimisation. A more complete time series using non-destructive real time measurements techniques would be the initial goal. The knowledge of collagen development and organisation in particular is incomplete with only a small window of the whole time series, and at a single point in the sinew acquired. Further study of the collagen deposition spatially and temporally is required to understand the loading forces present and the cells reaction and remodelling of the ECM to them. There is also the

potential to study samples under mechanical load through TP/SHG microscopy [163] and the optical anisotropy of collagen has been shown to allow polarisation microscopy and polarisation based Raman [286, 287, 288] under both static and loaded systems.

Finally for potential clinical application nondestructive imaging methods with non-invasive *in vitro* capabilities will be needed. Imaging during contraction would provide a greater level of information on the process the cells are undergoing. A number of means exist for this, such as those discussed at the start of Chapter 1 (section 3.1). MRI of the BBLC has been investigated by masters students in the group with inconclusive results. New techniques are constantly being developed that lend great potential such as lens array based polarisation techniques, not requiring thin samples for transmission [289] and single plane illumination microscopy [290].

CHAPTER 5

BRUSHITE CEMENT AGEING

One of the main functions of the brushite cement anchors used in the ligament construct is to allow efficient attachment of the BBLC implant to the bone. For effective attachment and integration, the construct will need to be attached to the femur and tibia via a bone tunnel at each end, similar to the BPTB graft. In this regard the bone-to-cement hard/hard tissue interface can essentially be considered to act as a bone graft, for this to function successfully the cement will need to encourage biological ingrowth and be resorbed and replaced by new bone tissue. Bone grafts will typically only need to withstand compression forces, here there will be a direct tensile load as the attached ligament is pulled. Complications could arise if the cement undergoes transformation into a more stable CaP phase. This would require substantially longer to be resorbed and replaced by bone, creating a long term weakly attached implant, or if high levels of fragmentation and/or dissolution occur then the cement may lack the structural integrity to function as a bone graft. During the production and maturation of the ligament construct the system is exposed to a high volume of dynamic media at 37°C which has been shown to cause compositional changes in Chapter 3 that could result in significant changes in properties. This chapter investigates the chemical and physical changes in brushite cements aged under physiological conditions; considering the applications as a bone graft material, both in this context and for the ligament construct.

5.1 Clinical need for bone grafts

Bone plays an essential role in the body; in addition to the well known function as structural support and protection for soft tissues, it also acts as a reservoir for mineral storage [291], and bone marrow is a source of blood cell production [292]. A number of factors including gender, age, diet, loading will affect the composition and mechanical properties of the bone [293]. In cases of damage caused by trauma or surgery, osteogenic cells can repair minor defects. However if the defect is too large for spontaneous healing, a bone graft will be required to restore functionality and/or prevent fiberous tissue ingrowth. Relating to ACL grafts there is a need to fill bone tunnels and allow them to heal over in cases of revision surgeries requiring a bone graft [47].

As with L/T grafting discussed in Chapter 1 there are a range of grafting material options available for bone grafts, with their own advantages and failings [59, 293, 294, 295]. As a result of the limitations with autografts and allografts there has been a growing interest in synthetic biomaterial based bone grafts [120]. The development of CaP cements as bone graft biomaterials was discussed in section 1.3.3.

5.2 Analysis of phase change in CaP cements

The fundamental importance of CaP phase, and transformation to other phases when implanted was discussed in section 1.3.3. Despite the importance of the phase composition for the behaviour of cements, the currently used methods to determine and monitor their evolution in 3D bodies are highly limited. Analysis of cements and their chemical and biological properties has generally relied on high resolution imaging, combined with bulk compositional measurements of the sample as a whole rather than with consideration to spatial variations. These methods are suitable for monitoring a mono-layer of crystals, however in a complex heterogeneous system such as a 3D cement scaffold in a dynamic environment a large information gap is created. This is especially important in hydraulic

cements such as brushite where handling and setting conditions can drastically reduce the properties and morphology of the cement.

This is of particular importance, given that despite the quantity of work performed on CaPs and number of *in vivo* studies there are still a number of areas with fragmented or very little understanding [120]. Most of the work has been performed on apatites with a comparatively low quantity looking at brushite cements [296]. The solubility values of CaPs have been questioned [297] and dissolution mechanics are poorly understood [298]. Imaging techniques have been employed to examine the topography of the cement at the macro scale and the nanoscale crystal structure. In cases of *in vivo* impants, light micrographs with histological staining provide a more detailed level of information on the cement resorbtion and advancing biological integration [131, 299, 300, 301]. However this requires an intensive and destructive level of sample preparation, and provides no information regarding the current CaP phase. SEM allows study of crystal morphology [119, 126, 302], but only elemental information which gives a rough idea at best of the phases present. Non-destructive tomographic reconstruction through CT [303] and X-ray synchrotron radiation [304] allow high resolution morphologies to be reconstructed, providing a wealth of information on the sample but again are unable to provide explicit chemical information. As a result of this the CaP phases and other components present are usually confirmed by analysis of chemical bond data obtained from IR [230], nuclear magnetic resonance (NMR) [305], or Raman [230] spectroscopy, or structural information from x-ray diffraction (XRD) patterns [230]. These measurements are generally taken from powdered samples so that the overall composition is acquired, but with the total loss of any spatial variations. XRD has generally been the gold standard for determining composition, however diffraction patterns depend on the crystalline nature of the sample with amorphous or non-crystalline samples being poorly or not detected. Dedicated papers on the subject of CaP cement analysis usually only apply a combination of SEM, micro-CT, and XRD [306].

In some cases spatial information has been provided through a series of points taken from multiple Raman spectra [179], or XRD patterns of regions [142]. However these are severely limited in their scope providing only a small quantity of data, and are liable to give misleading results if variations or impurities within the sample do not occur evenly across the whole structure. Chemical imaging techniques are available using Raman and IR spectroscopy. Raman spectroscopy in particular is well established for bone and CaP analysis [179, 269, 307]. In addition to the Raman techniques discussed already other chemical imaging methods are possible, such as attenuated total reflection Fourier transform infrared spectroscopic imaging which shares many similar capabilities but are not commonly available [308]. Synchrotron radiation can be used for high resolution X-ray micro-diffraction giving compositional information [309], however the limited resource time, lengthy organisation, and destructive preparation process severely limit the availability. Despite the obvious application the use of chemical imaging in CaPs has been limited. CRM has been reported for the mineralisation of biofilms [310], drug release from a brushite cement [311] and a limited study of osteointergration [312]. This has likely been due to the technique only developing to a technological level where acquiring data-sets with a large number of points is feasible within a practical time frame.

5.3 Chapter aim

The aim of this chapter was to investigate the use of CRM to map CaP phases in cement cylinders. To allow the visualisation of phase changes as a result of time spent in physiological conditions, and enable a better understanding of the fundamental behaviour of cements in 3D environments.

5.4 Materials and methods

5.4.1 Brushite cylinder production

To produce brushite cement cylinders, β-TCP was mixed with 3.5M orthophosphoric acid at a powder to liquid ratio of 1.75g/mL. The mixture was poured into custom made 12mm high by 6mm diameter cylindrical moulds, and left to set overnight.

5.4.2 Brushite cylinder ageing

Cement cylinders were sterilised under UV light overnight. Sterilised Cylinders were placed into 50mL centrifuge tubes with 20mL of either DMEM, sDMEM, or sterile PBS at a liquid to cement volume ratio (LCVR) of 60:1. Samples were incubated at 37°C for 10 days in the FBS and DMEM solutions, and for 5, 10, 20, 30 and 50 days in PBS, and 20 and 30 days for PBS raised to a pH of 12.5 by the addition of sodium hydroxide (Sigma-Aldrich, UK). Media was changed daily in each case. pH readings were taken for day 1 to 30 in the PBS aged cylinders. In each case care was taken to randomise the position the cylinder was in after each media change. Cylinders were removed from ageing medium, washed in distilled water, dried overnight at 37°C, cut using a scalpel across the midpoint to expose the cross-section. Individual halves were mounted on a sample holder using distilled water and frozen to -20°C in a cryostat (Starlet 2212, Bright Instruments, UK), samples were cryotomed in 2 μm steps to produce a smooth surface suitable for confocal imaging. Cylinders were then briefly washed with distilled water to remove any debris, and dried at 37°C before imaging.

5.4.3 Raman mapping

Mapping was performed using a confocal Raman microscope with a 785nm 300mW argon laser for DMEM, FBS and day 10 PBS samples, over a spectral range of 0-3000cm^{-1} with a mean spectral resolution of 3.6cm^{-1}, using a 300g/mm with 750nm blazing grating

spectrograph. For the extended PBS media ageing a 60mW 514nm argon laser was used, with data collected over a spectral range of 200-1200cm^{-1} with a mean spectral resolution of 1.2cm^{-1}, using a 1800g/mm with 500nm blazing grating. Mapping was collected for whole area scans using a 5x 0.1NA atmospheric lens, over a 6500x6500μm area with 100x100 points collected with an integration period of 1s. Higher resolution scans at the cross section edge were acquired with a 20x 0.45NA atmospheric lens, over an area of 1000x1000μm, with 100x100 points collected and 1s integration time. Acquisition of single spectra from points of interest was performed by taking 20 accumulations of 3 second integration periods. To minimise sample movement during scanning, cylinders were attached to a 35mm well plate using double-sided tape.

5.4.4 Processing Raman data

Data was pre-processed to remove cosmic rays using the instrument associated software, exported in SPC format into MATLAB, baseline corrected, and vector normalised. Least squares regression was used for fitting of individual Gaussians to each peak. False colour image maps were produced by integrating over the sum of peaks of interest. For further processing the dataset was segmented to separate the sample from background and allow calculation of the measured area and centroid. The dominant phase in each pixel location was determined by the association of the peak with the highest intensity. Measurement of OCP penetration distance at each time point, determined by the average distance into the sample of the OCP band based on five measurements, was performed using ImageJ.

5.4.5 Micro-CT

Samples from the dynamically aged PBS series were imaged after being sectioned and following CRM mapping. Half cylinders were attached to a sample holder by a small quantity of low radio attenuating dental gum and inserted into the micro-CT for scanning. Image scans were performed after flat field correction. X-ray shadow images were taken

180° about the sample, with a 0.4° step size, 280ms exposure time, 3 frame averaging, using a 50kV, 130μA X-ray beam, with aluminium and copper filters in place. Returning 499 2000x1200 pixel .tiff images with an image pixel size of 5.3μm. Reconstruction was performed using NRecon software with correction for ring artifacts applied. Visualisation and cross sections were produced using DataViewer. Further processing was performed using imageJ and MATLAB.

5.4.6 Helium pycnometry

Samples used were from the dynamically aged PBS series, after being cut and imaged with CRM. Geometric measurements of cylinders were made using a sliding calliper with the radius and height values taken as the mean of 3 measurements. Samples were mounted in a helium pycnometer (AccuPyc 1340 Gas Pycnometer, Micromeritics Instrument Corporation, GA USA). Analysis was performed by 10 initial helium purges with 10 subsequent measurements per sample. The true density and porosity for each sample were calculated and plotted.

5.4.7 Bulk analysis

Samples from each PBS and pH 12.5 PBS time point were dried, and ground using a mortar and pestle. Raman spectra were acquired at 5 randomly chosen points from each powder sample using the 514nm wavelength laser, 20x lens with 20 accumulations at 3 seconds integration time per accumulation. Resulting spectra were pre-processed to remove cosmic rays using the associated Witec Project software and averaged together. Average spectra were exported and base-line corrected in MATLAB. For XRD approximately 500mg of the powder was distributed over a 10mm diameter circular area of Scotch tape and attached to the sample holder. XRD patterns were acquired using a Bruker D8 Advance Diffractometer (ASX Gmbh. Bruker, Germany) using the copper K-alpha line 1.5406nm at 40kV and 30mA. Each data set was collected from 2-θ angles 5-60 degrees

at 0.05 degree/s step rate. The sample was rotated about its axis during the entire measurement to minimise the influence of preferential crystal orientation. Data was baseline corrected, and smoothed using MATLAB. Peak identification was performed using ICDD data cards.

5.5 Results

5.5.1 Cylinder production

Brushite cylinders (Fig. 5.1) were produced by mixing β-TCP and orthophosphoric acid, pouring the thoroughly mixed solution into a 6mm diameter by 12mm high custom made cylindrical mold and allowing them to set. A reactant to product ratio of 66% brushite to 34% TCP was expected given the reactions described in equation 3.1.

Figure 5.1: Photograph of Brushite cement cylinders.

5.5.2 Cylinder ageing

Cylinders were sterilised under UV light, and aged under dynamic physiological conditions in either PBS, DMEM, sDMEM, or FBS media changed every 24 hours. In every case the cylinders showed no visual sign of breakdown when removed from the media. Cylinders

aged in DMEM or FBS based media developed a visibly yellow hue on the outside of the cylinder that remained after multiple washes in PBS, but did not penetrate to the interior. The pH of PBS removed, showed a large initial drop in each case from the standard PBS pH of 7.3, to slightly acidic pH of 6.5 +/- 0.2, with the measured pH values steadily increasing over time reaching a high of 7 at day 30 (data not shown).

5.5.3 Raman image mapping

CRM mapping was performed using a 785nm laser on cylinders that were non-aged and aged for 10 days in PBS, DMEM, 100% FBS, or DMEM with 10%FBS. Regions covering whole cylinder cross sections with an image pixel size of 65x65μm, and a higher resolution of the cylinder edge with a with a pixel size of 10x10μm were collected. The main spectral region of interest was 830-1030cm^{-1}. Calcium phosphate phases were identified based on Raman spectral peak locations previously reported in the literature [230] (Table 5.1). The P-O stretching mode (ν_1) of the PO_4 group which has a unique peak shift for brushite (985cm^{-1}), OCP (958cm^{-1}), and TCP (970cm^{-1}) was used as the main reference peak for each CaP phase. Spectra at the centre and edge of a cylinder aged for 50 days in PBS are shown in Fig. 5.2. A -5cm^{-1} shift in the peak location was observed for samples aged in DMEM and FBS based media. Prior to image formation datasets were filtered to remove cosmic rays, baseline corrected, and vector normalisation was applied to compensate for variations in sample height. Due to the close proximity of the peaks (12cm^{-1}) relative to the spectral resolution of the grating (3.5cm^{-1}) and their FWHM (10cm^{-1}), a significant overlap was present which would give rise to misleading results as constructive interference increased the apparent intensity of weaker or non-present peaks. A classical least squares regression was performed to fit an individual Gaussian to each peak in the region for image mapping calculations to be taken from. It should be noted that intensity values were produced to be consistent across phases for each sample mapping but not between every data set. The heat map for normalised values is Fig. 5.2.

Image mapping of samples that were aged for 10 days in media for edge sections (Fig. 5.3) showed clear differences in the cement composition dependent on the media content. In non-aged samples a homogeneous structure was present with the most intense peak being that indicative of brushite, and lower more disperse peaks indicative of TCP. OCP was not detectable at this time point beyond the background noise. At 10 days a shell of OCP was observed to be forming around the outside of the cylinder in the PBS and

non-supplemented DMEM samples. A higher quantity of brushite dissolution and deeper penetration of OCP was apparent in the PBS aged sample, whereas the DMEM aged sample had a layer of build up on the outside of the cylinder itself which spectrally matched OCP. Conversely the supplemented DMEM and FBS samples, with 10% and 100% serum respectively, showed no evidence of brushite dissolution or OCP formation.

Image mapping data acquired was processed to provide further visualisation data on the phase quantity and distribution. Mappings were segmented, with the dominant phase at each spatial location determined based on maximum peak intensity. This was used to produce binary composite images showing the dominant phase at each time point for the edge areas (Fig. 5.3). This mapping of the dominant phase at each spatial location collaborated the heat map images for each peak, showing a solid ring of OCP around the outer edge of PBS and DMEM aged samples, with a higher density of TCP forming around and to a greater penetration depth than the OCP. Analysis of the Raman spectra showed no evidence of HA formation in any sample.

Table 5.1: Major Raman peaks from aged and non-aged brushite cylinders found in the 800-1050cm^{-1} wavenumber region and their phase assignments.

Wavenumber (cm^{-1})	Vibrational mode	Phase assignment
878m	P-O stretching mode of PO_4 group	Brushite
948m	P-OH stretching mode of HPO_4^{2-}	TCP
958vs	P-O stretching mode of PO_4 group	OCP
963vs	P-O stretching mode of PO_4 group	HA
970vs	P-O stretching mode of PO_4 group	TCP
985vs	P-O stretching mode of PO_4 group	Brushite
1010m	P-O stretching mode of HPO_4^{2-}	OCP

Having found that CRM mapping of brushite cylinders was able to spatially determine phase change in media with different compositions, the study was extended to encompass a longer time series allowing a deeper investigation of the material evolution. Raman

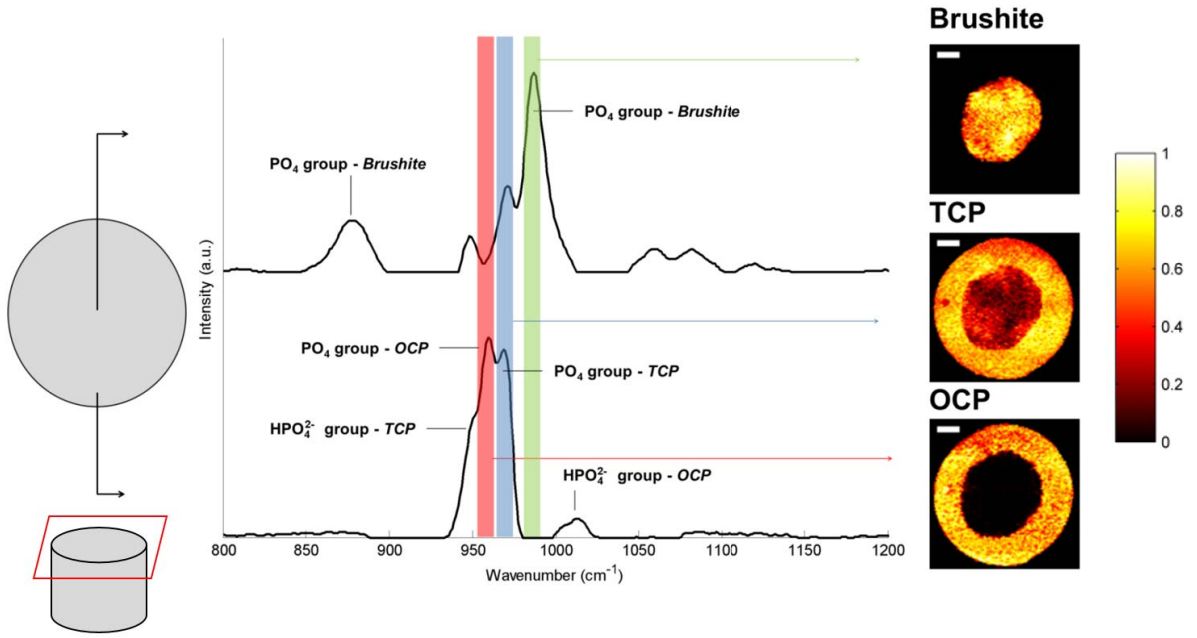

Figure 5.2: Formation of confocal Raman microscopy heat maps over cross section of cylinder surface. Scale bar $1000\mu m$.

imaging mapping of cylinders aged in dynamic PBS for 0, 5, 10, 20, 30 and 50 days was performed and processed as before over the whole cylinder cross section (Fig. 5.4) and at a higher resolution over the edge region (Fig. 5.5). A 514nm laser was used due to the minimal autofluorescence in PBS aged samples, enabling a higher signal intensity and access to a higher spectral resolution grating for improved differentiation of the PO_4 peaks.

Image mapping over the time series showed results similar to those from the PBS and non-supplemented DMEM seen in Fig. 5.3. An initial largely uniform phase distribution dominated by brushite, with a weak TCP signal, and no OCP was seen for the unaged cylinder. At 5 days a layer of OCP was observed at the outside of the cylinder, with a higher density of TCP both about the OCP and penetrating further into the sample. At each subsequent time point the layer of OCP and TCP increased in area and radial penetration. Further analysis of the spectra supported the results shown by the PO_4 peaks. With the decay of the 878cm^{-1} PO_4 peak associated with brushite alongside the drop in intensity and complete removal of the 985cm^{-1} peak at the outside of the cylinder, and

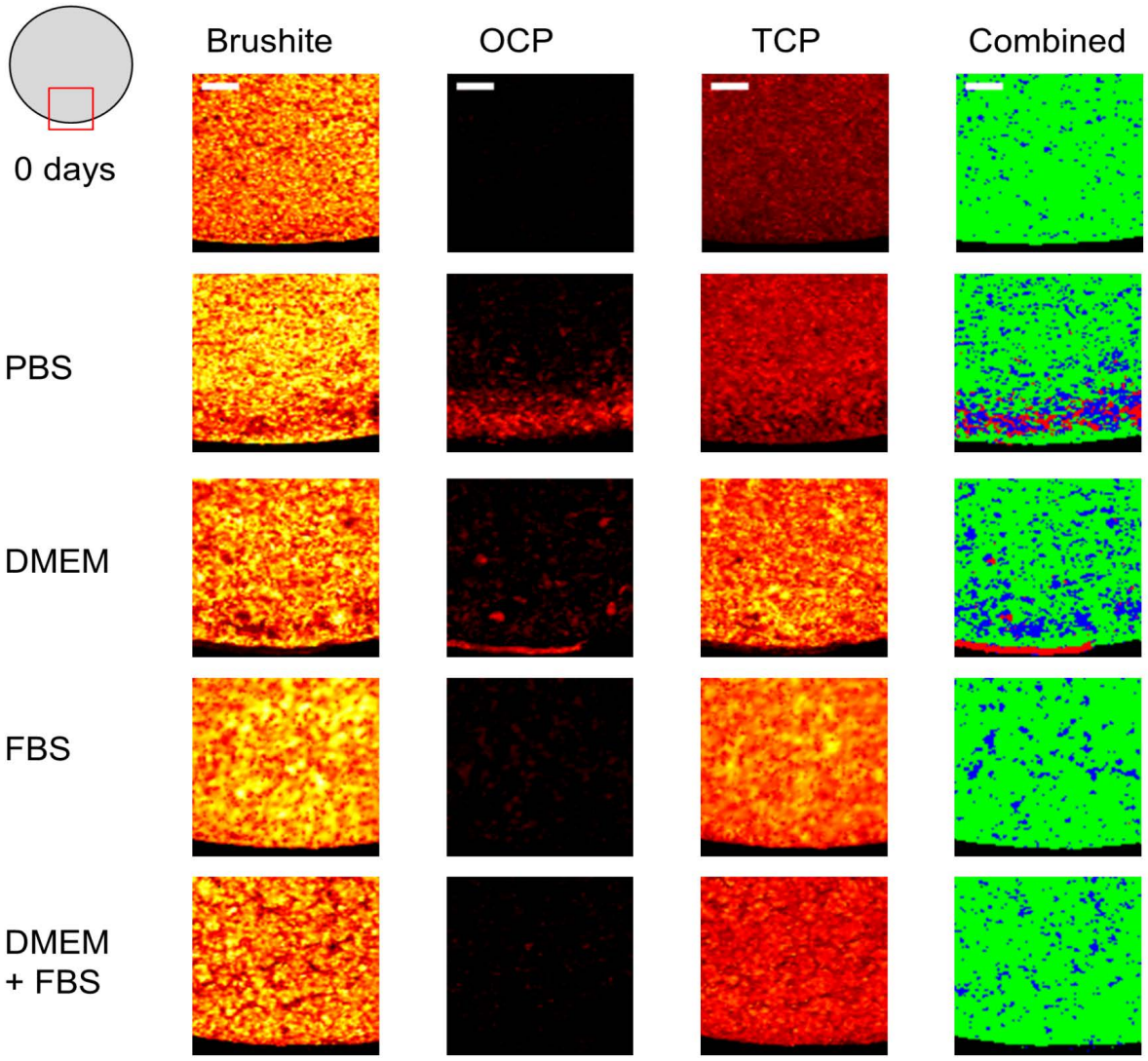

Figure 5.3: Confocal Raman microscopy heat maps of partial cross sections taken at the outside edge of the cylinders after 10 days ageing in dynamic media. Heat maps of the PO_4 peak for brushite, OCP and TCP phases are shown for cylinders aged in each media. Combined images shows the dominant phase at each location determined by highest peak intensity; green - brushite, red - OCP, blue - TCP. Scale bar $200\mu m$.

the appearance of the 1010cm^{-1} P-O HPO_4^{2-} OCP peak alongside the main PO_4 OCP peak.

The results suggest that over time in dynamic PBS, the outer brushite layer of the cylinder was eroded away by hydrolysis, leaving a TCP structure that is replaced by OCP. From these results it can be determined that the outer brushite layer of the cylinder was eroded

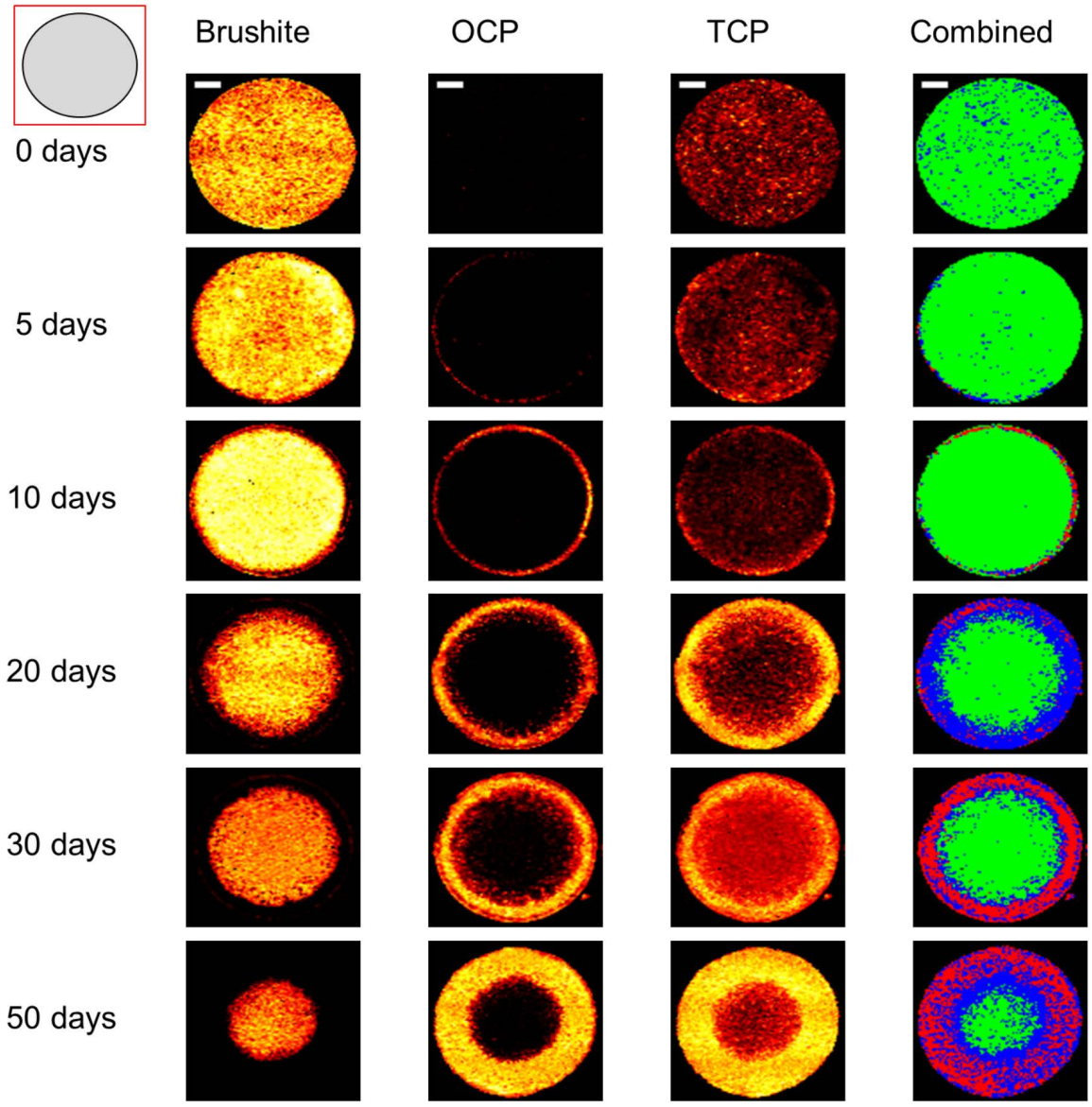

Figure 5.4: Confocal Raman microscopy heat maps of whole cylinder cross sections after up to 50 days ageing in dynamic PBS media. Heat maps of the PO_4 peak for brushite, OCP and TCP phases are shown for cylinders aged in each media. Combined images shows the dominant phase at each location determined by highest peak intensity; green - brushite, red - OCP, blue - TCP. Scale bar $200\mu m$.

away by hydrolysis over time while in dynamic PBS, leaving a TCP structure. The rate at which the dissolution of brushite and precipitation of OCP occurred for a particular location was clearly shown to be dependent on the distance from the cylinder edge, with initial OCP appearance by 5 days at the edge of the cylinder, the outer radius of brushite being completely replaced by 10 days, and only a small central core of brushite remaining

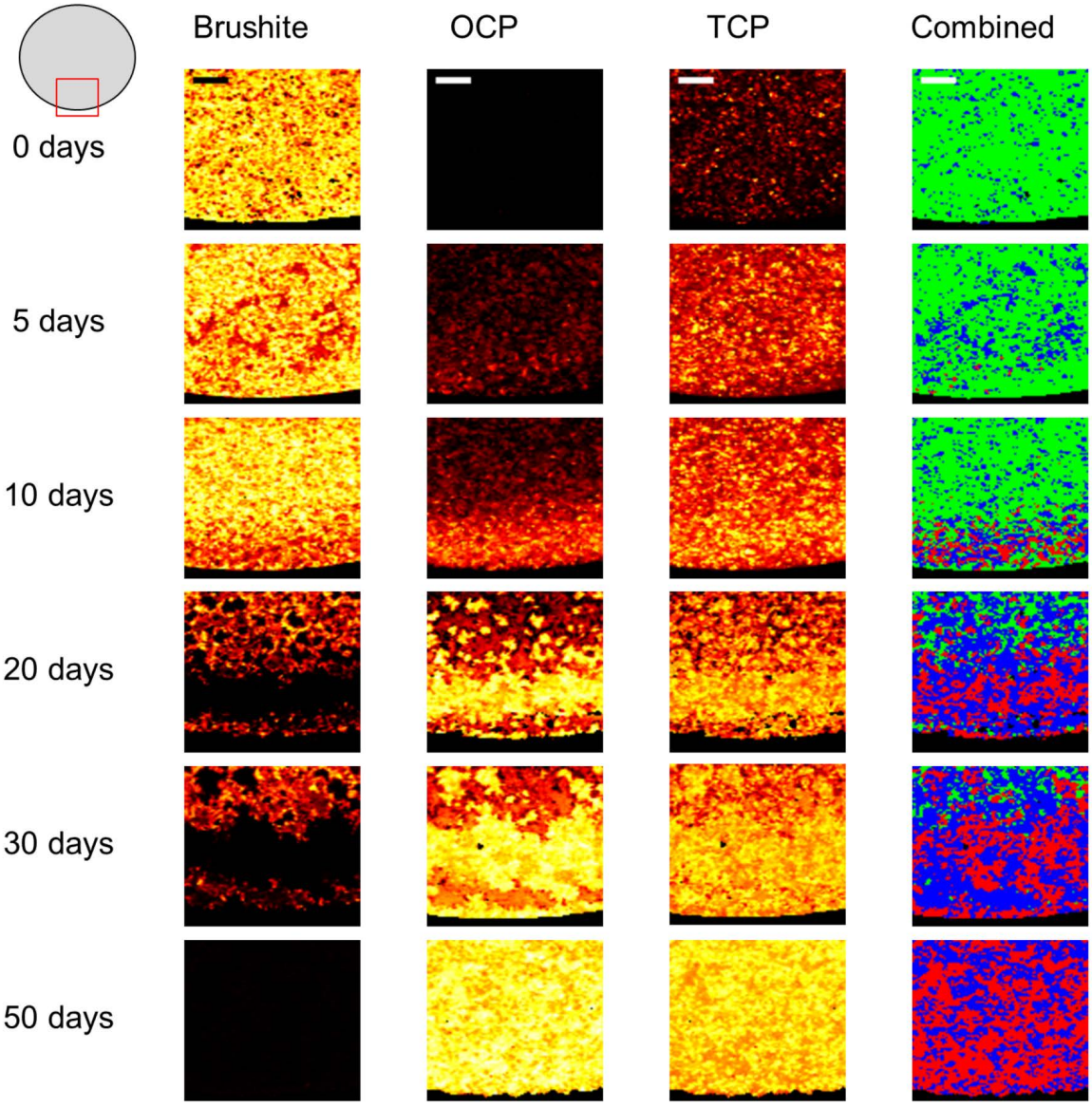

Figure 5.5: Confocal Raman microscopy heat maps of partial cross sections taken at the outside edge of the cylinders after up to 50 days ageing in dynamic PBS media. Heat maps of the PO_4 peak for brushite, OCP and TCP phases are shown for cylinders aged in each media. Combined images shows the dominant phase at each location determined by highest peak intensity; green - brushite, red - OCP, blue - TCP. Scale bar 200μm.

at 50 days. As seen in the PBS results for Fig. 5.3 a thin approximately 50-200μm layer of brushite was observed on the outside of the cylinder at aged time points - notably at day 20 and 30 in Fig. 5.5 - despite the otherwise complete dissolution of brushite 100μm or further into the sample. This layer was seen to degrade and be replaced by OCP at the 50 day time point. Composite images of the three phases showing the dominant phase at

each point showed the emergence of a distinct three phase structure with phases clustered by radial distance as the brushite underwent dissolution, leaving the TCP scaffold that was subsequently seeded by OCP. The percentage of the total area for each phase was calculated for each time point based on these results (Table. 5.2). In addition an estimate of the penetration distance of OCP was determined using composite images (Table. 5.2). Both of these supported the visual observations of brushite dissolution and OCP penetration. Such quantifications are limited by random variation of TCP distributions between samples and the assumption of the most intense peak being sufficiently dominant, but allow a reasonable estimate and insight of the phase composition at each time point and its evolution. The distribution of TCP may be a result of uneven mixing of the TCP powder and liquid phase creating regions with a higher density of brushite in some cases, and given that a full conversion is not expected there will be variations in the structure at the micro level in each sample.

Table 5.2: Quantification of approximate area and penetration changes for phases at each time point for samples aged in PBS based on the dominant phase calculated at each spatial location.

Time point (days)	Brushite %	OCP %	TCP %	OCP penetration (μm)
0	88.6	0.0	11.4	0
5	88.3	0.7	11.0	150
10	90.0	5.9	4.0	350
20	50.1	8.3	41.6	520
30	37.8	22.6	39.6	750
50	12.6	44.2	43.2	1300

In addition to the results shown above a small number of cylinders showed inhomogenous structure under CRM mapping. Mappings of day 0, and day 30 in dynamic DMEM are shown in Fig. 5.6. Heat maps for brushite and TCP in the day 0 cylinder suggest the cylinder set in a series of concentric circles, alternating between the two phases. Heat maps for day 30 show highly variable dissolution of brushite and penetration of TCP,

with up to 600μm radial differences suggesting that the variability in setting of the cements can be far more pronounced than the more stable brushite around the edge of the cylinder seen above. Care was taken to randomise the position of the cylinder each time the media was changed.

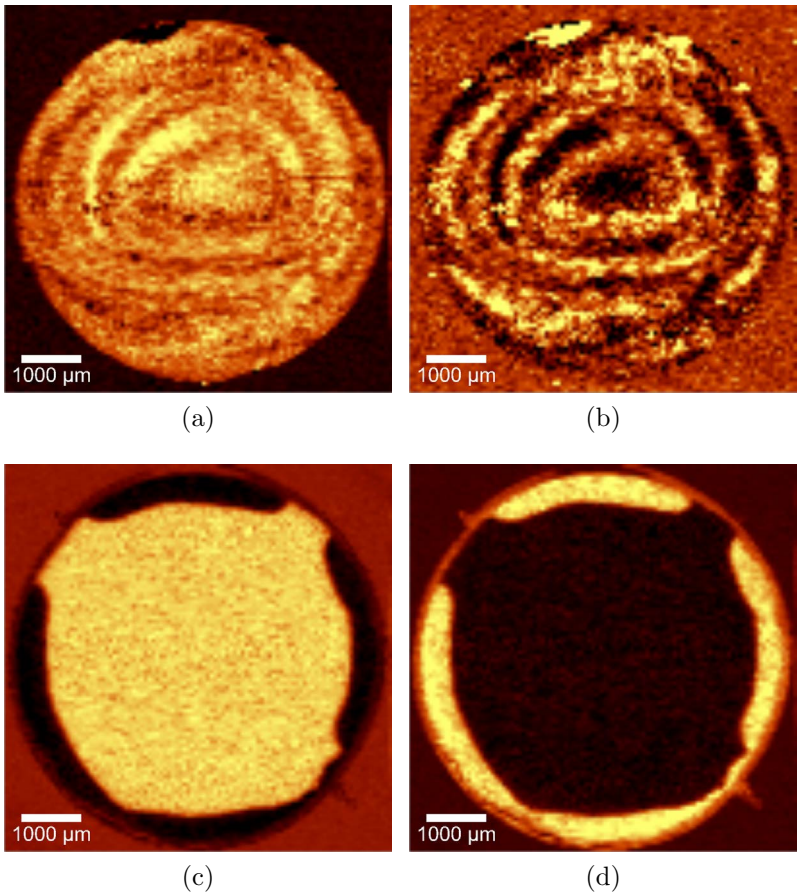

(a) (b)

(c) (d)

Figure 5.6: Raman mapping of inhomogeneous samples. Day 0 cylinder with (a) brushite and (b) TCP mappings, and a cylinder aged 30 days in DMEM with mappings for (c) brushite, and (d) OCP. Mappings produced using Witec Project software.

Brushite cylinders dynamically aged in PBS raised to a pH of 12.5 by the addition of sodium hydroxide were imaged using CRM at 10, 20 and 30 days (Fig. 5.7). Results showed similar results with brushite being replaced by OCP as a function of distance over time, but at a much higher rate with complete dissolution of brushite by 30 days. Importantly the determination of the presence of HA was complicated by the spectral proximity

of the PO_4 peak for OCP and HA liable to give false results. However analysis of the spectra with reference to other peaks associated with each phase, such as the HPO_4^{2-} peak for OCP, allowed identification with reasonable certainty (Fig. 5.8). As noted above there was inhomogeneous penetration with day 10 and 20 whole area scans showing the remaining core of brushite is off centre, despite being different samples in each case due to the destructive nature of the method.

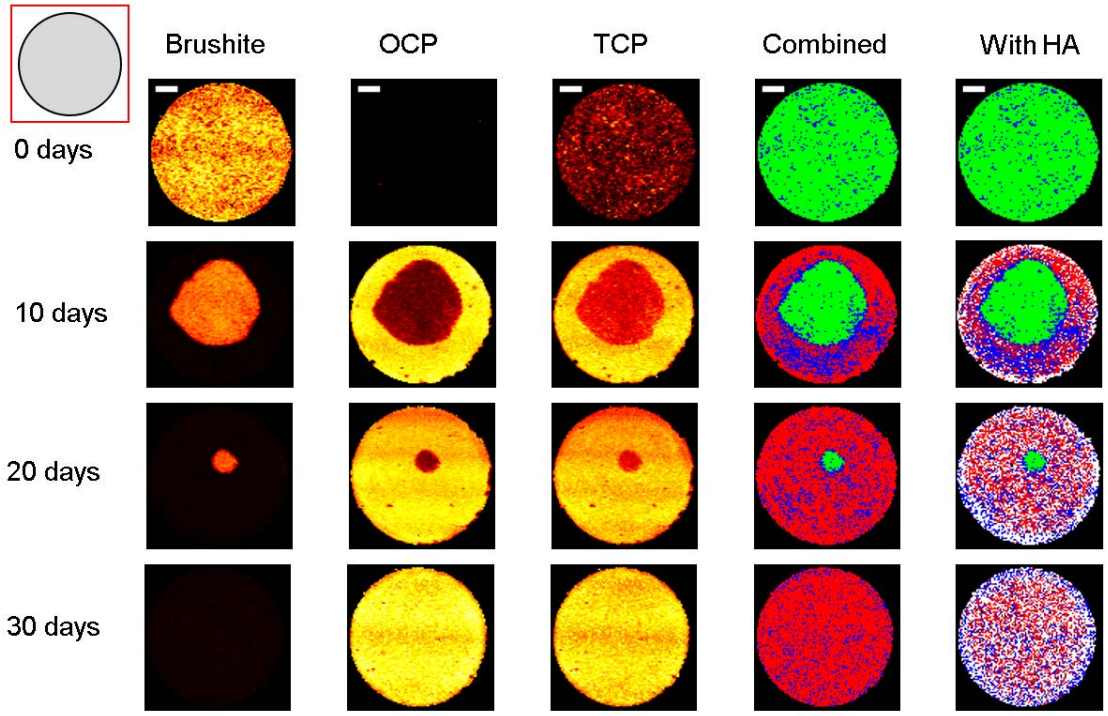

Figure 5.7: Confocal Raman microscopy heat maps of whole cylinder cross sections after up to 30 days ageing in dynamic pH 12.5 PBS media. Heat maps of the PO_4 peak for brushite, OCP and TCP phases are shown for cylinders aged in each media. Combined images shows the dominant phase at each location determined by highest peak intensity; green - brushite, red - OCP, blue - TCP, white - HA. Scale bar 1000μm.

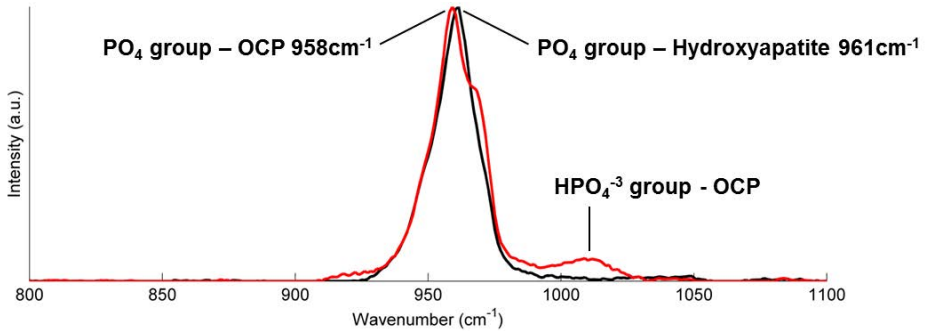

Figure 5.8: The spectral proximity of the PO_4 peak for OCP and HA in the Raman spectrum of CaP cements.

5.5.4 Micro-CT

Micro-CT reconstructions performed over the whole volume of the sectioned cylinder at a pixel size of $5.4\mu m$ are shown for 0 (Fig. 5.9) and 50 (Fig. 5.10) days in dynamic PBS. The coronal slice through the centre of the cylinder and transverse slices taken at the top, mid-point and bottom of each reconstruction provide a view of the gradient of exposure to fresh media. Slices over the time series show changes in density and porosity where aged constructs which aligned with the phase regions seen in the CRM image mapping series (Fig. 5.4). Comparing the reconstructions at day 0 to day 50 shows a clear change in structure as the brushite is removed and/or replaced by OCP leaving a volume of lower density and porosity that is seen to curve within the structure, with respect to the distance from the phase boundary to the nearest outside edge of the cylinder. Non-homogeneous regions of mineral density suggesting more or less complete cement setting, and air holes acting as large pores are apparent and may explain the variations seen in phase change (Fig. 5.6).

The presence of the outer shell of brushite seen under Raman microscopy was also observed in the micro-CT reconstructions as a band of highly attenuating mineral around the outside of the transverse slices (Fig. 5.11).

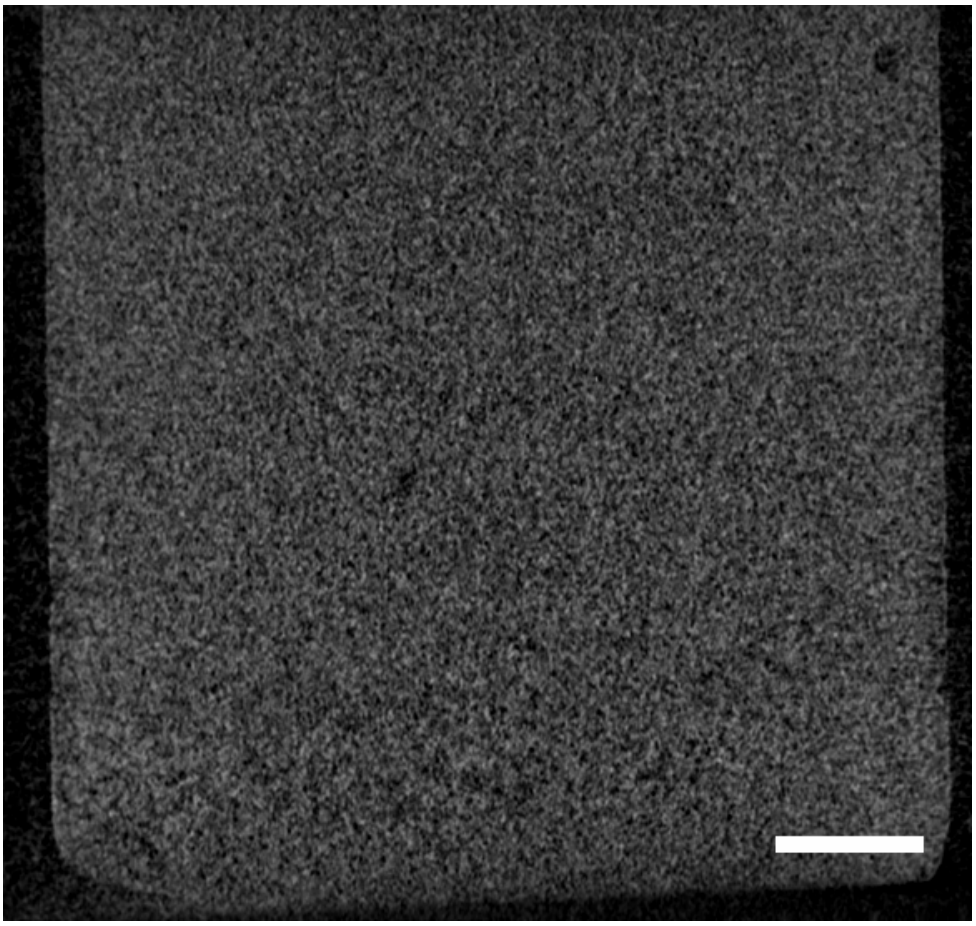

(a)

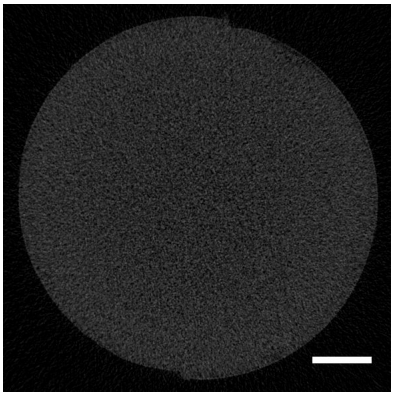

(b)

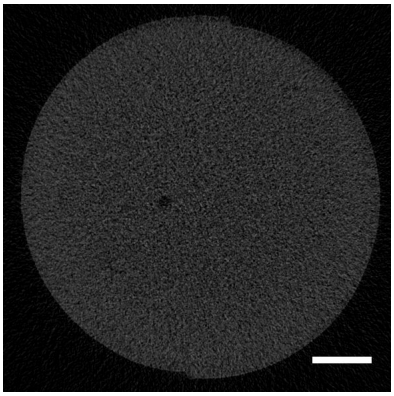

(c)

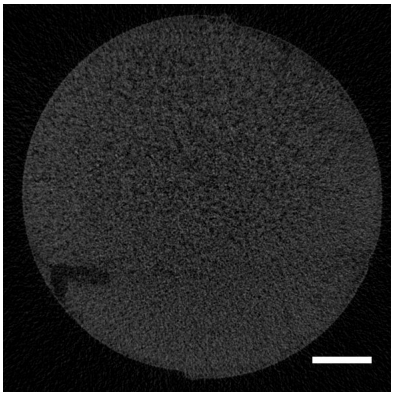

(d)

Figure 5.9: Micro-CT reconstruction of a day 0 cylinder. Showing (a) coronal slice through the centre of the cylinder and transverse slices at the (b) upper surface, (c) middle, and (d) lower surface. Scale bar 1mm.

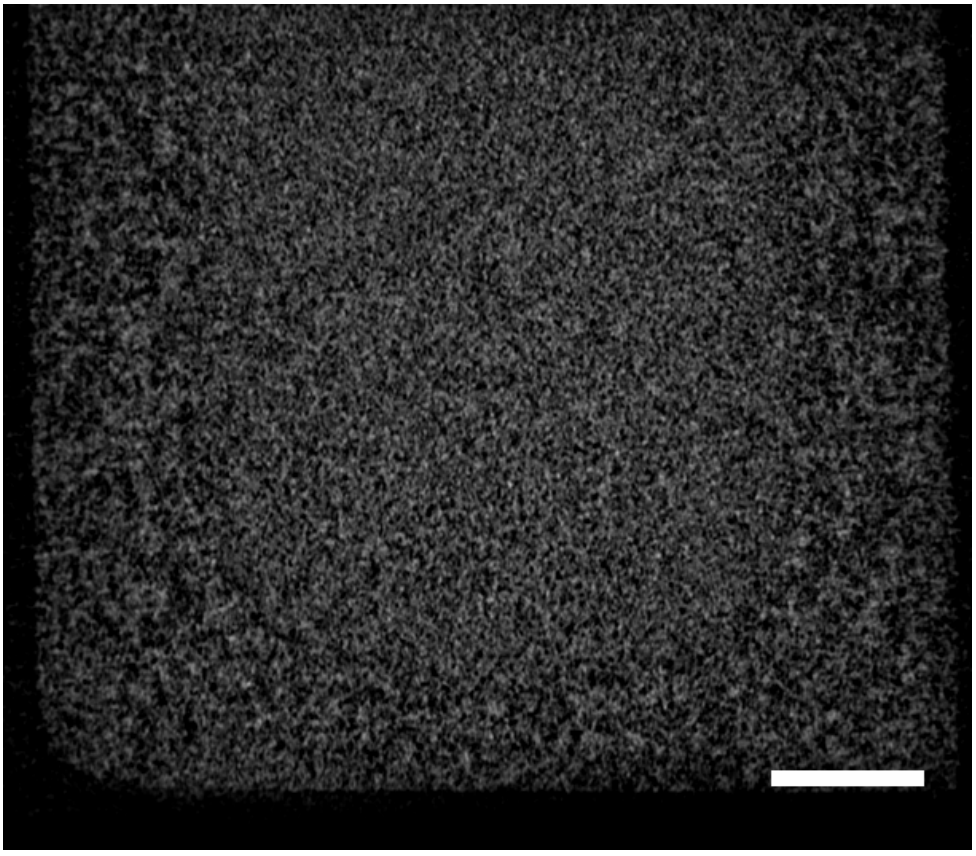

(a)

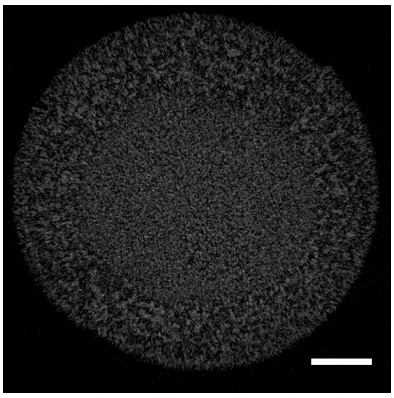

(b)

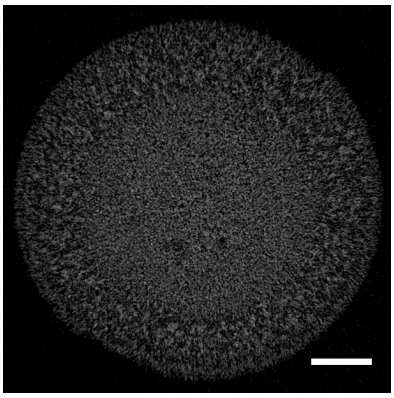

(c)

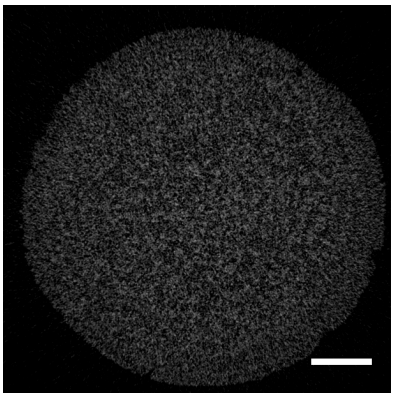

(d)

Figure 5.10: Micro-CT reconstruction of a cylinder aged for 50 days in dynamic PBS. Showing (a) coronal slice through the centre of the cylinder and transverse slices at the (b) upper surface, (c) middle, and (d) lower surface. Scale bar 1mm.

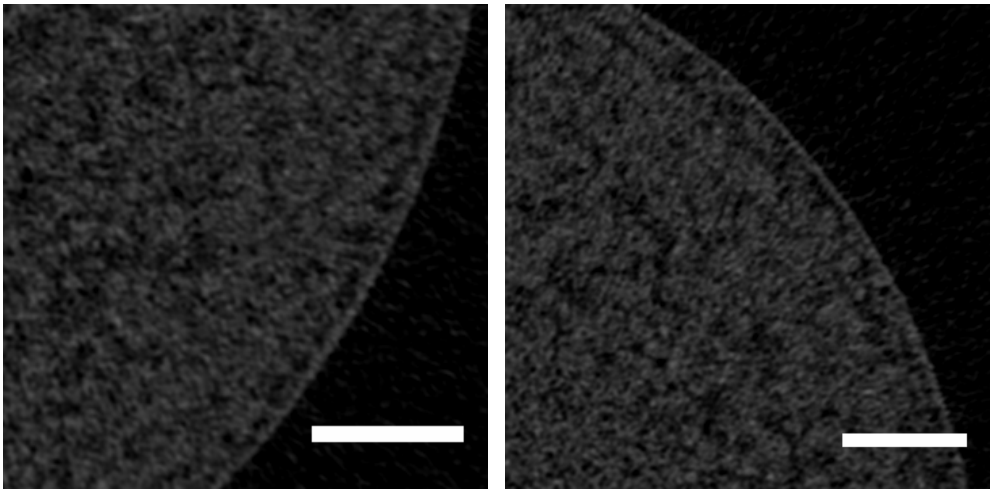

(a) (b)

Figure 5.11: Border layer of brushite seen in Micro-CT day 10 in pH 12.5 PBS. Scale bar $500\mu m$.

5.5.5 Bulk analysis

Helium pycnometry was performed on sectioned cylinders. Afterwards samples were ground to a powder for compositional analysis under Raman spectroscopy and XRD.

Helium pycnometry

Helium pycnometry was performed for each time point on half cylinder samples that had been aged in dynamic PBS (0,5,10,20,30,50 days) to determine the apparent and true densities. Helium pycnometry is able to obtain an accurate measurement of the material volume, with helium atoms able to penetrate pores down to a limit of 0.1nm [313]. The porosity was calculated as shown in equation 5.1:

$$Porosity[\%] = \frac{V_{app} - V_{true}}{V_{true}} \text{x} 100 \tag{5.1}$$

Where V_{app} is the sample volume measured by geometrical dimensions, and V_{true} is the real sample volume. The results are shown in Fig. 5.12. The porosity of the samples was seen to change over time when exposed to *in vitro* conditions. The calculated porosity results show a increase in porosity of the cylinders corresponding with *in vitro* time in PBS media. The changes in porosity collaborate the results seen under micro-CT.

Raman point spectroscopy

Raman spectrum of powdered samples were acquired by acquiring a number of spectra at points across the sample and taking the average spectrum for each time point (Fig. 5.13). Results correspond the same story as seen with mapping; a brushite and TCP sample with the brushite decreasing over time and the appearance of OCP later in the time series. Notably these results highlight that there is a much lower sensitivity in the point method. OCP does not become clearly detectable until 20 days, despite the presence and in some spatial locations dominance of OCP in the mapping time series at 5 and 10 days shown in Fig. 5.5.

XRD

XRD patterns collected from powdered cylinders aged in dynamic PBS are shown in Fig. 5.14. Analysis of diffraction patterns showed the same results as with point Raman spectroscopy above; brushite and TCP cement, with a decline in brushite over time and appearance of OCP at later points. Again OCP was not seen prior to day 20 showing the difference in sensitivity in addition to the loss in spatial information. No evidence of HA was found, with no distinct HA peaks detectable beyond the background noise or from peaks that would not be contributed by other confirmed phases.

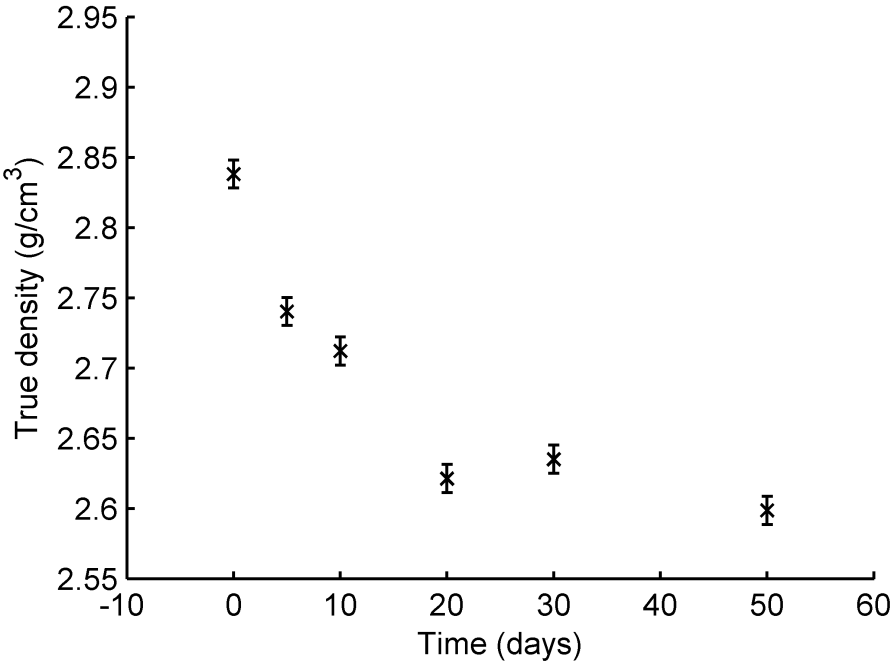

(a)

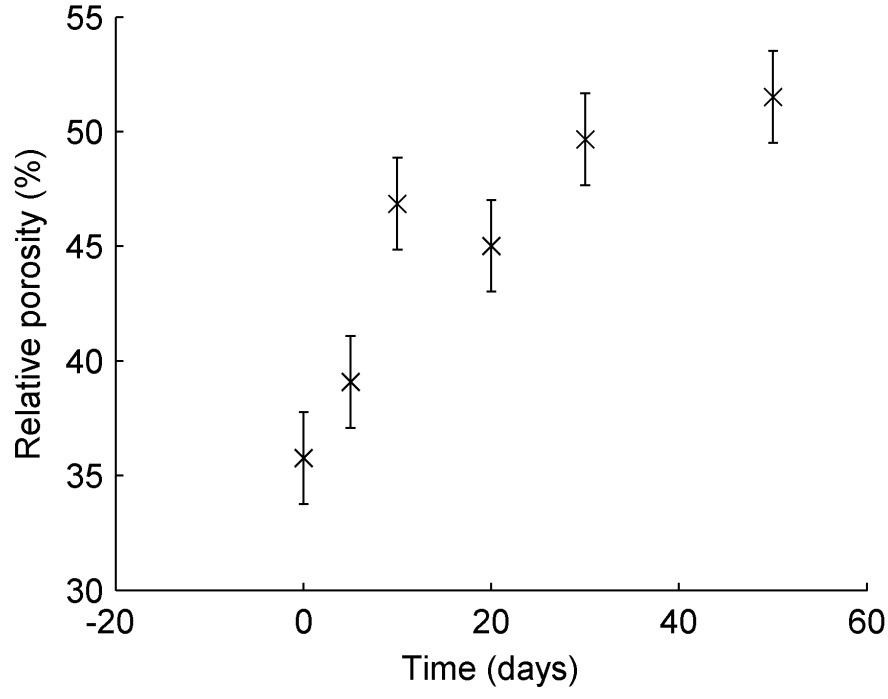

(b)

Figure 5.12: Helium pycnometry of PBS aged cylinders. Graphs show (a) True density and (b) the relative porosity fraction of the volume at each time point.

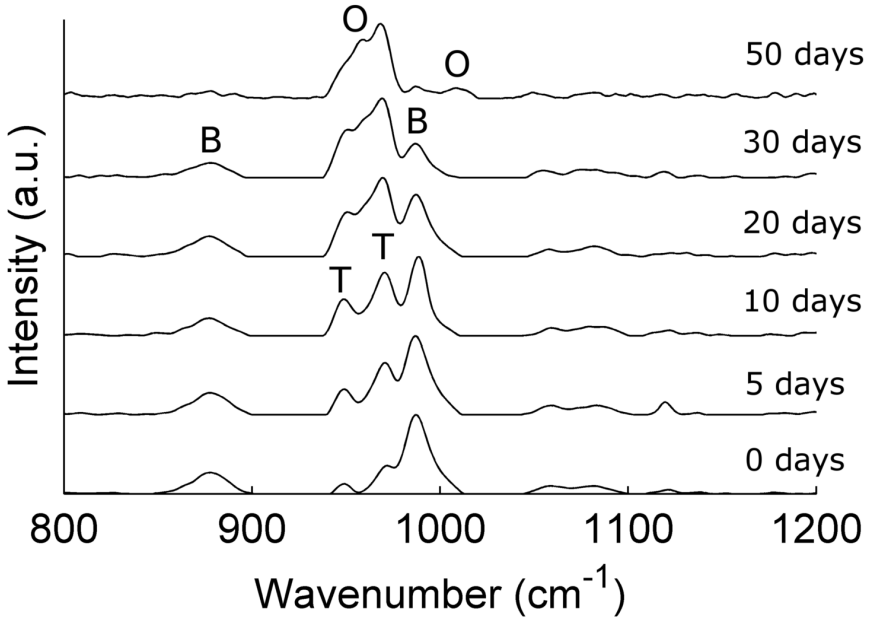

Figure 5.13: Raman spectrum of powdered brushite cylinders aged in PBS. Key: Brushite - B, OCP - O, TCP - T.

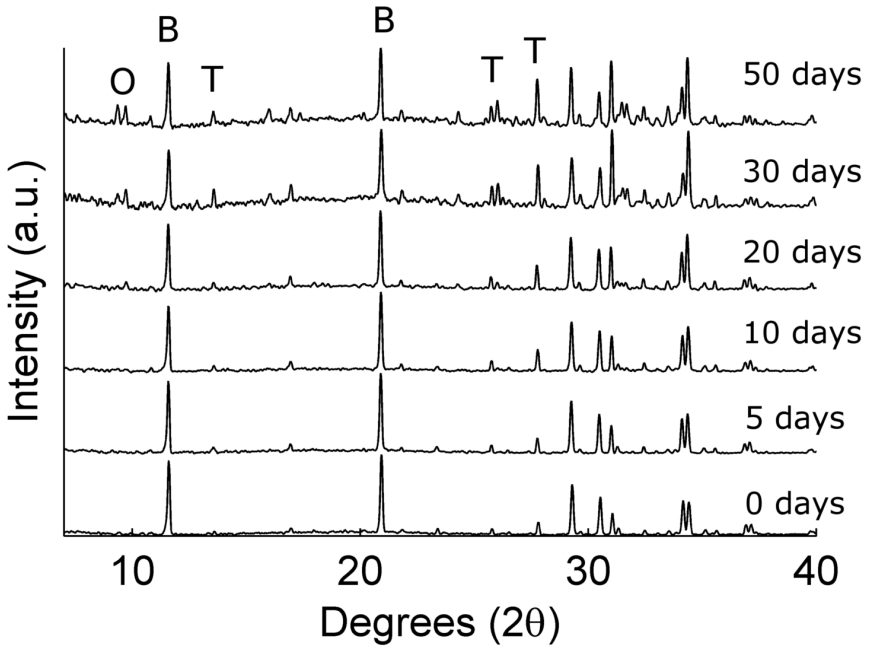

Figure 5.14: Powder XRD patterns of brushite cylinders aged in PBS. Normalised to the most intense brushite peak. Key: Brushite - B, OCP - O, TCP - T.

5.6 Discussion

The work presented in this chapter investigated the effect of physiological ageing conditions on brushite CaP cements as used in the BBLC. The brushite anchor in the BBLC will need to function as an effective bone graft material to rapidly bond with and be resorbed by the bone to avoid pullout or other failures. Additionally in revision surgeries where the primary graft has failed the first stage requires filling the previous bone tunnel, the use of brushite cement would avoid the need to harvest bone as an autograft. These needs are complicated by the currently poorly understood and varied results reported in the literature.

This study investigated the visualisation of phase changes using Raman imaging on brushite cement cylinders aged in a range of media. Dynamic media removal was used to encourage a higher rate of hydrolysis and dissolution, but with lower recrystalisation as the fresh media would remove ions from the system and reduce saturation. Importantly, it was observed that in PBS aged samples a shell of OCP formed but did not prevent further dissolution, with continued loss of brushite and penetration of OCP over the entire time course. Indeed, in samples with raised PBS pH total dissolution of brushite with replacement by OCP and then HA was observed. It was also shown that the presence of protein inhibited phase change, even at serum concentrations as low as 10vol% matching previously reported results [127].

The transformation from brushite to a more stable phase such as HA has been shown to be an important factor in the highly unpredictable degradation of brushite cements under physiological conditions [142]. Ageing of brushite cements *in vivo* [131, 142, 179, 299, 300, 301] and *in vitro* [126, 127, 231] has been undertaken by a number of studies with inconsistent results. For *in vitro* ageing a range of ageing mediums including distilled water [314], SBF [231], PBS [126, 127, 231], cell culture medium [315, 316], and bovine serum [127] have been used. In these studies brushite has been shown to undergo dissolution and

transformation to OCP, as reported here, or HA depending on the cement composition and conditions it has been aged in. OCP is known to be metastable and will quickly transform to HA [135], however this was only observed in the time frame of this study under accelerated conditions with a raised pH. As a result of these variations in phase transformation, amongst other differences in degradation, there is an ongoing debate as to which media composition most accurately duplicates native physiological bioactivity conditions [316, 317, 318].

As discussed earlier, much of the analysis in studies on the physiological aging of CaPs has focused on a combination of morphological imaging coupled with spectral bulk compositional properties. These measurements provide information on the overall composition and properties, such as crystal size, but severely limit the depth and scope of phase information available. The spatial distribution of the phases remains unknown leading to an assumption of homogeneous distribution, which as I have shown is not the case in 3D samples in an aqueous environment with dynamic ion composition which is known to chemically interact with CaPs. Some studies have used methods acquiring spectral information at a number of points; providing information on changes in calcium to phosphate ratios [142] and phase as a function of spatial location [142, 179]. However these are still limited, requiring wide point spacing to cover the whole sample, and leaving uncertainty as to whether a particular point is a true representation or an impurity. Raman imaging presents a potentially ideal solution as a means to resolve the stated information gap and the issue of bioactivity, being able to map chemical molecules and species without the need to label or destructively prepare samples. Whilst Raman spectroscopy is unable to to directly quantify the amount of each phase present, it is able to identify and provide information on the species present and their relative intensities. Previously we have applied Raman mapping to the interface in a brushite-hydrogel system; showing evidence of the cement undergoing dissolution or fragmentation, and transforming into OCP when aged in a PBS or SBF media [231]. The work presented in the current study gives a more

controlled experimental environment allowing a clearer visualisation of the phase changes occurring as the samples aged.

For cylinders aged in PBS a three phase structure was seen to emerge and continuously develop as brushite underwent dissolution, leaving a scaffold of the original TCP reactants, which was subsequently seeded with OCP. With an additional fourth phase observed in higher pH PBS as HA followed after OCP. This suggested a nondirect route of conversion from brushite to OCP given the buffer region dominated by TCP between the two phases. The presence of such a buffer region at the interface between the two phases could be due to brushite being partially hydrolysed to an amorphous calcium phosphate (ACP) phase, before reacting with ions from solution to form OCP. The conversion of ACP to OCP has been reported previously [312, 319, 320]. The characterisation of ACP by Raman spectroscopy is problematic due to the loose non-crystalline nature of the species resulting in very broad peaks [321]. This is further complicated by the presence of the two or three other phases at any given spatial point in the region, with largely overlapping spectra in the region of interest. The main vibrational peak indicative of ACP is given as a broad PO_4 shifted to 950cm^{-1} with a high width for all other associated peaks [319]. Analysis of the data failed to find sufficient evidence of the presence of such a peak in the buffer region. Comparison of the ratio of the peak intensity at 970cm^{-1} to 950cm^{-1} to look for variations which might be indicative of a ACP PO_4 shift contributing to the overall signal of the HPO_4^{2-} TCP peak about 950cm^{-1} found no significant variation across the buffer region compared to any other areas regardless of time point. Given the highly soluble nature of ACP at more acidic pH a high rate of conversion to OCP would be expected [305] leaving only a small quantity at any given time point. This discrepancy may be explained by the formation of more stable ACP2 phase as a precursor to OCP as described by Christoffersen *et al.* [320] or the effect of concentration gradients in the porous structure and kinetic stabilisation reducing the conversion rate. Regardless of the conversion mechanism, the outside shell of OCP was not seen to prevent brushite disso-

lution further into the sample. In the case of higher pH media HA formation from OCP appeared at later time points, as would be expected given the preferred stability of HA in this region over OCP and brushite [115]. The transformation appeared to follow direct conversion with no intermediates, however the weak ACP signal and fact the process has been shown to occur quickly with an intermediate ACP phase under similar pH conditions [322] means intermediate stages are likely but hard to detect.

The transformation of brushite to OCP itself is surprising given the lower stability of OCP compared to HA predicted in solubility isotherms, with the majority of cases in the literature reporting the transformation of brushite to HA when aged in a neutral or slightly alkaline media. Whilst isotherms allow a prediction of the thermodynamically preferred phase, the kinetics of conversion in supersaturated media can mean that a less stable but more kinetically favourable phase grows faster and defines the composition of the final structure. Hydrolysis of brushite to OCP in a pH environment of 6.2-7.4 between 25°C and 37°C due to much higher conversion rate to OCP over HA was reported by Tung and Brown [323]. Importantly the brushite cements used in this study were not formed with a setting retardant or calcification inhibitor unlike many others reported studies. In a similar circumstance Malsy *et al.* [324] reported brushite converted to OCP and apatite in magnesium free cement mixtures. The direct transformation of brushite to OCP is given by Mert *et al.* [325] as one of the following reactions:

$$10CaHPO_4.2H_20 \rightarrow Ca_8(HPO_4)_2(PO_4)_4.5H_2O + 2Ca^{2+} + 4H_2PO_4^- + 15H_20 \quad (5.2)$$

$$6CaHPO_4.2H_20 \; + \; 2Ca^{2+} \quad \rightarrow \quad Ca_8(HPO_4)_2(PO_4)_4.5H_2O \; + \; 7H_2O \; + \; 4H^+ \quad (5.3)$$

$$5CaHPO_4.2H_20 + 3Ca^{2+} + HPO_4^{2-} \rightarrow$$

$$Ca_8(HPO_4)_2(PO_4)_4.5H_2O + 5H_2O + 4H^+ \quad (5.4)$$

Such a direct route would explain the decrease in pH from 7.3 to 6.5 as the brushite was first exposed to PBS resulting in a high level of dissolution, with the PBS pH subsequently rising as the remaining quantity of brushite decreased and became more deeply entombed inside the cylinder reducing the quantity and rate of dissolution.

The heat maps in the Raman mapping results (Fig. 5.4 and 5.5) suggests an increase in TCP alongside the appearance of OCP, however this is a misleading effect due to the loss of brushite in areas where dissolution had taken place. TCP, which is less soluble than brushite [140], has a higher intensity signal in these positions compared to areas where brushite has not undergone dissolution. Formation of further TCP is unlikely without stabilisation from magnesium ions [140] which were not present in the cylinder or PBS media. Normalisation of this is complicated due to variations in each phase across each sample, and changes in overall phase intensity and quantities in each time point. Leading to a misleading result as the brushite degrades the TCP which is highly stable, and not expected to form more in media given the lack of magnesium, appears to increase dramatically. Likewise the intensity of OCP will be seen to increase faster than is true, due to the decrease in the brushite peaks. The positioning of an object of constant height and intensity or embedding a soft but highly stable object into the cement itself as a reference point might help compensate for some of the variables involved. Uneven distribution of phases was observed in some samples, even for nonaged cylinders. This suggests an uneven mixing/setting of reactants and may have important consequences for *in situ* use where the conditions will be more complex and harder to control.

The variation in initial OCP seeding location between the PBS and basic DMEM media in Fig. 5.3 suggests a difference in the precipitation routes. In DMEM aged samples the majority of OCP formed on the outside of the cylinder, whilst in the PBS aged samples the outside remained dominated by a thick band of brushite even after 30 days, with brushite further into the sample undergoing dissolution and being replaced by OCP. The formation of OCP on the outside of the cylinder may be caused by adsorption of components in the DMEM media on the cylinder surface enabling OCP precipitation and possibly limiting, but not preventing, transport in and out of the structure. The presence of a less soluble outer band of brushite as seen in the PBS aged samples raises the issue of uniformity in the cement as a result of local conditions during setting which may have significant consequences for *in vivo* implants. In such situations phase composition will determine local pH and have a marked affect on the ingrowth of cells on implanted cements. The stalling or reduced rate of cell migration could cause complications if conversion of brushite to a more stable phase outpaces resorption, and/or regions of highly insoluble cement are left after otherwise total resorption.

The results of this study have shown that the evolution of multiple CaP phases can be mapped based on their intensity distribution over a series of time points. Differences in phase transformation based on media were observed, matching previous reports that showed the presence of proteins in serum based media inhibiting dissolution [127]. Previous ageing work on similar samples has noted morphological changes around the outside of aged brushite cylinders under scanning electron microscopy [126] coinciding with detected overall sample degradation and mechanical changes. This matches the changes seen in the PBS ageing series as the outer ring of OCP was seen to emerge. The ability to accurately resolve and display spectral information at a number of points across the sample adds a considerable contribution to the understanding of the cement and its bioactivity. High resolution imaging of phases will enable a better understanding of the rate and consistency of phase conversion. This is especially significant as we have shown that

the acquisition of spectra through bulk methods gives a much less sensitive result, with the emergence of phases in small quantities not clearly detected until a number of days after they were observed under CRM. Furthermore the compositional information that can be obtained from the Raman spectra is far greater than can be obtained through the histological staining reported in the literature, and does not require lengthy and complex sample preparation (eg: producing thin sections, dehydrating, staining).

The major limitation of the presented methodology is that it is mildly destructive, requiring physical preparation of the sample to access the plane of interest and make it suitable for confocal imaging. The depth penetration of confocal microscopy in turbid media is under ideal conditions $200\mu m$ which will be much reduced in cements. This limits the application of CRM to processed *in vitro* and *ex vivo* samples. However recent development of techniques for deep Raman data collection in soft tissue and bone [326], and endoscopic probes [327] may make remote access *in vivo* imaging of cements to depths in the order of tens of millimetres plausible. Raman is also diffraction limited in its resolution to a maximum of about 200nm, which will be further reduced if a low numerical aperture lens is used to view a larger area, and/or a longer wavelength laser is used to minimise fluorescence and chance of damage to the sample. Depending on the cement system in question the resolution will likely be equivalent to or much greater than the size of individual crystals meaning that it may be unable to resolve to the level of individual crystals with each spectra being composed of a combination of multiple phases, as seen in this study. Due to the highly complex nature of brushite cements and the number of variables that affect the cement bioactivity degradation the use of multiple complimentary techniques is of course still required, though the application of chemical imaging adds a powerful tool for use in further investigations given that work will be over a similar size range.

We have shown that localised information on chemical composition and phase changes in

brushite CaP cements can be mapped and quantified using CRM. This enabled spatially resolved monitoring of the simultaneous evolution of brushite, TCP and OCP phases in samples aged *in vitro*, giving clear information on the distribution and relative quantity of each phase over time. Ultimately, this has facilitated a deeper insight into the mechanisms involved in the transformation between phases. This chemical mapping provides an important information bridge between the morphology based high resolution electron microscopy imaging, and bulk chemical composition results often applied in the literature. Applied to further *in vivo* and *in vitro* results such information will enable a deeper level of understanding into the chemical interaction between the sample and it's surrounding environment and the biochemical mechanisms involved, allowing for the improved optimisation of brushite cements for bone graft applications. This is the first case that the author is aware of where the phase composition, and evolution as a result of time in media of a CaP cement has been mapped. Outside of bone graft applications there are many areas in biomedicine where monitoring the development and evolution of mineralised regions is or importance. Brushite and HA are often the main constituents of kidney stones, whose formation is not fully understood [328] and variations in mineralisation as a result of change/decay in teeth [329].

The results have an important consequence for the BBLC. The possibility of partial or total conversion to more stable phases would be limiting to the mineralisation at the interface and later bone graft attachment. No previous study has looked at CaP cements that have been aged under *in vitro* conditions for a period of time followed by *in vivo* implantation. In the short term the presence of proteins from the serum in the media will inhibit brushite dissolution, as reported in Chapter 3.

5.7 Further work

Further work needs to be performed extending the experimental scope of the work presented here for both the BBLC and bone graft applications.

The systems studied here are very simple, using a basic geometry in a highly controlled acellular environment. Further *in vitro* studies using osteoblast cells to investigate biologically mediated breakdown are required to extend the scope and validate the mechanisms reported. Ultimately *ex vivo* samples from *in situ* studies are the only true way to determine how the CaP cements will behave, such a sample would ideally have a very high level of information that could be collected by Raman imaging showing the biological components alongside the CaP phases and aiding an understanding of the mechanisms between the two. Relating to the attachment of the anchors a study of osteointergration for pre-aged cements would be required to validate their potential.

Extension of the current imaging methodologies to incorporate multivariate analysis, in addition to the univariate analysis currently applied, would allow for a much higher level of information to be extracted possibly adding further insight. Inclusion of high spatial accuracy mechanical testing to correspond with phase distributions seen in Raman mapping. The potential for *in situ* analysis with the methodology used here would be limited due to the nature of confocal microscopy and slow imaging times requiring invasive and destructive removal of the sample region to effectively map over the implant at depths below the surface. Higher signal intensity techniques such as CARS and SRS may allow a higher throughput of *ex vivo* samples, but the need to tune for each PO_4 shift may make that potentially infeasible in practice.

As noted earlier there are a wide range of techniques applied to provide information on the properties and state of CaP cements. The work presented here was largely limited to a focus on imaging techniques. Combination with further analytical methods will be

required to provide a complete elucidation of the phase evolution and changes in material properties.

CHAPTER 6

SINEW BIOMINERALISATION

Biomineralisation is the process of organisms producing minerals to harden or stiffen tissues, most notably in humans as the mineralised skeleton. As discussed in section 5.1 there is a significant medical need for bone-implants, which has resulted in development and investigation of biomaterials with oesteoconductive properties. In addition to wanting to encourage bone growth, there is also a need to decrease or stop bone formation in unwanted places where it can severely impair function. Understanding biomineralisation and the factors involved may allow for the development of non or minimally invasive procedures to increase/decrease bone mineral density as needed. In Chapter 3 the extensive mineralisation of the ligament soft tissue was reported. In this chapter the potential for a more controlled and homogeneous mineralisation of the soft tissue, as a means to develop a model for biomineralisation is investigated.

6.1 Biomineralisation

6.1.1 Bone structure and native biomineralisation

Bone has a complex hierarchical structure (Fig. 6.1). The basic unit is a collagen-mineral composite, composed of mineral platelets of carbonated hydroxyapatite, protein and water [330]. The protein component is mostly in the form of collagen type I, with 85-90% of

bone protein [331]. The mineral component is stiff and brittle, whilst the wet protein is softer but tough. The composite formed from the two combines the stiff and tough material properties of the separate materials to produce a substance that is rigid and also resistant to fracture [330]. Below a certain size materials become insensitive to flaws [133]. The shape, size, volume fraction, and arrangement of the mineralised particles is fundamental to the mechanics of the composite and the tissue at large [330].

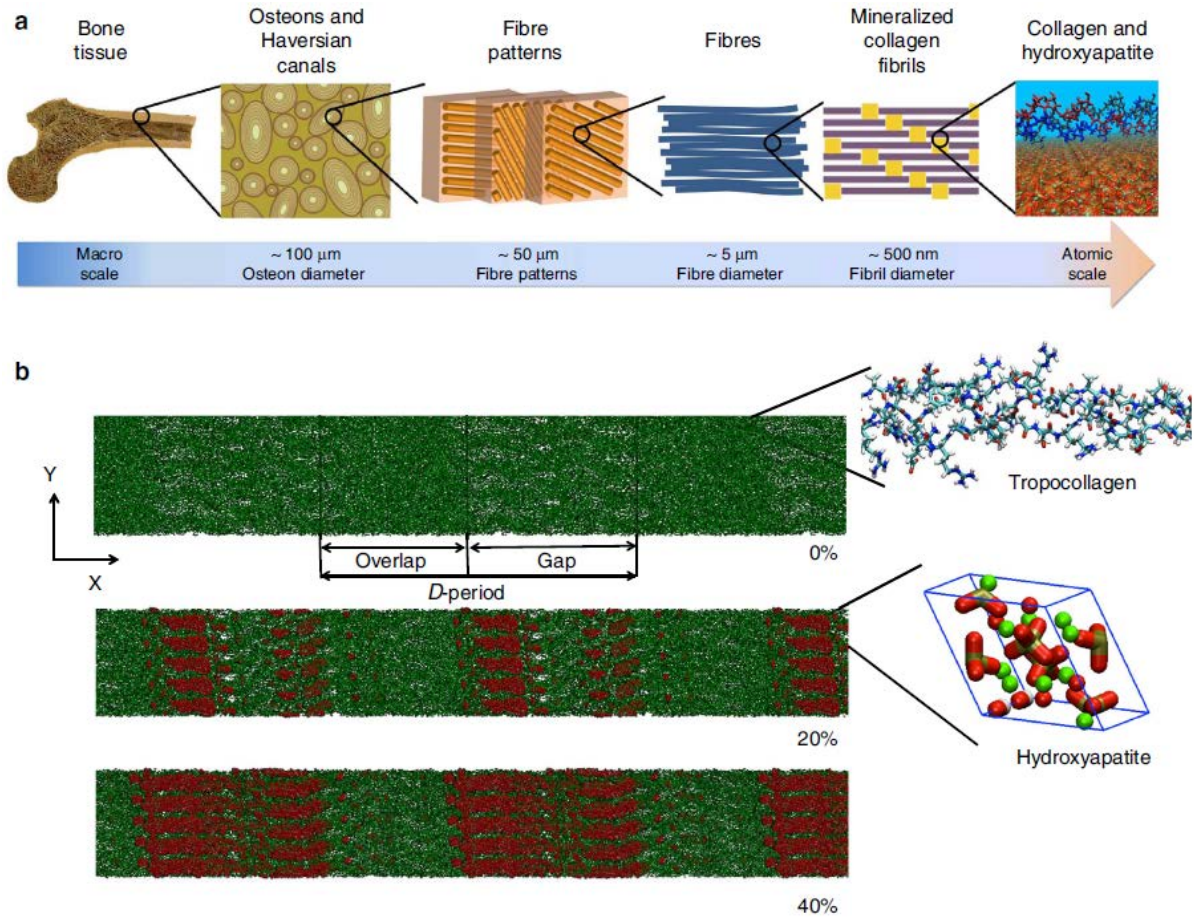

Figure 6.1: Multilayer structure of bone, and organisation of collagen and hydroxyapatite in mineralised collagen fibrils. Image modified from Nair *et al.* 2013 [332] with permission.

6.1.2 Medical need to control bone formation

As discussed previously in section 5.1 there is a large demand for bone implants, which far outstrips the availability and practicality of donor bone. Briefly: bone loss through disease, trauma, or genetic conditions can result in dehabilitation and loss of quality of

life. Grafts with native bone as autograft is ideal but limited, and allografts present a number of complications. In addition to the current medical issues other areas are likely to play a larger role in the future. As mankind reaches out into space with longer periods of time spent in orbit, or voyages to planets and beyond becoming more commonplace there will be a need to compensate for the bone mineral density loss in micro-gravity environments [333]. Losses of bone mineral as a result of long-duration space-flights have been calculated to range between 2% and 9%, with a predicted recovery of 50% within 9 months after landing [334]. In such cases bone loss limits the physical tasks an individual can safely perform and leaves them vulnerable to injury. Repeated surgical intervention using bone grafting materials to speed up the recovery process is undesirable and impractical.

Conversely to encourage the formation of new bone there is also a need to understand the biomineralisation process to prevent uncontrolled formation. Heterotopic ossification (HO) is the process by which bone forms in non-osseous tissues, as either a result of trauma, neurogenics or genetics. Depending on the quantity and location of bone formed it can be unobtrusive and only noticed by chance on clinical radiography [335], or it can severely limit function and affect the quality of life of individuals. The main cause has been as a result of trauma or damage to the central nervous system. Surgery presents a risk of HO formation with over 10% of surgeries resulting in HO formation [335]. HO has become an increasingly commonplace amongst war veterans in recent years with up to 65% of injuries resulting in HO formation [336], due to a higher proportion of blast injuries in theatres such as Afghanistan and Iraq [337]. Treatment of HO is currently very limited with the current methods involving surgery to block, or remove the osseous tissue.

6.1.3 Experimental mimicry of biomineralisation

A number of studies have taken place in the last decade looking at the transformation of collagen into a bone-like material by mineralisation at multiple length scales [338, 339,

340, 341, 342]. Generally methods are split between biochemically driven mineralisation of collagen scaffolds, and cellular modulated mechanisms. These have provided much information on the roles and effect of each material. However the collagen tempate used is generally not aligned and in low quantities limiting their representative nature and effective use.

6.1.4 Chapter aim

The sinew component of the BBLC, is essentially a highly aligned collagenous structure. By providing a source of phosphates to induce mineralisation a bone like structure can ideally be formed. The formation of a mineralised construct would allow for a model to be developed based on the observed changes during the mineralisation process, allowing for testing of treatments and potentially be translatable for use as a bone replacement graft. Hence the aim of this chapter was to investigate the biomineralisation potential of the BBLC.

6.2 Materials and methods

6.2.1 Construct production

Constructs were incubated for 7 days in supplemented DMEM, with additional P and AA supplements after 7 days to encourage collagen growth, after 21 days from initiation mineralised solutions were added. At 45 days constructs were removed from culture, washed in PBS, fixed in 4% formaldehyde, and washed and stored in PBS.

6.2.2 Potassium phosphate supplemented constructs

Construct production

Constructs were produced as described above (section 6.2.1) either without supplementation as a control, or were supplemented with one of either potassium phosphate (Sigma-Aldrich, UK), sodium pyrophosphate (Sigma-Aldrich, UK), or sodium triphosphate pentabasic (Sigma-Aldrich, UK) from 21 days. 0.1%wt of each in powder form was added to supplemented DMEM with no pH neutralisation. Constructs were aged for a further 21 days in the phosphate supplemented DMEM media, with the media changed on a 2-3 day basis as before. On removal from media constructs were washed in PBS 3x5mins, fixed in 4% formaldehyde, washed in PBS 3x5mins.

Raman spectroscopy

Raman spectra were acquired of each phosphate powder, and at the surface of each of the supplemented and non-supplemented sinews. Using a 785nm laser combined with 20x lens, 20 accumulations of 3 seconds were used to produce each spectra. Spectra were preprocessed to remove cosmic rays and baseline corrected. In addition to the spectral data, video images were acquired under the 20x and 5x lens of each sinew using the CRM.

TEM

TEM images were acquired of the 0.1%wt potassium phosphate sample that had been sectioned to a thin slice, using a schottky field emitter TEM (Technai F20, Philips, UK) at 200kV. Bright image TEM and selected area diffraction (SAD) modes were acquired.

6.2.3 Potassium phosphate supplemented constructs (controlled pH)

Constructs were produced as described above (section 6.2.1) either without supplementation as a control or were supplemented with potassium phosphate solution. Solutions used

were: unsupplemented control, 0.1%wt potassium phosphate as described above, PBS with 10% or 20% potassium phosphate, pH neutralised with sodium hydroxide (Sigma-Aldrich). For the PBS solutions 100μL of either was added to the media in each well plate after the replacement of sDMEM producing a 0.5%wt and 1%wt solution respectively. Constructs were aged for a further 21 days in the phosphate supplemented media, with some removed at this stage and the remaining in a 1%wt for a further 10 days. On removal from media constructs were washed in PBS 3x5mins, fixed in 4% formaldehyde, and washed in PBS 3x5mins.

Micro-CT

Samples supplemented using each solution were scanned in a micro-CT. Sinews were mounted in 1.5mL eppendorf tubes, using the sylgard base to provide support, and scanned in an air atmosphere as described in Chapter 3 (section 3.3.2). 0.4 degree step size about 180 degrees, with X-ray beam parameters of 20kV, 100μA. Producing 9.38μm pixel size shadow images. Scans were reconstructed as before (section 3.3.2) and analysed using ImageJ and DataViewer.

Drying sinews

After the wet sample data was acquired, samples were dried by removal from PBS and kept in an incubator at 37°C for 2-3 hours.

Optical microscopy

Reflection microscopy images were acquired of dried sinews using confocal microscopy with 10x lens and 1x-1.5x digital zoom (section 2.7.2). Further images were acquired under brightfield microscopy (Modified Axio Observer Z1 microscope, Zeiss, Germany) using a 10x lens with images saved as png format.

SEM

Backscattered electron (BSE) images and elemental X-ray analysis were acquired on the outside and a cross section of the 1%wt neutralised sample, sputter coated with gold, using a SEM (XL-30 LaB6, Philips, UK) with an accelerating voltage of 4-8kV. Elemental data from crystals was collected from objects by energy dispersive x-ray spectroscopy (EDS). For crystal only, regions of interest protruding from the sample body were chosen to minimise the chance of background influence.

Further secondary BSE images and X-ray elemental spectrum were acquired of the surface, protruding crystals, and sinew interior via a cross section of a 1%wt non-neutralised sample, non-sputter coated, in an environmental SEM (XL-30 FEG Environmental, Philips, UK) with an accelerating voltage of 20kV. Images were acquired at magnifications between 65x and 2100x for general and crystal specific images respectively. Elemental data was collected using EDS taken at the surface, and inside the sinew via a cross sectional cutting. Spectra from crystals was collected from objects overhanging the sample to minimise background influence.

Measurement of spherical particles and needles was performed using ImageJ to determine the sizes and range, with at least 10 measurements taken for each per image.

6.2.4 MC3T3 seeded constructs

Constructs were produced as described above (section 6.2.1) with the differences that osteoblast potential lineage MC3T3 cells were used in place of CTF cells, AA and P supplementation was added after 14 days in culture, and no mineralisation supplementation was added. Samples were removed at day 25 and analysed using CRM and TP/SHG imaging.

6.3 Results

6.3.1 Potassium phosphate supplemented constructs

Constructs were developed using stainless steel pins as anchors in place of the brushite cement reported previously to remove the source of early mineralisation (Fig. 6.2). Once the sinews contracted, phosphate compounds were added to the media. Either potassium phosphate monobasic (KH_2PO_4), sodium pyrophosphate tetrabasic ($Na_4P_2O_7$), or sodium triphosphate pentabasic ($Na_5P_3O_{10}$) were added directly to cell media at 0.1%wt after 21 days with no pH neutralisation. Providing a control source of mineral material to the mature constructs. High levels of colour change were apparent in the media due to the drop in pH from the quantity of phosphate added, suggesting much more acidic nature and likely total cell death. Constructs were supplemented with mineralised media for a further 21 days before analysis. Visually constructs showed no variation between the mineralised and control samples. However a high level of precipitate was observed to form on the well plate in constructs supplemented with phosphates.

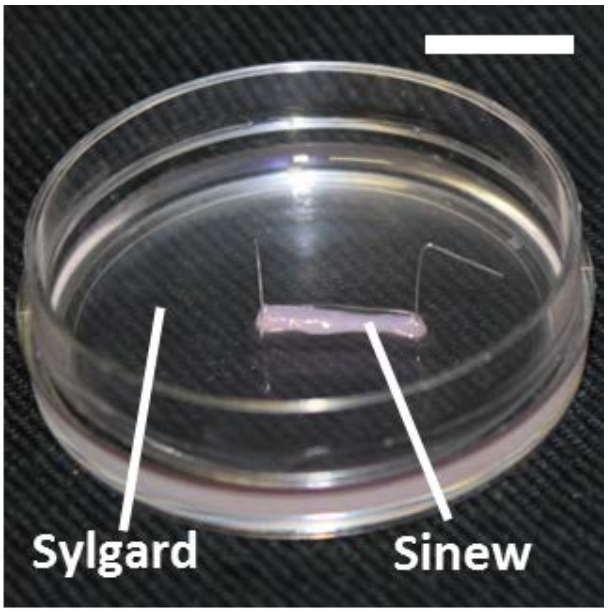

Figure 6.2: Ligament construct produced using stainless steel pins as anchors. Scale bar 1mm.

Raman spectroscopy

Raman spectroscopy was performed on the surface of control and phosphate supplemented sinews (Fig. 6.3). Widefield images provided no detail or contrast of the samples due to their still hydrated state and the low intensity of the microscope lamp. The majority of Raman peaks observed in each supplemented sample correlated with those present in the control spectrum which showed collagen bands at positions recorded in literature [174, 269] and covered previously in section 4.4.6 showing the collagen dominated structure remained. Most notably the potassium phosphate sample showed a phosphate peak at 960cm^{-1}, the phosphate peak combined with the collagen gives a spectrum that is at least superficially identical to that of bone [269] (Fig. 6.4).

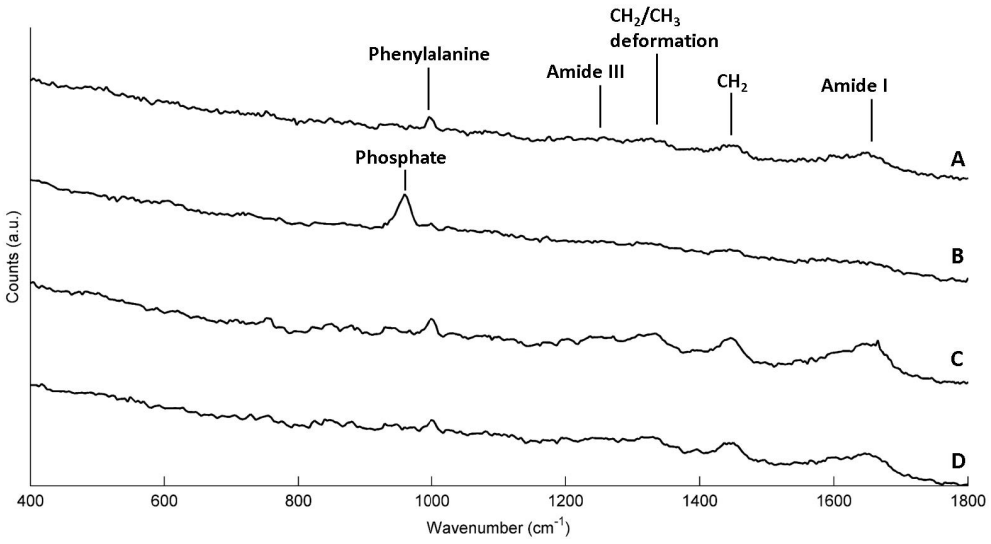

Figure 6.3: Raman spectra of sinews supplemented with phosphate based media. (a) Unsupplemented control sinew, and sinews supplemented with (b) potassium phosphate, (c) triphosphate, and (d) pyrophosphate.

Comparison was performed of the Raman spectrum of mineralised sinews to the Raman spectrum of the dry phosphate powders (Not shown). The results showed a significant shift in the observed peaks associated with the phosphates, suggesting a change in the chemical composition of the phosphate compounds on the sinew; though it was uncertain whether this was as a result of dissolution in the cell media or bonding with the sinew.

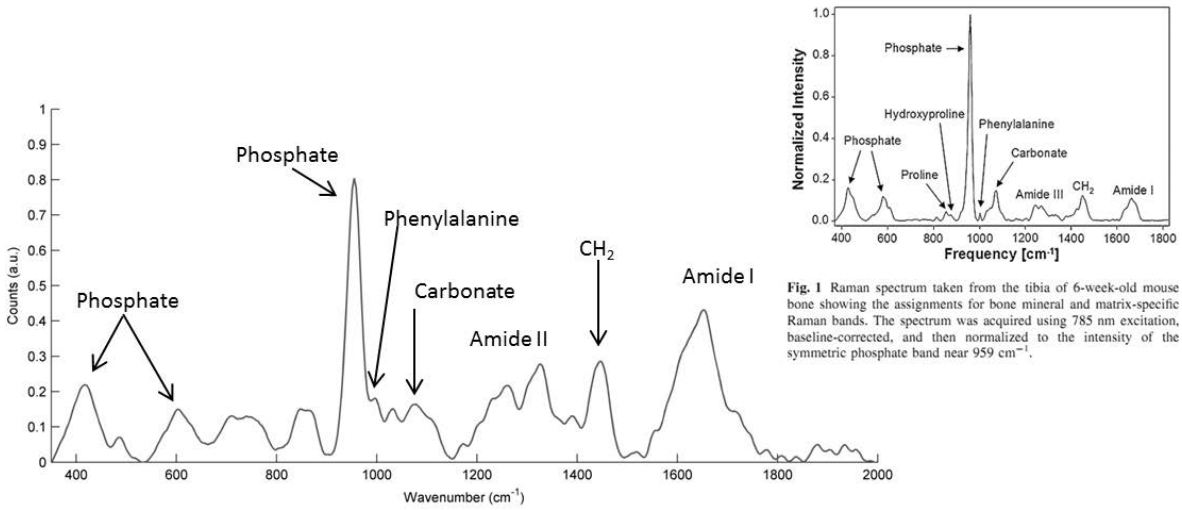

Fig. 1 Raman spectrum taken from the tibia of 6-week-old mouse bone showing the assignments for bone mineral and matrix-specific Raman bands. The spectrum was acquired using 785 nm excitation, baseline-corrected, and then normalized to the intensity of the symmetric phosphate band near 959 cm^{-1}.

Figure 6.4: Raman spectrum of potassium phosphate sinew compared to bone. Bone spectrum insert reproduced from Morris *et al.* [269] with permission.

TEM

High resolution TEM images were acquired of the 0.1%wt potassium phosphate sample on sections taken from the midpoint of the sinew (Fig. 6.5). This allowed images with nm resolution, below the size of collagen fibrils, to be acquired. The images showed an ordered structure with very densely packed and highly aligned organic structure. Darker regions on the sample possibly are likely indicative of mineral deposits, similar in contrast to the dark banding seen in native mineralised collagen. SAD patterns were acquired alongside each TEM image (Fig. 6.6). SAD shows electron scattering in the sample at a number of discrete locations, from which the crystalline structure of the sample can be determined, and the presence of native like HA could be confirmed. The presence of such scattering points in the SAD images suggest a highly crystalline structure. A systemic acquisition of TEM and SAD data for control samples was not achieved, preventing simple comparison of SAD results between samples with known differences in mineralisation that would help determine the source of the diffraction pattern. Likewise the complex crystal structure was not determined from the SAD images, which would have provided further information on the sample composition.

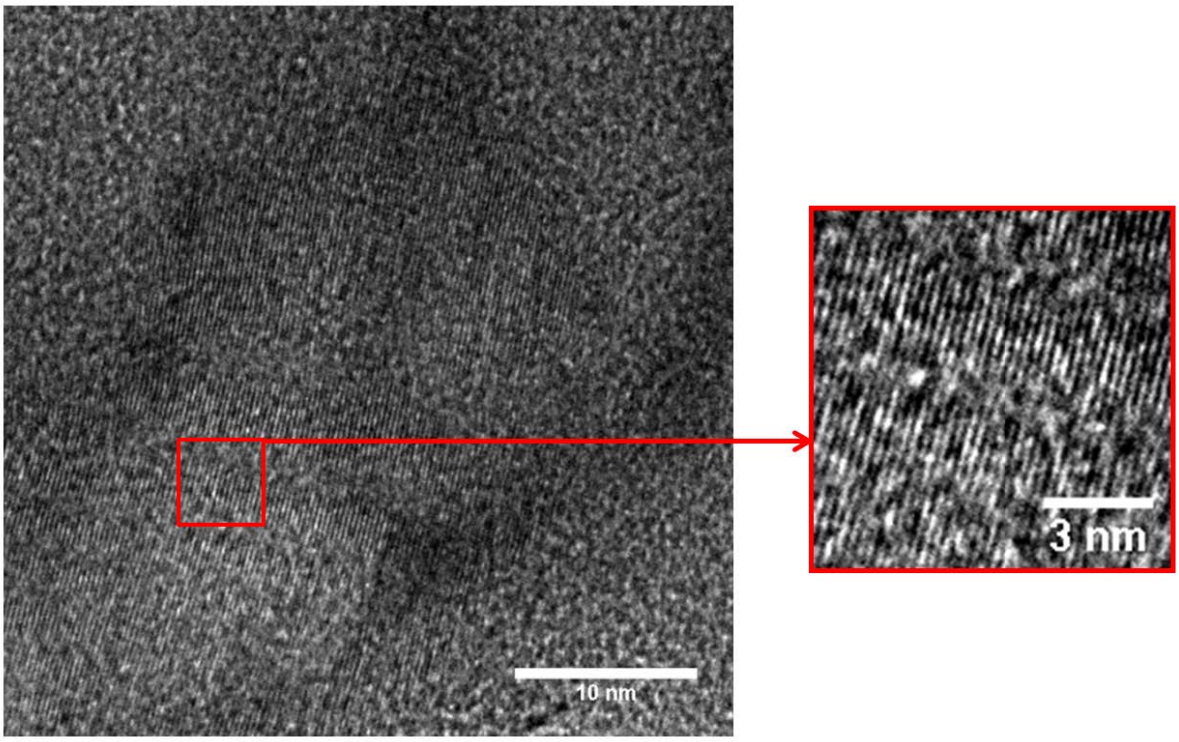

Figure 6.5: TEM image of 0.1wt% potassium phosphate supplemented sinew, magnified inset showing individual fibrils. Inset modified via ImageJ to increase contrast.

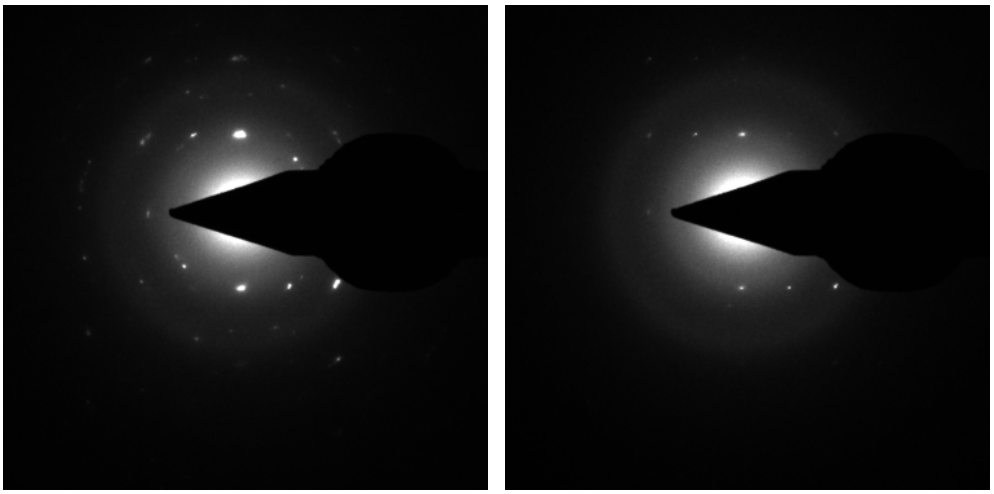

(a)

(b)

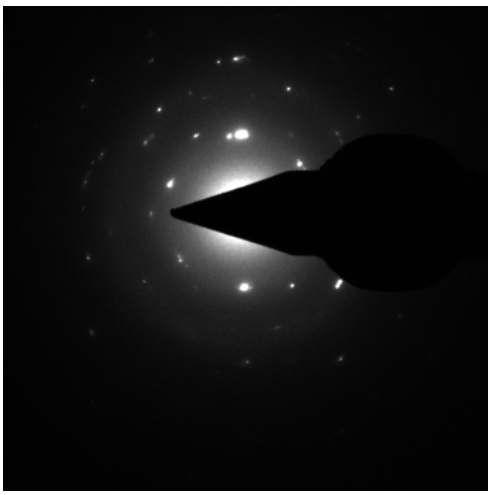

(c)

(d)

Figure 6.6: SAD patterns from TEM images of 0.1wt% potassium phosphate supplemented sinews.

6.3.2 Potassium phosphate supplemented constructs (controlled pH)

After the promising results of the initial supplementation, a more controlled experiment was undertaken with potassium phosphate. Potassium phosphate was added to the media either directly as before as 0.1wt%, or in a pH neutralised PBS solution at 0.5wt% and 1wt%. Contraction of sinews occurred as reported previously. After 7 days supplementation with AA and P was performed. 21 days since initiation potassium phosphate supplementation was performed for 24 days. The use of neutralised phosphate solutions resulted in a much more neutral media about pH 7.3 with less pH induced colour change compared to the direct powder method (Fig. 6.7).

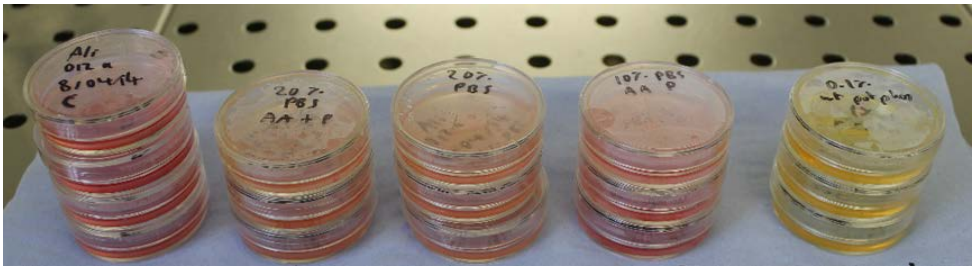

Figure 6.7: Effect of potassium phosphate supplementation on DMEM cell media colour. Left to right: control, 1wt% neutralised, 1wt% neutralised and with aa+p, 0.5% neutralised and with aa+p, 0.1%wt non-neutralised

Raman spectroscopy

Raman spectroscopy performed on the control and potassium phosphate supplemented sinews gave peaks identical to those presented in the un-neutralised samples (section 6.3.1) shown in Fig. 6.4. Raman spectra taken at points along the sample showed more significant variations in the intensity of the v_1PO_4 phosphate peak for each of the neutralised samples with respect to the collagen peaks, suggesting an uneven coating of the mineralised particles on the surface of the sinew. The poor quality of the widefield microscopy images obtained from hydrated samples limited the ability to match observed spectra to topography.

Micro-CT

Micro-CT reconstructions of each sample were performed to determine the quantity and distribution of minerals inside the sinew. Sinews developed using control and neutralised/non-neutralised potassium phosphate supplementation were reconstructed with an image pixel size of $9.38\mu m$. A partial three dimensional reconstruction of a 0.1% non-neutralised potassium phosphate sinew is shown in Fig. 6.8 with sagittal and transverse cross sections for each sample shown in 6.9.

Reconstructions of the supplemented sinews shown in Fig 6.9 exhibit little variation in the morphology and radio attenuating composition between each sample. A small number of high X-ray attenuation points, possibly associated with a build-up of mineralised particles, were apparent on the surface of samples. It is unclear whether these were caused by build ups of mineralisation or other sources such as contamination during preparation. Regardless of the source the sinews as a whole exhibited little variation between the control and supplemented samples suggesting that any overall mineralisation has occurred at a very low scale, below the sensitivity of the micro-CT.

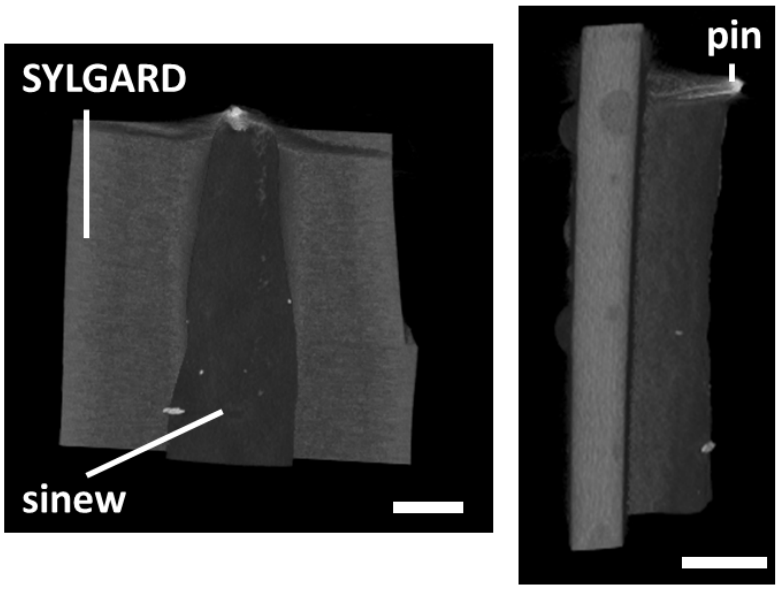

Figure 6.8: Three-dimensional micro-CT reconstruction of 0.1% non-neutralised potassium phosphate supplemented scaffold showing (a) top down and (b) side on view of the sinew, pins and SYLGARD base. Scale bar 0.1mm.

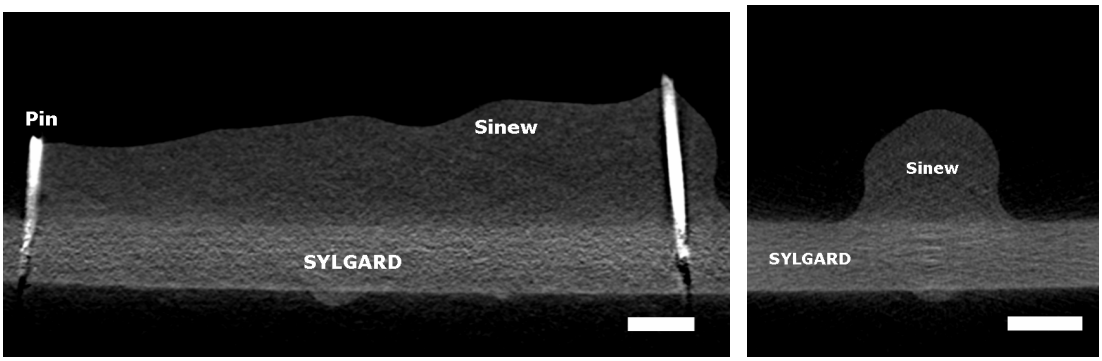

(a)

(b)

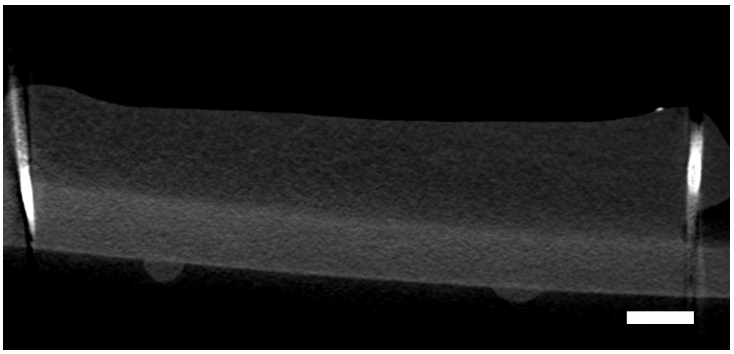

(c)

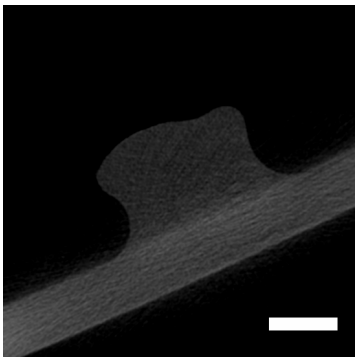

(d)

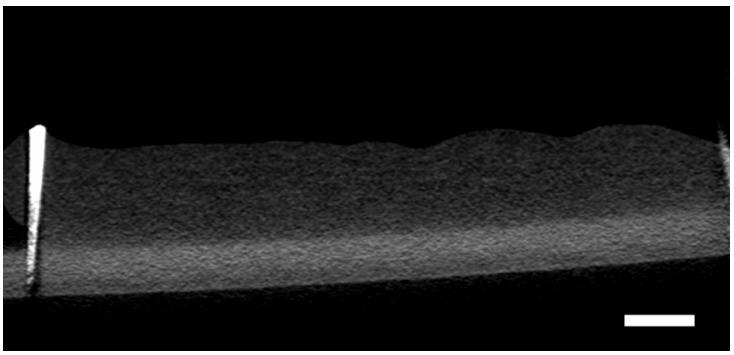

(e)

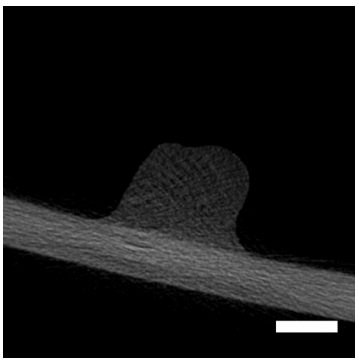

(f)

Figure 6.9: Micro-CT cross sections of potassium phosphate supplemented sinews. Showing the (a,c,e) sagittal and (b,d,f) transverse cross sections. For (a,b) unsupplemented control, and (c,d) 0.1%wt non-neutralised (e,f) 1%wt neutralised supplemented sinews. Scale bar $1000\mu m$.

Two photon and second harmonic generation

Image stacks of TP-SHG images were acquired on day 45 control and 1%wt neutralised sinews. Image stacks were acquired looking down into the midpoint of sample at the centre (Fig. 6.10), and at the edges (Fig. 6.11). In addition to cells the TP was able to produce signal and contrast for mineralised particles. No label was used so the signal would be entirely due to autofluorescence from the particles. A build up of mineralisation observed on the ligament surface at depths of $100\mu m$ measured from the edge of the collagen SHG signal, with up to $130\mu m$ in some cases (Fig. 6.11c). A much lower penetration of particles into the sinew body was observed with a much smaller and less dense quantity of mineralisation observed inside the collagen sheath (Fig. 6.11d). As with the BBLCs grown under standard conditions (section 4.4.7), organised collagen was seen to be present in the day 45 sample from the SHG signal. As before a dense layer of collagen correlated with the dense outer wall of cells with much lower density inside the sinew body itself (Fig. 6.10). The SHG signal was weaker in mineralised sample, likely as a result of the increased scattering caused by the dense and opaque phosphate particles on the surface.

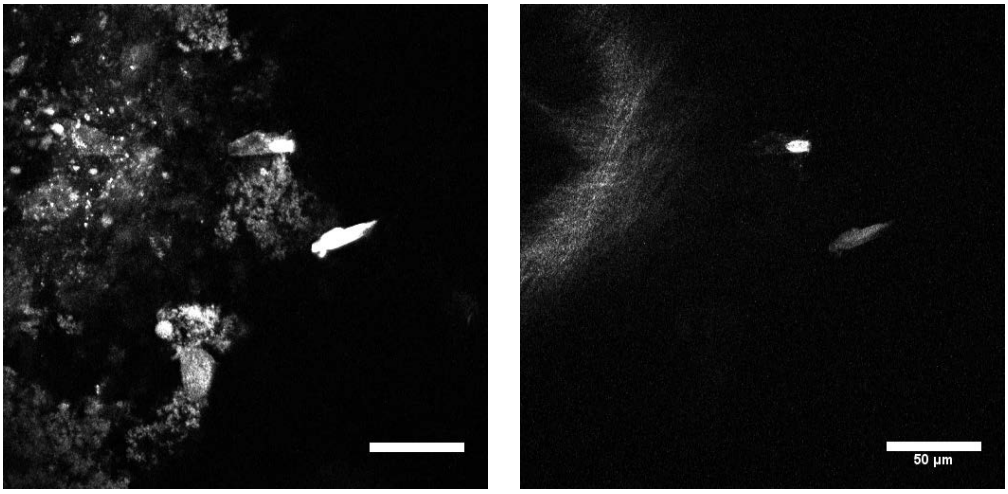

(a) (b)

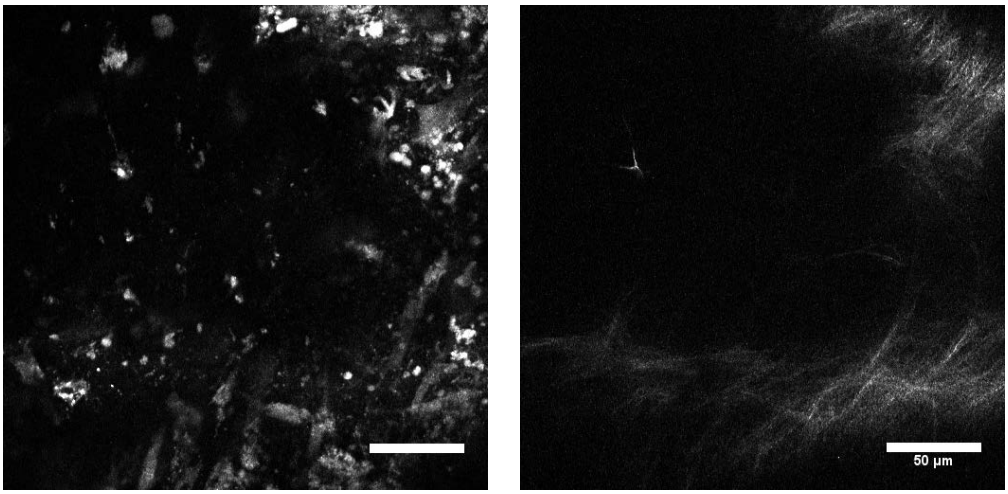

(c) (d)

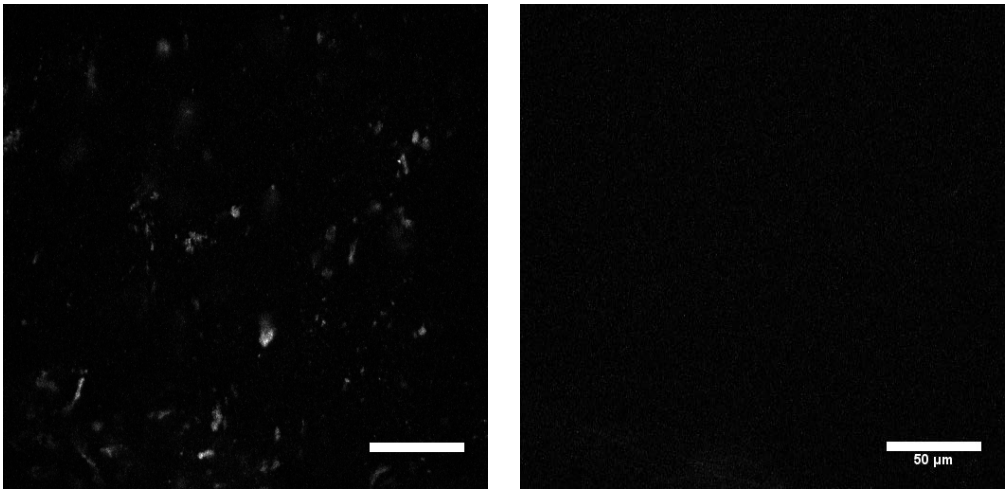

(e) (f)

Figure 6.10: Two photon (a,c,e) and SHG (b,d,f) microscopy of the surface of a day 45 1%wt neutralised sinew. (a,b) At the sinew surface, (c,d) $30\mu m$ and (e,f) $60\mu m$ into the sample.

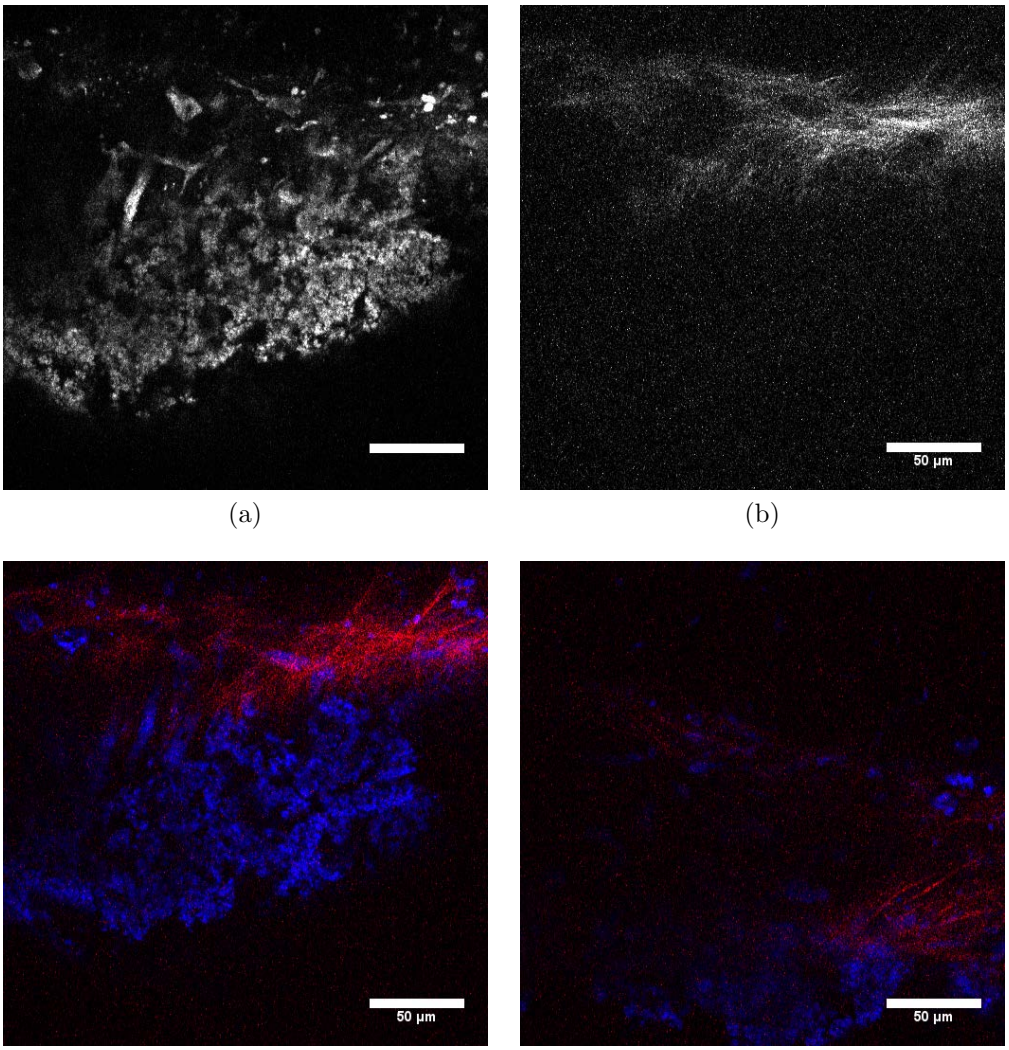

(a) (b)

(c) (d)

Figure 6.11: Two photon and SHG microscopy of day 45 1%wt neutralised taken at the edge showing a cross sectional view. (a) TP and (b) SHG (right) images of the outside of the sinew, (c,d) Merged signals (TP blue, SHG red) showing the extent of mineralisation (c) outside the collagen sheath and (d) into the sample.

Optical microscopy

After Raman spectroscopy, micro-CT and TP/SHG data were obtained, ligaments were dried for 3+ hours in an incubator at 37°C. The drying process resulting a reduced sample volume and change in colour from white to a dark brown. Dried samples were imaged under CRM, reflectance confocal microscopy, reflectance microscopy and SEM to study the mineralisation over the surface.

Optical imaging under the widefield mode of the CRM allowed detailed observation of the surface to be seen (Fig. 6.12). However the drying process resulted in a significantly higher autofluorescence in subsequent Raman spectroscopy. Dramatically reducing the signal quality with high autofluorescence, and in many points making it impossible to differentiate sample peaks from the background and preventing detailed comparison of topography to spectral content. Burning of samples by the excitation laser due to the reduced water content was also clearly visible in some instances and possibly the cause of the high autofluorescence observed in the acquired Raman spectra. The Under images obtained at 20x magnification bright reflective mineralisation seen distributed in clumps on surface of phosphate supplemented samples (Fig. 6.12a ,c , e). 0.1%wt non-neutralised were almost fully coated in mineralised particles, whilst the neutralised samples had a much lower and variable distribution, and no mineralisation present in the control. In non-mineralised regions structural alignment was observed in control and neutralised samples. The low intensity and collection of the light under the 5x objective prevented surface mineralisation being effectively studied over a larger area. But allowed clear observation of long needle-like crystals protruding from the surface of mineralised samples (Fig. 6.12 b, d, f). A total mineral coverage of the 0.1%wt samples with high quantities of long (up to 200μm) needle-like mineralised particles in the potassium phosphate supplemented samples.

Reflectance confocal microscopy performed on the samples (Fig. 6.13) backed up the re-

sults seen under the CRM video mode with control samples exhibiting no mineralisation and regions of high alignment (Fig. 6.13a,b), and supplemented samples showing mineralisation and the presence of long needle-like crystals (Fig. 6.13c,d). Similar results were seen with further optical imaging under reflectance microscopy (Fig. 6.14).

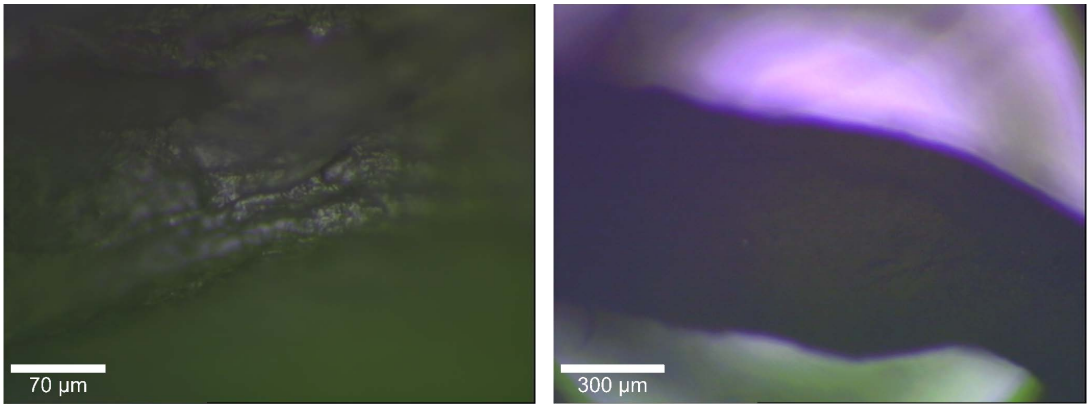

(a) (b)

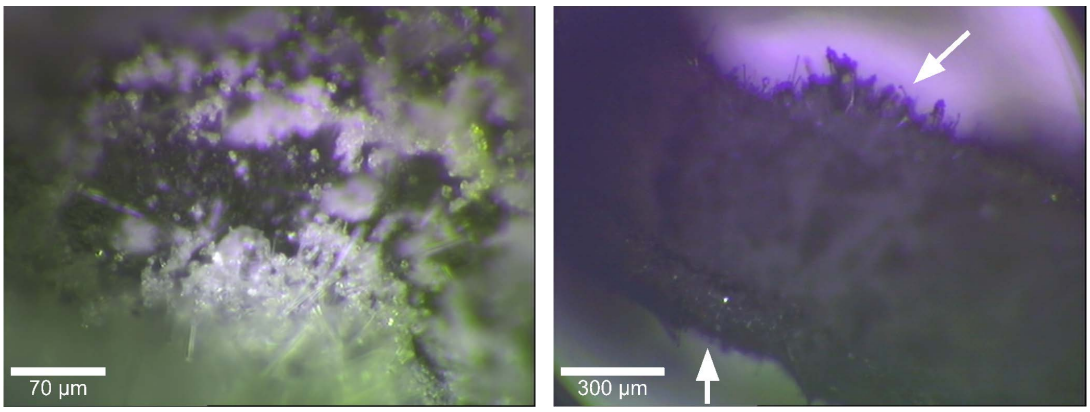

(c) (d)

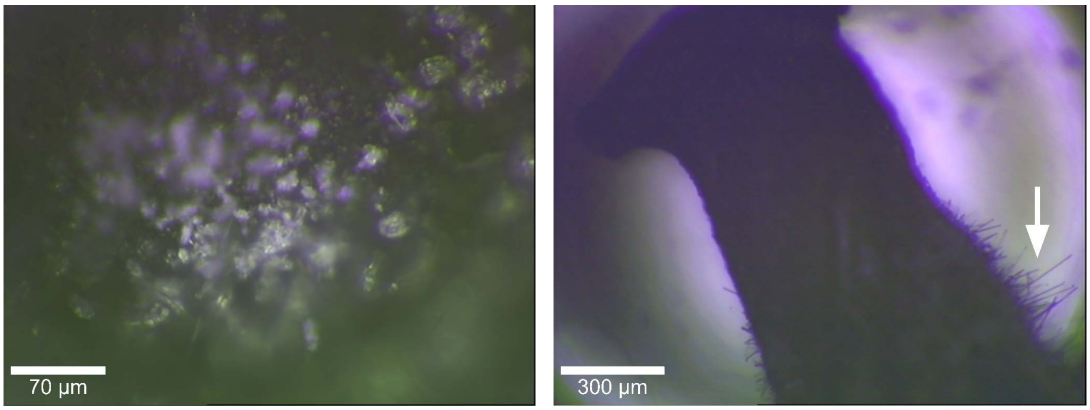

(e) (f)

Figure 6.12: Confocal microscopy reflectance images of construct surfaces obtained under the widefield mode of the CRM at (a,c,e) 20x and (b,d,f) 5x of (a,b) control, (c,d) 0.1%wt non-neutralised (e,f) 1% neutralised. Arrows show mineralisation and crystals on the sinew surface.

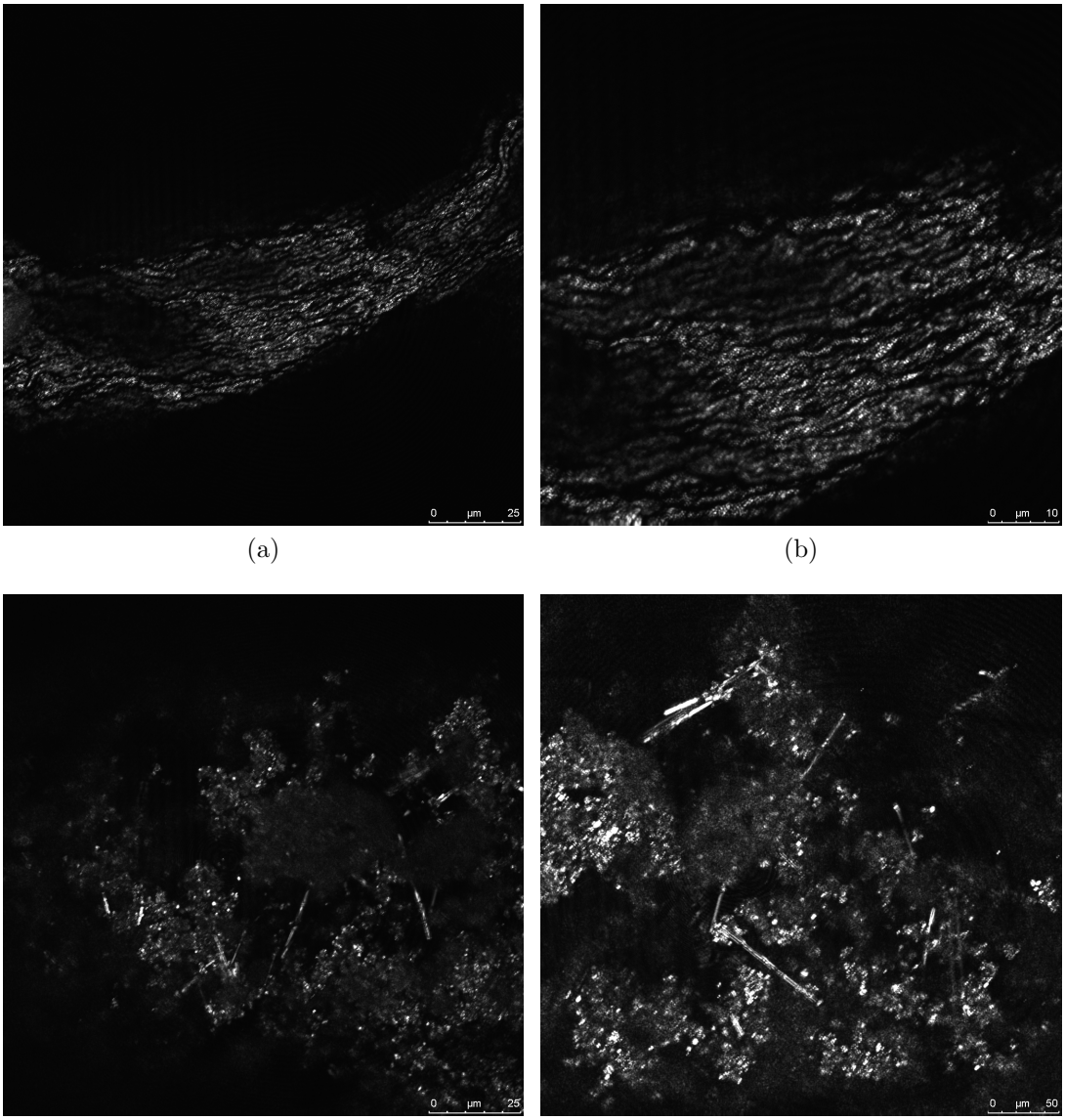

(a) (b)

(c) (d)

Figure 6.13: Confocal reflectance microscopy of the surface of dried potassium phosphate supplemented sinews. (a,b) control, (c,d) 0.1% non-neutralised potassium phosphate.

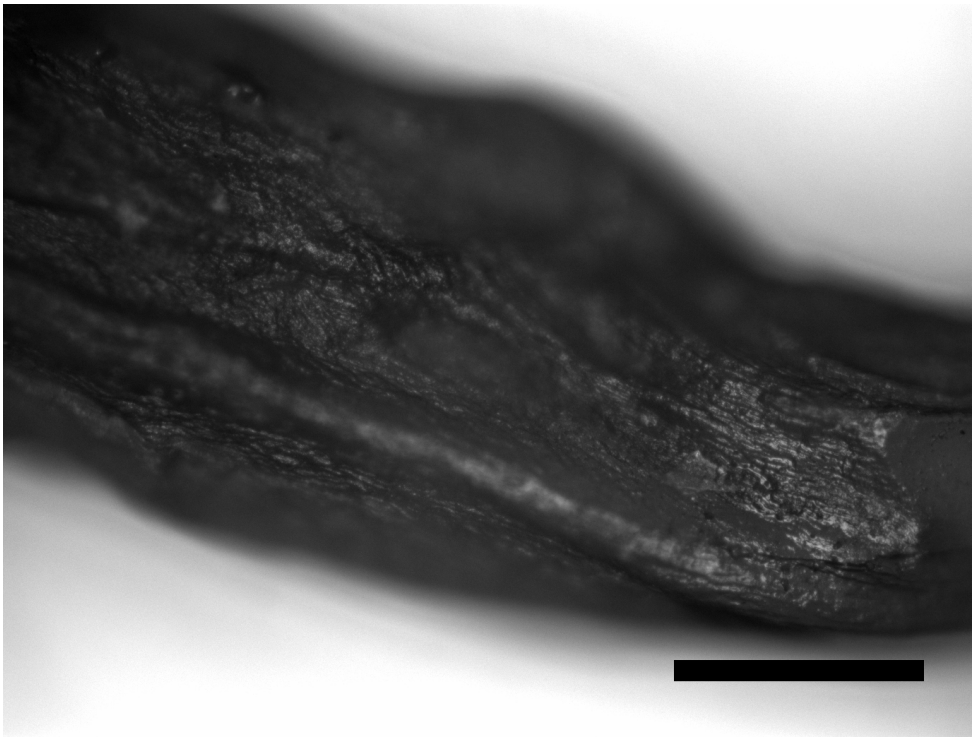

(a)

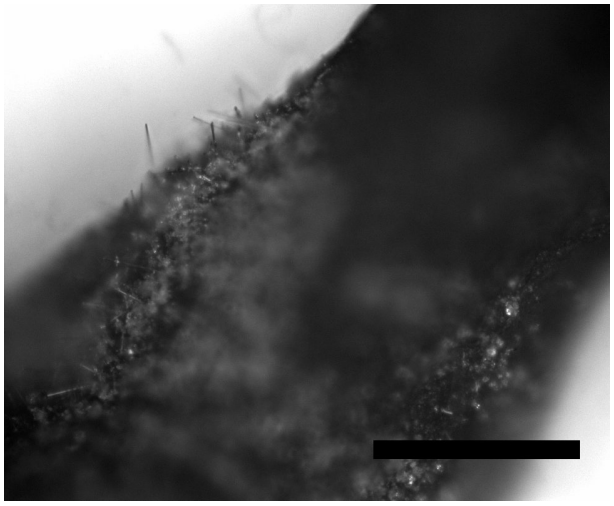

(b)

Figure 6.14: Reflectance microscopy of the surface of dried potassium phosphate supplemented sinews. (a) control (b) 0.1%wt non-neutralised potassium phosphate. Scale bar 0.5mm.

SEM

SEM was used to provide high resolution images of the mineralised particles on the sample surface and determine elementary composition via X-ray energy spectra. BSE images and EDS acquired of 1%wt neutralised sputtered with gold (Fig. 6.15), and 0.1%wt non-neutralised non gold sputtered (Fig. 6.16, 6.17, 6.18, 6.19), samples.

SEM backscattered electron images and EDS data were acquired for 0.1%wt neutralised sinews at multiple points over the surface (Fig. 6.18, and 6.19). Backscattered electron images showed high levels of debris on the surface of the phosphate supplemented samples, present as a mixture of irregular spherical-like and needle-like crystals. Elemental analysis suggested only carbon and oxygen were present at a given location on the debris, despite the visual observation of mineralised particles present in the area and compositional information on such areas acquired from Raman spectroscopy. Similar debris was seen in 0.1%wt non-neutralised sinew BSE images, however conversely a much more varied elemental composition was given. The detected elemental composition of each sample is given in Table 6.1. The XRD data suggests the crystals on the surface are formed largely of sodium-chloride, with very low levels of phosphate present. An exception is the case of point 3 of the data shown in Fig.6.19 where at the surface of the sample the quantity of Ca and P is comparable to and higher than the Na and Cl content. Image scans showing the cross section of the sinew near the surface showed much lower levels of mineralisation, and were largely dominated by oxygen, nitrogen and carbon (Fig. 6.17). The difference in elements detected between samples may be due to variations instrument sensitivity and sampling settings.

Measurement of particle and needle sizes was performed. In the 1%wt neutralised sinew measurements on the surface gave a mean length of $60\mu m$ with width of $1.1\mu m$ for long needle-like crystals. Spherical mineral particles varied in diameter between 1–$15\mu m$ with a median value of $5\mu m$. Mean penetration of $50\mu m$ into the sinew based on cross sec-

tions, assuming that the mineralisation present occurred during time *in vitro*, and was not a result of contamination during preparation. Measurements of debris on 0.1%wt non-neutralise was made difficult by lower magnification and image resolution, crude measurements suggested size distributions comparable to the neutralised ones given above.

Table 6.1: Elemental content from each 0.1%wt non-neutralised potassium phosphate supplemented sample, as determined by SEM EDS.

Sample	Content (%)	C-K	O-K	Na-K	P-K	Cl-K	K-K	Ca-K
Sinew – surface								
Fig. 6.16a	Weight	40.15	7.96	10.92	18.31	0.83	20.86	0.92
	Atom	55.43	9.42	11.32	13.21	0.47	9.76	0.38
Fig. 6.19a p2	Weight	37.75	5.86	21.88	0.50	33.61		0.41
	Atom	57.83	6.73	17.51	0.30	17.44		0.19
Fig. 6.19a p3	Weight	46.74	26.06	7.76	6.05	5.44	0.53	7.42
	Atom	60.75	25.43	5.27	3.05	2.40	0.21	2.89
Sinew – internal								
Fig. 6.17a	Weight	48.55	16.37	22.82	4.29	0.94	5.25	0.72
	Atom	57.30	16.57	20.22	2.65	0.43	2.10	0.26
Needle-like crystal								
Fig. 6.18a	Weight	64.03	10.95	12.26	0.14	11.80	0.03	0.40
	Atom	77.16	9.90	7.72	0.07	4.82	0.01	0.15
Fig. 6.18c	Weight	60.90	8.71	15.19		14.97		0.24
	Atom	75.64	8.12	9.85		6.30		0.09

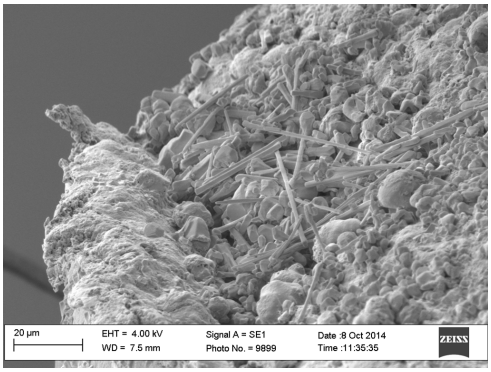

(a)

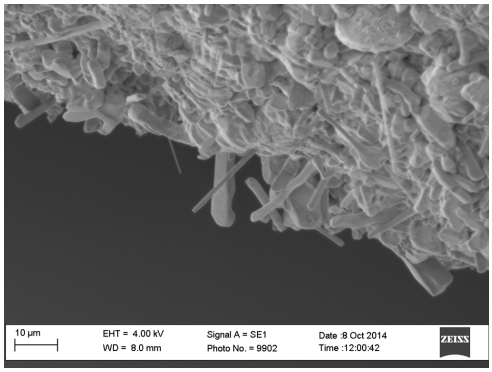

(b)

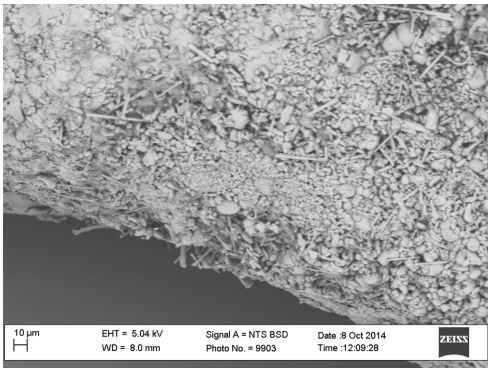

(c)

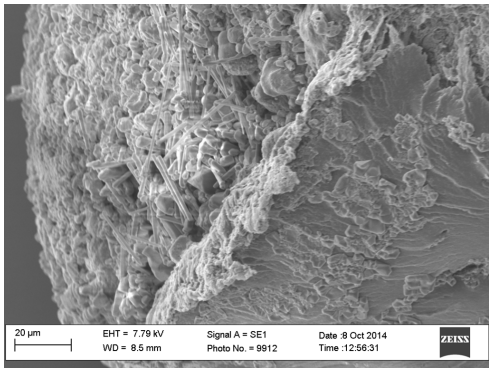

(d)

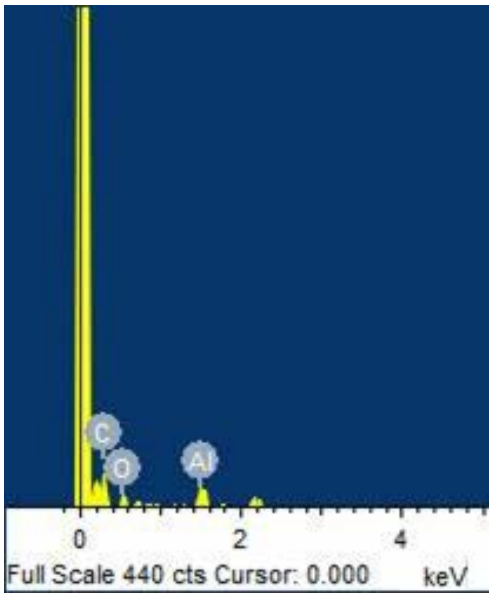

(e)

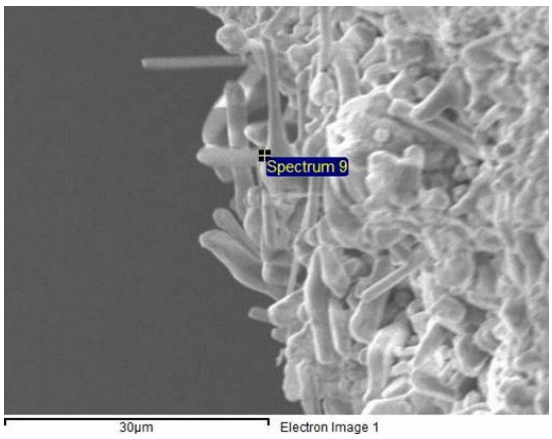

(f)

Figure 6.15: SEM topography and compositional information of the surface of a day 45 1%wt neutralised sinew. Showing (a-c) secondary backscattered electron imaging for the surface, (d) the surface and immediate inside of the sinew, and (e) the EDS elemental composition spectrum at (f) a point taken on the mineral debris.

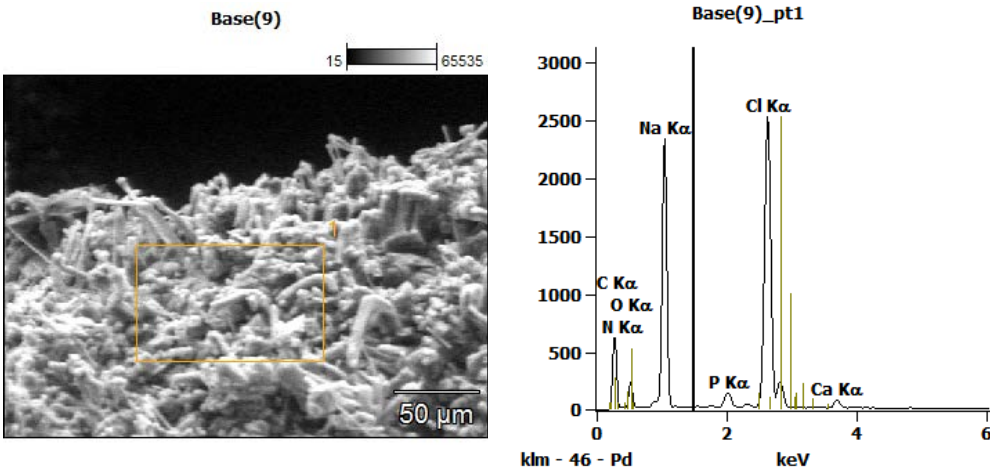

(a) (b)

Figure 6.16: SEM topography and compositional information of the surface of a day 45 0.1wt% non-neutralised sinew. Showing (a) secondary backscattered electron imaging for the surface, and (b) the elemental composition spectrum. Weight and composition % for each element at each point present are given in Table 6.1.

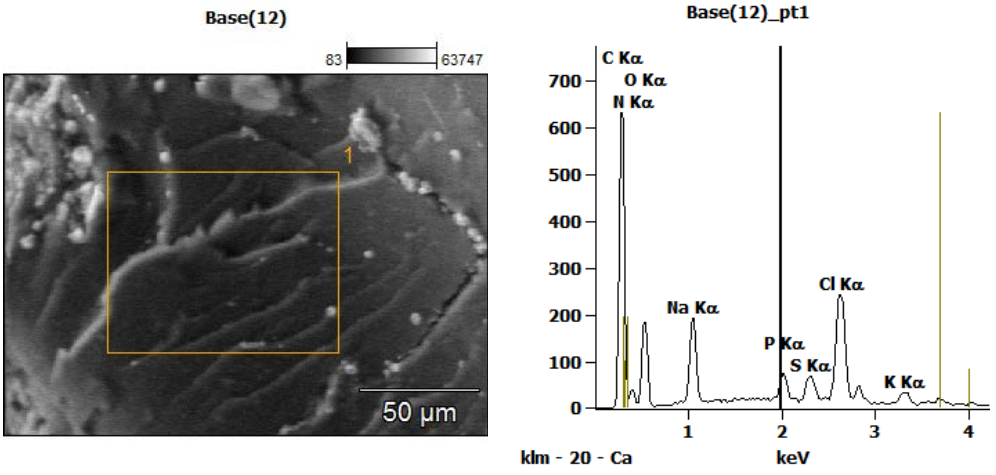

(a) (b)

Figure 6.17: SEM topography and compositional information of the inside of a day 45 0.1wt% non-neutralised sinew. Showing (a) secondary backscattered electron imaging for the surface, and (b) the elemental composition spectrum. Weight and composition % for each element at each point present are given in Table 6.1.

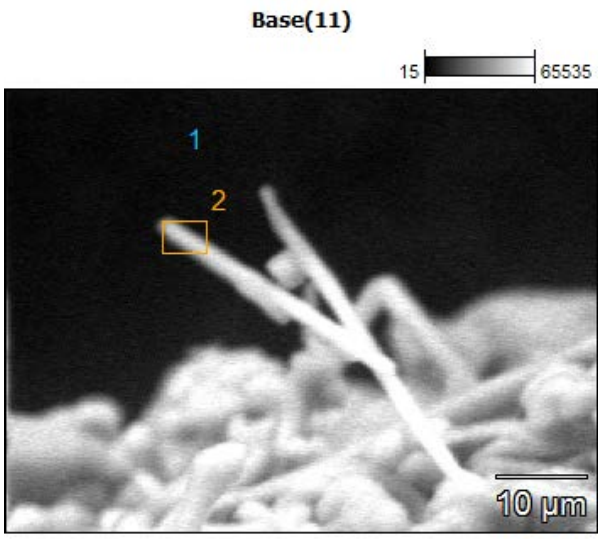

(a)

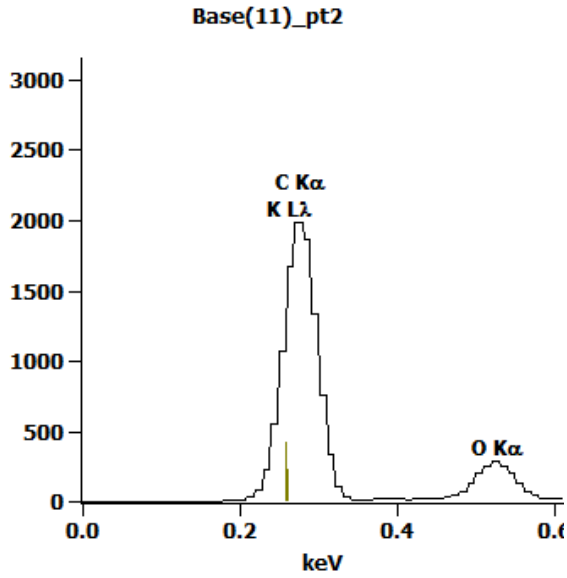

(b)

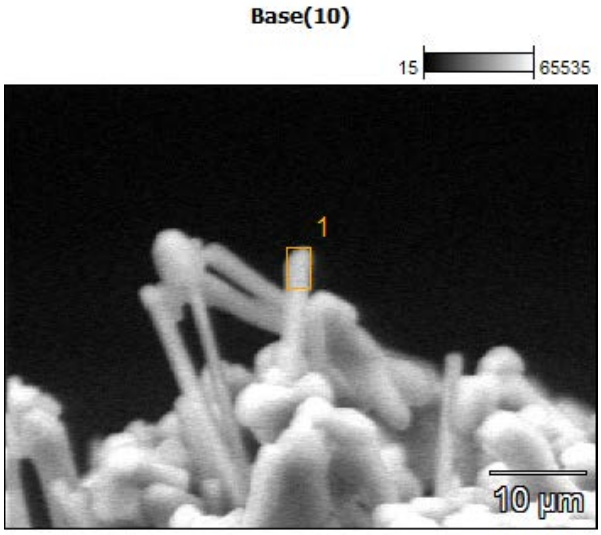

(c)

Figure 6.18: SEM topography and compositional information of a protruding crystal from a day 45 0.1wt% non-neutralised sinew. Showing (a,c) secondary backscattered electron imaging for the surface, and (b) the elemental composition spectrum for a). Weight and composition % for each element at each point present are given in Table 6.1.

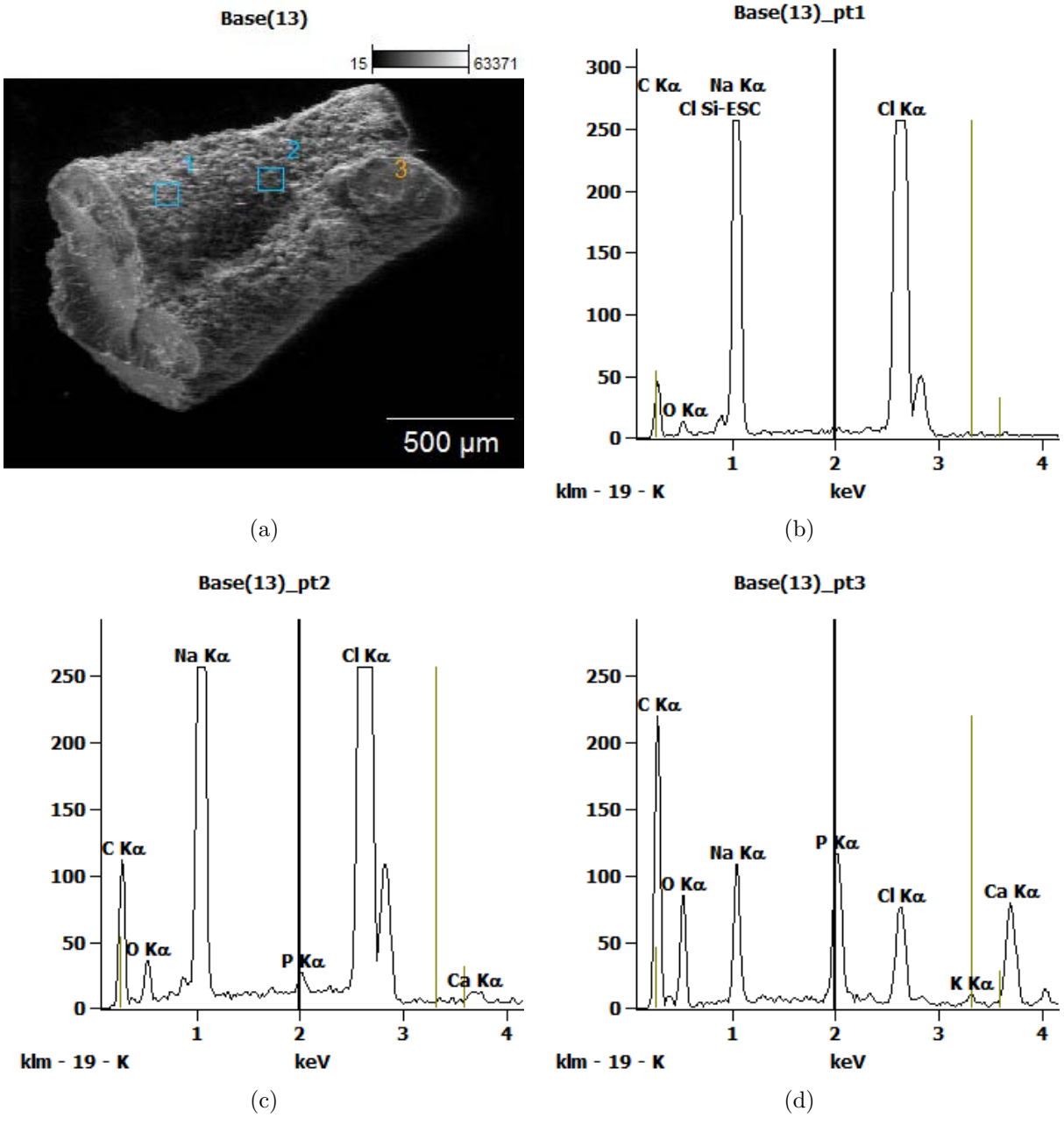

Figure 6.19: SEM topography and compositional information of the surface for a day 45 0.1wt% non-neutralised sinew. Showing (a) secondary backscattered electron imaging for the surface, and (b,c,d) the elemental composition spectrum at each labelled point. Weight and composition % for each element at each point present are given in Table 6.1.

6.3.3 MC3T3 seeded constructs

As an alternative to phosphate supplementation the use of mouse osteoblastic cell line MC3T3 cells for construct seeding, instead of the CTF cells that had been used previously for all reported construct development, was investigated with the intention of allowing biologically modulated mineralisation to occur through the propensity of osteoblast cells to initiate mineralisation or their differentiation to osteoblast cells. The MC3T3 cell based sinews exhibited significantly slower contraction in comparison to CTF cells after contraction terminated, the constructs remained rounded with a non-uniform structure with variations in the thickness of sinew leaving a highly porous pattern (Fig. 6.20). In a high proportion of samples the sinew was torn by the pins and floated free, suggesting a much weaker soft tissue, possibly due to a lower collagen content.

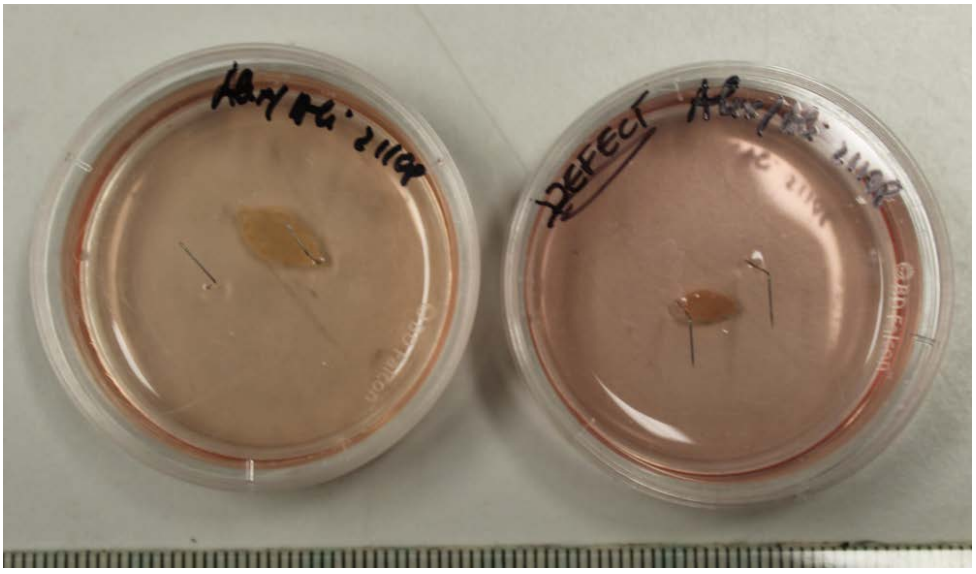

Figure 6.20: MC3T3 constructs after 20 days. Both samples show the ovular final shape with one end torn off from the anchor pin.

Raman spectroscopy of points taken on the surface of the sinew for day 25 MC3T3 samples showed a collagen based content similar to that seen in the CTF cell samples (Fig. 6.21). A peak associated with HA is present at 963cm^{-1}, suggesting mineralisation has occurred.

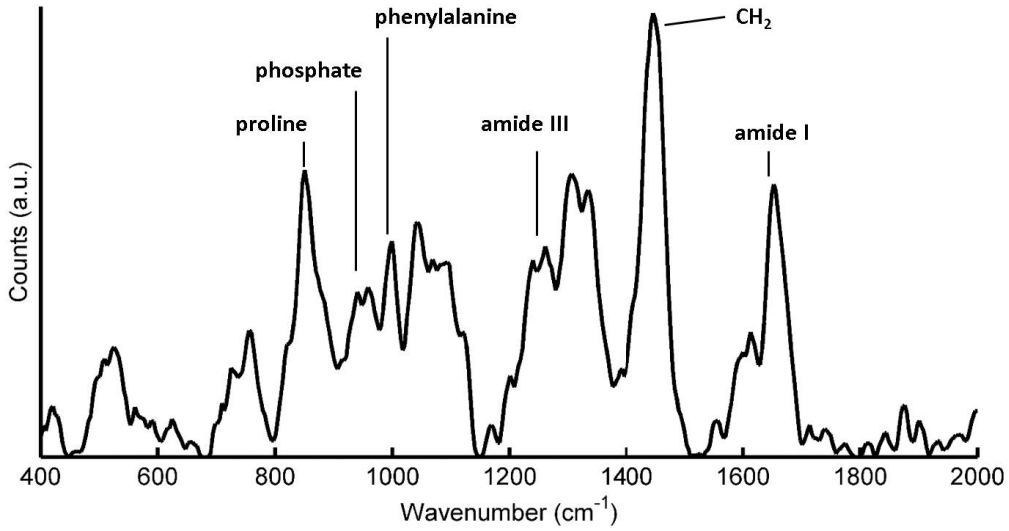

Figure 6.21: Raman spectrum of MC3T3 sinew at 20 days.

TP and SHG microscopy performed on the day 25 MC3T3 construct (Fig. 6.22) showed a dense cell wall on the surface of the sinew as observed with CTF cells, but very low to no migration of cells inside the sinew body. No SHG signal for collagen content was apparent at any point.

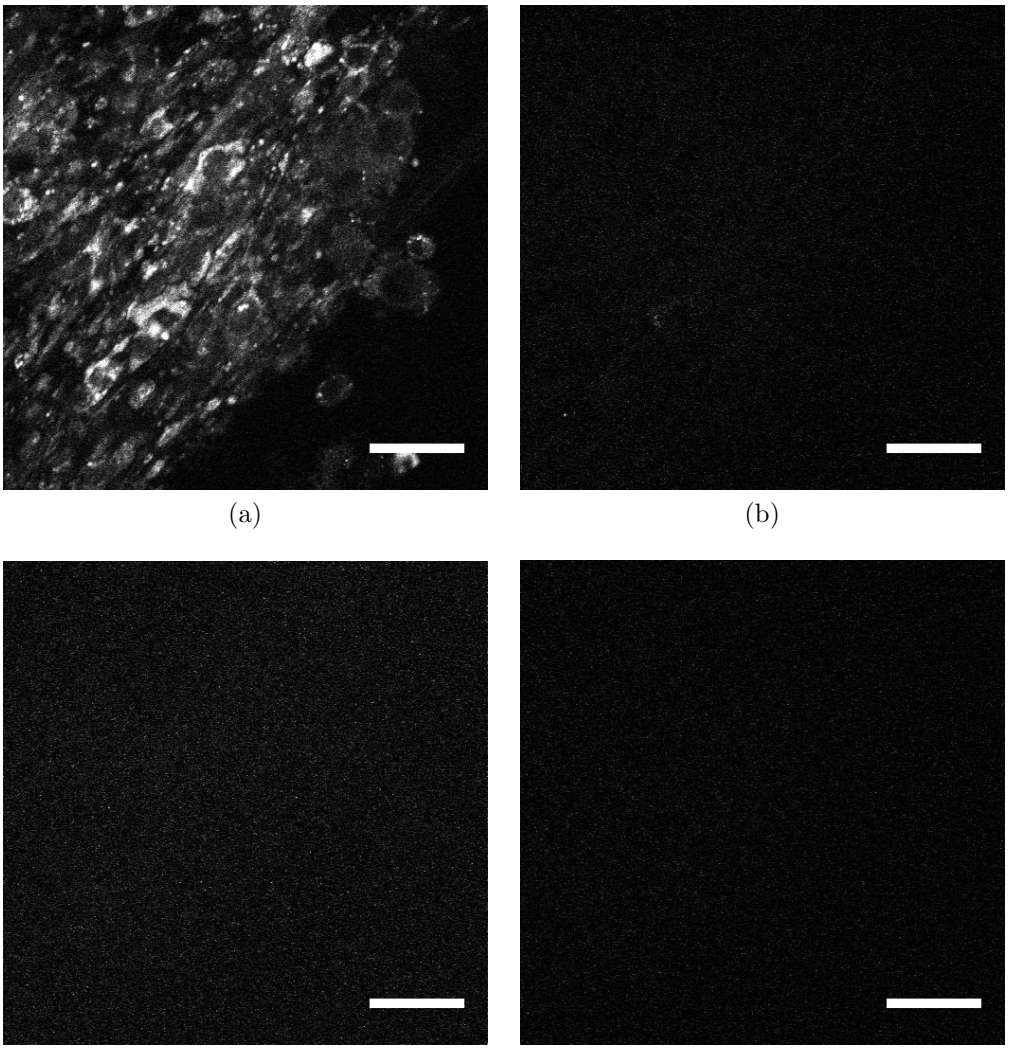

(a) (b)

(c) (d)

Figure 6.22: Two photon (a,c) / SHG (b,d) images of MC3T3 sinew. (a,b) surface (c,d) $40\mu m$ below the surface. Scale bar 50um.

6.4 Discussion

Biomineralisation and the formation of bone tissue is vital to the function of the human body, with significant issues arising as a result of excessive or insufficient bone formation as discussed earlier (section 6.1.2). A number of studies have investigated biomineralisation of collagen through chemically or biologically driven mechanisms. The BBLC, as a matrix of highly aligned collagenous tissue, provides an ideal basis as a model for further study of biomineralisation, and may itself function as an effective tissue engineered bone graft if successful. Micro-CT results from Chapter 3 showed significant build up of mineralised particles along the sinew. The aim of this chapter was to develop a model for the large scale mineralisation of the BBLC system.

Initially the addition of phosphate ions based on methods such as those reported by Liu *et al.* [338] was investigated. The addition of polyphosphates or pyrophosphates showed a build up of chemically altered mineralisation detectable by Raman spectroscopy of sinews. Potassium phosphate supplemented sinews in particular produced a Raman spectrum which alone highly matched that of bone (Fig. 6.4), and showed mineralised particles mixed in with the aligned collagen in TEM (Fig. 6.5) and crystalline structure under SAD (Fig. 6.6). Extension of potassium phosphate supplementation with pH neutralised solutions and a range of supplement concentrations, however were less promising when investigated more thoroughly. Images from multiple microscopy methods showed a build up of mineralised particles was only present on the surface of the sinew (Fig. 6.11). EDS showed that the top layer of crystals were predominantly NaCl, including needle-like crystals reaching 100s of microns away from the surface (Fig. 6.15 - 6.19). As an alternative to phosphate supplementation, the biologically mediated mineralisation through seeding of MC3T3 osteoblast-like cells instead of CTFs was also investigated. However despite evidence of mineralisation, MC3T3 seeded sinews showed poor contraction with the cells not migrating into the fibrin and the sinews becoming so weak they tore away from the anchors However these were only developed to day 25 compared to the day 45

sinews seeded with .

Initially biomineralisation by the addition of a poly or pyro phosphates to the sDMEM cell media was investigated. The use of polyphosphates to induce mineralisation was decided based on previous reports in the literature using similar materials, most notably the use of polyphosphate by Liu *et al.* [338]. The presence of a bioavaliable polyphosphate is thought to play an important role in the biomineralisation of apatite and collagen [343]. It has been shown that phosphorylation - the addition of a phosphate (PO_4^3) group to an organic molecule - is essential for calcification of bone [344], with phosphates thought to provide electrostatic attraction and act as nucleation sites for apatite [345, 346].

A large quantity of precipitate was observed on the sinew and well plate in all phosphate supplemented samples. The attached mineral was not displaced from either by multiple washes. The presence of the mineralised peaks and their differences in spectral distribution from that seen in the basic powders suggests that they had undergone chemical change. Variation in the mineralisation observed under microscopy, with some regions dense in precipitate and others mostly consisting of exposed sinew. Interestingly the coverage of mineralised particles was greater in the 0.1%wt non-neutralised than 1%wt neutralised samples, suggesting the repreciptiation process is highly dependent on the environmental pH. Micro-CT results suggested minimal or non-existent distribution of mineralised particles at the micron scale range with only a small number of highly attenuating regions apparent. This was in contrast to the brushite anchor based sinews shown in Chapter 2 where large (over $100\mu m$) mineralised particles were seen to be internally distributed along the length of the sinew. The outer layer of mineralisation was not detected in the micro-CT reconstructions, shown to be up to the order of 100s of microns thick. Suggesting that the mineralisation seen under microscopy is largely of a low density with weak radio attenuation. It may alternatively be that the layer of debris is only thick in small regions, by chance those selected to study in TP/SHG.

Microscopy images suggested an inability of larger crystals to grow within the structure, resulting in build up of mineralised particles over the surface, further blocking access into the ligament body. Use of nano scale crystals may encourage a more uniform distribution of mineralised particles into the sinews. However given the density and size of the sinews under the conditions used here the total penetration may prove impossible or highly impractical, and the separate mineralisation and later combination of multiple thinner sinew sheets may be required to achieve the goal of mineralised tissue formation.

The composition of the crystals when analysed via EDS revealed a very low phosphate content, with sodium and chlorine content being a number of factors higher. The high sodium and chlorine peaks present is in direct contrast. However the small depth penetration of the SEM interaction volume limits elemental information to the very top layer of the sample. Due to the ionic nature of such compounds, Raman peaks associated with NaCl are highly dependent on the surrounding lattice [175]. Generally they are expected to be broad and in the region below $200cm^{-1}$ [175]. In the BBLC sinews a broad and high autofluorescence background from the biological components is already present in that spectral region making a determination of the presence of NaCl in the Raman spectrum problematic. Microscopy images showed no precipitation in control sinews so it is unlikely that observed debris is a result of other processes such as formaldehyde crystallisation. The state of the precipitate on the surface prevented use of other analytical methods such as XRD to further quantify the structure and composition.

The formation of so many long ($200\mu m$ or greater) needle like structures lying on and protruding from the surface of the sinews is unexpected. The formation of long needle-like NaCL crystals has been reported [347], but has not been observed before in BBLCs. The difference in pH level of the media for straight phosphate and neutralised may explain the large variation seen in the quantity of crystals deposited in the supplemented samples.

The quantity, size and dispersion of particles were not seen to vary significantly between supplemented samples when imaged suggesting that the NaCl crystals may be dependent on the phosphate as a seeding site. Storage in PBS after removal from culture is likely to be responsible for the crystal formation due to its high NaCl content. Interestingly this has not been observed before on samples stored in PBS, so must be related to the potassium phosphate supplementation in some way. It is assumed that the initial phosphate mineralisation might have acted as a nucleation core attracting the NaCl salt layer on top.

Variations in the distribution of the mineral density and chemical composition are not necessarily a sign of failure. Native bone itself is not a flawless uniform and pure system. In native bone the mineralisation of the bone matrix varies greatly from 0-43% volume as a result of bone material being resorbed and a delay in the mineralisation process [330]. The difference in areas as a result of remodelling, known as the bone mineralisation density distribution, is thought to play a role in fracture resistance [330]. Poorly crystalline HA phase with ion and active group substitutions a common and dynamic process. However the high difference in mineral density at the surface and inside the sinew, along with the dominance of NaCl crystals seen here does not provide such beneficial effects.

The major failure here from the point of view of mineralisation was the accumulation of a large mineralised layer on the outside of the sinew with very little. It is thought that an ACP intermediate phase is needed for collagen mineralisation by apatites. In the absence of an agent, such as carboxylic acid, to stabilise ACP it has been reported previously that the phosphoprotein accumulated in large extrafibular mineralised spheres in the collagen matrix [348, 349], preventing movement into the superstructure of the collagen [350] and stopping full phosphorylation of the collagen molecules [351]. Such results are similar to the large build up of mineral seen here and may be the cause of the poor mineral infiltration. The low quantity of Ca ions present in the media will also have played a role in the poor mineralisation and possibly outright prevented apatite formation regardless of

ACP stabilisation and mineral infiltration. The collagen matrix itself may also prove a problem. Collagen is known to influence bone formation and organisation of apatites at the atomic and large length scales [339]. The presence of type I collagen in large quantities in the BBLC has been shown and quantified before [64]. However the organisation of collagen imaged here and in Chapter 4 by SHG microscopy shows an organisation not representative of native tissue, with uncertainty to how it will react to phosphorylation.

The final investigation explored the use of osteoblast-like cells, in the place of CTF cells, to reorganise the sinew and deposit the ECM and later induce mineralisation. Whilst it has been shown that the presence of cells is not required for mineralisation [209, 338], the use of osteo-line cells which are able to mediate mineralisation will ideally allow a more biologically favourable and controlled system to be produced. Particularly with regard to mineralisation inside the dense sinew which they can migrate into. MC3T3 cells are an osteoblast precursor with fibroblast like morphology and properties. Their behaviour can be controlled, with ascorbic acid having been shown to encourage MC3T3 differentiation to osteoblast lines and hence increase the mineralisation output [352, 353]. ECM alignment has been shown to be important for osteoblast behaviour [354]. The use of an established three-dimensional aligned collagenous scaffold like the BBLC will allow ideal circumstances for exploitation of this.

MC3T3 cells exhibited significantly slower contraction and uneven ligament construct formation compared to CTFs in the work performed. Taking 14+ days to contract down to a final size which was less elliptical than that achieved with CTF cells, and a higher failure rate of sinews tearing away from anchors. The presence of a Raman band at 963cm^{-1} is suggestive of mineral formation as or similar to HA. However MC3T3 also were seen to undergo poor migration into the sinew as seen under TP microscopy Fig. 6.22, which may result in a construct with a highly mineralised outside and non-mineralised inner. Scaffolds seeded with CTF cells with MC3T3 or direct lineage osteoblasts added at a later

time point may have a more promising effect.

The MC3T3 work presented here was performed under short time constraints and was very limited in its scope. Since this work was performed, further studies using different MC3T3 cell lines has found that the contraction is much faster with MC3T3 than CTF cells, and significant mineralisation by them has been detected suggesting that poor results shown here may be due to unhealthy cells.

The work presented in this chapter has shown interesting results, with significant promise for further extension of this work and the application of chemical and biological methods to form a biomineralisation model. However a number of limitations were present. Due to time constraints and the availability of instruments a very low quantity and consistency of results was obtained.

Two important parameters that were not tested were the cell viability and mechanical properties of the supplemented sinews. Given the large change in media colour as a result of both the neutralised and non-neutralised phosphate supplementation the sDMEM media underwent a significant pH change beyond the capability of the HEPES buffer to correct. Cell viability and function may be badly effected by the large drop in pH. Despite this no evidence of large scale decomposition that would be suggestive of total cell death was observed. In the case of osteoblasts a higher optimisation has been observed in acidic pH environments. As a result of the mineralisation of the sinews a change in the mechanical properties, most notably an increase in the stiffness, would be expected. Crude estimates of the mechanical properties based on handling and simple tests performed by manipulating the sinew body with tweezers showed no large scale change into a more rigid bone like structure.

6.5 Future work

As noted above the work presented in this chapter has shown interesting results and potential for further work. However much highly quantitative work needs to be performed to ensure that the results and data are consistent for each condition to allow for effective optimisation and understanding of the mechanisms involved.

Materials and supplements need to be expanded for example the use of a stabilising agent for the formation of ACP, and Ca ion source and further investigation of other ion and biological sources to encourage mineralisation. One option is to reintroduce the brushite anchors (removed to study the ability to control mineralisation without their influence and prevent the large mineralised particles observed in Chapter 3) as a source of Ca and P ions for phosphorylation and apatite formation. Such a use of cements as mineral sources for biomineralisation has been successfully reported before [355, 356]. The BBLC is a soft tissue, even with mineralisation will be in need of support to produce a more rigid and robust tissue. To this end various supplements have been considered such as methionine.

Osteoblast cell work reported was very limited due to time constraints. As noted above, work performed by others using alternative MC3T3 cell lines has shown much higher quality sinew formation and mineralisation present. Co-culture, CTFs to produce collagen then add osteoblasts to induce mineralisation. Use of the decellularisation described for the constructs previously by Labled *et al.* [98] to remove CTFs and allow seeding of osteoblasts onto an empty highly aligned collagenous scaffold may prove an effective route.

A combination of mineral supplementation and osteoblast cell lines may be required. Calcium and phosphate ions are known to play an important role in bone osteointergration of soft tissues. Phosphate ions delivered using a drug based approach have been shown to regulate osteoblast apoptosis [357], osteopontin production [358], and mineralisation rate [359]. Habibovic *et al.* demonstrated an osteogenic effect of phosphate ions released into

thoracic muscles of mice [360].

The techniques used here including the high-resolution TEM and TP/SHG were very limited in their availability, leaving a large variation in the information available for each sample. A more consistent application of these and further techniques to provide information on the mineralised sinews is important for building a fuller picture. Mechanical properties would be expected to change with mineralisation and so mechanical testing will be essential to measure changes in properties such as stiffness. In the study of mineralised tissue small angle X-ray scattering is commonly used to provide information on the shape, orientation and degree of alignment inside of bone [361].

CHAPTER 7

CONCLUSIONS

The work presented in this study has provided further insight into previous research on the ligament construct. The main conclusions that are drawn from this work and their consequences are:

- The presented results show evidence for the self–assembly of a complex heterogeneous system from initially homogeneous clearly separated starting materials. The formation of a mineralised interface between a bone–like anchor and highly aligned collagenous sinew creates the desired super-structure for an engineered BPTB replacement. However the deposition of mineralisation particles along the length of the sinew, and divergence of the sinew away from the interface region provides complications and shows flaws in the design and formation of the system. The ultimate mechanical strength to perform as a replacement ligament will require a means of further guiding the formation to control mineralisation and tissue formation.

- Mineralisation of the soft tissue sinew at the anchor/tissue interface was observed across nano and micro length scales. A mixed material graded interface is an important step in recreating the enthesis to allow smooth transfer of load between the differing materials. However evidence was seen of significant mineralisation build up beyond the interface and along the length of the entire sinew. Such extensive mineralisation will change the mechanical properties of the ligament and effect the biological behaviour. One of the major reasons for the extensive mineralisation

is thought to be the use of semi-dynamic media allowing saturation of dissolved ions followed by re-precipitation along the sinew. Future work using bioreactors to put periodic stretching and co-culture of other cell lines may encourage regulation of mineralised components and prevent saturation along the anchor if constantly dynamic media is used.

- Chemical imaging of the CaP anchors showed the brushite phase retreating away from the surface as a result of dissolution, leaving a TCP scaffold with subsequent seeding by OCP. Such an evolution of CaP phases has not been shown through imaging before. Whilst the dissolution of brushite is expected, and required to create the mineralised interface, extensive dissolution will weaken the already fragile CaP which is in a unique application of being required to tolerate a tensile load. The observed formation of OCP may counter the loss of brushite, whilst providing a suitable biomaterial for bone graft purposes.

- High levels of cellular reordering were observed inside the sinew as it contracted. The transformation from a flat sheet to ligament was shown to result in highly aligned cells and deposited collagen similar to that of native L/T. The presence of cells about the anchors showed that the lower pH environment caused by dissolution brushite was not preventing cellular activity at the forming interface. However as with mineralisation complications were observed. The density, elongation and alignment of cells was seen to vary at different points in the same cross section of contracted sinews, suggesting that the load driving organisation is uneven across the sinew resulting in relaxed regions. This may be due to the static loading environment which is not representative of the cyclic loading that native tissue undergoes. Variations in collagen organisation, an important factor in tensile load, was shown to be complex with initially deposited collagen detected via Raman spectroscopy but only detectable under SHG at later time points suggesting significant time may be required to allow the formation of organised collagen, a factor that will require

further investigation to determine.

- Imaging showed a large flaw in the formation of the BBLC as result of the contracting fibrin sinew interacting with the anchors. With cells and ECM in the front interface region diverting away from the anchor, providing a lower quantity of biological matter for the interface to be formed with. Additionally this will shelter the interface region from load making it unprepared for the application of tensile forces and susceptible to failure. Producing an interface region with minimal tissue volume/content and poor organisation for load bearing preventing the development of an interface similar to that seen in native tissues. This will require soft tissue looped around the anchor to achieve the maximum tensile load, which is clearly not plausible in an *in situ* graft. This weakness was highlighted by the preparation process for imaging finding pull-off from the front on the anchor was a common problem. Redesigned anchor shape or other forms of controlled guidance will be needed to encourage growth and alignment to produce the desired interface attachment region anatomy.

- An extension of the observed mineralisation to investigate the feasibility of producing a biomineralisation model/bone graft material through biomineralisation of deposited collagen in the BBLC by phospoylation or cellular deposition was unsuccessful. In sinews supplemented with phosphates a high level of debris was observed on the surface of the sample as a mixture of sphere like particles and long needle-like crystals with a high NaCl composition. Work performed with osteoblast rather than CTF cells showed poor construct formation and no internal cellular migration. However due to time constraints only a very limited quantity of basic investigative work was performed. Subsequent studies following on this by other workers have shown much higher success rates with alternate osteoblast cell lines.

- Consistency has been one of the major issues with this work, as mentioned in section 2.5. Large variations in the properties and development of sinews have been seen to

be caused by differences in the batch or age of a single material used. Variation is inevitable in biological samples. One of the most problematic components is FBS; which due to the nature of how it is collected is highly variable, with the content between batches very likely to effect metabolic activity [362, 363, 364]. Importantly FBS is either not permitted or strongly discouraged in the development of scaffolds for human implantation. So other more consistent and clinically acceptable serum options may be required.

- The use of multiple techniques allowed the fundamentals of a comprehensive understanding of the BBLC to be established. With optical microscopy, CRM and micro-CT showing the structure of the soft tissue from the cellular to gross structural level. Whilst CRM and micro-CT providing information on the composition and extension of mineralisation in the soft tissue. The differences in preparation, signal and image area for each technique leaves some gaps in the bigger picture. However the results from each method were in agreement where the signals provided mutual information. Future work with regards to imaging needs to focus on submicron and mechanical to determine the nano-level mineralisation that was not observable with the techniques used, and whether a mechanical gradient between the materials can be shown. As mentioned in the discussion section of previous chapters the methods used were often highly perpetuating, so less or non invasive methods such as further micro-CT and extension to MRI or ultrasound to provide structural information. However reduced instrument availability, and limitations in information and resolution would potentially limit their effectiveness.

- The failure to collect a complete time-series of the BBLC formation under any given modality leaves gaps in the knowledge for formation and uncertainties about the collected data and results. In addition to variations in the materials and biological behaviour, there was also limited access to some of the instruments used, preventing data being acquired thoroughly. However the general picture shown has provided

significant increases in the understanding of the biological and chemical behaviour of the BBLC and its components during the formation process.

The work presented here is only one line of investigation on the BBLC, with other workers investigating other areas such as the materials used and their biochemical effects. Significant further work remains to be performed to further optimisation the construct, and complete the elucidation of the mechanisms and biochemical changes that drive the contraction and maturation of the BBLC.

Appendices

.1 Appendix A: Published articles

Biotechnol Lett
DOI 10.1007/s10529-013-1374-4

REVIEW

Imaging the hard/soft tissue interface

Alistair Bannerman · Jennifer Z. Paxton · Liam M. Grover

Received: 12 March 2013 / Accepted: 25 September 2013

Abstract Interfaces between different tissues play an essential role in the biomechanics of native tissues and their recapitulation is now recognized as critical to function. As a consequence, imaging the hard/soft tissue interface has become increasingly important in the area of tissue engineering. Particularly as several biotechnology based products have made it onto the market or are close to human trials and an understanding of their function and development is essential. A range of imaging modalities have been developed that allow a wealth of information on the morphological and physical properties of samples to be obtained non-destructively in vivo or via destructive means. This review summarizes the use of a selection of imaging modalities on interfaces to date considering the strengths and weaknesses of each. We will also consider techniques which have not yet been utilized to their full potential or are likely to play a role in future work in the area.

Keywords Biomechanics · Enthesis · Interface · Imaging · Native tissues · Osteochondral junction · Osteotendinous junction

A. Bannerman · J. Z. Paxton · L. M. Grover (✉)
School of Chemical Engineering, University of Birmingham, Birmingham, UK
e-mail: l.m.grover@bham.ac.uk

A. Bannerman
e-mail: axb088@bham.ac.uk

J. Z. Paxton
e-mail: j.paxton@bham.ac.uk

Published online: 16 October 2013

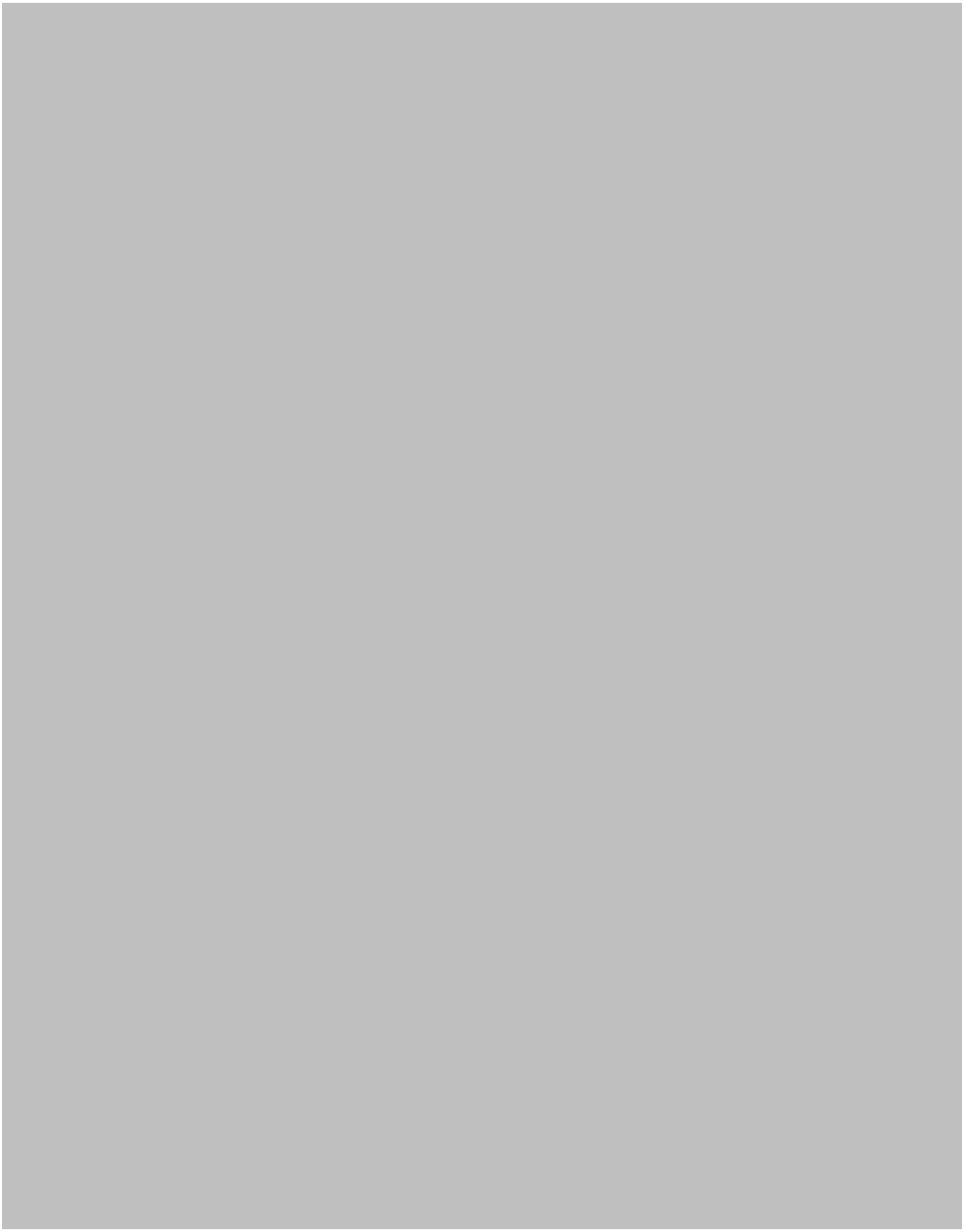

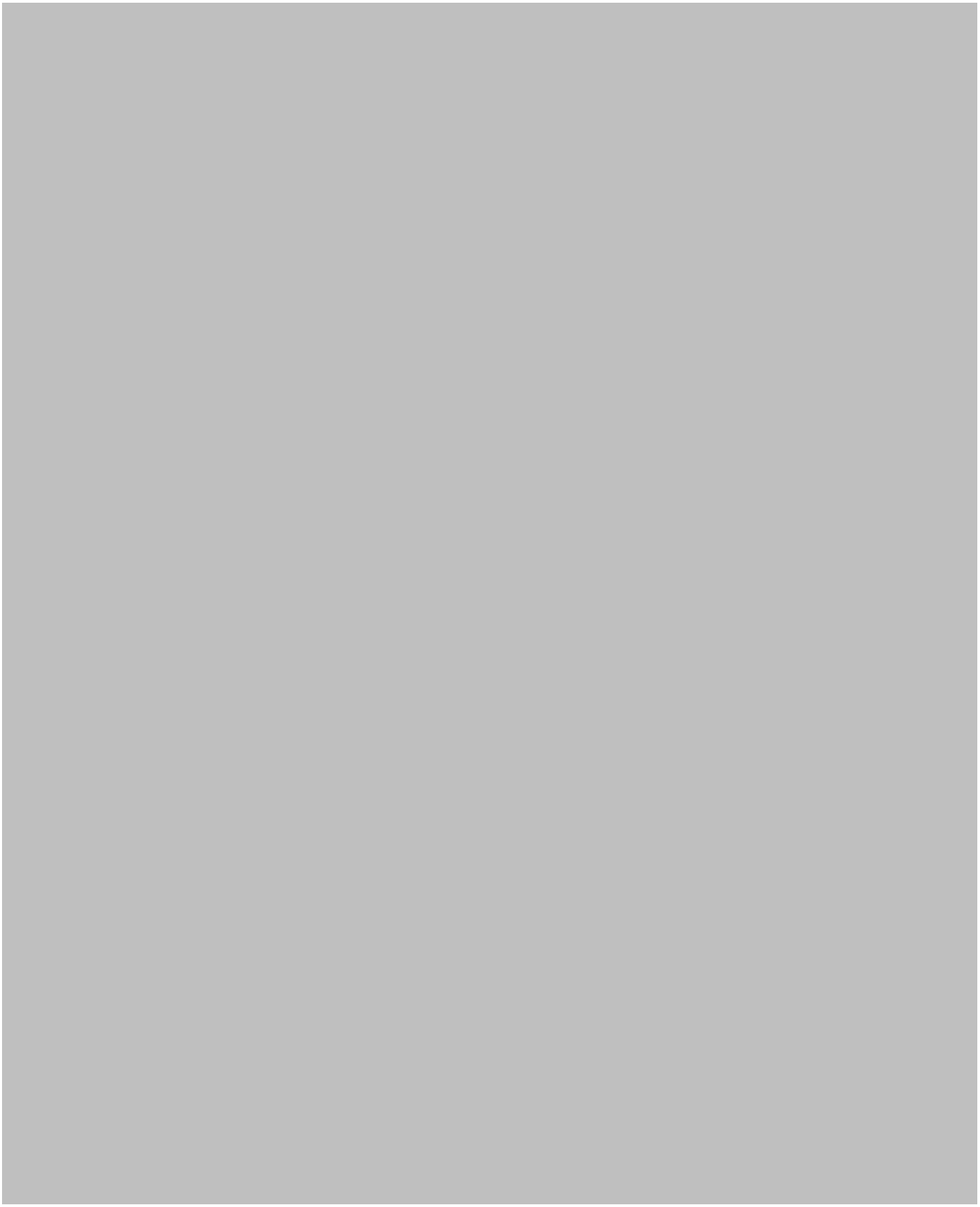

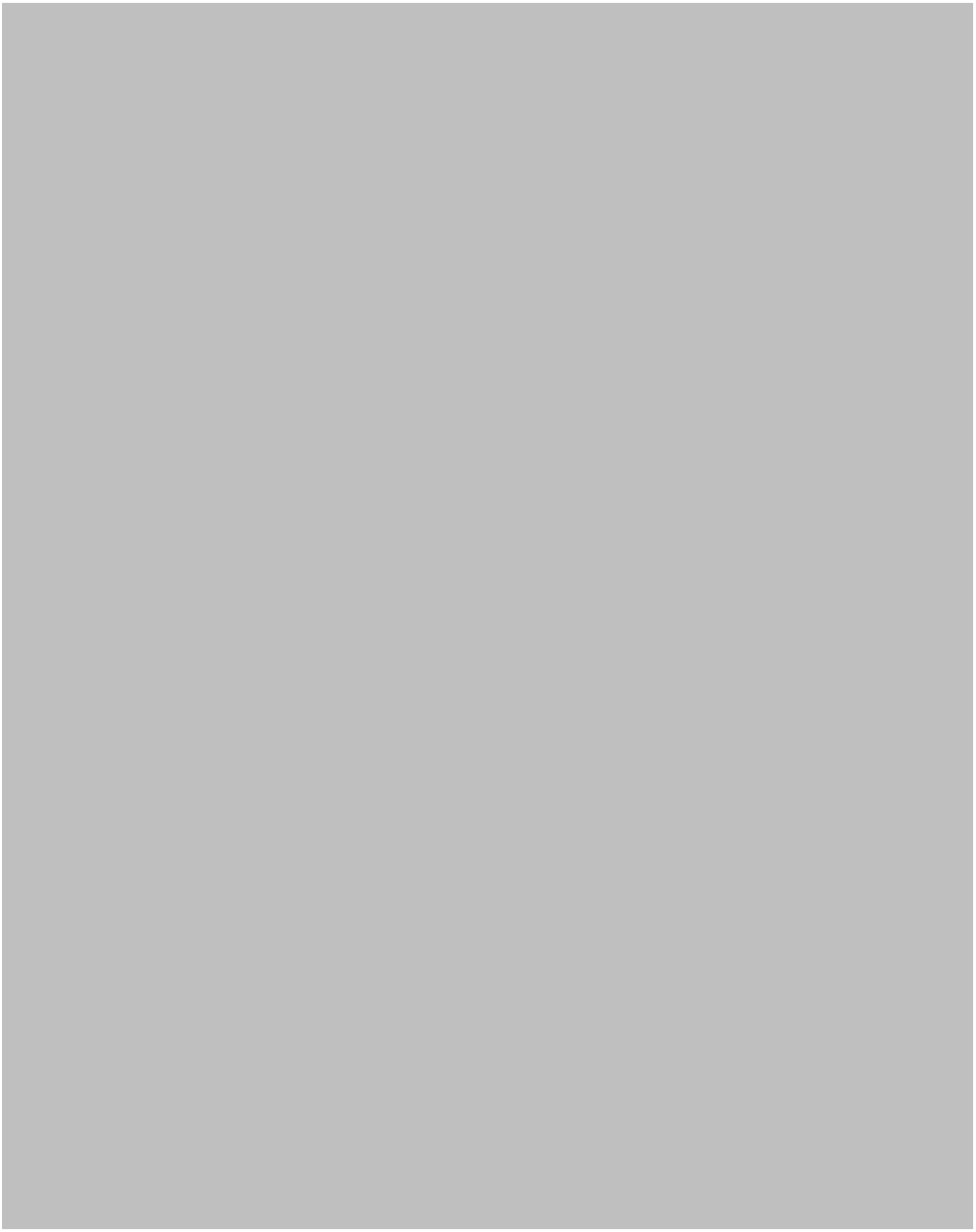

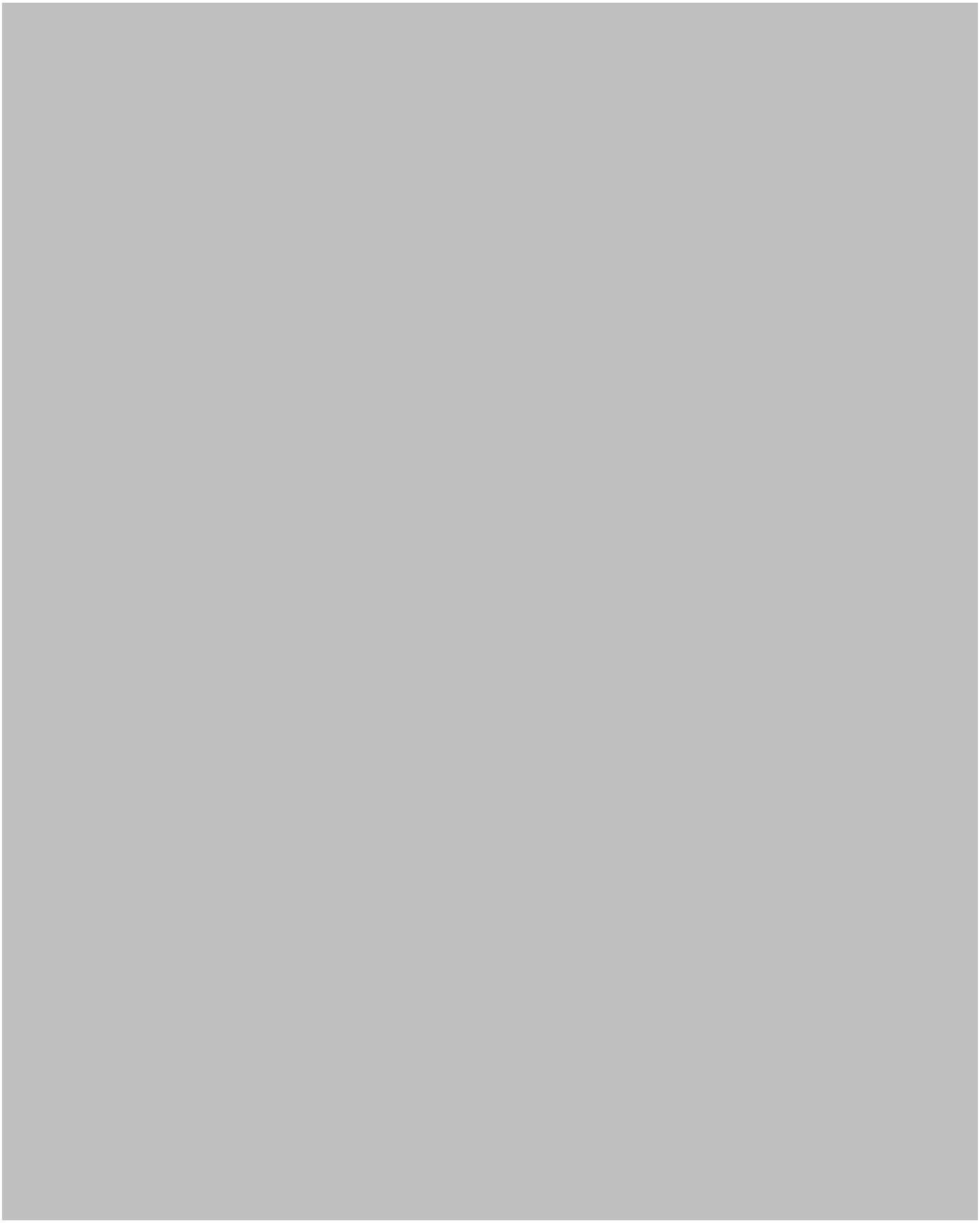

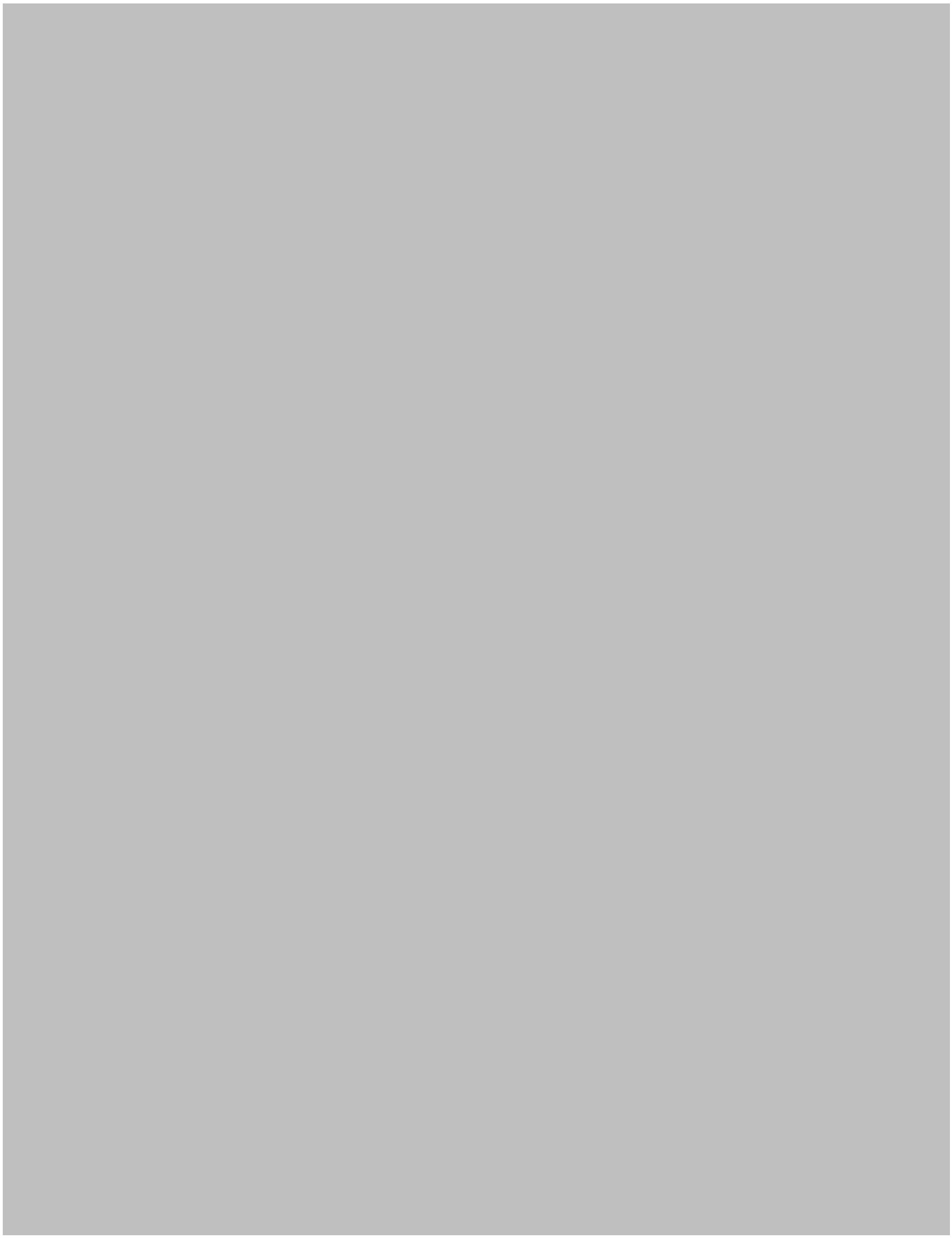

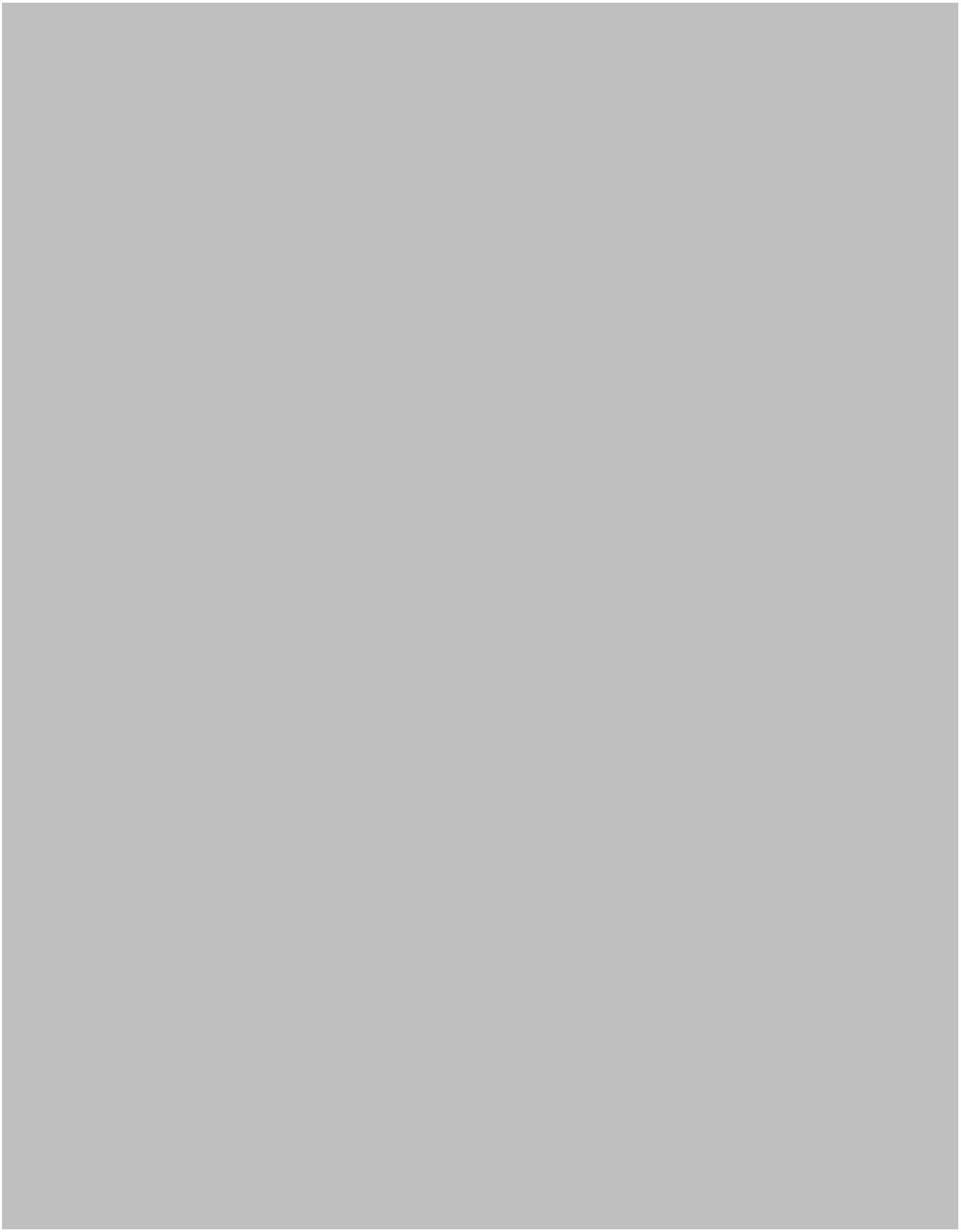

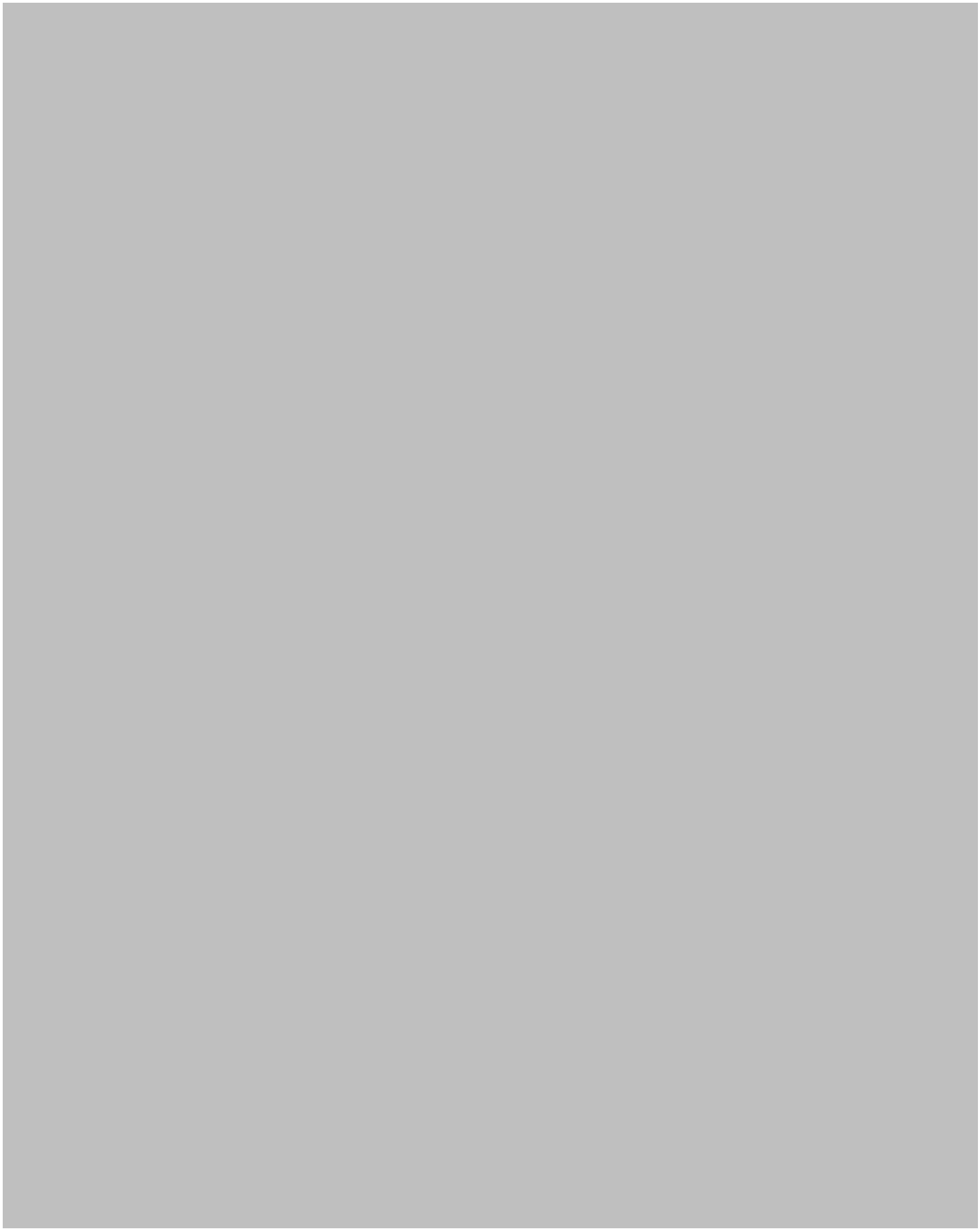

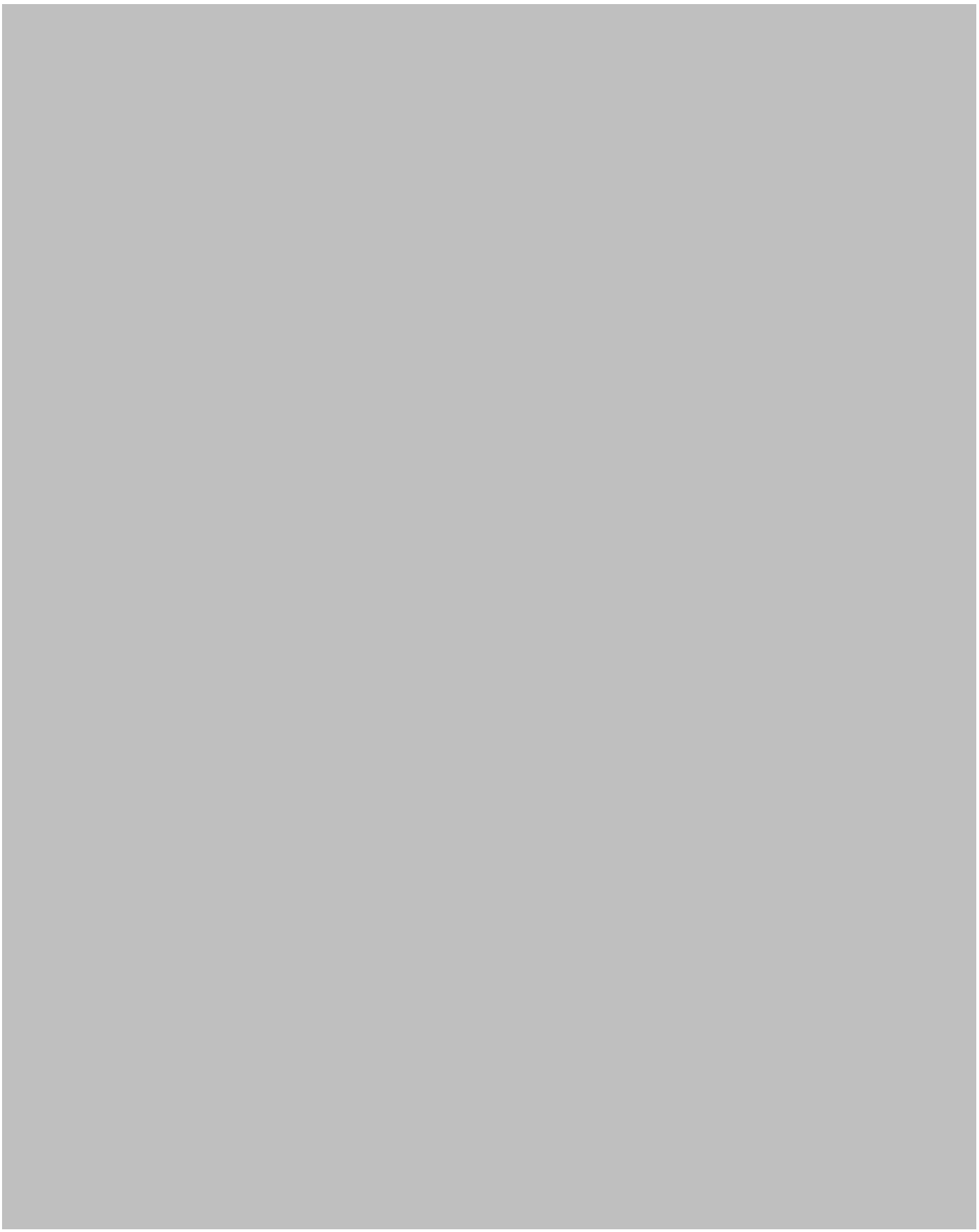

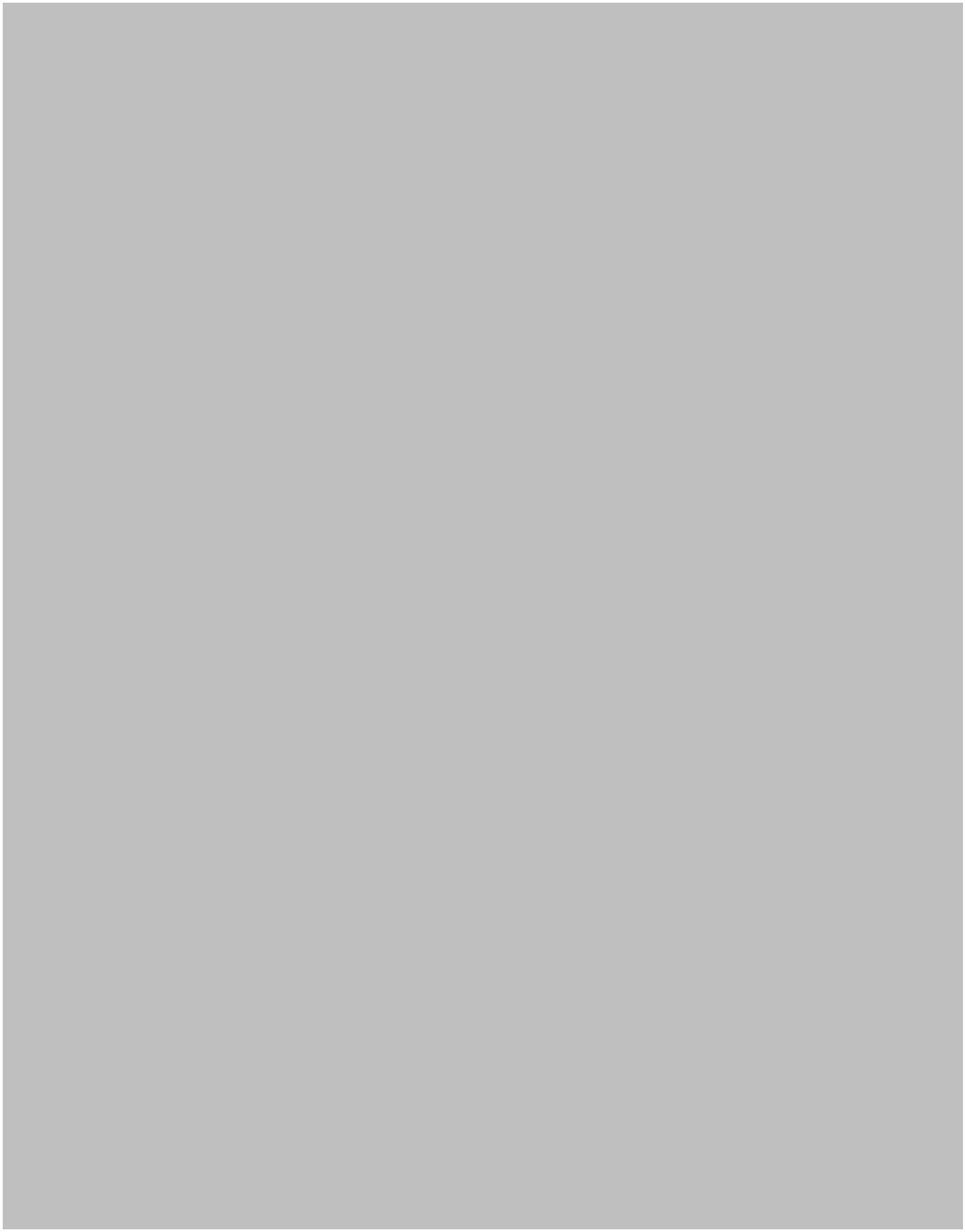

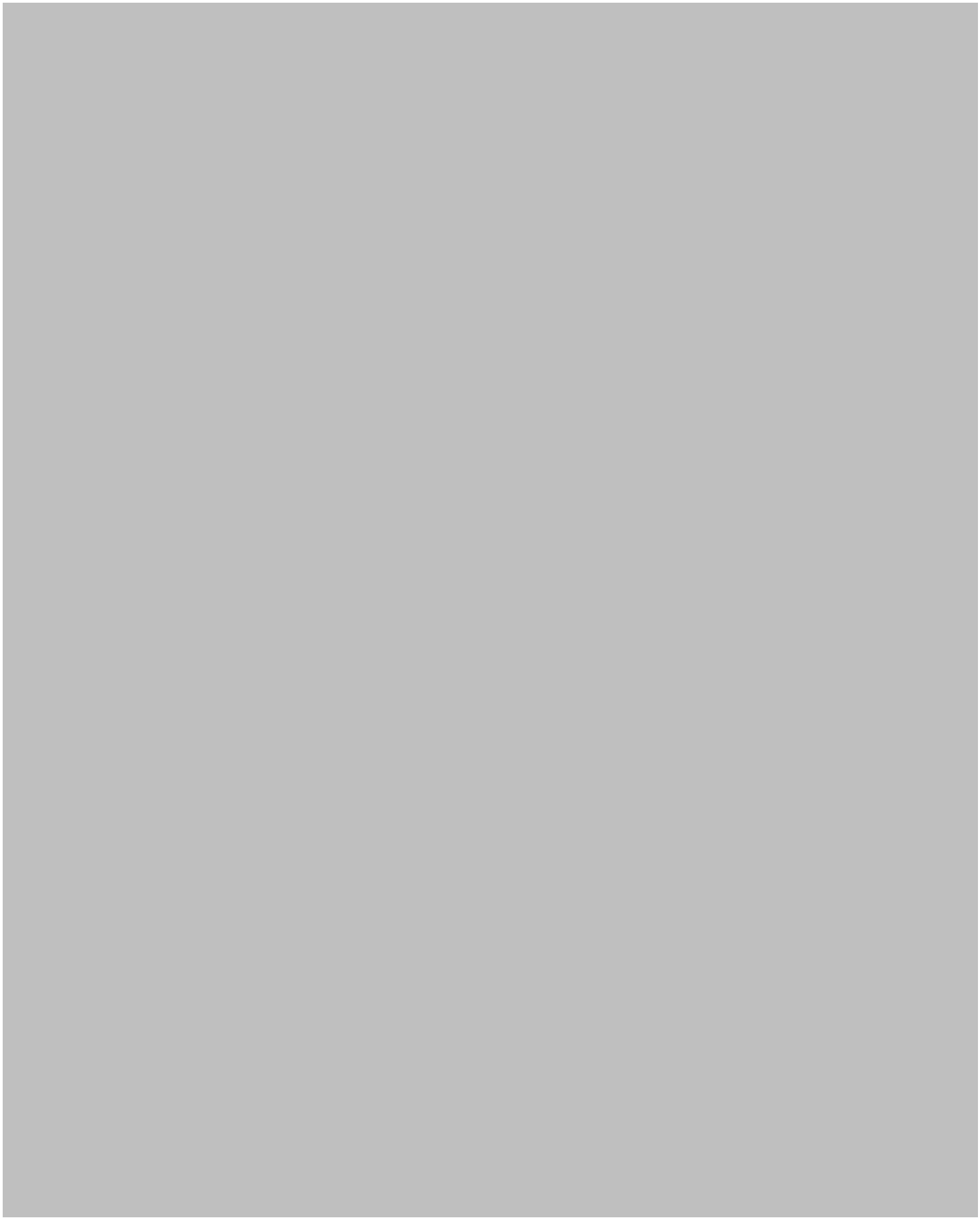

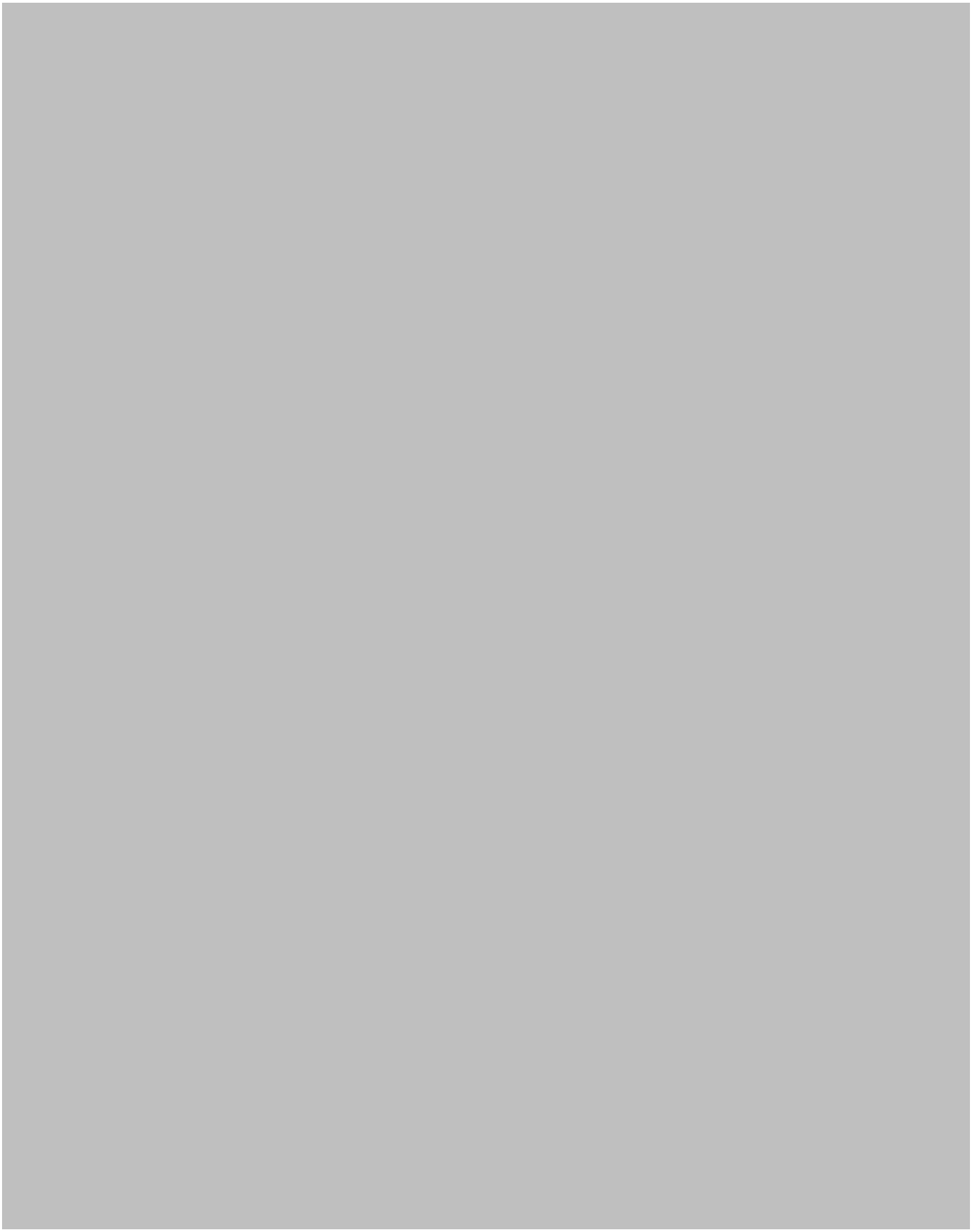

Volume 2 | Number 1 | January 2014 | Pages 1–140

Biomaterials Science

www.rsc.org/biomaterialsscience

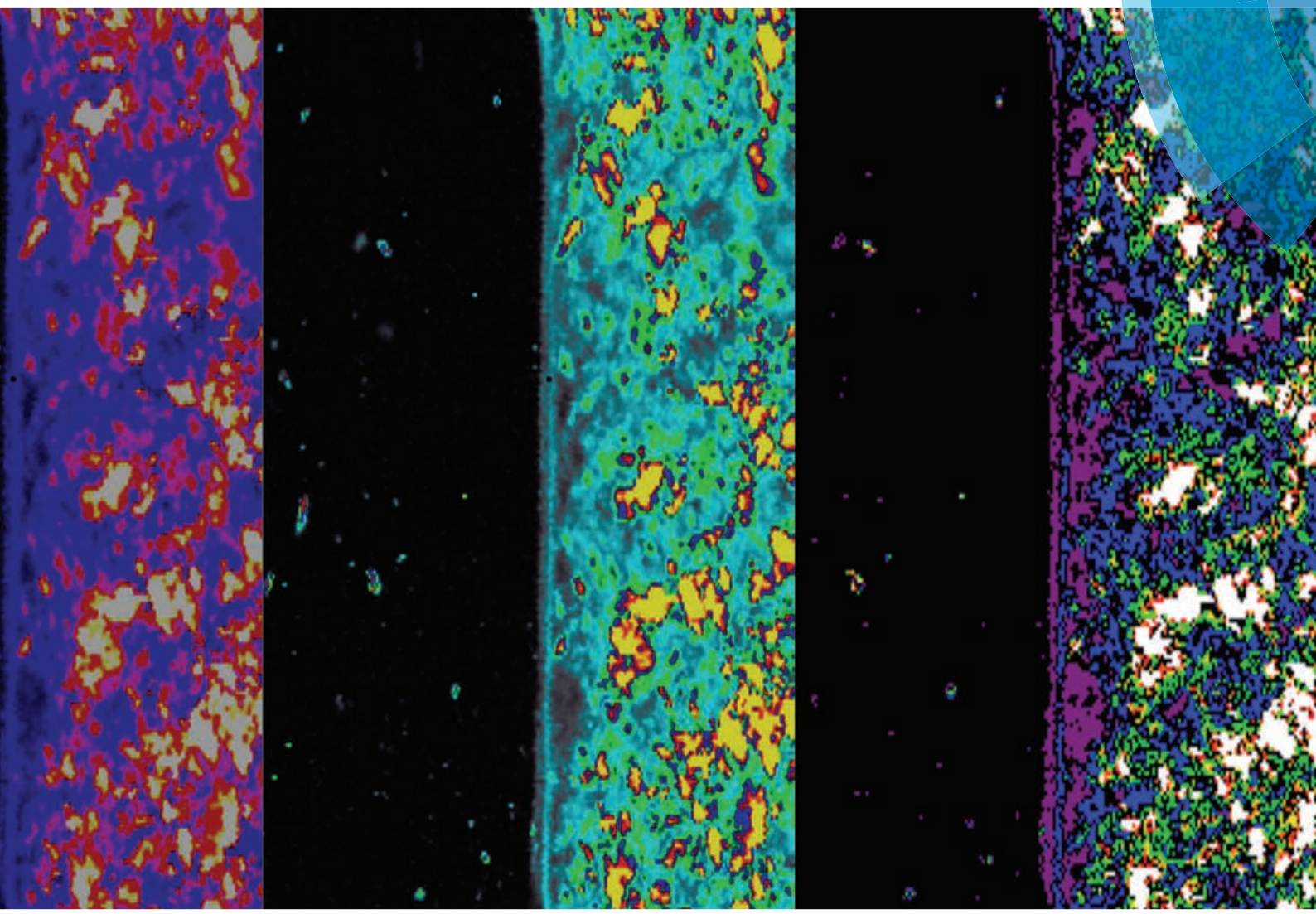

ISSN 2047-4830

ROYAL SOCIETY OF CHEMISTRY

PAPER

Jennifer Z. Paxton *et al.*

A novel method for monitoring mineralisation in hydrogels at the engineered hard–soft tissue interface

iCeMS KYOTO UNIVERSITY WPI Research Center

Biomaterials Science

PAPER

A novel method for monitoring mineralisation in hydrogels at the engineered hard–soft tissue interface†

Cite this: *Biomater. Sci.*, 2014, **2**, 41

Susanne Koburger,[a,b] Alistair Bannerman,[a,c] Liam M. Grover,[a] Frank A. Müller,[b] James Bowen[a] and Jennifer Z. Paxton*[a]

Received 22nd April 2013,
Accepted 17th September 2013

DOI: 10.1039/c3bm60102a

www.rsc.org/biomaterialsscience

The capacity to study the deposition of mineral within a hydrogel structure is of significant interest to a range of therapies that seek to replace the hard tissues and the hard–soft tissue interface. Here, a method is presented that utilises Confocal Raman microscopy as a tool for monitoring mineralisation within hydrogels. Synthetic hard–soft material interfaces were fabricated by apposing brushite (a sparingly soluble calcium phosphate) and biopolymer gel monoliths. The resulting structures were matured over a period of 28 days in phosphate buffered saline. Confocal Raman microscopy of the interfacial region showed the appearance of calcium phosphate salt deposits away from the original interface within the biopolymeric structures. Furthermore, the appearance of octacalcium phosphate and carbonated hydroxyapatite was observed in the region of the brushite cement opposing the biopolymer gel. This study describes not only a method for analysing these composite structures, but also suggests a method for recapitulating the graduated tissue structures that are often found *in vivo*.

Introduction

Interfacial tissue engineering aims to regenerate the intricate structure of musculoskeletal interfaces.[1] These interfaces possess complex matrix heterogeneity[2] and their specific arrangement has evolved to assist force transmission through tissues with very different mechanical properties. For example, at the junction between the soft tissue sinews tendon/ligament and bone (the osteotendinous junction), the interface is comprised of four interconnected regions, namely the tendon/ligament proper, unmineralised fibrocartilage, mineralised fibrocartilage and bone.[3–5] Similarly, the junction between bone and cartilage (the osteochondral junction) has a multiphasic structure, with 5 different regions; bone, mineralised cartilage, and deep, middle and superficial layers of cartilage.[6,7] In both tissue transitions, the gradient of mineralisation, along with changes in cell type, matrix composition and collagen fibre alignment, affects the mechanical properties across the soft to hard tissue transition.[6–8] In fact, a study on the ligament to bone interface identified that mineralisation was a key regulator in determining the compressive modulus of the tissue across the soft to hard tissue junction[9] and therefore demonstrates an important structure–function relationship at the attachment points of dissimilar tissues.

There are several different approaches to engineering graded tissue transitions *in vitro*. Some groups have focussed on the manufacture of bi- or multiphasic plugs, by layering different materials and cell types together and designed to be implanted with native tissue at the bone-tendon[10–12] or bone-cartilage[7,13–17] interfaces. A vast array of both natural and synthetic materials have been utilised to mimic the hard and soft tissue regions (for reviews see ref. 7 and 8) but these typically involve the use of a form of calcium phosphate for the bone region and a hydrogel for the soft tissue region. Two commercial osteochondral scaffolds are available; TruFit® Bone Graft Substitute (BGS) resorbable porous plugs (Smith & Nephew) and Osseofit® (Kensey Nash).[18] Both these biphasic plugs are bioresorbable and have a bone and cartilage-mimicking region. The TruFit® BGS has a chondral region manufactured from polyglycolic acid and a bone region consisting of porous poly-D,L-lactide-*co*-glycolide (PGLA) and calcium sulphate whereas the Osseofit® consists of a type I collagen chondral region and a porous tricalcium phosphate–polylactic acid mix underneath.[18] Despite their use in the repair of damaged cartilage, it is unknown whether mineral deposition across the

[a]*School of Chemical Engineering, University of Birmingham, Edgbaston, Birmingham B15 2TT, UK. E-mail: jzpaxton.research@gmail.com*
[b]*Institute of Materials Science and Technology (IMT), Friedrich-Schiller-University of Jena, Löbdergraben 32, D-07743 Jena, Germany*
[c]*Centre for Physical Sciences of Imaging in the Biomedical Sciences (PSIBS), School of Chemistry, University of Birmingham, Edgbaston, Birmingham B15 2TT, UK*
†Electronic supplementary information (ESI) available. See DOI: 10.1039/c3bm60102a

bone-cartilage region occurs in a graded fashion. In the case of osteotendinous junction regeneration, rather than the manufacture of an isolated plug, others have utilised cellular co-culture to create whole tissue constructs with an intact interfacial region.[19,20] Similar to this approach, we have reported the creation of a whole bone-ligament-bone construct from a cell-seeded hydrogel and artificial bone blocks manufactured from a bioresorbable calcium phosphate cement.[21–23] While an intact interface can be produced *in vitro*,[21,22] the processes governing interface formation in the system are not well understood.

Although the importance of recapitulating the hard–soft tissue interface is widely recognised and a number of the above implants have found clinical application, little is currently known of how these materials are structured on a nanoscopic level and how this structuring changes with time. The principal reason for this is that imaging material interfaces in composites formed from hard materials and soft hydrated materials is challenging. The difficulty encountered in imaging is as a result of the different approaches taken to histologically process mineralised and non-mineralised tissues – the former usually requiring dehydration and the latter demineralisation. Clearly, these processing steps result in disruption of the apposing phase. This is particularly challenging when the mineral component formed within the gel is nanoscopic in nature.

Several methods have been used to visualise mineralisation in hydrogel scaffolds, with many recent studies reporting the use of techniques such as Fourier Transform Infrared spectroscopy (FTIR),[24–26] scanning electron microscopy (SEM),[24–28] Energy-dispersive X-ray spectroscopy (EDS),[25–27] high resolution spectral ultrasound imaging (SUSI)[29] and the staining technique of von Kossa.[25–27,29,30] These studies have enhanced our understanding the structure of interfaces, however, each method requires a special means of characterisation or is more sensitive to one or other of the phases, meaning that the information on the whole structure is difficult to determine.

Confocal Raman microscopy (CRM) is a technique that provides information about the vibrational properties of chemical bonds within a sample, and therefore allows the presence of a certain molecular bond to be ascertained. CRM has several advantages over the techniques describes above, such as the ability to observe both hard and soft structures easily. Furthermore, since CRM does not require the fixation or staining of samples, preparation time and complications arising from processing are reduced. Raman microscopy has been used previously to identify deterioration in the quality of native bone, by studying the ratio of the phosphate peaks (PO_4^{3-}) to matrix protein peaks,[31–33] and to quantify mineralisation across the native bone–tendon interface[34,35] but, to our knowledge, has not been used to identify and/or quantify mineralisation within hydrogel scaffolds.

The aim of this study was to develop a method using CRM that enabled us to determine the chemical and physical nature of the interface between a sparingly soluble calcium phosphate cement and a biopolymeric gel. In addition to providing visual information, this method will enable us to quantify mineralisation and to identify the phase changes occurring within the structures during *in vitro* maturation.

Experimental

Production of the hard–soft material interface composite

Two natural polymers were chosen to represent the soft portion of the composite construct, alginate and gellan. A 4% (w/w) alginate solution (Alginic acid, sodium salt, Sigma-Aldrich, UK) and a 1% (w/w) gellan solution (Gelrite® Gellan Gum, Sigma-Aldrich, UK) were prepared by dissolving the respective powders in double distilled water by stirring for at least 1 h at >85 °C. Both alginate and gellan solutions were sterilised using an autoclave and stored at room temperature before use. Brushite ($CaHPO_4{\cdot}2H_2O$) cement was chosen for the hard portion of the composite. The preparation procedure used for the manufacture of moulds and cement samples is schematically displayed in Fig. 1A (parts 1–3). For the cement mould preparation, PVC tube rings of 5 mm in height were

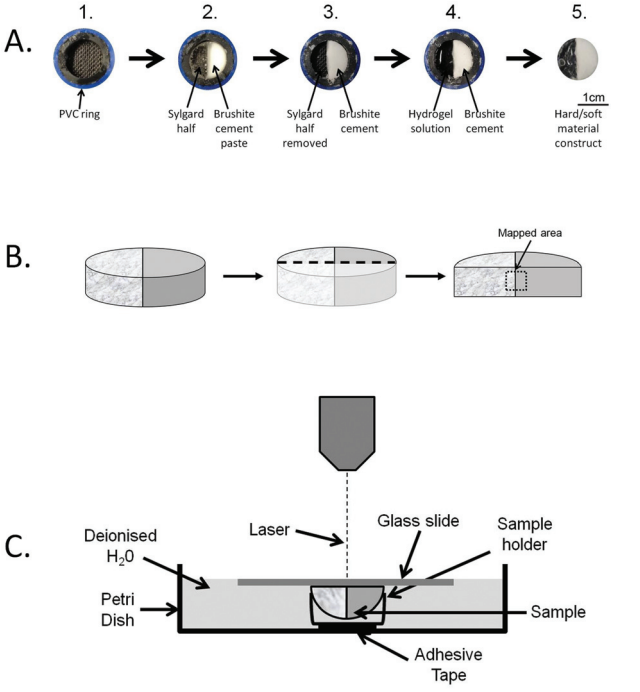

Fig. 1 Construct manufacture and experimental set up for the CRM. (A) Hard soft material constructs were manufactured in several stages. First, a PVC ring was used as mould (1) in which a Sylgard semi-cylinder was placed followed by filling the void with brushite cement paste (2). Once the cement had hardened, the Sylgard piece was removed (3) and hydrogel solution (gellan or alginate) was added (4). Once cross-linked, the hard–soft tissue constructs were removed from the PVC ring (5). (B) Constructs were sliced perpendicular to the hard–soft tissue interface to expose an area suitable for mapping. (C) The cut construct was placed in a sample holder, fixed to the bottom of a Petri dish. The Petri dish was filled with deionised water to allow the visualisation of the construct in a hydrated state.

placed into a polystyrene (PS) 24-well plate (diameter 1.6 cm), prior to filling with a Sylgard silicone polymer (Sylgard 184, Dow Corning, US). After polymerisation for four days at 60 °C, the Sylgard layer was halved along its long-axis and one half was removed from the tube ring, leaving a gap to be replaced by the brushite cement. The brushite cement was made by mixing β-tricalcium phosphate (β-TCP) with H_3PO_4. The β-TCP was manufactured by reactive sintering of a powder containing $CaHPO_4$ (Mallinckdrodt-Baker, Germany) and $CaCO_3$ (Merck, Germany) with a theoretical calcium to phosphate molar ratio of 1.5. The powder mixture was suspended in absolute ethanol and mixed for 12 h. The suspension was then filtered and the resulting cake heated in an alumina crucible to 1400 °C for 12 h and 1000 °C for 6 h prior to quenching in a dessicator in ambient conditions. The resulting sinter cake was then crushed using a pestle and mortar and was passed through a 125 μm sieve. Then, the brushite cement halves were fabricated by combining β-TCP with 3.5 M H_3PO_4 (with 200 mM citric acid + 200 mM sodium pyrophosphate) at a powder to liquid ratio of 1.75 g mL^{-1} and the resulting cement slurry was cast into the mould before setting occurred (Fig. 1A, part 3). The brushite cement samples were then dried for four days at 37 °C and subsequently sterilised by immersion in 70% ethanol for 20 min, followed by UV radiation overnight. The resulting composite samples containing an interface between brushite cement and alginate/gellan hydrogel were prepared in a sterile environment in a laminar flow hood. Furthermore, all of the solutions used were sterilised prior to composite preparation by either immersion in 70% ethanol, UV irradiation overnight or filtration through a 0.22 μm filter to prevent fungal and bacteria growth. Preparation of the composite samples was carried out in 24-well plates. PVC tube rings were placed into the wells and the brushite disc halves were added to the moulds leaving the remaining half to be filled with the hydrogel (Fig. 1, part 3). For the alginate/brushite samples, 250 μL of the 4 wt% alginate solution were pipetted next to the cement and covered with a sterile filter paper. Afterwards, the filter paper was covered with 0.1 M $CaCl_2$ solution. The alginate was left to crosslink for 2 h, followed by rinsing the alginate/cement sample with sterile deionised water and placing it into a new PS well plate. In case of the gellan/brushite samples, the gellan gum solution was heated to <85 °C, prior to combining 1 mL of the solution with 50 μL of sterile 0.1 M $CaCl_2$ solution. 250 μL of the solution was pipetted into the mould next to a brushite cement half, before being transferred to a sterile 24-well plate. Once prepared, the hard–soft material composites were covered with 1 mL of sterile PBS (Sigma-Aldrich, UK). Two different protocols were employed, either the static protocol, where the PBS was not exchanged or the dynamic protocol, where the PBS was exchanged every 2–3 days throughout the duration of the experiment. The samples were kept under high humidity at 37 °C for a total of 28 days.

Sample preparation

Prior to analysis, the samples were rinsed with double distilled water and cut vertically (perpendicular to the phase interface) using a scalpel. Then, one half was mounted on a sample holder and frozen in a cryostat chamber (Starlet 2212, Bright, UK) with cryospray to −52 °C (Cryospray 134, Bright, UK). After this, the sample was cut at using a cryotome −25 °C to create a flat surface suitable for CRM observation (Fig. 1B). In order to avoid shrinkage of the gel during the CRM mapping, the sample was immersed in deionised water throughout the CRM analysis. The assembly of the immersed sample is shown in Fig. 1C. To hold the sample in place, it was positioned in a microcentrifuge tube lid, which was fixed to the Petri dish using adhesive tape. The lid containing the sample was covered with a glass slide, allowing the laser beam to be focussed on the immersed sample surface. Utilisation of this technique allowed for the simultaneous visualisation of a hydrated hard–soft material sample, more representative of the hydrogels used for cell culture in tissue engineering applications.

Characterisation

Confocal Raman microscopy. Raman spectra acquisition and mapping was performed using a confocal Raman microscope (alpha 300R, Witec Germany) with a 785 nm laser and 20× objective lens. For the single spectrum of brushite as displayed in Fig. 2B, the brushite cement was crushed using a pestle and mortar, before acquiring the spectra with an

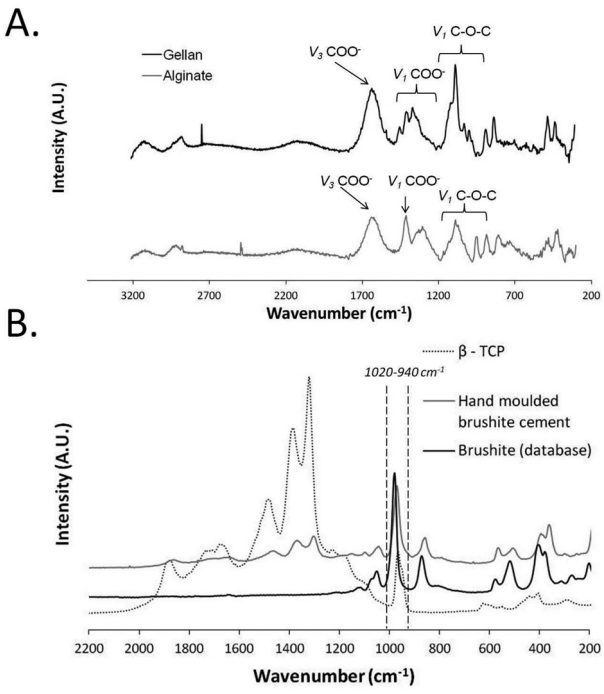

Fig. 2 Raman spectra for the individual components of the hard–soft material construct (A) Raman spectra for the cross-linked soft materials, gellan and alginate. (B) Raman spectra for the hard material, brushite cement, in comparison to pure β-tricalcium phosphate (β-TCP) and brushite. Note that the hand moulded brushite cement contains peaks assigned to both pure brushite and β-TCP. Note that the range 940–1040 cm^{-1} has been identified as this marks the peak range used to collect data for following figures.

integration time of 0.2 s and 500 accumulations. For a comparison, reference spectra from pure samples of β-TCP and brushite (Fig. 2B), (Merck, Germany) were recorded. In case of the gels, the respective hydrogel was cross-linked as described earlier and dried at 37 °C for 2 h. The single spectrum was gained using an integration time of 0.8 s and 500 accumulations and a background subtraction with a 9th order polynomial function was applied (Fig. 2A).

For the hard–soft material composite samples, image mapping was performed over 500 μm × 1000 μm/1200 μm × 1470 μm (width height) areas about the interface using 92/221 data points along each horizontal line and 184/271 lines with an integration time of 0.53 s/0.23 s at each data point. After each mapping processing was performed (Witec Project 2.02, Witec Germany) a sum integration was performed over the peaks of interest (115–200 cm^{-1} autofluorescence, 940–1020 cm^{-1} orthophosphate group) to produce heat map images. Count line scans over the interface for the orthophosphate group and whole spectra at various points along cross section were collected and normalised to their maximum peak and plotted in Microsoft Excel.

Quantification of mineralisation. In order to quantify the number and size of precipitates observed in the soft material portion of the composite constructs, quantification of the Raman mapping was performed using MATLAB (MATLAB 2011a, Mathworks, USA) on images exported from the Witec Project software. The original image maps were thresholded to determine the boundary line between the hard and soft portions of the image. Based on this, mineralised particles in the soft material were detected and labelled and data on the number and size of the mineralised particles were extracted.

Environmental scanning electron microscopy (ESEM) and energy dispersive X-ray (EDX). In order to further evaluate the morphology of the interface between the hard and soft materials, Environmental Scanning Electron Microscopy (ESEM) was used (Philips-FEI, XL30 ESEM-FEG/EDAX, The Netherlands). In addition, EDX analysis was used to provide information about the elemental concentrations of the samples. The composite samples were prepared as described for CRM and sputter coated with platinum prior to visualisation in cryo-ESEM mode.

Interferometry. To obtain information about changes in topography of the brushite interface, roughness measurements were conducted using an interferometer (MicroXAM2, Omniscan, UK), equipped with a 10× objective and a white light source. After ageing the interface samples for 21 days using either the static or dynamic protocol, the hydrogel was removed from the brushite and the latter was subsequently dried at 37 °C for 5 days. Prior to the interferometry analysis, the brushite surface which had been exposed to the gel was gold coated using a sputter coater. For each condition, two samples were scanned across their surfaces at 48 sequence positions across a total area of 3.85 mm^2. Images were acquired and analysed using Scanning Probe Image Processor software (Image Metrology, Denmark) to generate S_a, S_q and S_z values for surface roughness.

Helium pycnometry. To assess cement degradation, brushite samples were prepared as described earlier (Fig. 1, stages 1–3). The samples were kept at 37 °C and high humidity under sterile conditions throughout the experiment. After 14 and 28 days, 3 samples of each group (static *vs.* dynamic), were removed from the moulds, rinsed with deionised water and dried at 105 °C for 4 days. Helium Pycnometry was used to determine the true density of the brushite cement (Micromeritics AccuPyc 1340 Gas Pycnometer, Micromeritics Instrument Corporation, USA). The samples were freeze dried overnight prior to the analysis which was performed with 10 initial helium purges, followed by 10 measurements per sample. For each sample group, 3 samples were analysed, making the resulting value a mean of 30 measurements. The true density was yielded by calculating the ratio of the sample mass and the measured true volume, and was then used to calculate porosity of each sample using eqn (1) whereby V_{true} is the sample volume measured by helium infiltration and V_{app} is the volume calculated from geometrical dimensions of the halved cement cylinders.

$$\text{Porosity} = \frac{V_{app} - V_{true}}{V_{true}} \times 100 \quad (1)$$

Statistical analysis

Where appropriate, results are presented as mean ± SEM. Mean values were compared using ANOVA followed by Tukey HSD test using Brightstat.[36] The significance level was set at 0.05.

Results and discussion

Raman spectra of individual components

Prior to investigation of the hard–soft interface composite samples, the individual components of the composites were analysed using CRM to identify their chemical composition (Fig. 2). The Raman spectra of the soft components (Fig. 2A) and hard components (Fig. 2B) show characteristic peaks for each individual material as previously reported in the literature.[37,38] For the alginate hydrogel, the asymmetric stretching of the COO– group (ν_3) appears around 1614 cm^{-1}, while the symmetrical stretching of this side group (ν_1) is present at 1414 cm^{-1}. Also, C–O–C stretching modes (ν_1) are seen at wavenumbers around 1290 cm^{-1} and 820–1140 cm^{-1}. In case of gellan, the asymmetrical COO– stretching mode (ν_3) is located at 1616 cm^{-1} and the symmetrical carboxyl group stretching (ν_1) at 1330–1430 cm^{-1}. In addition, the peaks at around 820–1140 cm^{-1} are caused by the symmetrical stretching of the C–O–C bonds (ν_1) (Fig. 2A). Fig. 2B displays the Raman spectrum acquired for brushite cement in comparison to brushite and β-TCP reference spectra. The strongest brushite peak around 985 cm^{-1} (due to P–O stretching of the PO_4^{3-}-ion) is present in all three displayed spectra. The shoulder peak at 891 cm^{-1} represents the HPO_4^{2-}-ions in the hydrated sample and appears in both β-TCP and brushite cement. Also, weak

shoulder peaks around 1079–1166 cm^{-1} (ν_1, ν_2 and ν_3 P–O modes) are present in these both materials. O–H stretching modes around 388 cm^{-1} and P–O bending of the PO_4^{3-} ion at 413 and 549 cm^{-1} are present in all the three spectra. Despite these similarities, the peaks around 1318–1376 cm^{-1} are only characteristic for β-TCP but not for pure brushite and could be assigned to P═O stretching, sometimes appearing as a doublet around the 1150–1350 cm^{-1} region.[38] The presence of these characteristic β-TCP peaks in the brushite cement reveal the presence of β-TCP in the prepared brushite cement samples. Indeed, brushite cements formed using this stoichiometry of reactants have previously been shown to consist of around 66 wt% β-TCP.[39]

Investigation of the hard–soft material interface

The intensity of the P–O peak was mapped across the hard–soft material interface on day 0 and day 28 in samples manufactured from gellan hydrogels (Fig. 3). At day 0, a clear demarcation was observed between the hydrogel and the cement portions of the construct, with no obvious areas of intensity in the hydrogel portion (Fig. 3A). Multiple line-scans measuring the intensity of the P–O peaks were plotted perpendicular to the material interface and demonstrated a lack of intensity up until approximately 250 μm across the interface where, as expected, intensity increases at the brushite cement. Conversely, after static ageing in PBS for 28 days, intense areas of P–O can be observed in the soft portion of the construct (Fig. 3B). These areas of increased intensity can also been seen in the line scans taken at several points across the interface, indicating that phosphate deposition is occurring within the soft material portion of the composite.

In order to identify changes in chemical composition across the hard–soft material composite, individual Raman spectra were collected at designated points across the sample surface in both alginate (ESI Fig. 1A–C†) and gellan composites (ESI Fig. 1D–E†). As expected in un-aged samples, Point 1 shows the typical spectrum obtained for brushite cement, consisting of a single peak around 980 cm^{-1}, indicative of brushite and peaks around 1200–1500 cm^{-1}, indicative of β-TCP as described previously (Fig. 2B). Spectra obtained from further across the interface (points 2–3) contained phosphate peaks around 940 cm^{-1}, however points 4–6 show no appreciable peaks pertaining to the vibrational modes of any phosphate groups. After ageing for 28 days with the static or dynamic protocol (ESI Fig. 1B, C, E, F†), points 1 and 2 on the cement portion of the construct display peaks around 980 cm^{-1} and 1200–1500 cm^{-1} as seen previously. In general, these peaks disappear as the points of interest go across the interface into

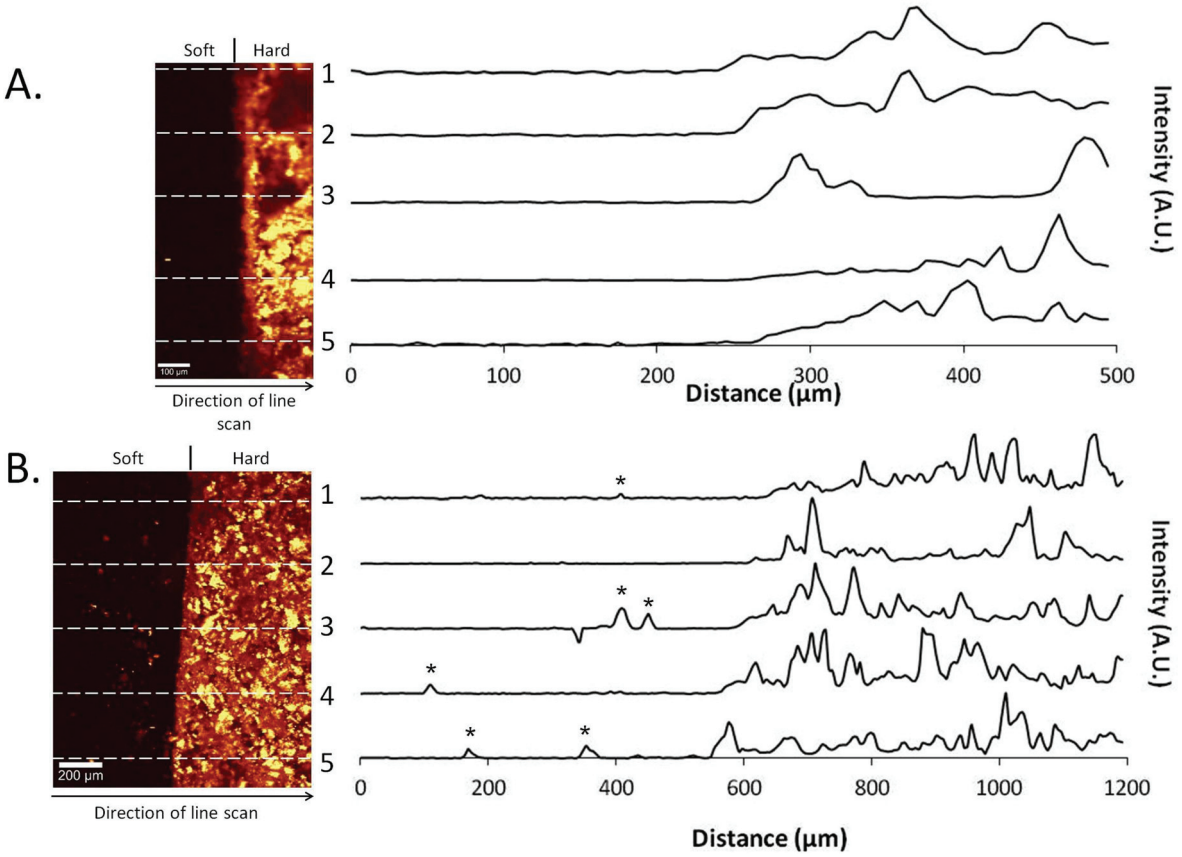

Fig. 3 Intensity-map images and corresponding line-scans of the hard–soft material interface indicating the presence of P–O peaks. (A) Gellan Day 0. Little evidence of P–O in the gellan portion of the image. This is supported by the line scans across the interface. (B) Gellan day 28, static ageing protocol. Areas of increased intensity are seen in the gellan portion of the composite and demonstrated in the line scans across the interface (*).

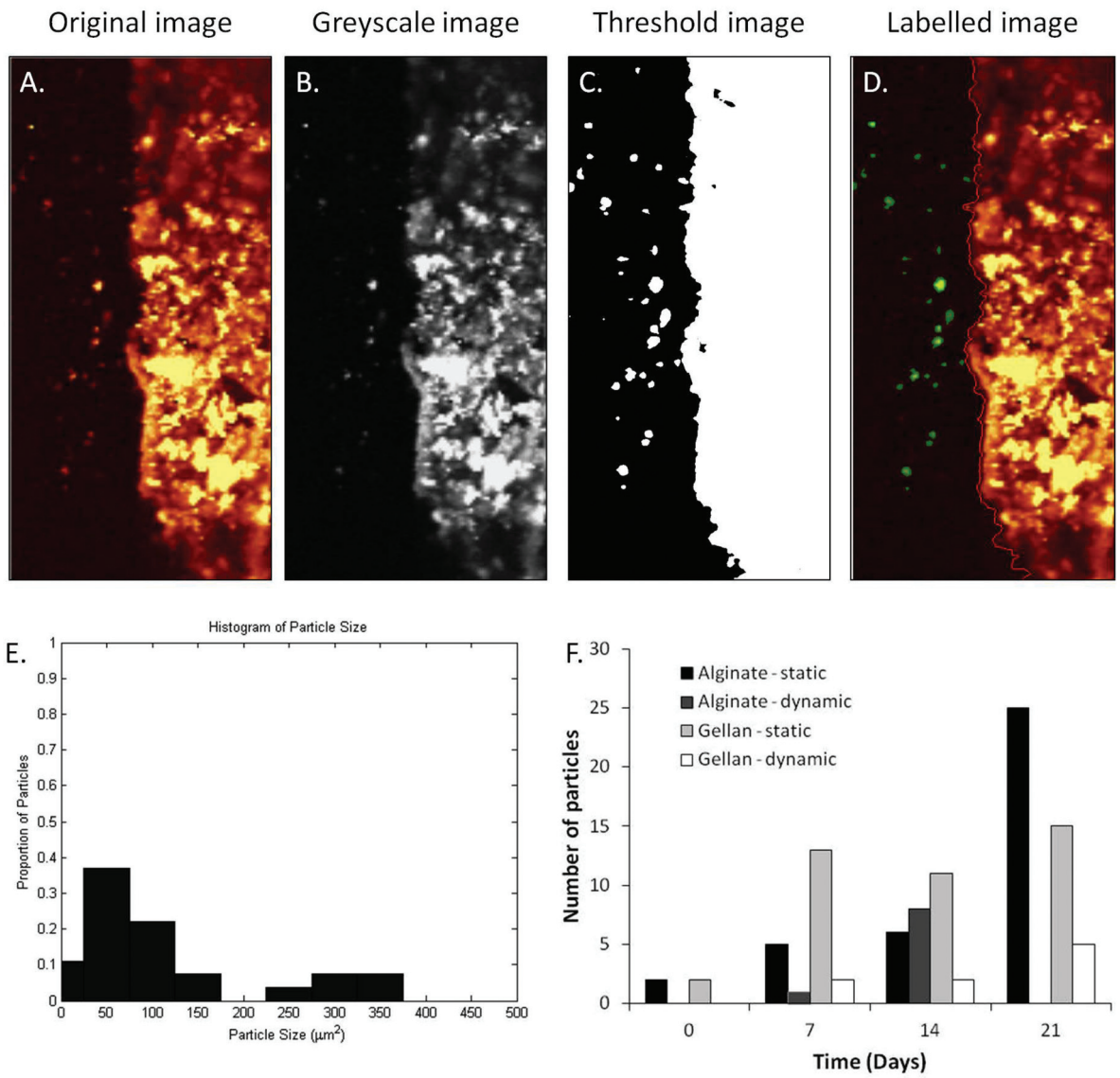

Fig. 4 Demonstration of quantification of mineralisation in the soft material portion of the composite construct. (A) Original image of alginate, day 21 aged in static conditions. The image was greyscaled (B) and then thresholded to obtain the boundary layer between the hard and soft portions of the composite (C). The detected particles in the soft portion were then labelled (D). (E) Histogram determining the range of particle sizes in the soft material portion shown in A–D. (E) Quantification of all samples over the period 0–21 days.

the soft material but reappear in points 6 and 7, at discrete areas in the body of the soft material portion of the construct. This confirms the presence of phosphate within the soft material that was not seen in the un-aged sample. To quantify the presence of mineral within the soft material portion of the composites, each Raman mapping was analysed to provide details on the number and size of particles present following ageing using image analysis software (Fig. 4A–E). The Raman mappings used for image analysis are displayed in ESI Fig. 2A and 2B.† The number of particles present in the soft material portion is displayed in Fig. 4F, and shows a general trend of increasing particle numbers with ageing, best observed in the statically aged alginate group (Fig. 4F). In addition to the number of particles appearing the soft material portion of the composite, the maximum, minimum and mean size of particles was also determined (Table 1). Maximum particle size obtained increased from day 0 to day 21 in static ageing conditions in both alginate and gellan composites. This was coupled with a reduction in minimum particle size in both alginate and gellan hydrogels. Mean particle size spanned a large range, demonstrated by the large standard deviations present, but shows that both the number of and the size of particles in the soft material portion are important features to be monitored and can easily be assessed using the method presented here. Conversely, in the dynamically aged groups, there was no trend to increasing or decreasing particle sizes, although notably, no particles were observed in the alginate day 21, dynamically aged samples (Fig. 4F, Table 1).

Table 1 Maximum, minimum and mean particle sizes in alginate/brushite and gellan/brushite composites

	Maximum particle size (μm²)		Minimum particle size (μm²)		Mean particle size ± st. dev. (μm²)	
Alginate/brushite	Static	Dynamic	Static	Dynamic	Static	Dynamic
Day 0	83.92	n/a	72.93	n/a	78.42 ± 7.78	n/a
Day 7	61.94	71.93	19.98	71.93	36.56 ± 18.35	71.93
Day 14	134.86	616.38	20.98	41.96	58.27 ± 41.09	n/a
Day 21	556.44	n/a	27.97	n/a	157.32 ± 130.57	186.56 ± 207.52
Gellan/brushite	Static	Dynamic	Static	Dynamic	Static	Dynamic
Day 0	83.92	n/a	72.93	n/a	133.37 ± 140.71	n/a
Day 7	414.58	42.96	19.98	42.96	124.11 ± 124.10	42.96
Day 14	405.59	115.88	22.98	77.92	166.38 ± 126.10	96.91 ± 26.88
Day 21	575.42	52.95	19.98	19.98	186.87 ± 176.13	33.57 ± 14.67

Note: minimum recordable particle size is set at 9.2752 μm². Weaker particles or parts of particles outside of focal plane may be missed or ignored by the threshold. Mean particle size without st. dev. is a result of only 1 particle visible in image.

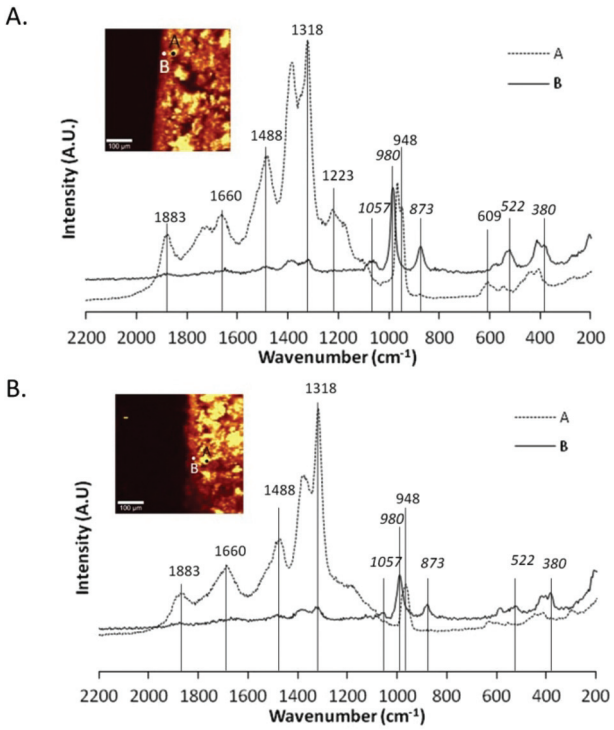

Fig. 5 Physiochemical changes occurring within the cement matrix. Raman spectra of two separate areas within the cement matrix in (A) alginate and (B) gellan. In both cases, Point B lies on the boundary of the hard and soft materials, and the addition of peaks around wavenumbers 522, 873 and 980 are indicative of an additional phase appearing within the cement matrix as it transitions to the soft material.

Although the chemical composition of the brushite cement portion of the composite had been characterised prior to combination with the gellan or alginate hydrogels (Fig. 2B), the composition following combination was also acquired (Fig. 5). Fig. 5A displays the Raman spectra for two distinct areas within the cement matrix only a few hours after combination with the alginate hydrogel as described in Fig. 1A. Point A demonstrates the peaks assigned to the components of the brushite cement matrix, namely a single peak around 980 cm^{-1}, indicative of brushite and peaks around 1200–1500 cm^{-1}, indicative of β-TCP (Fig. 5A, point A). However, at point B, the spectrum contains different peaks (Fig. 5A, point B). Point B lies on the boundary of the hard and soft materials and at this point, the intensity of the peaks indicative of β-TCP was reduced and there is the presence of peaks at 522 cm^{-1}, 873 cm^{-1} and 609 cm^{-1} of note (Fig. 5A, point B). This shows the appearance of another phase within the cement matrix as it transitions into the soft material. Peaks at 522 cm^{-1} ($\nu_2PO_4^{-3}$) and 580 cm^{-1} ($\nu_4PO_4^{-3}$) can be assigned to octacalcium phosphate (OCP)[40–42] and peaks at 609 cm^{-1} ($\nu_4PO_4^{-3}$), 873 cm^{-1} (P–OH stretching) and 1057 cm^{-1} ($\nu_3PO_4^{-3}$) can be assigned to carbonated hydroxyapatite (HA).[41,43,44] This compositional change within the brushite cement matrix also is observed in hard material portion of the gellan composite construct (Fig. 5B, point B). Since OCP is known to be an intermediate in the precipitation of HA,[45] hydrolysis of brushite to OCP occurs within a pH range 6.2–7.4 and a temperature range 25–37 °C[46] and OCP is formed on β-TCP crystals within hours,[47] its presence here is not surprising. Similarly, carbonated apatites (type A and type B) can be produced *via* precipitation *via* the reactions between carbonates, phosphates and hydroxyl groups.[45] Perhaps the presence of the hydrogel at the boundary of the cement allows the transformation of brushite into OCP or carbonated apatite.

After ageing of the composite constructs with the static ageing protocol, it has already been described that precipitates are observed within the soft material portion of the composite construct. The chemical composition of three of these precipitates was identified in both alginate (Fig. 6A) and gellan (Fig. 6B) composite constructs. Interestingly, the Raman spectra for the cement bulk and each individual precipitate revealed similar compositions, with peaks present that are indicative of β-TCP and brushite as described previously for the brushite cement. In fact, little difference was observed between the spectra for the precipitates and the cement bulk,

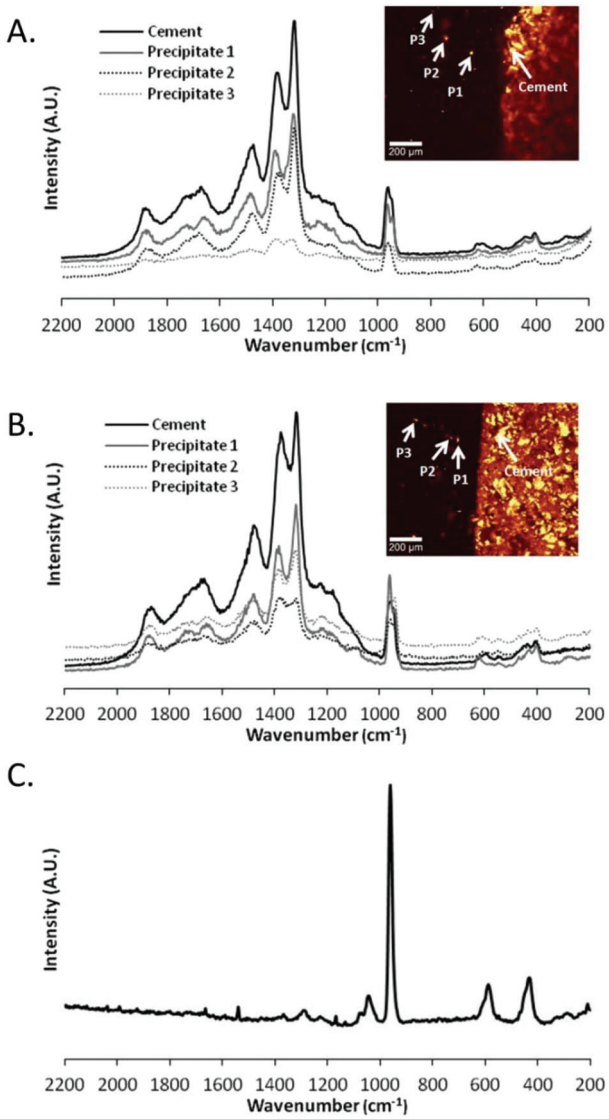

Fig. 6 Physiochemical analysis of the precipitates within the hydrogel matrix. Raman spectra for the cement bulk and three separate precipitates in (A) alginate and (B) gellan hydrogels after 28 days of ageing under static conditions. In both alginate and gellan, the precipitates exhibit the same chemical composition as the cement bulk, with major peaks in the range 940–1020 cm^{-1} and 1200–1400 cm^{-1} attributed to brushite and β-TCP respectively. Both these are the constituents of the cement matrix. (C) Database spectrum for hydroxyapatite.

only the intensity was decreased (Fig. 6). The Raman spectra not only contained peaks indicating the P–O stretching (980 cm^{-1}) and bending of the orthophosphate group but also modes characteristic for β-TCP (peaks around 1317–1376 cm^{-1}). These spectra can be compared to the Raman spectrum obtained for HA (Fig. 6C). The spectrum for HA displayed a very strong peak around 961 cm^{-1}, assigned to P–O stretching, and other peaks around 425 cm^{-1}, 576 cm^{-1} and 1025 cm^{-1}, assigned to ν_2, ν_4 and ν_3 PO_4 modes respectively,[42,45] and thus it can be concluded that the deposits in the soft material are not composed of HA. The origin of these deposits is likely to be from the cement itself, especially when the CRM mappings of the experimental conditions of static and dynamic ageing conditions are compared. However, the method by which precipitation occurs within the hydrogel is not clear *i.e.* does it originate from the cement bulk at the interface or from the ageing medium. The fact that both the alginate and the gellan hydrogel portions of the composite constructs possess higher amounts of phosphate deposits when the PBS is not exchanged throughout the experiment (static ageing) than in the dynamic state, suggests that the medium itself plays a more important role in the mineralisation of the hydrogel than the actual hydrogel–cement interface. This is a trend that is observed in both hydrogel species at several time points up until 28 days (ESI Fig. 2,† Fig. 4F, Table 1) with the exception of 1 time point (ESI Fig. 2,† alginate, day 14, compare static to dynamic). While this trend exists, it is important to note that the produced CRM mapping depends entirely on the particular location of the scanned area of the interface, of which it is only a small sampled area, rather than the entire interface. It is suggested that the calcium phosphate particles found in the hydrogel derive from the medium instead of directly from the brushite interface. The similarity of the Raman spectra of the particles compared to the cement material further allows the assumption that the particles initially originate from the brushite cement–PBS interface, where the cement dissolves and disintegrates, rather than form reprecipitations of HA as would perhaps be expected.[39] When placed in aqueous medium, brushite cements will either remain stable, dissolve, disintegrate or transform into hydroxyapatite.[39] If the surrounding medium is under-saturated with calcium and phosphate ions, dissolution will occur. The transformation of brushite into hydroxyapatite can then ensue once saturation of calcium and phosphate ions occurs.[39] Previous work has shown that a dynamic ageing protocol will lead to an increase in dissolution of brushite cements when compared to a static ageing protocol.[39] This was attributed to the balance in calcium and phosphate ion concentration in the medium; when dissolution products were removed from the solution on a daily basis, a higher rate of dissolution was maintained when compared to statically aged samples.[39] In this case, to identify the origin of the precipitates observed within the hydrogel matrices, both the surface roughness and porosity of the brushite cements were measured at day 0 and then at day 21 and day 28 respectively. Table 2 displays three different surface roughness

Table 2 Roughness measurements of brushite cement

	Day 0	Day 21	
		Static	Dynamic
S_a (μm)	6.3 ± 0.5	20.6 ± 12.8	17.8 ± 1.2
S_q (μm)	7.3 ± 1.0	28.8 ± 16.0	23.1 ± 2.0
S_z (μm)	123 ± 16.3	635 ± 87.0	500 ± 73.0

S_a: average roughness, S_q: root-mean-square roughness, S_z: ten-point height roughness.

Table 3 Porosity of brushite cement

	Day 0	Day 28	
		Static	Dynamic
Porosity (%)	49.45 ± 1.07	52.88 ± 2.28	56.02 ± 3.52

measurements for the brushite cement segments in contact with gellan hydrogels for the duration of the study. Under a static ageing regime for 21 days, the average surface roughness (S_a) increases 3.3 fold from 6.3 ± 0.5 μm to 20.6 ± 12.8 μm (Table 2). A similar increase in the root mean square roughness (S_q) is observed, increasing 3.9 fold from 7.3 ± 1.0 μm to 28.8 ± 16.0 μm. Furthermore, the ten-point height roughness (S_z) increases 5.2 fold from 123 ± 16.3 μm to 635 ± 82 μm. A similar trend is observed in the dynamically aged samples with S_a, S_q and S_z increasing 2.8 fold (6.3 ± 0.5 to 17.8 ± 1.2), 3.2 fold (7.3 ± 1.0 to 23.1 ± 2.0) and 4.1 fold (123 ± 16.3 to 500 ± 73) respectively. This increase in surface roughness on the microscale can be attributed to the gradual breakdown of the cement as it degrades and suggests the creation of large pits/pores on the cement surface where it was in contact with the hydrogel. In addition to an increase in surface roughness, the porosity of the brushite cement portions of the composite constructs was measured. Table 3 displays the porosity measurements for cements on day 0 and day 28 following ageing with the static or dynamic protocol. As expected, the porosity of the brushite cement changed over time. On day 0, porosity was measured as 49.5 ± 1.07%. This was increased following static ageing to 52.9 ± 2.28%, and following dynamic ageing to 56.0 ± 3.5% (Table 3) although these were not considered significantly different (p = 0.3). The trends of increasing surface roughness, porosity and the presence of calcium phosphate precipitates within the gel matrices aged dynamically indicate an increase in brushite cement dissolution when compared to the statically aged group as has been described before.[39] Despite this, the deposits in the hydrogel matrix are not HA (Fig. 6) as may be expected, but resemble the components of the cement matrix, β-TCP and brushite. β-TCP is impossible to precipitate at ambient temperatures,[47] however it has been shown to be released from the surface of brushite cement *in vitro*.[48] Incorporation of carboxyl acids into the brushite cement matrix leads to an increase in disintegration of the cement matrix, releasing solid β-TCP crystals into the surrounding media.[48] The acid component of the hard material used here included citric acid, therefore could reduce cement cohesion and facilitate the release of entrapped β-TCP particles from the cement matrix. The β-TCP particles are less soluble than brushite particles, and so remain within the medium. As shown in Table 1, the particle sizes detected are varied, and this particular technique has a minimum particle size detection of around 9 μm. Mesh sizes for gellan hydrogels have been reported to be in the range of ~0.5 μm,[49] but it is feasible that smaller, undetectable particles may find their way into the gel network and provide nucleation sites for further growth.

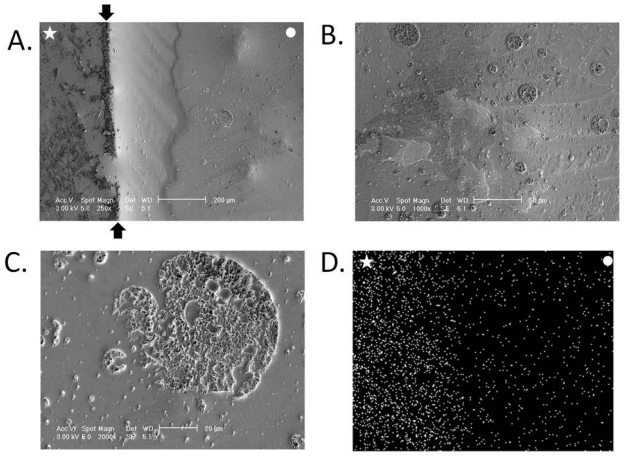

Fig. 7 ESEM evaluation of the hard–soft material interface after statically ageing in PBS for 21 days. (A) Hard–soft material interface of brushite-gellan composite construct. (B,C) Precipitates found within the gellan matrix of composite. (D) EDX mapping across the interface in brushite-alginate composite construct. *Cement* (*star*), *gel* (*circle*), *arrows, interface*.

The use of CRM in the observation of the hard–soft material interface was compared with the use of Environmental Scanning Electron Microscopy (ESEM) and Energy dispersive X-ray spectroscopy (Fig. 7). Fig. 7A shows the hard–soft material interface after statically ageing in PBS for 21 days. The boundary between the brushite (star) and gellan (circle) is clearly observed (arrows), however, the presence of precipitates in the soft material portion is not obvious at lower magnification. Increased magnification allows the identification of precipitates within the gellan portion of the composite (Fig. 7B, C) having a diameter up to 90 μm, which is within the same range as measured by image analysis (Table 1). The precipitates are randomly distributed in the gel matrix are not seen to be predominantly located near the interfacial region as seen with the CRM. As expected, EDX mapping due to phosphorus in Fig. 7D reveals a greater occurrence of this element at the side of the brushite cement (Fig. 7, star) than the alginate gel portion (Fig. 7, circle). However, identification of a definite interfacial region of the composite construct remains impossible to detect as no precise change in distribution from one phase to the other is evident. Although both the choice of integration limits for the CRM mapping and the location of the laser focus affect the resulting image, CRM outplays cryo-ESEM as a technique for the investigation of the soft–hard material interface. Firstly, no artefacts caused by other materials were detected with CRM. At this juncture, molecular vibrations of Raman active bonds are excited, thus, if their distribution is plotted across the interface of the sample, the detection of other materials having other bonds is excluded. In contrast, the ESEM image is the result of the number of emitted electrons reaching the detector, which are in turn caused by a combination of topography and material contrast. Therefore, the ESEM image contains information which makes an exclusive consideration of a certain bond of a molecule in

the sample impossible. Secondly, CRM yields a very specific material contrast, namely of one particular intramolecular bond, while ESEM yields an image showing the information of surface topography and material contrast, since the detector does not distinguish between secondary and backscattered electrons. As mentioned previously, the EDX mapping across the interface (Fig. 7D) failed to identify the interface between the cement and gel portions of the composite construct. Finally, the time taken to acquire individual images *via* CRM and ESEM differ. CRM mapping requires several hours depending on the resolution and size of the scanned area, whereas ESEM images can be obtained in several seconds. Despite this, the effort required for the sample preparation involved in cryo-ESEM is lengthy compared to CRM. Here, we have described a technique for being able to view hard–soft material construct almost immediately, where the only sample preparation conditions are an even sample surface and the immersion of the construct in liquid to prevent dehydration and shrinkage of the gel.

The fact that static ageing appears to result in the deposition of more mineral within the soft material portion of the composite construct will have significance in future studies. The long-term aim of the composite materials described here is to culture in the presence of cells, as described in our engineered bone-to-bone ligament model.[22] With this in mind, a static ageing protocol would not be employed, since culture media will need to be removed and replenished throughout the experiment. Furthermore, since culture media often contains serum, and serum is known to affect both the dissolution of brushite[39] and control of precipitation of calcium phosphates,[39,50,51] the effect in this area will be interesting to explore. The long-term aim is to form a graded interface between the hard and soft materials to replicate what is seen *in vivo*, therefore a reproduction of this structure *in vitro* is an important step to achieve.

Conclusions

This study has demonstrated the ability to study mineralisation within the soft material portion of hard–soft material composite structures. A simple method for observing hydrogels in a hydrated state has been developed for use with CRM. CRM far outplays other methods used for the observation of mineral within soft material analogue such as histology or SEM. Furthermore, it allows the quantification and chemical composition of precipitates within the matrix to be analysed. The methodology and results of this study will be of interest to those studying composite structures for the manufacture of composite tissues, or bone analogues for tissue engineering applications.

Acknowledgments

The WiTec Confocal Raman Microscope used in this research was obtained through Birmingham Science City: Innovative Uses for Advanced Materials in the Modern World (West Midlands Centre for Advanced Materials Project 2), with support from Advantage West Midlands (AWM) and part funded by the European Regional Development Fund (ERDF).

Notes and references

1 J. Z. Paxton, K. Baar and L. M. Grover, *Orthop. Muscul. Syst.: Curr. Res.*, 2012, DOI: 10.4172/2161-0533.S1-003.
2 A. G. Mikos, S. W. Herring, P. Ochareon, J. Elisseeff, H. H. Lu, R. Kandel, F. J. Schoen, M. Toner, D. Mooney, A. Atala, M. E. Van Dyke, D. Kaplan and G. Vunjak-Novakovic, *Tissue Eng.*, 2006, **12**, 3307–3339.
3 M. Benjamin, T. Kumai, S. Milz, B. M. Boszczyk, A. A. Boszczyk and J. R. Ralphs, *Comp. Biochem. Physiol., Part A: Mol. Integr. Physiol.*, 2002, **133**, 931–945.
4 M. Benjamin and D. McGonagle, *Scand. J. Med. Sci. Sports*, 2009, **19**, 520–527.
5 M. Benjamin and J. R. Ralphs, *Ital. J. Anat. Embryol.*, 2001, **106**, 151–157.
6 N. J. Castro, S. A. Hacking and L. G. Zhang, *Ann. Biomed. Eng.*, 2012, **40**, 1628–1640.
7 M. Keeney and A. Pandit, *Tissue Eng., Part B*, 2009, **15**, 55–73.
8 P. J. Yang and J. S. Temenoff, *Tissue Eng., Part B*, 2009, **15**, 127–141.
9 K. L. Moffat, W. H. Sun, P. E. Pena, N. O. Chahine, S. B. Doty, G. A. Ateshian, C. T. Hung and H. H. Lu, *Proc. Natl. Acad. Sci. U. S. A.*, 2008, **105**, 7947–7952.
10 J. P. Spalazzi, E. Dagher, S. B. Doty, X. E. Guo, S. A. Rodeo and H. H. Lu, *J. Biomed. Mater. Res. A*, 2008, **86**, 1–12.
11 J. P. Spalazzi, E. Dagher, S. B. Doty, X. E. Guo, S. A. Rodeo and H. H. Lu, *Conf. Proc. IEEE Eng. Med. Biol. Soc.*, 2006, **1**, 525–528.
12 J. P. Spalazzi, S. B. Doty, K. L. Moffat, W. N. Levine and H. H. Lu, *Tissue Eng.*, 2006, **12**, 3497–3508.
13 N. T. Khanarian, N. M. Haney, R. A. Burga and H. H. Lu, *Biomaterials*, 2012, **33**, 5247–5258.
14 N. T. Khanarian, J. Jiang, L. Q. Wan, V. C. Mow and H. H. Lu, *Tissue Eng., Part A*, 2012, **18**, 533–545.
15 B. A. Harley, A. K. Lynn, Z. Wissner-Gross, W. Bonfield, I. V. Yannas and L. J. Gibson, *J. Biomed. Mater. Res. A*, 2010, **92**, 1066–1077.
16 B. A. Harley, A. K. Lynn, Z. Wissner-Gross, W. Bonfield, I. V. Yannas and L. J. Gibson, *J. Biomed. Mater. Res. A*, 2010, **92**, 1078–1093.
17 A. K. Lynn, S. M. Best, R. E. Cameron, B. A. Harley, I. V. Yannas, L. J. Gibson and W. Bonfield, *J. Biomed. Mater. Res. A*, 2010, **92**, 1057–1065.
18 S. Elguizaoui, D. C. Flanigan, J. D. Harris, E. Parsons, A. S. Litsky and R. A. Siston, *Knee*, 2012, **19**, 812–817.
19 J. Ma, K. Goble, M. Smietana, T. Kostrominova, L. Larkin and E. M. Arruda, *J. Biomech. Eng.*, 2009, **131**, 101017.

20 J. Ma, M. J. Smietana, T. Y. Kostrominova, E. M. Wojtys, L. M. Larkin and E. M. Arruda, *Tissue Eng., Part A*, 2012, **8**(1–2), 103–116.

21 J. Z. Paxton, K. Donnelly, R. P. Keatch, K. Baar and L. M. Grover, *Ann. Biomed. Eng.*, 2010, **38**, 2155–2166.

22 J. Z. Paxton, L. M. Grover and K. Baar, *Tissue Eng., Part A*, 2010, **16**, 3515–3525.

23 J. Z. Paxton, U. Wudebwe, A. Wang, D. Woods and L. M. Grover, *Tissue Eng., Part A*, 2012, **18**(15–16), 1596–1607.

24 M. R. Nejadnik, A. G. Mikos, J. A. Jansen and S. C. Leeuwenburgh, *J. Biomed. Mater. Res. A*, 2012, **100**, 1316–1323.

25 T. Douglas, M. Wlodarczyk, E. Pamula, H. Declercq, E. de Mulder, M. Bucko, L. Balcaen, F. Vanhaecke, R. Cornelissen, P. Dubruel, J. Jansen and S. Leeuwenburgh, *J. Tissue Eng. Regen. Med.*, 2012, DOI: 10.1002/term.1616.

26 T. E. Douglas, P. B. Messersmith, S. Chasan, A. G. Mikos, E. L. de Mulder, G. Dickson, D. Schaubroeck, L. Balcaen, F. Vanhaecke, P. Dubruel, J. A. Jansen and S. C. Leeuwenburgh, *Macromol. Biosci.*, 2012, **12**, 1077–1089.

27 R. J. DeVolder, I. W. Kim, E. S. Kim and H. Kong, *Tissue Eng., Part A*, 2012, **18**, 1642–1651.

28 G. Liu, D. Zhao, A. P. Tomsia, A. M. Minor, X. Song and E. Saiz, *J. Am. Chem. Soc.*, 2009, **131**, 9937–9939.

29 M. Gudur, R. R. Rao, Y. S. Hsiao, A. W. Peterson, C. X. Deng and J. P. Stegemann, *Tissue Eng., Part C*, 2012, **18**(12), 935–946.

30 R. R. Rao, A. Jiao, D. H. Kohn and J. P. Stegemann, *Acta Biomater.*, 2011, **8**, 1560–1565.

31 X. Bi, C. A. Patil, C. C. Lynch, G. M. Pharr, A. Mahadevan-Jansen and J. S. Nyman, *J. Biomech.*, 2011, **44**, 297–303.

32 J. S. Nyman, A. J. Makowski, C. A. Patil, T. P. Masui, E. C. O'Quinn, X. Bi, S. A. Guelcher, D. P. Nicollela and A. Mahadevan-Jansen, *Calcif. Tissue Int.*, 2011, **89**, 111–122.

33 J. R. Maher, M. Takahata, H. A. Awad and A. J. Berger, *J. Biomed. Opt.*, 2011, **16**, 087012.

34 B. Wopenka, A. Kent, J. D. Pasteris, Y. Yoon and S. Thomopoulos, *Appl. Spectrosc.*, 2008, **62**, 1285–1294.

35 A. G. Schwartz, J. D. Pasteris, G. M. Genin, T. L. Daulton and S. Thomopoulos, *PLoS One*, 2012, **7**, e48630.

36 D. Stricker, *Comput. Methods Programs Biomed.*, 2008, **92**, 135–143.

37 N. Mehrban, J. Z. Paxton, J. Bowen, A. Bolarinwa, E. Vorndran, U. Gbureck and L. M. Grover, *Adv. Appl. Ceram.*, 2010, **110**, 162–167.

38 G. Socrates, *Infrared and Raman Characteristic Group Frequencies*, Wiley, 2001.

39 L. M. Grover, J. C. Knowles, G. J. Fleming and J. E. Barralet, *Biomaterials*, 2003, **24**, 4133–4141.

40 N. J. Crane, V. Popescu, M. D. Morris, P. Steenhuis and M. A. Ignelzi, Jr., *Bone*, 2006, **39**, 434–442.

41 P. Jamshidi, R. H. Bridson, A. J. Wright and L. M. Grover, *Biotechnol. Bioeng.*, 2013, **110**(5), 1487–1494.

42 S. Koutsopoulos, *J. Biomed. Mater. Res.*, 2002, **62**, 600–612.

43 G. Penel, G. Leroy, C. Rey and E. Bres, *Calcif. Tissue Int.*, 1998, **63**, 475–481.

44 G. Penel, N. Leroy, P. Van Landuyt, B. Flautre, P. Hardouin, J. Lemaitre and G. Leroy, *Bone*, 1999, **25**, 81S–84S.

45 J. C. Elliot, *Structure and Chemistry of the Apatites and other Calcium Phosphates*, Elsevier, Amsterdam, 1994, pp. 111–189.

46 J. C. Elliot, *Structure and Chemistry of the Apatites and other Calcium Phosphates*, Elsevier Science, Amsterdam, 1994, pp. 1–62.

47 J. Heughbaert, S. J. Zawacki and G. H. Nancollas, *J. Cryst. Growth*, 1983, **63**, 83–90.

48 M. H. Alkhraisat, F. T. Marino, J. R. Retama, L. B. Jerez and E. Lopez-Cabarcos, *J. Biomed. Mater. Res. A*, 2008, **84**, 710–717.

49 P. Jamshidi, P. Ma, K. Khosrowyar, A. M. Smith and L. M. Grover, *J. Exp. Nanosci.*, 2012, **7**, 652–661.

50 D. C. Bassett, L. M. Grover, F. A. Muller, M. D. McKee and J. E. Barralet, *Adv. Funct. Mater.*, 2011, **21**, 2968–2977.

51 L. M. Grover, U. Gbureck, A. J. Wright, M. Tremayne and J. E. Barralet, *Biomaterials*, 2006, **27**, 2178–2185.

PHILOSOPHICAL TRANSACTIONS B

rstb.royalsocietypublishing.org

Review

Cite this article: Wudebwe UNG, Bannerman A, Goldberg-Oppenheimer P, Paxton JZ, Williams RL, Grover LM. 2015 Exploiting cell-mediated contraction and adhesion to structure tissues *in vitro*. *Phil. Trans. R. Soc. B* **370**: 20140200.
http://dx.doi.org/10.1098/rstb.2014.0200

One contribution of 19 to a discussion meeting issue 'Cell adhesion century: culture breakthrough'.

Subject Areas:
structural biology, physiology, synthetic biology, biomaterials

Keywords:
extracellular matrix, ligament, tendon, tissue engineering, collagen, ceramic

Author for correspondence:
Liam M. Grover
e-mail: l.m.grover@bham.ac.uk

Exploiting cell-mediated contraction and adhesion to structure tissues *in vitro*

Uchena N. G. Wudebwe[1], Alistair Bannerman[1], Pola Goldberg-Oppenheimer[1], Jennifer Z. Paxton[2], Richard L. Williams[1] and Liam M. Grover[1]

[1]School of Chemical Engineering, University of Birmingham, Birmingham B15 2TT, UK
[2]School of Biomedical Sciences, University of Edinburgh, Edinburgh EH8 9AG, UK

Progress in tissue engineering is now impacting beyond the field of regenerative medicine. Engineered tissues are now used as tools to evaluate the toxicity of compounds or even to enable the modelling of disease. While many of the materials that are used to facilitate tissue growth are designed to enable cell attachment, many researchers consider that the contraction and modification of these matrices by attached cells is not desirable and take measures to prevent this from occurring. Where substantial alignment of the molecules within tissues, however, is a feature of structure the process of contraction can be exploited to guide new matrix deposition. In this paper, we will demonstrate how we have used the cell contraction process to generate tissues with high levels of organization. The tissues that have been grown in the laboratory have been characterized using a suite of analytical techniques to demonstrate significant levels of matrix organization and mechanical behaviour analogous to natural tissues. This paper provides an overview of research that has been undertaken to determine how tissues have been grown *in vitro* with structuring from the molecular, right through to the macroscopic level.

1. Introduction

Adhesion is important at all levels of biology and is critical to both structure and function. At the molecular level, it is the adhesion of enzymes to their substrates that facilitates many of the chemical reactions that are vital to life. Beyond this scale, the attachment of cells to an extracellular matrix (ECM) controls how cells behave and can respond to their environment [1,2]. Subsequent levels of organization, facilitated through adhesion between molecules within the ECM, are what enable connective tissues to perform under demanding mechanical loads placed on them by the body [3]. This paper summarizes the adhesions that are important at each length scale and describes how adhesion is being exploited to regenerate tissues and recapitulate the impressive levels of organization. The main focus of the review is on highly aligned tissues, ligament and tendon, but the methods reported could be used to generate more complex structure. The review is organized so that the adhesive forces important at the ECM level, cell-matrix level and tissue level are discussed in turn.

2. The extracellular matrix: molecular nature and structural adaptation

The ECM is a three-dimensional space within an organ or tissue that surrounds populations of cells and functions as an adhesive and supportive structure. The ECM is formed from water, proteins, proteoglycans and glycosaminoglycans (GAGs), each of which have important mechanical and biological roles. It is the proportions and orientations of each of these components that determine tissue function and physical performance and any damage to this structure

THE ROYAL SOCIETY PUBLISHING

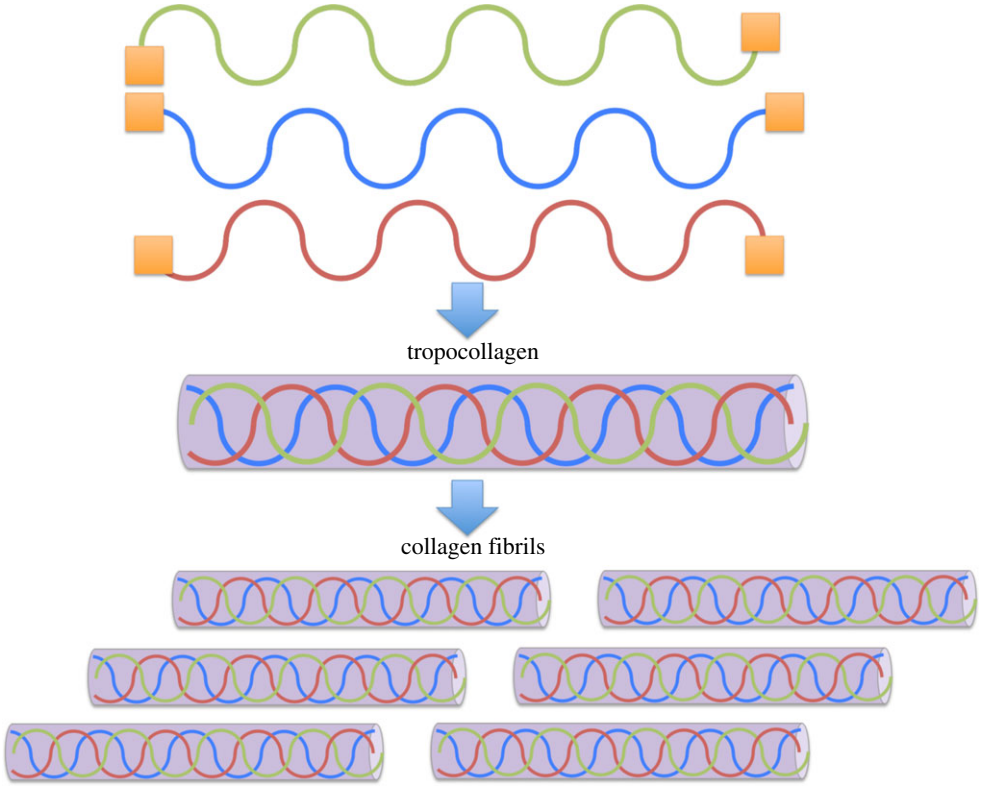

Figure 1. The assembly of collagen fibrils from tropocollagen molecules. Procollagen molecules are expressed within the cell and are modified via the cleavage of N and C termini. The resulting molecules self assemble to form tropocollagen molecules, which are subsequently self-assembled into collagen fibrils. Fibrillar diameter depends strongly on tissue type. (Online version in colour.)

can have important physical and biological consequences, potentially resulting in long-term disability. In addition to playing an important structural role, the organization of these ECM components strongly influences cell behaviour, offering cues that control cell differentiation, attachment, recruitment, migration and further ECM production [4]. The interplay between the embedded cells and the ECM itself means that tissues are able to constantly remodel in response to changes in loading and oxygen levels so that they are able to respond to the demands that are placed on the body. This impressive ability to adapt also makes the regeneration of tissues to their native states challenging. Soft connective tissues contain high proportions of structural fibrillar proteins such as collagen types I and II with modifications in structure that enable them to exhibit impressive mechanical properties. Cartilage, for example, obtains its shock-absorbing properties from high concentrations of hyaluronan and proteoglycan aggrecans and the rigidity of bone is a function of calcium phosphate present in the fibrillar collagen matrix. Below, the principle roles of collagen, GAGs and proteoglycans are introduced in more detail. It is noted that other molecules within the ECM (elastin, laminin and vitronection) have important mechanical and biological functions, but these lay beyond the scope of this paper.

(a) Collagen

Collagen is the most abundant protein that is found in the human body [5]. There are, at present, 28 known collagen types, which can be classified into fibril forming (I, II and XI), fibril associated (IX, XII and XIV), transmembrane (XIII and XVII), network forming (VI, VII and X), anchoring basement membrane (IV) and a selection of others with highly specific functions. In ligaments and tendons, type I is the most prevalent, constituting up to 90% of the total weight. Collagen type I is a structural protein with a triple helical conformation made up of two α1 chains and one α2 chain, that offers load-bearing tissue sufficient mechanical strength to withstand uniaxial and multiaxial loads [5]. The folding of the triple helix is due to glycine (Gly—the smallest amino acid) recurring in the Gly-X-Y amino acid sequence from which collagen is formed. X and Y are most commonly the amino acids proline and hydroxyproline, giving a repeating motif of Gly-Pro-Hyp [6]. It is the close packing of the three strands, hydrogen bonding and the high concentration of amino acids proline and hydroxyproline that stabilizes the triple helix [6]. The amino acids proline and 4-hydroxyproline are also referred to as imino acids [6,7] as they have one hydrogen atom attached to the nitrogen atom and when this forms part of an additional bond, there are no free hydrogen atoms available for hydrogen bonding. As a result, the presence of proline/hydroxyproline in the collagen molecule provides the flexibility needed to maintain the helical conformation for stability. When X and Y residues are not imino acids, they allow collagen fibril formation through attachment to other collagen molecules, integrins or ECM molecules [7,8]. Further stabilization of the collagen triple helix is achieved through binding of individual helices (tropocollagens) into collagen fibrils [9]. These fibrils can also join to form bundles and cross-link for enhanced stability [9] (figure 1).

(b) Glycosaminoglycans

Glycosaminoglycans (GAGs) are linear polysaccharide chains, which are usually highly sulfated and negatively charged [10]. Sulfated GAGs include chondroitin, dermatan

and keratan, whereas heparan, a basement membrane GAG and hyaluronan are unsulfated [11]. GAGs have extensive interaction with proteins such as growth factors, chemokines and cytokines [12] and the GAG long chains shield the proteins from proteolysis [13]. Connective tissues have high quantities of hyaluronan (hyaluronic acid), which aids cell migration and proliferation and maintains tissue hydration [14]. While the long chains are not very flexible, they are highly soluble in water and assume conformations that can trap large volumes of aqueous medium to form hydrated gels, a property that gives connective tissues their resistance to compressive stress [1].

(c) Proteoglycans

Proteoglycans are GAGs that are covalently bonded to a protein and, as with GAGs, proteoglycans are important for signal transduction and also provide additional structural support to tissues [15]. Aggrecan, versican, neurocan and brevican, collectively known as lecticans, are members of the chondroitin sulfate proteoglycan family that offer resilience to compressive force [16]. Other small proteoglycans whose proteins have leucine-rich repeat structures (SLRPs), form u-shaped structures suitable for protein–protein interactions [17]. Members of the SLRP family are decorin, biglycan, fibromodulin, lumican and keratoca. Decorin is present in connective tissue and, along with other SLRPs, contributes to collagen fibril assembly and its regulation [17]. A study by Matuszewski *et al.* [18] with the human supraspinatus tendon, located in the shoulder, showed that aggregan and biglycan distribution varied throughout the tendon with the highest concentration being in the anterior and posterior regions that experience the highest compressive stress within this tissue and are prone to injury; decorin concentration was high throughout the tendon as expected in areas of high tensile strength. Proteoglycans that contain heparan sulfate can bind with growth factors and other signalling molecules that can accelerate cell proliferation and modulate behaviour [1].

The distribution of matrix components through tissues is critical to mechanical performance. In the case of ligaments, the ligament midsubstance consists of collagen type I fibrils, which are aligned parallel to the principle axis of loading (figure 2). Moving towards the extremities of a ligament, there is a disruption in this order such that the collagenous matrix becomes richer in proteoglycan and GAG molecules with the formation of a homogeneous fibrocartilage structure. Directly adjacent to the bone, there is a region of mineralized fibrocartilage that directly abuts the subchondral bone. This exquisite level of structural adaptation means that the sinew is loaded almost purely in tension at its central portion and the mineralized region is placed under compression. This places each of the tissue components in a loading environment in which they may perform optimally and minimizes the chances of failure during locomotion [3]. It is this level of ordering which also provides a significant challenge within the field of regenerative medicine. It is, at present, impossible to reproduce these properties in a synthetic material; there is therefore a move towards using cells to create such structures outside the body for subsequent implantation. In order to understand how this may be done, it is important to understand how cells may interact with and be influenced by matrix components and other cells.

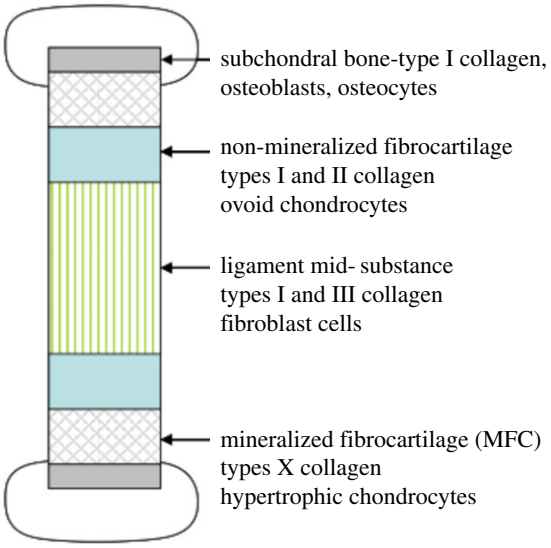

Figure 2. The heterogeneous structure of ligament tissue which prevents failure at the interface between bone and sinew. (Online version in colour.)

3. Cell–matrix interactions

Cells that are found within the ECM are critical to long-term adaptation and can therefore have an important role in the process of regeneration, particularly, in tissue deposition and restructuring. As the majority of human cells are anchorage dependent, their ability to form an adhesion with the ECM is critical to cell survival and behaviour [19]. The cell membrane consists of a phospholipid bilayer engulfed by a polysaccharide layer called the glycocalyx, which is ionizable resulting in a net negative charge on the cell surface [1]. The polymeric materials used for culturing cells *in vitro* are typically coated with poly-L-lysine, which has positively charged amine groups [1,20]. As a consequence, non-specific adhesion of various types of cells to solid surfaces occurs through weakly attractive electrostatic van der Waals forces [1]. The attachment of cells to the ECM is more specific and occurs through the interaction of moieties on ECM molecules with cell-surface glycoproteins known as integrins (figure 3). Integrin molecules contain 1–18 α and 1–8 β subunits arranged in different combinations. Many integrins bind to the same ligands on ECM components that contain the amino acid sequence Arg-Gly-Asp commonly known as RGD [1,21]. Typical ECM components that have the RGD sequence are vitronectin, bronectin and tenascin, though on collagen and laminin these are more obscure [22].

Fibroblasts express integrins with subunit arrangement $\alpha_1\beta_1$ and $\alpha_2\beta_1$ that bind to collagen simultaneously, however $\alpha_2\beta_1$ has been found to have a greater affinity for collagen type I [23]. In three-dimensional collagen matrices, cells deficient in $\alpha_1\beta_1$ receptors showed decreased growth, whereas presence of $\alpha_2\beta_1$ enhanced the expression of collagen-degrading enzymes MMP-1 and MMP-13 [23,24], which mediates matrix renewal. The two integrins appear to have different roles because during wound healing $\alpha_2\beta_1$ expression is upregulated by fibroblasts while that of $\alpha_1\beta_1$ is downregulated [23]. Endothelial cells proliferate during wound healing and they possess $\alpha_V\beta_3$ as their most prominent integrin [24]. In addition, dermal endothelial cells cultured in fibronectin or fibrin gels expressed higher mRNA levels of $\alpha_V\beta_3$ than when cultured in collagen gels. As a result, $\alpha_V\beta_3$ is an integrin implicated in cell–fibrin

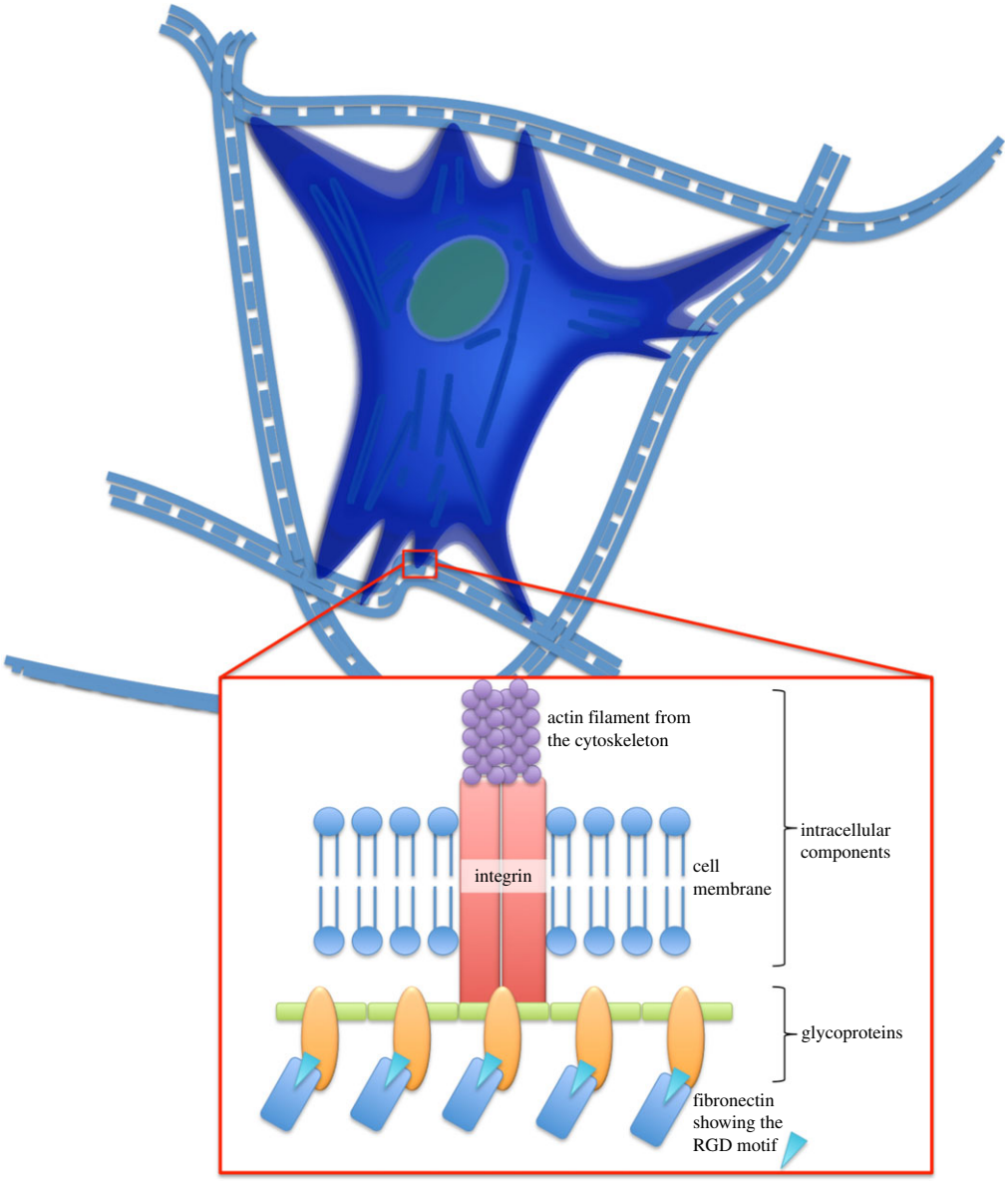

Figure 3. The interactions that occur between a cell adhesive fibrillar matrix bearing the RGD motif and an adhesion-dependent mammalian cell. The integrin subunits mediate attachment of the matrix to the actin cytoskeleton and enable stress transfer that can initiate tissue remodelling. (Online version in colour.)

adhesion. Cell–cell adhesion can also be mediated by fibrinogen though binding of $\alpha_{IIb}\beta_3$ and $\alpha_X\beta_1$ on fibrinogen motifs Lys-Gln-Ala-Gly-Asp-Val (KQAGDV) and Gly-Pro-Arg-Pro (GPRP), respectively [25].

The clustering of integrins between a cell membrane and ECM molecules results in the formation of a focal adhesion complex, which anchors a network of actin stress fibres within the cell. This link between the cell and the ECM is what enables the cells to experience the mechanical loading applied to the cell population and critically activates pathways that enable the digestion of matrix and the concomitant deposition of new ECM. An improved understanding of the processes that occur during cell adhesion and how such processes govern tissue formation has opened the possibility of creating tissues *in vitro*. This may be achieved by placing the cell population in an environment that can stimulate the attached cells to secrete new ECM. Given the reported differences in cell behaviour when cultured in a three-dimensional structure as compared with in a monolayer system, much work has recently been dedicated to understanding the fundamental differences in behaviour between cell populations that are cultured in two and three dimensions. There is a now a general consensus that reproducing the complex tissue architectures that are found *in vivo* requires the provision of a three-dimensional support that provides cues to stimulate the embedded cell population to develop new matrix. The remainder of the paper will detail how three-dimensional culture in biologically derived matrices may enable the formation of organized tissue structures.

4. Tissue production *in vitro* exploiting cell–matrix interactions

One way to encourage cells to secrete their own matrix and digest that to which they are attached is through the use of a temporary matrix to support the cells during growth. A matrix that has been shown to enable this is fibrin which facilitates cell attachment through an integrin matrix and may be readily reorganized by seeded cells. It is readily available through the collection of a small blood sample and fulfils an important haemostatic role during the process of wound healing in the body, providing a matrix onto which cells can attach and eventually be replaced by native tissue. It is formed from the cleavage of fibrinogen by thrombin, which

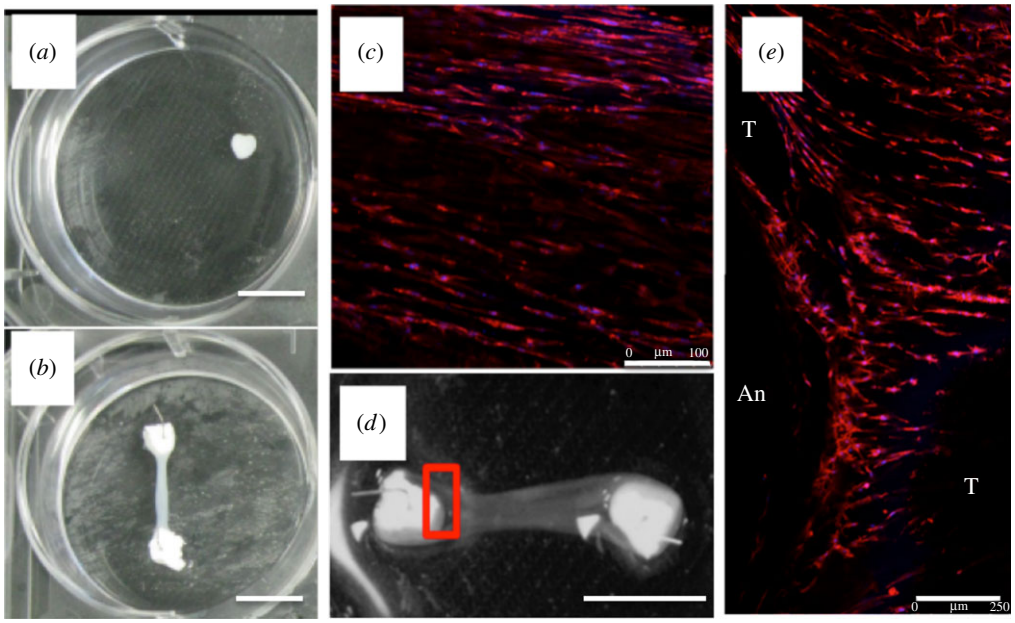

Figure 4. Free floating (*a*) and attached (*b*) fibrin-gel cultures seeded with fibroblasts after three weeks in culture (scale bars, 10 mm). (*c*) By 15 days of culture, cells in the central portion (stained with DAPI and phalloidin) were elongated and were orientated along the long axis of the sinew structure (scale bar, 100 µm). (*d*,*e*) Close examination of the interface with the ceramic brackets showed that levels of orientation varied from the ligament midsubstance (labelled T) to the interface with the anchor (labelled An). Scale bar, 8 mm in (*d*), 250 mm in (*e*). (Online version in colour.)

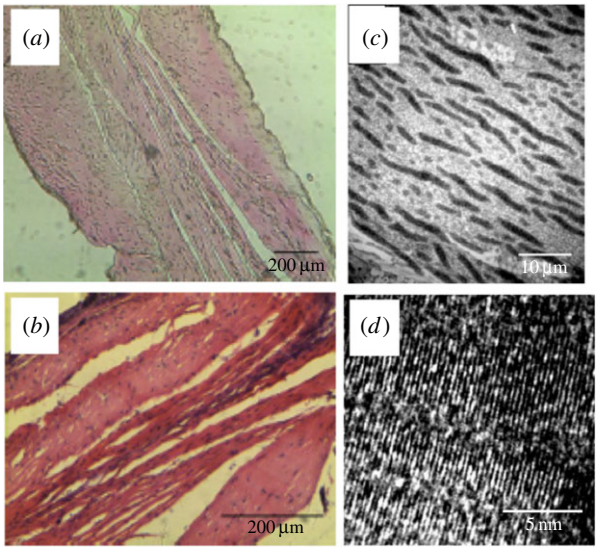

Figure 5. Imaging of ECM in the engineered tissues. Haematoxylin and eosin staining demonstrated the extent of cell and matrix alignment within the structure (*a*,*b*) and the enhanced density of the sinews following treatment with anabolic agents (*b*). Transmission electron microscopy demonstrated the presence of aligned fibrillar structures along the long axis of the sinew on the micro- (*c*) and nano-scales (*d*). (Online version in colour.)

results in the formation of fibrinopeptides A and B. It is the affinity of what are known as knobs A and B, which fit into holes a and b and result in gelation through the formation of protofibrils, which eventually self assemble to form a fibrillar network [26–28]. Fibroblasts seeded into a fibrin gel on the surface of a culture dish then associate with the fibrillar structure and will begin to contract the matrix and eventually a sphere of gelatinous material will be formed within the culture dish (figure 4*a*). By retaining the fibrin gel in the dish by using pins and sutures [29,30] or a calcium-phosphate ceramic with an inherently tissue-adhesive nature (figure 4*b*) [31,32], a gel cylinder is formed between the points of retention. The retention of the sinew-like structure by the ceramic brackets results in a passive tension between the ceramics [33] and this forces cell and molecular alignment [34] within the newly formed matrix (figure 4*c–f*). The cells have elongated cell bodies and nuclei suggestive of a tenocytic phenotype [35]. Interestingly, the level of orientation is significantly lower at the interface with the calcium phosphate ceramic suggestive of the development of a structure with multiple levels of organization (figure 4*e*).

After short periods of culture, the sinews typically consist of very small quantities of collagen (less than 5 wt%) [29,30]. However, it has been shown that it is possible to accelerate type I collagen deposition within the sinew by chemical treatment with ascorbic acid and proline [31], the former of which is involved in processing the procollagen molecules and the latter is added to prevent substrate limitation of collagen I production. Others have also demonstrated that it is possible to enhance collagen production through the application of a cocktail of growth factors [36]. It has also been demonstrated that intermittent bouts of cyclic mechanical conditioning of the sinew model results in an enhancement of collagen deposition and the mechanical strength of the resulting structures, although care must be taken to prevent matrix damage that can occur as a consequence of the application of more than 5% strain [37]. Recent unpublished results from our group have shown that it is possible to generate sinews with as high as 50 wt% of collagen I by also optimizing the mechanical properties of the supporting fibrin gel. Our hypothesis for this phenomenon is that an increase in local modulus enhances the mechanical stimulus provided to the cell population and upregulates collagen through the ERK pathway. Histological analysis demonstrated that the sinew itself had a highly orientated ECM (figure 5*a*) with the use of the collagen promotors ascorbic acid (AA) and proline (P) causing an enhancement in the density of the matrix (figure 5*b*). Examination of the ultrastructure using transmission electron microscopy (TEM) demonstrated the alignment of fibrils at the micro (figure 5*c*) and nano scales (figure 5*d*).

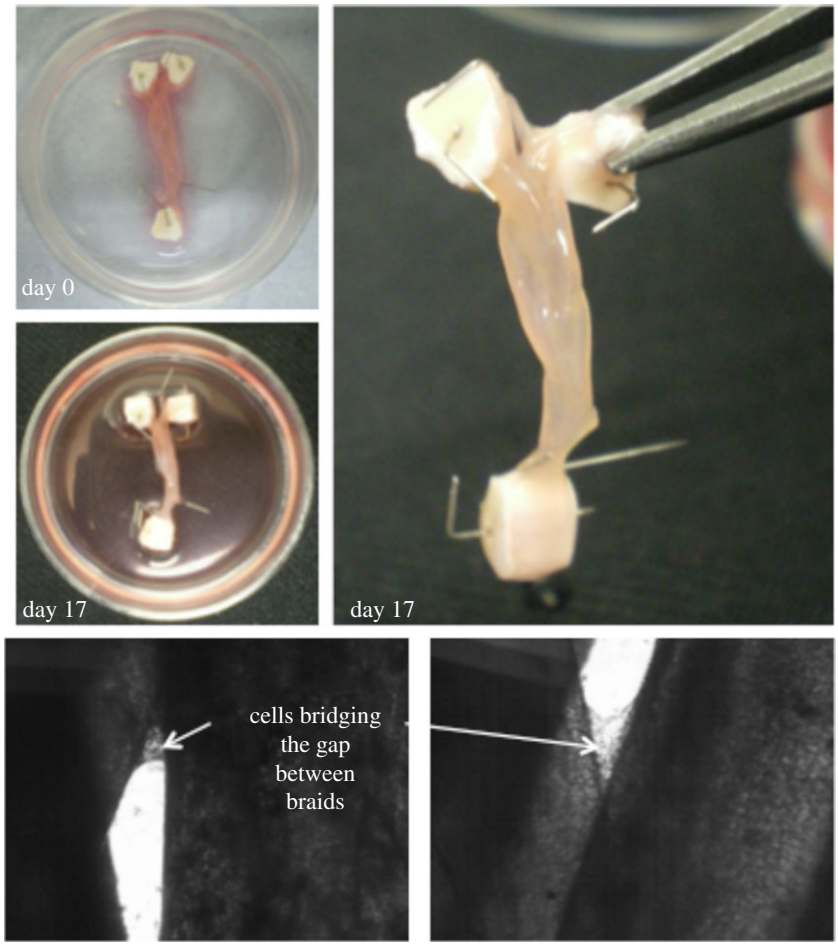

Figure 6. Macrostructral organization of the engineered sinews demonstrating the amalgamation of the individual strands over a period of 17 days in culture. (Online version in colour.)

5. Structuring tissue on the macroscopic scale

Ligaments and tendons are formed from multiple fascicles that interact with one another. The interactions that form between individual fascicles have been proposed to be responsible for enhancing the mechanical properties exhibited by native ligaments and tendon. The fascicles themselves are bundled together and surrounded by a membranous structure known as the epitenon [38]. In order to replicate this arrangement, it is possible to culture individual sinews in close proximity over a period of weeks. In the course of this time, the individual strands grow together and eventually amalgamate. The amalgamation is as a consequence of cellular bridging between the structures in addition to the formation of ECM between the individual strands (figure 6). Importantly, this kind of macrostructural organization of the sinew-like structures results in mechanical augmentation of the structure and deformation behaviour similar to that observed for native sinews.

6. Conclusion and future directions

By controlling how cells are able to manipulate a soft matrix *in vitro* it is possible to generate a heterogeneously structured material with structure and deformation characteristics that resemble those of native ligaments and tendons. The mechanical properties that are exhibited by these structures are orders of magnitude lower than those exhibited by native ligaments and tendons and so it is unlikely that they will replace current methods for ligament and tendon reconstruction in the very near future. Current directions of research are seeking to use this structured material as a means to augment healing in the body. We have recently published a method for decellularizing these structures [39] so that they may be manufactured and stored prior to implantation into patients to enhance the success of currently existing methods of tissue reconstruction. The aligned collagenous matrix is also being used as a model for diseases where mineral deposition within the soft tissues is a debilitating side effect.

References

1. Saltzman WM. 2004 *Tissue engineering: engineering principles for the design of replacement organs and tissues*, vol. 4. New York, NY: Oxford University Press.
2. Discher DE, Janmey P, Wang YL. 2005 Tissue cells feel and respond to the stiffness of their substrate. *Science* **310**, 1139–1143. (doi:10.1126/science.1116995)
3. Moffat KL, Sun WA, Pena PE, Chahine NO, Doty SB, Ateshian GA, Hung CT, Lu HH. 2008 Characterisation of the structure-function relationship in the ligament to bone interface. *Proc. Natl Acad. Sci. USA* **105**, 7947–7952. (doi:10.1073/pnas.0712150105)
4. Watt FM, Huck WT. 2013 Role of the extracellular matrix in regulating stem cell fate. *Nat. Rev. Mol. Cell Biol.* **14**, 467–473. (doi:10.1038/nrm3620)
5. Gelse K, Poschi E, Aigner T. 2003 Collagens—structure, function, and biosynthesis. *Adv. Drug*

Deliv. Rev. **55**, 1531–1546. (doi:10.1016/j.addr.2003.08.002)

6. Ramshaw JA, Shah NK, Brodksy B. 1998 Gly-X-Y tripeptide frequencies in collagen: a context for host-guest triple-helical peptides. *J. Struct. Biol.* **122**, 86–91. (doi:10.1006/jsbi.1998.3977)
7. Wu G *et al*. 2011 Proline and hydroxyproline metabolism: implications for animal and human nutrition. *Amino Acids* **40**, 1053–1063. (doi:10.1007/s00726-010-0715-z)
8. Brodsky B, Ramshaw JA. 1997 The collagen triple-helix structure. *Matrix Biol.* **15**, 545–554. (doi:10.1016/S0945-053X(97)90030-5)
9. Bhattacharee A, Bansal M. 2005 Collagen structure: the Madras triple helix and the current scenario. *IUBMB Life* **57**, 161–172. (doi:10.1080/15216540500090710)
10. Rudd T, Skidmore M, Guerrini M, Hricovini M, Powell A, Siligard G, Yates E. 2010 The conformation and structure of GAGs: recent progress and perspectives. *Curr. Opin. Struct. Biol.* **20**, 567–574. (doi:10.1016/j.sbi.2010.08.004)
11. Gandhi NS, Mancera RL. 2008 The structure of glycosaminoglycans and their interactions with proteins. *Chem. Biol. Drug Des.* **72**, 455–482. (doi:10.1111/j.1747-0285.2008.00741.x)
12. Taylor KR, Gallo RL. 2006 Glycosaminoglycans and their proteoglycans: host associated molecular patterns for initiation and modulation of inflammation. *FASEB J.* **20**, 9–22. (doi:10.1096/fj.05-4682rev)
13. Antonio JDS, Iozzo RV. 2001 *Glycosaminoglycans: structure and biological functions*. London, UK: John Wiley and Sons.
14. Kogan G, Soltes L, Stern R, Gemeiner P. 2007 Hyaluronic acid: a natural biopolymer with a broad range of biomedical and industrial applications. *Biotechnol. Lett.* **29**, 17–25. (doi:10.1007/s10529-006-9219-z)
15. Lindhardt RJ, Toida T. 2004 Role of gycosaminoglycans in cellular communication. *Acc. Chem. Res.* **37**, 431–438. (doi:10.1021/ar030138x)
16. Yamaguchi Y. 2000 Lecticans: organizers of the brain extracellular matrix. *Cell. Mol. Life Sci.* **57**, 276–289. (doi:10.1007/PL00000690)
17. Kresse H, Shonherr E. 2001 Proteoglycans of the extracellular matrix and growth control. *J. Cell. Physiol.* **189**, 266–274. (doi:10.1002/jcp.10030)
18. Matuszewski PE, Chen Y-L, Szczesny SE, Lake SP, Elliott DM, Soslowsky LJ, Dodge GR. 2012 Regional variation in human supraspinatus tendon proteoglycans: decorin, biglycan and aggrecan. *Connect. Tissue Res.* **53**, 343–348. (doi:10.3109/03008207.2012.654866)
19. Frame KK, Hu W-S. 1988 A model for density-dependent growth of anchorage dependent mammalian cells. *Biotechnol. Bioeng.* **32**, 1061–1066. (doi:10.1002/bit.260320813)
20. Mazia D, Schatten G, Sale W. 1975 Adhesion of cells to surfaces coated with polylysine: applications to electron microscopy. *J. Cell Biol.* **66**, 198–200. (doi:10.1083/jcb.66.1.198)
21. Dalby MJ, Gadegaard N, Oreffor ROC. 2014 Harnessing nanotopography and integrin-matrix interactions to influence stem cell fate. *Nat. Mater.* **13**, 558–569. (doi:10.1038/nmat3980)
22. van der Flier A, Sonnenberg A. 2001 Function and interactions of integrins. *Cell Tissue Res.* **305**, 285–298. (doi:10.1007/s004410100417)
23. Heino J. 2000 The collagen receptor integrins have distinct ligand recognition and signalling functions. *Matrix Biol.* **19**, 319–323. (doi:10.1016/S0945-053X(00)00076-7)
24. White DJ, Puranen S, Johnson MS, Heino J. 2004 The collagen receptor subfamily of the integrins. *Int. J. Biochem. Cell Biol.* **36**, 1405–1410. (doi:10.1016/j.biocel.2003.08.016)
25. Hynes RO. 1992 Integrins: versatility, modulation and signalling in cell adhesion. *Cell* **69**, 11–25. (doi:10.1016/0092-8674(92)90115-S)
26. Mosesson MW. 2005 Fibrinogen and fibrin structure and functions. *J. Thromb. Haemost.* **3**, 1894–1904. (doi:10.1111/j.1538-7836.2005.01365.x)
27. Ferry JD, Miller M, Shulman S. 1951 The conversion of fibrinogen to fibrin. VII. Rigidity and stress relaxation of fibrin clots; effect of calcium. *Arch. Biochem.* **34**, 424–436. (doi:10.1016/0003-9861(51)90021-5)
28. Janmey PA, Winer JP, Weisel JW. 2009 Fibrin gels and their clinical and bioengineering applications. *J. R. Soc. Interface* **6**, 1–10. (doi:10.1098/rsif.2008.0327)
29. Calve S, Dennis RG, Kosnik PE, Baar K, Grish K, Arruda EM. 2004 Engineering of functional tendon. *Tissue Eng.* **10**, 755–761. (doi:10.1089/10763 27041348464)
30. Paxton JZ, Donnelly K, Keatch RP, Baar K. 2008 Engineering the bone-ligament interface using poly(ethylene) glycol diacrylate incorporated with hydroxyapatite. *Tissue Eng. A* **15**, 1201–1209. (doi:10.1089/ten.tea.2008.0105)
31. Paxton JZ, Grover LM, Baar K. 2010 Engineering and *in vitro* model of a functional ligament from bone to bone. *Tissue Eng. A* **16**, 3515–3525. (doi:10.1089/ten.tea.2010.0039)
32. Paxton JZ, Donnelly K, Keatch RP, Baar K, Grover LM. 2010 Factors affecting the longevity and strength in an *in vitro* model of the bone-ligament interface. *Ann. Biomed. Eng.* **38**, 2155–2166. (doi:10.1007/s10439-010-0044-0)
33. Paxton JZ, Wudebwe UNG, Wang A, Woods D, Grover LM. 2012 Monitoring sinew contraction during formation of tissue engineered fibrin-based ligament constructs. *Tissue Eng. A* **18**, 1596–1607. (doi:10.1089/ten.tea.2011.0535)
34. Bayer M *et al*. 2010 The initiation of embryonic-like collagen fibrillogenesis by adult human tendon fibroblasts when cultured under tension. *Biomaterials* **31**, 4889–4897. (doi:10.1016/j.biomaterials.2010.02.062)
35. Kapacee Z, Richardson SH, Lu Y, Holmes DF, Baar K, Kadler KE. 2008 Tension is required for fibripositor formation. *Matrix Biol.* **27**, 371–375. (doi:10.1016/j.matbio.2007.11.006)
36. Hagerty J, Lee A, Calve S, Lee CA, Vidal M, Baar K. 2012 The effect of growth factors on both collagen synthesis and tensile strength of engineered human ligaments. *Biomaterials* **33**, 6355–6361. (doi:10.1016/j.biomaterials.2012.05.045)
37. Paxton JZ, Hagerty P, Andrick JJ, Baar K. 2012 Optimizing an intermittent stretch paradigm using ERK1/2 phosphorylation results in increased collagen synthesis in engineered ligaments. *Tissue Eng. A.* **18**, 277–284. (doi:10.1089/ten.tea.2011.0336)
38. Kannus P. 2000 Structure of the tendon connective tissue. *Scand. J. Med. Sci. Sports* **10**, 312–320. (doi:10.1034/j.1600-0838.2000.010006312.x)
39. Lebled C, Grover LM, Paxton JZ. 2014 Combined decellularisation and dehydration improves the mechanical properties of tissue-engineered sinews. *J. Tissue Eng.* **5**, 2041731414536720. (doi:10.1177/2041731414536720)

.2 Appendix B: Articles in preparation

Visualising phase change in a brushite-based calcium phosphate cement†

Alistair Bannerman, Richard L. Williams, and Liam M. Grover*

Received Xth XXXXXXXXXX 20XX, Accepted Xth XXXXXXXXX 20XX
First published on the web Xth XXXXXXXXXX 200X
DOI: 10.1039/b000000x

The resorption of brushite cements has been shown to be highly unpredictable, with strong dependence on a number of conditions. One of the major factors is phase transformation, with the rate of change to more stable phases such as hydroxyapatite significantly affecting the rate of resorption. Despite the importance of this, the analysis of phase transformation has largely been performed using methods that can detect the crystalline composition on bulk specimens, with no information on the spatial distribution of phases through the structure. In this study we used confocal Raman microscopy to map cross-sections of brushite cylinders dynamically aged in Phosphate Buffered Saline (PBS), Foetal Bovine Serum (FBS), Dulbeccos Minimum Essential Medium (DMEM), and DMEM supplemented with FBS. Image maps showed the importance of ageing medium on the evolution of phase composition throughout the cement structure. When aged in the absence of serum, there was an apparent dissolution of the brushite phase concomitant to the deposition of octacalcium phosphate (OCP) around the periphery of the sample. The deposition of this phase was detectable within 5 days and reduced the rate of brushite dissolution from the material. The use of serum, even at a concentration of only 10vol% prevented this phase transformation from occurring. This work reports a method for evaluating changes in phase composition in a metastable calcium phosphate cement regardless of crystallinity using Raman microscopy. It also demonstrates the weakness of predicting the resorption of such cements in protein free media.

1 Introduction

Calcium phosphate (CaP) cements have attracted significant interest in recent decades as potential bone graft biomaterials due to their ability to facilitate bone growth across their surface *in-vivo*[1]. As they are a cement, however, they are brittle, which can lead to a long-term risk of failure if they are not resorbed and replaced by new bone. Consequently, there has been a growing interest in the development of sparingly soluble cements that have a high resorption rate as they are not only resorbed through osteoclastic action, but also through dissolution. Brushite ($CaHPO_4 \cdot 2H_2O$) is one such material that exhibits a solubility of orders of magnitude higher than hydroxyapatite[2] ($Ca_{10}(PO_4)_6(OH)_2$; HA). A number of studies have investigated the degradation and biological resorption of brushite cements under both *in-vitro* and *in-vivo* conditions. These studies have shown brushite dissolution to be irregular with implants having been shown to remain stable[3], undergo fragmentation[4], or be resorbed[5,6]. Degradation is still poorly understood, but research has shown a close relationship between local conditions and cement composition. Enhancing the understanding of the chemical and biological mechanisms involved in resorption is essential to optimising the cement for successful long-term bone regeneration.

School of Chemical Engineering, University of Birmingham, Birmingham, B15 2TT, UK. E-mail: l.m.grover@bham.ac.uk

Analysis of the temporal changes in brushite and other resorbable samples has largely focused on changes in crystalline composition studied through high resolution topological imaging such as scanning electron microscopy, coupled with bulk compositional properties obtained via spectroscopy of powdered samples[7–9]. This provides high resolution information of the porosity and crystal structure, but gives poor to no spatial resolution of the chemical constituents in a system where the structure and environment cannot be considered as homogeneous. Further to this, the reliance of crystalline analysis limits the information that can be gained, with X-ray diffraction only able to detect greater than 5wt% of a material. This is a major flaw when it is known that extensive reprecipitiation slows degradation and previous work has shown amorphous phases have been detected early during ageing in some cases[10]. Radiographs and histology[3–6] can provide further information on compositional changes during resorption on *in-vivo* implanted samples, but are limited in the level of chemical and biological information they can provide. The geometrical distribution of phases may be of particular importance where a coating in a less soluble phase in physiological conditions will impede dissolution of the other phases.

In order to detect smaller quantities of a material, regardless of crystallinity and provide geometrical information of these phases, it may be possible to utilise a chemical imaging method such as confocal Raman microscopy (CRM). The

use of Raman spectroscopy in the analysis of brushite is well established with phases and their vibrational modes assigned to Raman peaks[11], and numerous studies applying the technique as a means to probe the composition of samples[12–15] have been reported. Confocal Raman microscopy (CRM) extends the scope of Raman spectroscopy; by taking individual spectra at a number of locations it allows intensity maps of peaks to be plotted showing the intensity and distribution of each phase to a high resolution - up to 200nm - over a single plane[16].

Despite the advantages offered, the number of image mapping based Raman studies in the field is limited with only a small number of studies looking at or relating to the ageing of calcium phosphate cement implants known to the authors[17–20]. In part the low level of use in the literature has been due to technological limitations with long spectral acquisition times, limiting data quality. With technological improvements in recent years and a range of related techniques that provide a stronger signal allowing much shorter acquisition times.

This study reports the use of CRM to evaluate the phase changes that occur during the ageing of brushite based calcium phosphate cements. In doing this, it is now possible to gain an unprecedented insight into the chemical changes that occur within this material during ageing. CRM was utilised to map the evolution of chemical changes in brushite CaP cement cylinders aged in different media; phosphate buffered saline (PBS), foetal bovine serum (FBS), and Dulbeccos modified eagle media (DMEM) standalone or supplemented with serum. The Raman maps were compared to bulk composition/structure of the samples acquired through X-ray diffraction (XRD) and single point Raman spectroscopy.

2 Materials and Methods

2.1 Cylinder Production

To produce brushite cement cylinders β tricalcium phosphate ($Ca_3(PO_4)_2$; $\beta - TCP$) (Plasma-Biotal, Tideswell, Derbyshire, UK) was mixed with 3.5M orthophosphoric acid (Sigma-Aldrich, Gillingham, UK) at a powder to liquid ratio of 1.75g/ml. The mixture was poured into custom made 12mm high by 6mm diameter cylindrical moulds, and left to harden overnight.

2.2 Brushite Cement Ageing

Cement cylinders were sterilised under UV light overnight. Sterilised Cylinders were placed into 50ml centrifuge tubes with 20ml of either DMEM (Sigma-Aldrich, Gillingham, UK), supplemented DMEM as used in cell culture (supplemented with 10% foetal bovine serum (Sigma-Aldrich, Gillingham, UK), 2.4% HEPES buffer (Sigma-Aldrich, Gillingham, UK), or sterile PBS (Oxoid, Basingstoke, UK) at a LCVR (liquid to cement volume ratio) of 60:1. Samples were incubated at 37°C for 10 days in the FBS and DMEM solutions, and for 5, 10, 20, 30 and 50 in PBS. Media was changed daily in each case. pH readings were taken for from day 1 to 30 in the PBS aged cylinders. Cylinders were removed from ageing medium, washed in distilled water, dried overnight at 37°C, cut using a scalpel across the midpoint to expose the cross-section. Individual halves were mounted on a sample holder using distilled water and frozen at -20°C in a cryostat (Starlet 2212, Bright, Cambridge, UK), samples were cryotomed in 2 μm steps to produce a smooth surface suitable for confocal imaging. They were then briefly washed with distilled water to remove any debris, and dried at 37°C before imaging.

2.3 Raman Mapping

Mapping was performed using a confocal Raman microscope (Alpha300r, Witec, Ulm Germany). With a 785nm 300mW argon laser (Toptica photonics, Munich, Germany) for DMEM, FBS and day 10 PBS samples, over a spectral range of 0-3000cm^{-1} with a mean spectral resolution of 3.6cm^{-1}, using a 300g/mm with 750nm blazing grating spectrograph (Acton SP2300, Princeton instruments, Trenton, NJ, USA). For the extended PBS media ageing a 60mW 514nm argon laser (Spectra-Physics, Santa Clara, California, USA) was used, with data collected over a spectral range of 200-1200cm^{-1} with a mean spectral resolution of 1.2cm^{-1}, using a 1800g/mm with 500nm blazing grating (Acton SP2300, Princeton instruments, Trenton, New Jersey, USA). Mapping was collected for whole area scans using a 5x 0.1NA atmospheric lens (Nikon, Tokyo, Japan), over a 6500x6500μm area with 100x100 points collected with an integration period of 1s. Higher resolution scans at the cross section edge were acquired with a 20x 0.45NA atmospheric lens (Nikon, Tokyo, Japan), over an area of 1000x1000μm, with 100x100 points collected and 1s integration time. Laser spot sizes were calculated for the 100x lens (λ=514nm D_{xy}391nm, D_z900nm, and λ=785nm D_{xy}598nm, D_z126nm), and for the 20x lens (λ=514nm D_{xy} 696nm, D_z2538nm and λ=785nm D_{xy}1064nm D_z3876nm). Acquisition of single spectra from points of interest was performed by taking 20 accumulations of 3 second integration periods. To prevent movement during scanning, samples were attached to a 35mm well plate using double-sided tape.

2.4 Processing Raman Data

Data was pre-processed to remove cosmic rays using the instrument associated software (Witec Project v2.10. Witec, Ulm, Germany), exported in SPC format into MATLAB

(MATLAB 2011a. Mathworks, Natick, Massachusetts, USA), baseline corrected using a least squares penalised method[21], and vector normalised. Least squares regression was used for fitting of individual Gaussians to each peak. False colour image maps were produced by integrating over the sum of peaks of interest. For further processing the dataset was segmented to separate the sample from background and allow calculation of the measured area and centroid. The dominant phase in each pixel location was determined by the association of the peak with the highest intensity. Measurement of OCP penetration distance at each time point was performed using ImageJ (ImageJ v1.43u. National Institutes of Health, Bethesda, Maryland, USA).

2.5 Bulk Analysis

Samples from each PBS time point were dried, and ground using a mortar and pestle. Raman spectra were acquired at 5 randomly chosen points from each powder sample with 20 accumulations at 3 seconds integration time per accumulation. Resulting spectra were pre-processed to remove cosmic rays using the associated Witec Project software and averaged together. Average spectra were exported and base-line corrected in MATLAB. For XRD approximately 500mg of the powder was distributed over a 10mm diameter circular area of Scotch tape and attached to the sample holder. XRD patterns were acquired using a Bruker D8 Advance Diffractometer (ASX Gmbh. Bruker, Karlsruhe, Germany) using the copper K-alpha line 1.5406nm at 40kV and 30mA. Each data set was collected from 2-θ angles 5-60 degrees at 0.05 degree/s step rate. The sample was rotated about its axis during the entire measurement to minimise the influence of preferential crystal orientation. Data was baseline corrected, and smoothed using MATLAB. Peak identification was performed using ICDD data cards.

3 Results

3.1 Brushite cement ageing

Brushite cement samples were made from a 1.75g/ml mixture of β-TCP and orthophosphoric acid, set in molds to produce 12mm long by 6mm diameter cement cylinders. A 60% maximum conversion of β-TCP to brushite was expected based on the materials used and the reaction shown in equation 1.

$$Ca_3(PO_4)_2 + H_3PO_4 + 6H_2O \rightarrow 3CaHPO_4.2H_2O \qquad (1)$$

Cylinders were aged in a dynamic 60:1 liquid to cement volume ratio solution of either: FBS, DMEM, DMEM supplemented with 10% FBS, or PBS for 10 days with the respective media changed daily. A longer study of PBS aged samples was performed for 0, 5, 10, 20, 30 and 50 days, with PBS changed on a daily basis. After removal from media, cylinders were cut to expose the cross section and polished for confocal imaging. In each case aged samples showed no visible signs of degradation compared to non-aged. pH readings taken from the removed media the first 30 days of the PBS ageing series showed an initial drop from the standard PBS of 7.3 to 6.5, which increased towards 7 as the time series proceeded.

3.2 Confocal Raman mapping of samples aged in different media

CRM mapping was performed on cylinders that were non-aged and aged for 10 days in each media using a 785nm laser. Regions covering whole cylinder cross sections with a pixel size of 65x65μm, and a higher resolution of the cylinder edge with a with a pixel size of 10x10μm were collected. The main spectral region of interest was 830-1030cm^{-1}. Calcium phosphate phases were identified based on Raman spectral peak locations previously reported in the literature[11] (Table 1.). The P-O stretching mode (ν_1) of the PO_4 group which has a unique peak shift for brushite (985cm^{-1}), octacalcium phosphate ($Ca_8(HPO_4)_2(PO_4)_4$; OCP) (958cm^{-1}), and TCP (970cm^{-1}) was used as the main reference peak for each CaP phase. Spectra at the centre and edge of a cylinder aged for 50 days in PBS are shown in Fig. 1. A -5cm^{-1} shift in the peak location was observed for samples aged in DMEM and FBS based media. Prior to image formation datasets were filtered to remove cosmic rays, baseline corrected, and normalised. Due to the close proximity of the peaks (12cm^{-1}) relative to the spectral resolution of the grating (3.5cm^{-1}) and their full width half maximum (10cm^{-1}), a significant overlap was present which would give rise to misleading results as constructive interference increased the apparent intensity of weaker or non-present peaks. A classical least squares regression was performed to fit an individual Gaussian to each peak in the region for image mapping calculations to be taken from. It should be noted that intensity values were produced to be consistent across phases for each sample mapping but not between every data set.

Table 1 Major Raman peaks found in the 800-1050cm^{-1} region of interest and their phase assignments based on the literature[11]

Wavenumber (cm^{-1})	Vibrational mode	Phase assignment
878	P-O stretching mode of PO_4 group	Brushite
948	P-OH stretching mode of HPO_4^{2-}	TCP
960	P-O stretching mode of PO_4 group	OCP
970	P-O stretching mode of PO_4 group	TCP
985	P-O stretching mode of PO_4 group	Brushite
1010	P-O stretching mode of HPO_4^{2-}	OCP

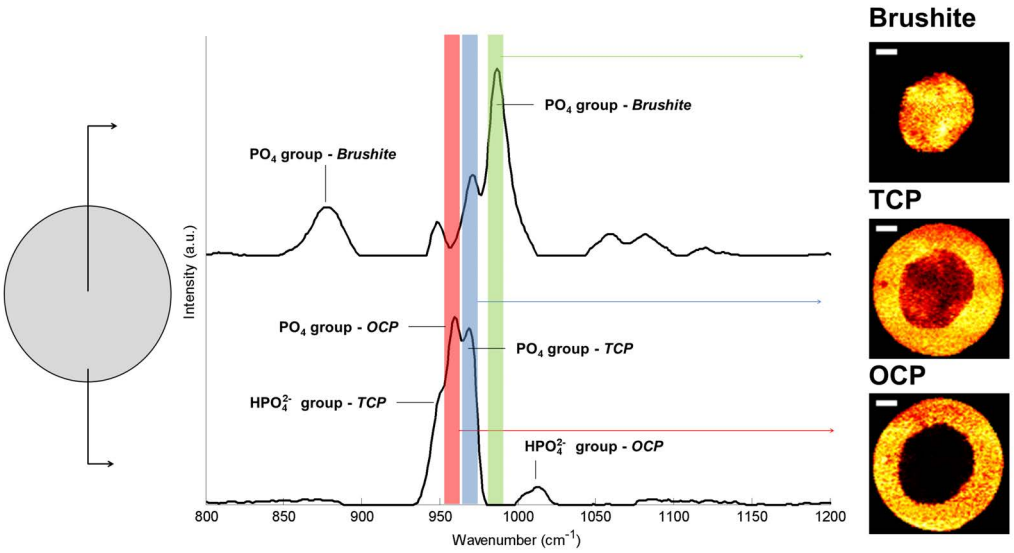

Fig. 1 Raman image formation from a day 50 cylinder cross section. Showing spectra taken from the centre and outside of the cross section, the relative intensities of the main peaks associated with each phase, and the mapping of the PO_4 peak showing the distribution of brushite, TCP and OCP over the cross section. Scale bar $1000\mu m$.

Image mapping of samples that were aged for 10 days in media for edge sections (Fig. 2) showed clear differences in the cement composition dependent on the media content. In unaged samples a homogeneous structure was present with the most intense peak being that indicative of brushite, and lower more disperse peaks indicative of TCP. OCP was not detectable at this time point beyond the background noise. At 10 days a shell of OCP was observed to be forming around the outside of the cylinder in the PBS and non-supplemented DMEM samples. A higher quantity of brushite dissolution and deeper penetration of OCP was apparent in the PBS aged sample, whereas the DMEM aged sample had OCP form largely on the outside of the cylinder itself. Conversely the supplemented DMEM and FBS samples, with 10% and 100% serum respectively, showed no evidence of brushite dissolution or OCP formation.

Image mapping data acquired was processed to provide further visualisation data on the phase quantity and distribution. Mappings were segmented, with the dominant phase at each spatial location determined based on maximum peak intensity. This was used to produce composite images showing the dominance of the phases at each time point for the edge areas (Fig. 2). Mapping of the dominant phase at each spatial location collaborated the heat map images for each peak, showing a solid ring of OCP around the outer edge of PBS and DMEM aged samples, with a higher density of TCP forming around and to a greater penetration depth than the OCP. Analysis of the Raman spectra showed no evidence of HA formation in any sample.

3.3 Confocal Raman mapping of samples aged in PBS

Having found that CRM mapping of brushite cylinders was able to spatially determine phase change in media with different compositions, the study was extended to encompass a longer time series allowing a deeper investigation of the material evolution. Raman imaging mapping of cylinders aged in dynamic PBS for 0, 5, 10, 20, 30 and 50 days was performed and processed as before over the whole cylinder cross section (Fig. 3) and at a higher resolution over the edge region (Fig. 3). A 514nm laser was used due to the minimal autofluorescence in PBS aged samples, enabling a higher signal intensity and access to a higher spectral resolution grating for improved differentiation of the PO_4 peaks.

Image mapping over the time series showed results similar to those from the PBS and non-supplemented DMEM seen in Fig. 2. An initial largely uniform phase distribution dominated by brushite, with a weak TCP signal, and no OCP was seen for the unaged cylinder. At 5 days a layer of OCP was observed at the outside of the cylinder, with a higher density of TCP both about the OCP and penetrating further into the sample. At each subsequent time point the layer of OCP and TCP increased in area and radial penetration. Further analysis of the spectra supported the results shown by the PO_4 peaks. With the decay of the $878cm^{-1}$ PO_4 peak associated with brushite alongside the drop in intensity and complete removal of the $985cm^{-1}$ peak at the outside of the cylinder, and the appear-

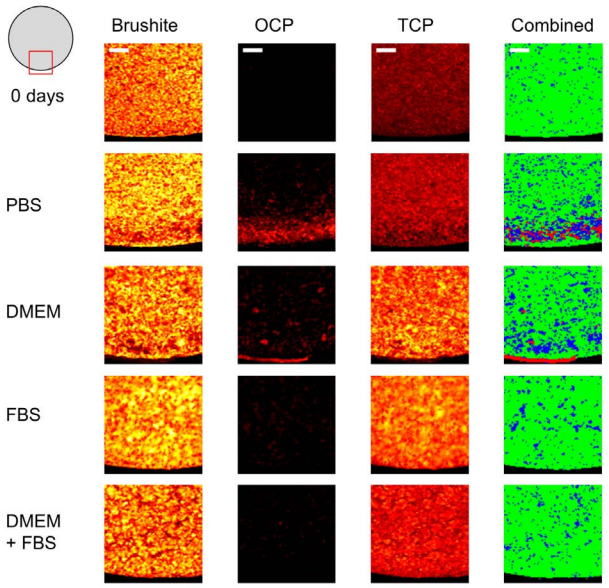

Fig. 2 Confocal Raman microscopy heat maps of partial cross sections taken at the outside edge of the cylinders after 10 days ageing in dynamic media. Heat maps of the PO_4 peak for brushite, OCP and TCP phases are shown for cylinders aged in each media. Combined images shows the dominant phase at each location determined by highest peak intensity; green - brushite, red - OCP, blue - TCP. Scale bar 200μm.

ance of the 1010cm^{-1} P-O HPO_4^{2-} OCP peak alongside the main PO_4 OCP peak.

The results suggest that over time in dynamic PBS, the outer brushite layer of the cylinder was eroded away by hydrolysis, leaving a TCP structure that replaced by OCP. From these results it can be determined that the outer brushite layer of the cylinder was eroded away by hydrolysis over time while in dynamic PBS, leaving a TCP structure . The rate at which the dissolution of brushite and precipitation of OCP occurred for a particular location was clearly shown to be dependent on the distance from the cylinder edge, with initial OCP appearance by 5 days at the edge of the cylinder, the outer radius of brushite being completely replaced by 10 days, and only a small central core of brushite remaining at 50 days. As seen in the PBS results for Fig. 2 a thin approximately 50-200μm layer of brushite was observed on the outside of the cylinder at aged time points - notably at day 20 and 30 in Fig. 3 - despite the otherwise complete dissolution of brushite 100μm or further into the sample. This layer was seen to degrade and be replaced by OCP at the 50 day time point. Composite images of the three phases showing of the dominant phase at each point showed the emergence of a distinct three phase structure with phases clustered by radial distance as the brushite underwent dissolution, leaving the TCP scaffold that was subsequently seeded by OCP. The percentage of the total area for each phase was calculated for each time point based on these results (Table. 2). In addition an estimate of the penetration distance of OCP was determined using composite images (Table. 2). Both of these supported the visual observations of brushite dissolution and OCP penetration. Such quantifications are limited by random variation of TCP distributions between samples and the assumption of the most intense peak being sufficiently dominant, but allow a reasonable estimate and insight of the phase composition at each time point and its evolution.

Table 2 Quantification of approximate area and penetration changes for phases at each time point for samples aged in PBS based on the dominant phase calculated at each spatial location

	Brushite %	OCP %	TCP %	OCP penetration (μm)
0 days	88.6	0.0	11.4	0
5 days	88.3	0.7	11.0	150
10 days	90.0	5.9	4.0	350
20 days	50.1	8.3	41.6	520
30 days	37.8	22.6	39.6	750
50 days	12.6	44.2	43.2	1300

3.4 Bulk analysis

Bulk composition and crystal structure of powdered samples at each time point was determined from a combination of XRD and Raman spectroscopy analysis for the extended PBS ageing series. The Raman spectra time series (Fig. 4(A)) showed clear evidence of a decrease in the 987cm^{-1} PO_4 brushite peak from initially the strongest, to almost dropping beyond the background noise at day 50. Whilst the OCP and TCP PO_4 peaks increased in intensity becoming the dominant phases. Likewise the XRD pattern time series (Fig. 4(B)) sshowed a decrease in the intensity of the peaks associated with brushite compared to those of TCP along with the appearance and rise in OCP associated peaks over the 50 day time period, matching the general CRM results. In both the XRD patterns and Raman spectra the presence of OCP was not detected beyond the background at the day 5 or day 10 time points despite the presence being observed in the CRM image mapping results. This was most likely due to the relatively small quantities of OCP at those time points being below the lower limit of detection for those instruments. 'As with the Raman imaging series, no major peaks corresponding to HA were identified. While minor HA peaks may have been present in the XRD patterns, they could not be clearly distinguished from the major phases in the sample. We therefore conclude the HA was not present in any detectable quantity.

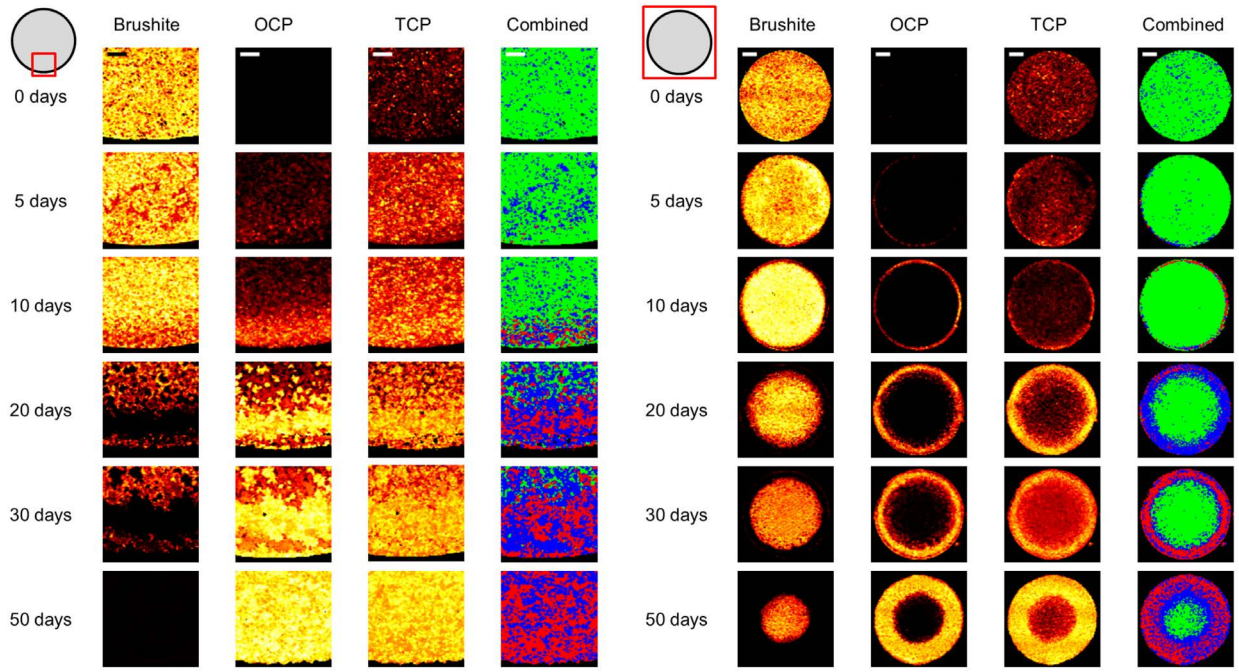

Fig. 3 Confocal Raman microscopy heat maps of cylinder cross sections for partial area at the outside of the cylinder, and whole area after 0, 5, 10, 20, 30 and 50 days in dynamic PBS showing the intensity mapping of the PO_4 peak for brushite, OCP and TCP at each time point. Combined image shows the dominant phase at each location; green - brushite, red - OCP, blue - TCP. Scale bar 200μm (edge section) 1000μm (whole area).

4 Discussion

This study investigated the visualisation of phase changes using Raman imaging on brushite cement cylinders aged in a range of media. Importantly, it was observed that in PBS aged samples a shell of OCP formed but did not prevent further dissolution, with continued loss of brushite and penetration of OCP over the entire time course. It was also shown that the presence of protein inhibited phase change, even at serum concentrations as low as 10vol%.

The transformation from brushite to a more stable phase such as HA has been shown to be an important factor in the highly unpredictable degradation of brushite cements under physiological conditions[22]. Ageing of brushite cements *in-vivo*[3–6,14,22] and *in-vitro*[12,19,23] has been undertaken by a number of studies with inconsistent results. For *in-vitro* ageing a range of ageing mediums including distilled water[24], simulated body fluid (SBF)[19], PBS[12,19,23], cell culture medium[13,25], and bovine serum[12] have been used. In these studies brushite has been shown to undergo dissolution and transformation to OCP, as reported here, or HA depending on the cement composition and conditions it has been aged in. OCP is known to be metastable and will transform to HA[2], however this was not observed in the time frame of this study. As a result of these variations in phase transformation, amongst other differences in degradation, there is an ongoing debate as to which media composition most accurately duplicates native physiological bioactivity conditions[25,26].

As discussed earlier, much of the analysis in studies on the physiological aging of CaPs has focused on a combination of morphological imaging coupled with spectral bulk compositional properties. These measurements provide information on the overall composition and properties, such as crystal size, but severely limit the depth and scope of phase information available. The distribution of the phases remains unknown leading to an assumption of homogeneous distribution, which as we have shown breaks 3D samples in a liquid environment with dynamic ion composition. which is known to chemically interact with CaPs. Some studies have used methods acquiring spectral information at a number of points; providing information on changes in calcium to phosphate ratios[22] and phase as a function of spatial location[14,22]. However these are still limited, requiring wide point spacing to cover the whole sample, leaving uncertainty as to whether a particular point is a true representation or an impurity. Raman imaging presents a potentially ideal solution as a means to resolve the stated information gap and the issue of bioactivity, being able to map chemical molecules and species without the need to label or

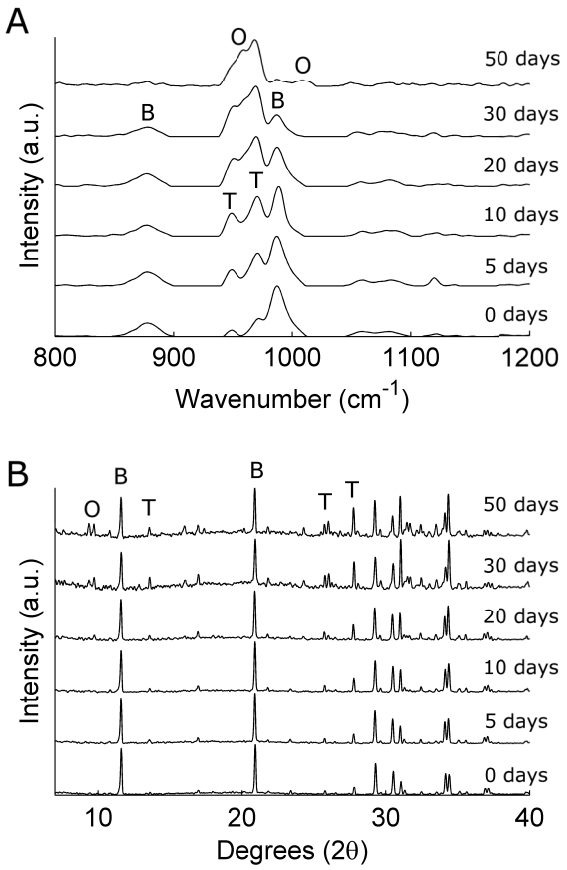

Fig. 4 Bulk analysis of powdered samples at each time point from the PBS ageing series acquired using (A) Raman spectroscopy and (B) XRD pattens. Peak labels: B- brushite, O- OCP, T - TCP.

destructively prepare samples. Whilst Raman spectroscopy is unable to to directly quantify the amount of each phase present, it is able to identify and provide information on the species present and their relative intensities. Previously we have applied Raman mapping to the interface in a brushite-hydrogel system; showing evidence of the cement undergoing dissolution or fragmentation, and transforming into OCP when aged in a PBS or SBF media[19]. The work presented in the current study gives a more controlled experimental environment allowing a clearer visualisation of the phase changes occurring as the samples aged.

For cylinders aged in PBS a three phase structure was seen to emerge and continuously develop as brushite underwent dissolution, leaving a scaffold of the original TCP reactants, which was subsequently precipitated by OCP. This suggested a nondirect route of conversion from brushite to OCP given the buffer region dominated by TCP between the two phases. The presence of such a buffer region at the interface between the two phases could be due to brushite being partially hydrolysed to an amorphous calcium phosphate (ACP) phase, before reacting with ions from solution to form OCP. The conversion of ACP to OCP has been reported previously[18,27,28]. The characterisation of ACP by Raman spectroscopy is problematic due to the loose non-crystalline nature of the species resulting in very broad peaks[29]. This is further complicated by the presence of the two or three other phases at any given spatial point in the region, with largely overlapping spectra in the region of interest. The main vibrational peak indicative of ACP is given as a broad PO_4 shifted to 950cm^{-1} with a high width for all other associated peaks[27]. Analysis of the data failed to find sufficient evidence of the presence of such a peak in the buffer region. Comparison of the ratio of the peak intensity at 970cm^{-1} to 950cm^{-1} to look for variations which might be indicative of a ACP PO_4 shift contributing to the overall signal of the HPO_4^{2-} TCP peak about 950cm^{-1} found no significant variation across the buffer region compared to any other areas regardless of time point. Given the highly soluble nature of ACP at more acidic pH a high rate of conversion to OCP would be expected[30] leaving only a small quantity at any given time point. This discrepancy may be explained by the formation of more stable ACP2 phase as a precursor to OCP as described by Christoffersen *et al.*[28] or the effect of concentration gradients in the porous structure and kinetic stabilisation reducing the conversion rate. Regardless of the conversion mechanism, the outside shell of OCP was not seen to prevent brushite dissolution further into the sample.

The transformation of brushite to OCP itself is surprising given the lower stability of OCP compared to HA predicted in solubility isotherms, with the majority of cases in the literature reporting the transformation of brushite to HA when aged in a neutral or slightly alkaline media. Whilst isotherms allow a prediction of the thermodynamically preferred phase, the kinetics of conversion in supersaturated media can mean that a less stable but more kinetically favourable phase grows faster and defines the final structure. Hydrolysis of brushite to OCP in a pH environment of 6.2-7.4 between 25°C and 37°C due to much higher conversion rate to OCP over HA was reported by Tung and Brown[31]. Importantly the brushite cements used in this study were not formed with a setting retardant or calcification inhibitor unlike many others reported studies. In a similar circumstance Malsy *et al.*[32] reported brushite converted to OCP and apatite in magnesium free cement mixtures. The direct transformation of brushite to OCP is given by Mert *et al.*[33] as one of the following reactions:

$$10CaHPO_4.2H_20 \rightarrow Ca_8(HPO_4)_2(PO_4)_4.5H_2O \\ +2Ca^{2+} + 4H_2PO_4^- + 15H_20 \quad (2)$$

$$6CaHPO_4.2H_20 + 2Ca^{2+} \rightarrow Ca_8(HPO_4)_2(PO_4)_4.5H_2O + 7H_2O + 4H^+ \quad (3)$$

$$5CaHPO_4.2H_20 + 3Ca^{2+} + HPO_4^{2-} \rightarrow Ca_8(HPO_4)_2(PO_4)_4.5H_2O + 5H_2O + 4H^+ \quad (4)$$

Such a direct route would explain the decrease in pH from 7.3 to 6.5 as the brushite was first exposed to PBS resulting a high level of dissolution, with the pH subsequently rising toward 7.3 as the remaining quantity of brushite decreased and became more deeply entombed inside the cylinder.

The heat maps in Fig. 2 and Fig. 3 suggests an increase in TCP alongside the appearance of OCP, however this is a misleading effect due to the loss of brushite in areas where dissolution had taken place. TCP, which is less soluble than brushite[34], has a higher intensity signal in these positions compared to areas where brushite has not undergone dissolution. Formation of further TCP is unlikely without stabilisation from magnesium ions[34] which were not present in the cylinder or PBS media.

The variation in initial OCP seeding location between the PBS and basic DMEM media in Fig. 2 suggests a difference in the precipitation routes. In DMEM aged samples the majority of OCP formed on the outside of the cylinder, whilst in the PBS aged samples the outside remained dominated by a thick band of brushite even after 30 days, with brushite further into the sample undergoing dissolution and being replaced by OCP. The formation of OCP on the outside of the cylinder may be caused by adsorbtion of components in the DMEM media on the cylinder surface enabling OCP precipitation and possibly limiting, but not preventing, transport in and out of the structure. The presence of a less soluble outer band of brushite as seen in the PBS aged samples raises the issue of uniformity in the cement as a result of local conditions during setting which may have significant consequences for *in-vivo* implants. In such situations phase composition will determine local pH and have a marked effect on the ingrowth of cells on implanted cements. The stalling or reduced rate of cell migration could cause complications if conversion of brushite to a more stable phase outpaces resorption, and/or regions of highly insoluble cement are left after otherwise total resorption.

The results of this study have shown that the evolution of multiple CaP phases can be mapped based on their intensity distribution over a series of time points. Differences in phase transformation based on media were observed, matching previous reports that showed the presence of proteins in serum based media inhibiting dissolution[12]. Previous ageing work on similar samples has noted morphological changes around the outside of aged brushite cylinders under scanning electron microscopy[23] coinciding with detected overall sample degradation and mechanical changes. This matches the changes seen in the PBS ageing series as the outer ring of OCP was seen to emerge. The ability to accurately resolve and display spectral information at a number of points across the sample adds a considerable contribution to the understanding of the cement and its bioactivity. High resolution imaging of phases will enable a better understanding of the rate and consistency of phase conversion. This is especially significant as we have shown that the acquisition of spectra through bulk methods gives a much less sensitive result, with the emergence of phases in small quantities not clearly detected until a number of days after they were observed under CRM. Furthermore the compositional information that can be obtained from the Raman spectra is far greater than can be obtained through the histological staining reported in the literature, and does not require lengthy and complex sample preparation.

The major limitation of the presented methodology is that it is mildly destructive, requiring physical preparation of the sample to access the plane of interest and make it suitable for confocal imaging. The depth penetration of confocal microscopy in turbid media is about $200\mu m$ which will be further reduced in cements. This limits the application of CRM to processed *in-vitro* and ex-vivo samples. However recent development of techniques for deep Raman data collection in soft tissue and bone[35], and endoscopic probes[36] may make non-invasive *in-vivo* imaging of cements to depths in the order of tens of millimetres plausible. Raman is also diffraction limited in its resolution to a maximum of about 200nm, which will be further reduced if a low numerical aperture lens is used to view a larger area, and/or a longer wavelength laser is used to minimise fluorescence and chance of damage to the sample. Depending on the cement system in question the resolution will likely be equivalent to or much greater than the size of individual crystals meaning that it may be unable to resolve to the level of individual crystals with each spectra being composed of a combination of multiple phases, as seen in this study. Due to the highly complex nature of brushite cements and the number of variables that affect the cement bioactivity degradation the use of multiple complimentary techniques is of course still required, though the application of chemical imaging adds a powerful tool for use in further investigations.

5 Conclusions

We have shown that localised information on chemical composition and phase changes in brushite CaP cements can be mapped and quantified using CRM. This enabled spatially resolved monitoring of the simultaneous evolution of brushite, TCP and OCP phases in samples aged *in-vitro*. Giving clear information on the distribution and relative quantity of each phase over time. Ultimately, this has facilitated a deeper insight into the mechanisms involved in the transformation between phases. This chemical mapping provides an important information bridge between the morphology based high resolution electron microscopy imaging, and bulk chemical com-

position results often applied in the literature. Applied to further *in-vivo* and *in-vitro* results such information will enable a deeper level of understanding into the chemical interaction between the sample and it's surrounding environment and the biochemical mechanisms involved, allowing for the improved optimisation of brushite cements for bone graft applications.

6 Acknowledgements

The authors acknowledge the EPSRC for funding (grant code: EP/F50053X/1) via the PSIBS DTC centre. The confocal Raman microscope used in this research were obtained through Birmingham Science City: Innovative Uses for Advanced Materials in the Modern World (West Midlands Centre for Advanced Materials Project 2), with support from Advantage West Midlands (AWM) and part funded by the European Regional Development Fund (ERDF).

References

1 S. V. Dorozhkin, *Biomatter*, 2011, **1**, 121–164.
2 J. C. Elliott, *Structure and Chemistry of the Apatites and Other Calcium Orthophosphates*, Elsevier, Amsterdam, 4th edn, 1994.
3 B. Flautre, C. Delecourt, M.-C. Blary, P. Van Landuyt, J. Lemaıtre and P. Hardouin, *Bone*, 1999, **25**, 35S–39S.
4 P. Frayssinet, L. Gineste, P. Conte, J. Fages and N. Rouquet, *Biomaterials*, 1998, **19**, 971–977.
5 D. Apelt, F. Theiss, A. El-Warrak, K. Zlinszky, R. Bettschart-Wolfisberger, M. Bohner, S. Matter, J. Auer and B. Von Rechenberg, *Biomaterials*, 2004, **25**, 1439–1451.
6 K. Ohura, M. Bohner, P. Hardouin, J. Lemaitre, G. Pasquier and B. Flautre, *J. Biomed. Mater. Res.*, 1996, **30**, 193–200.
7 L. Morejón-Alonso, R. García Carrodeguas and J. A. Delgado García-Menocal, *J. Biomed. Mater. Res.*, 2008, **84**, 386–393.
8 G. Cama, F. Barberis, M. Capurro, L. Di Silvio and S. Deb, *Mater. Chem. Phys.*, 2011, **130**, 1139–1145.
9 D. Tadic and M. Epple, *Biomaterials*, 2004, **25**, 987–994.
10 Y. N. Tan, S. Patel, U. Gbureck and L. M. Grover, *Adv. Appl. Ceram.*, 2011, **110**, 457–463.
11 S. Koutsopoulos, *J. Biomed. Mater. Res.*, 2002, **62**, 600–612.
12 L. M. Grover, U. Gbureck, A. J. Wright, M. Tremayne and J. E. Barralet, *Biomaterials*, 2006, **27**, 2178–2185.
13 P. Jamshidi, R. H. Bridson, A. J. Wright and L. M. Grover, *Biotechnol. Bioeng.*, 2013, **110**, 1487–1494.
14 G. Penel, N. Leroy, P. Van Landuyt, B. Flautre, P. Hardouin, J. Lemaitre and G. Leroy, *Bone*, 1999, **25**, 81S–84S.
15 G. Penel, C. Delfosse, M. Descamps and G. Leroy, *Bone*, 2005, **36**, 893–901.
16 T. Dieing, *Confocal Raman Microscopy*, Springer, Berlin, 2011, vol. 1.
17 K. Abdelkebir, S. Morin-Grognet, F. Gaudière, G. Coquerel, B. Labat, H. Atmani and G. Ladam, *Acta Biomater.*, 2012, **8**, 3419–3428.
18 N. J. Crane, V. Popescu, M. D. Morris, P. Steenhuis and M. A. Ignelzi Jr, *Bone*, 2006, **39**, 434–442.
19 S. Koburger, A. Bannerman, L. M. Grover, F. A. Müller, J. Bowen and J. Z. Paxton, *Biomater. Sci.*, 2014, **2**, 41–51.
20 A. M. Young, P. Y. J. Ng, U. Gbureck, S. N. Nazhat, J. E. Barralet and M. P. Hofmann, *Acta Biomater.*, 2008, **4**, 1081–1088.
21 Z.-M. Zhang, S. Chen and Y.-Z. Liang, *Analyst*, 2010, **135**, 1138–1146.
22 M. Bohner, F. Theiss, D. Apelt, W. Hirsiger, R. Houriet, G. Rizzoli, E. Gnos, C. Frei, J. Auer and B. Von Rechenberg, *Biomaterials*, 2003, **24**, 3463–3474.
23 L. Grover, J. Knowles, G. Fleming and J. Barralet, *Biomaterials*, 2003, **24**, 4133–4141.
24 M. Bohner, H. Merkle and J. Lemai, *J. Mater. Sci.: Mater. Med*, 2000, **11**, 155–162.
25 S. Mandel and A. C. Tas, *Mater. Sci. Eng., C*, 2010, **30**, 245–254.
26 M. Bohner and J. Lemaitre, *Biomaterials*, 2009, **30**, 2175–2179.
27 M. Kazanci, P. Fratzl, K. Klaushofer and E. Paschalis, *Calcif. Tissue Int.*, 2006, **79**, 354–359.
28 J. Christoffersen, M. R. Christoffersen, W. Kibalczyc and F. A. Andersen, *J. Cryst. Growth*, 1989, **94**, 767–777.
29 S. Somrani, C. Rey and M. Jemal, *J. Mater. Chem.*, 2003, **13**, 888–892.
30 C. Combes and C. Rey, *Acta Biomater.*, 2010, **6**, 3362–3378.
31 M. Tung and W. Brown, *Calcif. Tissue Int.*, 1985, **37**, 329–331.
32 A. Malsy and M. Bohner, *Eur. Cells Mater.*, 2005, **10**, 28.
33 S. Widjaja, *Advances in Bioceramics and Porous Ceramics IV Ceramic Engineering and Science Proceedings*.
34 M. S. A. Johnsson and G. H. Nancollas, *Crit. Rev. Oral Biol. Med.*, 1992, **3**, 61–82.
35 P. Matousek, *Chem. Soc. Rev.*, 2007, **36**, 1292–1304.
36 C. Kendall, J. Day, J. Hutchings, B. Smith, N. Shepherd, H. Barr and N. Stone, *Analyst*, 2010, **135**, 3038–3041.

.3 Appendix C: List of achievements

Refereed Journal Publications

- Bannerman A, Paxton JZ, and Grover LM. "Imaging the hard/soft tissue interface" *Biotechnology letters*, 1–13, 2013.

- Koburger S, Bannerman A, Grover LM, Muller FA, Bowen J, and Paxton JZ. "A novel method for monitoring mineralisation in hydrogels at the engineered hardsoft tissue interface" *Biomaterials Science*, 2(1):41–51, 2014.

- Wudebwe UNG, Bannerman A, Goldberg-Oppenheimer P, Paxton JZ, Williams RL, and Grover LM. "Exploiting contraction to structure tissues in vitro". *Philosophical Transactions of the Royal Society B: Biological Sciences*, 370(1661):20140200, 2015

Journal Publications In Preparation

- Bannerman A, Williams RL, and Grover LM. "Visualising phase change in a brushite-based calcium phosphate".

- Bannerman A, Paxton JZ, and Grover LM. "Monitoring cellular alignment in the development of a three-dimensional bone-bone ligament construct"

Conference Proceedings

- Paxton JZ, Bannerman A, Wang A, and Grover LM. "Engineering the enthesis-formation of a multiphase tissue transition in vitro" *International Journal of Experimental Pathology*, 94:A6-A7, 2013.

- Palmer AD, Bannerman A, Grover LM, and Styles IB. "Faster tissue interface analysis from Raman microscopy images using compressed factorisation" *European Conferences on Biomedical Optics*, 2:41–51, 2014.

Conference Presentations

Oral Presentations

- Paxton JZ, Bannerman A, Koburger S, Tan Y, Bowen J, Dehghani H and Grover LM. "*In-vitro* formation and maturation of a hard/soft tissue interface" World Biomaterial Congress. May 2012. Chengdu, China.

- Bannerman A, Paxton JZ, Mendes P, Dehghani H and Grover LM. "Imaging the development of a heterogeneous bone-bone ligament construct" UK Society for Biomaterials. June 2012. Nottingham, UK.

- Bannerman A, Williams RL, and Grover LM. "Mapping Phase Changes in Brushite Cements" European Society for Biomaterials. August 2014. Liverpool, UK.

Posters presentations

- Bannerman A, Paxton JZ, Mendes P, Dehghani H and Grover LM. "Imaging the hard/soft tissue interface" Tissue engineering DTC conference. August 2012. Keele, UK.

- Bannerman A, Koburger S, Paxton JZ, Dehghani H, Mendes P, and Grover LM. "Imaging the development of a hard/soft tissue interface" UK Society for Biomaterials. June 2013. Birmingham, UK.

- Bannerman A, Paxton JZ, Wang A, Sammons R, and Grover LM. "Imaging and quantification of mineralisation in a collagenous system" Gordon Research Conference Collagen. July 2013. New London, USA.

Invited talks

- Guest lecture. "Visualising phase changes in a calcium phosphate cement system using Raman spectroscopy". Norwegian University of Science and Technology. 18th November, 2014. Trondheim, Norway.

Awards

- Best poster presentation, UK Society for Biomaterials. June 2013.

- Journal front cover. "A novel method for monitoring mineralisation in hydrogels at the engineered hardsoft tissue interface" *Biomaterials Science*, volume 2, number 1, 2014.

LIST OF REFERENCES

[1] M Benjamin and JR Ralphs. Tendons and ligaments - An overview. *Histology and histopathology*, 12(4):1135–1144, 1997.

[2] W Al-Hakim, A Noorani, and S Lambert. Assessment and treatment strategies for rotator cuff tears. *Shoulder and elbow*, 0(0):1–9, 2014.

[3] B Wopenka, A Kent, JD Pasteris, Y Yoon, and S Thomopoulos. The tendon-to-bone transition of the rotator cuff: a preliminary Raman spectroscopic study documenting the gradual mineralization across the insertion in rat tissue samples. *Applied spectroscopy*, 62(12):1285–1294, 2008.

[4] GW Hess. Achilles tendon rupture: A review of etiology, population, anatomy, risk factors, and injury prevention. *Foot and ankle specialist*, 3(1):29–32, 2009.

[5] FH Fu, CH Bennett, C Lattermann, and CB Ma. Current trends in anterior cruciate ligament reconstruction part I: Biology and biomechanics of reconstruction. *The American journal of sports medicine*, 27(6):821–830, 1999.

[6] FH Fu, CH Bennett, CB Ma, J Menetrey, and C Lattermann. Current trends in anterior cruciate ligament reconstruction part II: Operative procedures and clinical correlations. *The American journal of sports medicine*, 28(1):124–130, 2000.

[7] J Chen, J Xu, A Wang, and M Zheng. Scaffolds for tendon and ligament repair: Review of the efficacy of commercial products. *Expert reviews, medical devices*, 6(1):61–73, 2009.

[8] CA Gottlob and CL Baker Jr. Anterior cruciate ligament reconstruction: Socioeconomic issues and cost effectiveness. *American journal of orthopedics*, 29(6):472–476, 2000.

[9] C Hurschler, B Loitz-Ramage, and R Vanderby. A structurally based stress-stretch relationship for tendon and ligament. *Journal of biomechanical engineering*, 119(4):392–399, 1997.

[10] P Sharma and N Maffulli. Biology of tendon injury: Healing, modeling and remodeling. *Journal of musculoskeletal and neuronal interactions*, 6(2):181–190, 2006.

[11] SA Fenwick, BL Hazleman, and GP Riley. The vasculature and its role in the damaged and healing tendon. *Arthritis research*, 4(4):252–260, 2002.

[12] Y Liu, HS Ramanath, and DA Wang. Tendon tissue engineering using scaffold enhancing strategies. *Trends in biotechnology*, 26(4):201–209, 2008.

[13] CM McNeilly, AJ Banes, M Benjamin, and JR Ralphs. Tendon cells *in vivo* form a three dimensional network of cell processes linked by gap junctions. *Journal of anatomy*, 189(3):593–600, 1996.

[14] S Calve, RG Dennis, PE Kosnik, K Baar, K Grosh, and EM Arruda. Engineering of functional tendon. *Tissue engineering*, 10(5-6):755–761, 2004.

[15] DA Faryniarz, C Chaponnier, G Gabbiani, IV Yannas, and M Spector. Myofibroblasts in the healing lapine medial collateral ligament: Possible mechanisms of contraction. *Journal of orthopaedic research*, 14(2):228–237, 1996.

[16] S Tozer and D Duprez. Tendon and ligament: Development, repair and disease. *Birth defects research part C*, 75(3):226–236, 2005.

[17] CM Kielty, MJ Sherratt, and CA Shuttleworth. Elastic fibres. *Journal of cell science*, 115(14):2817–2828, 2002.

[18] CK Kuo, JE Marturano, and RS Tuan. Novel strategies in tendon and ligament tissue engineering: Advanced biomaterials and regeneration motifs. *BMC sports science, medicine and rehabilitation*, 2(1):20–34, 2010.

[19] FR Noyes and ES Grood. The strength of the anterior cruciate ligament in humans and Rhesus monkeys. *The journal of bone and joint surgery*, 58(8):1074–1082, 1976.

[20] SLY Woo, TM Vogrin, and SD Abramowitch. Healing and repair of ligament injuries in the knee. *Journal of the American academy of orthopaedic surgeons*, 8(6):364–372, 2000.

[21] M Benjamin, H Toumi, JR Ralphs, G Bydder, TM Best, and S Milz. Where tendons and ligaments meet bone: Attachment sites (entheses) in relation to exercise and/or mechanical load. *Journal of anatomy*, 208(4):471–490, 2006.

[22] MR Doschak and RF Zernicke. Structure, function and adaptation of bone-tendon and bone-ligament complexes. *Journal of musculoskeletal and neuronal interactions*, 5(1):35–40, 2005.

[23] KL Moffat, WHS Sun, PE Pena, NO Chahine, SB Doty, GA Ateshian, CT Hung, and HH Lu. Characterization of the structure–function relationship at the ligament-to-bone interface. *Proceedings of the national academy of sciences*, 105(23):7947–7952, 2008.

[24] FG Girgis, JL Marshall, and AAM Jem. The cruciate ligaments of the knee joint: Anatomical, functional and experimental analysis. *Clinical orthopaedics and related research*, 106:216–231, 1975.

[25] FR Noyes, DL Butler, ES Grood, RF Zernicke, and MS Hefzy. Biomechanical analysis of human ligament grafts used in knee-ligament. *Journal of bone and joint surgery*, 66:344–352, 1984.

[26] T Zantop, W Petersen, JK Sekiya, V Musahl, and FH Fu. Anterior cruciate ligament anatomy and function relating to anatomical reconstruction. *Knee surgery, sports traumatology, arthroscopy*, 14(10):982–992, 2006.

[27] VB Duthon, C Barea, S Abrassart, JH Fasel, D Fritschy, and J Ménétrey. Anatomy of the anterior cruciate ligament. *Knee surgery, sports traumatology, arthroscopy*, 14(3):204–213, 2006.

[28] F Cimino, BS Volk, and D Setter. Anterior cruciate ligament injury: Diagnosis, management, and prevention. *American family physician*, 82(8):917–922, 2010.

[29] TE Hewett, SJ Shultz, and LY Griffin, editors. *Understanding and preventing non-contact ACL injuries*. Human Kinetics, Champaign, IL, 2007.

[30] DT Nguyen, TH Ramwadhdoebe, CP van der Hart, L Blankevoort, PP Tak, and CN van Dijk. Intrinsic healing response of the human anterior cruciate ligament: A histological study of reattached ACL remnants. *Journal of orthopaedic research*, 32(2):296–301, 2014.

[31] H Louboutin, R Debarge, J Richou, TAS Selmi, ST Donell, P Neyret, and F Dubrana. Osteoarthritis in patients with anterior cruciate ligament rupture: A review of risk factors. *The knee*, 16(4):239–244, 2009.

[32] VK Tjong, ML Murnaghan, JM Nyhof-Young, and DJ Ogilvie-Harris. A qualitative investigation of the decision to return to sport after anterior cruciate ligament reconstruction: To play or not to play. *The American journal of sports medicine*, 42(2):336–342, 2014.

[33] PT Simonian, SD Harrison, VJ Cooley, EM Escabedo, DA Deneka, and RV Larson. Assessment of morbidity of semitendinosus and gracilis tendon harvest for ACL reconstruction. *The American journal of knee surgery*, 10(2):54–59, 1996.

[34] SK Dheerendra, WS Khan, R Singhal, DG Shivarathre, R Pydisetty, and D Johnstone. Anterior cruciate ligament graft choices: A review of current concepts. *The open orthopaedics journal*, 6(Supplement 2):281–286, 2012.

[35] KP Spindler, JE Kuhn, KB Freedman, CE Matthews, RS Dittus, and FE Harrell. Anterior cruciate ligament reconstruction autograft choice: Bone-tendon-bone versus hamstring does it really matter? A systematic review. *The American journal of sports medicine*, 32(8):1986–1995, 2004.

[36] JR Carmichael and MJ Cross. Why bone–patella tendon–bone grafts should still be considered the gold standard for anterior cruciate ligament reconstruction. *British journal of sports medicine*, 43(5):323–325, 2009.

[37] L Pinczewski, J Roe, and L Salmon. Why autologous hamstring tendon reconstruction should now be considered the gold standard for anterior cruciate ligament reconstruction in athletes. *British journal of sports medicine*, 43(5):325–327, 2009.

[38] CA Borbon, G Mouzopoulos, and R Siebold. Why perform an ACL augmentation? *Knee surgery, sports traumatology, arthroscopy*, 20(2):245–251, 2012.

[39] Q Huang, E Ingham, P Rooney, and JN Kearney. Production of a sterilised decellularised tendon allograft for clinical use. *Cell and tissue banking*, 14(4):645–654, 2013.

[40] TS Roberts, D Drez, W McCarthy, and R Paine. Anterior cruciate ligament reconstruction using freeze-dried, ethylene oxide-sterilized, bone-patellar tendon-bone allografts two year results in thirty-six patients. *The American journal of sports medicine*, 19(1):35–41, 1991.

[41] CR Balsly, AT Cotter, LA Williams, BD Gaskins, MA Moore, and L Wolfinbarger Jr. Effect of low dose and moderate dose gamma irradiation on the mechan-

ical properties of bone and soft tissue allografts. *Cell and tissue banking*, 9(4):289–298, 2008.

[42] EY Elenes and SA Hunter. Soft-tissue allografts terminally sterilized with an electron beam are biomechanically equivalent to aseptic, nonsterilized tendons. *The journal of bone and joint surgery. American volume*, 96(16):1321–1326, 2014.

[43] MG Dunn. Tissue engineering strategies for regeneration of the anterior cruciate ligament. In *Repair and regeneration of ligaments, tendons, and joint capsule*, pages 279–296, 2006.

[44] R Mascarenhas and PB MacDonald. Anterior cruciate ligament reconstruction: A look at prosthetics-past, present and possible future. *McGill journal of medicine*, 11(1):29, 2008.

[45] K Fujikawa, F Iseki, and BB Seedhom. Arthroscopy after anterior cruciate reconstruction with the Leeds-Keio ligament. *Journal of bone and joint surgery, British volume*, 71(4):566–570, 1989.

[46] J Rading and L Peterson. Clinical experience with the Leeds-Keio artificial ligament in anterior cruciate ligament reconstruction. A prospective two-year follow-up study. *The American journal of sports medicine*, 23(3):316–319, 1995.

[47] NP Thomas, R Kankate, F Wandless, and H Pandit. Revision anterior cruciate ligament reconstruction using a 2-stage technique with bone grafting of the tibial tunnel. *The American journal of sports medicine*, 33(11):1701–1709, 2005.

[48] EW Carson, EM Anisko, C Restrepo, RA Panariello, SJ O'Brien, and RF Warren. Revision anterior cruciate ligament reconstruction – Etiology of failures and clinical results. *Journal of knee surgery*, 17(03):127–132, 2004.

[49] JW Jaureguito and LE Paulos. Why grafts fail. *Clinical orthopaedics and related research*, 325:25–41, 1996.

[50] S Thomopoulos, GM Genin, and LM Galatz. The development and morphogenesis of the tendon-to-bone insertion – What development can teach us about healing. *Journal of musculoskeletal and neuronal interactions*, 10(1):35–45, 2010.

[51] RS Wolf and LJ Lemak. Revision anterior cruciate ligament reconstruction surgery. *Journal of the southern orthopedic association*, 11(1):25–32, 2002.

[52] DJ Deehan and TE Cawston. The biology of integration of the anterior cruciate ligament. *Journal of bone and joint surgery, British volume*, 87(7):889–895, 2005.

[53] KL Moffat, I Wang, SA Rodeo, and HH Lu. Orthopedic interface tissue engineering for the biological fixation of soft tissue grafts. *Clinics in sports medicine*, 28(1):157–176, 2009.

[54] J Qu, AR Thoreson, Q Chen, KN An, PC Amadio, and C Zhao. Tendon gradient mineralization for tendon to bone interface integration. *Journal of orthopaedic research*, 31(11):1713–1719, 2013.

[55] SA Rodeo, SP Arnoczky, PA Torzilli, C Hidaka, and RF Warren. Tendon-healing in a bone tunnel. A biomechanical and histological study in the dog. *The journal of bone and joint surgery*, 75(12):1795–1803, 1993.

[56] EK Song, SM Rowe, JY Chung, ES Moon, and KB Lee. Failure of osteointegration of hamstring tendon autograft after anterior cruciate ligament reconstruction. *Arthroscopy: The journal of arthroscopic and related surgery*, 20(4):424–428, 2004.

[57] NE Ohly, IR Murray, and JF Keating. Revision anterior cruciate ligament reconstruction – Timing of surgery and the incidence of meniscal tears and degenerative change. *Journal of bone and joint surgery, British volume*, 89(8):1051–1054, 2007.

[58] ED Arrington, WJ Smith, HG Chambers, AL Bucknell, and NA Davino. Complications of iliac crest bone graft harvesting. *Clinical orthopaedics and related research*, 329:300–309, 1996.

[59] Kyle F Dickson, Jacob Friedman, James G Buchholz, and Frederick D Flandry. The use of BoneSource hydroxyapatite cement for traumatic metaphyseal bone void filling. *Journal of trauma-injury, infection, and critical care*, 53(6):1103–1108, 2002.

[60] LG Griffith and MA Swartz. Capturing complex 3D tissue physiology *in vitro*. *Nature reviews molecular cell biology*, 7(3):211–224, 2006.

[61] E Sachlos, N Reis, C Ainsley, B Derby, and JT Czernuszka. Novel collagen scaffolds with predefined internal morphology made by solid freeform fabrication. *Biomaterials*, 24(8):1487–1497, 2003.

[62] SJ Kew, JH Gwynne, D Enea, M Abu-Rub, A Pandit, D Zeugolis, RA Brooks, N Rushton, SM Best, and RE Cameron. Regeneration and repair of tendon and

ligament tissue using collagen fibre biomaterials. *Acta biomaterialia*, 7(9):3237–3247, 2011.

[63] X Li and JG Snedeker. Wired silk architectures provide a biomimetic ACL tissue engineering scaffold. *Journal of the mechanical behavior of biomedical materials*, 22:30–40, 2013.

[64] JZ Paxton, LM Grover, and K Baar. Engineering an *in vitro* model of a functional ligament from bone to bone. *Tissue engineering part A*, 16(11):3515–3525, 2010.

[65] TKH Teh, SL Toh, and JCH Goh. Aligned fibrous scaffolds for enhanced mechanoresponse and tenogenesis of mesenchymal stem cells. *Tissue engineering part A*, 19(11-12):1360–1372, 2013.

[66] Y Xu, J Wu, H Wang, H Li, N Di, L Song, S Li, D Li, Y Xiang, and W Liu. Fabrication of electrospun poly (L-lactide-co-ϵ-caprolactone)/collagen nanoyarn network as a novel, three-dimensional, macroporous, aligned scaffold for tendon tissue engineering. *Tissue engineering part C*, 19(12):925–936, 2013.

[67] WJ Li, CT Laurencin, EJ Caterson, RS Tuan, and FK Ko. Electrospun nanofibrous structure: A novel scaffold for tissue engineering. *Journal of biomedical materials research*, 60(4):613–621, 2002.

[68] CT Laurencin, AMA Ambrosio, MD Borden, and JA Cooper Jr. Tissue engineering: Orthopedic applications. *Annual review of biomedical engineering*, 1(1):19–46, 1999.

[69] DC Surrao, JWS Hayami, SD Waldman, and BG Amsden. Self-crimping, biodegradable, electrospun polymer microfibers. *Biomacromolecules*, 11(12):3624–3629, 2010.

[70] DC Surrao, JCY Fan, SD Waldman, and BG Amsden. A crimp-like microarchitecture improves tissue production in fibrous ligament scaffolds in response to mechanical stimuli. *Acta biomaterialia*, 8(10):3704–3713, 2012.

[71] Z Wang, Y Zhang, J Zhu, S Dong, T Jiang, Y Zhou, and X Zhang. *In vitro* investigation of a tissue-engineered cell-tendon complex mimicking the transitional architecture at the ligament-bone interface. *Journal of biomaterials applications*, 0(0):1–13, 2014.

[72] EJ Chung, MJ Sugimoto, JL Koh, and GA Ameer. A biodegradable tri-component graft for anterior cruciate ligament reconstruction. *Journal of tissue engineering and regenerative medicine*, 2014.

[73] SD Subramony, D Qu, R Ma, and HH Lu. *In vitro* optimization and *in vivo* evaluation of a multi-phased nanofiberbased synthetic ACL scaffold. In *Transactions of the 60th orthopaedic research society*, 2014.

[74] JO Cooper, JD Bumgardner, JA Cole, RA Smith, and WO Haggard. Co-cultured tissue-specific scaffolds for tendon/bone interface engineering. *Journal of tissue engineering*, 5:1–10, 2014.

[75] P He, KS Ng, SL Toh, and JCH Goh. *In vitro* ligament–bone interface regeneration using a trilineage coculture system on a hybrid silk scaffold. *Biomacromolecules*, 13(9):2692–2703, 2012.

[76] S Sahoo. Tendon and ligament tissue engineering. *AsiaBiotech*, 15(1), 2011.

[77] S Sahoo, SL Toh, and JCH Goh. A bFGF-releasing silk/PGLA-based biohybrid scaffold for ligament/tendon tissue engineering using mesenchymal progenitor cells. *Biomaterials*, 31(11):2990–2998, 2010.

[78] D Wendt, SA Riboldi, M Cioffi, and I Martin. Potential and bottlenecks of bioreactors in 3D cell culture and tissue manufacturing. *Advanced materials*, 21(32-33):3352–3367, 2009.

[79] T Wang, BS Gardiner, Z Lin, J Rubenson, TB Kirk, A Wang, J Xu, DW Smith, DG Lloyd, and MH Zheng. Bioreactor design for tendon/ligament engineering. *Tissue engineering part B*, 19(2):133–146, 2012.

[80] RK Birla, YC Huang, and RG Dennis. Development of a novel bioreactor for the mechanical loading of tissue-engineered heart muscle. *Tissue engineering*, 13(9):2239–2248, 2007.

[81] AA Gurjarpadhye, BM Whited, A Sampson, G Niu, KS Sharma, WC Vogt, G Wang, Y Xu, S Soker, and MN Rylander. Imaging and characterization of bioengineered blood vessels within a bioreactor using free-space and catheter-based OCT. *Lasers in surgery and medicine*, 45(6):391–400, 2013.

[82] A Ward, KP Quinn, E Bellas, I Georgakoudi, and DL Kaplan. Noninvasive metabolic imaging of engineered 3D human adipose tissue in a perfusion bioreactor. *PloS one*, 8(2):e55696, 2013.

[83] P He, S Sahoo, KS Ng, K Chen, SL Toh, and JCH Goh. Enhanced osteoinductivity and osteoconductivity through hydroxyapatite coating of silk-based tissue-engineered ligament scaffold. *Journal of biomedical materials research part A*, 101(2):555–566, 2013.

[84] J He, W Zhang, Y Liu, X Li, D Li, and Z Jin. Design and fabrication of biomimetic multiphased scaffolds for ligament-to-bone fixation. *Materials science and engineering: C*, 50:12–18, 2015.

[85] JP Spalazzi, SB Doty, KL Moffat, WN Levine, and HH Lu. Development of controlled matrix heterogeneity on a triphasic scaffold for orthopedic interface tissue engineering. *Tissue engineering*, 12(12):3497–3508, 2006.

[86] JP Spalazzi, E Dagher, SB Doty, XE Guo, SA Rodeo, and HH Lu. *In vivo* evaluation of a multiphased scaffold designed for orthopaedic interface tissue engineering and soft tissue-to-bone integration. *Journal of biomedical materials research part A*, 86(1):1–12, 2008.

[87] HH Lu and JP Spalazzi. Biomimetic stratified scaffold design for ligament-to-bone interface tissue engineering. *Combinatorial chemistry and high throughput screening*, 12(6):589–597, 2009.

[88] JP Spalazzi, E Dagher, SB Doty, XE Guo, SA Rodeo, and HH Lu. *In vivo* evaluation of a tri-phasic composite scaffold for anterior cruciate ligament-to-bone integration. In *Engineering in medicine and biology society, 2006. EMBS'06. 28th annual international conference of the IEEE*, pages 525–528, 2006.

[89] JZ Paxton, K Baar, and LM Grover. Current progress in enthesis repair: Strategies for interfacial tissue engineering. *Orthopedic and muscular system: current research*, 2012.

[90] D Qu, CZ Mosher, MK Boushell, and HH Lu. Engineering complex orthopaedic tissues via strategic biomimicry. *Annals of biomedical engineering*, pages 1–21, 2014.

[91] J Ma, MJ Smietana, TY Kostrominova, EM Wojtys, LM Larkin, and EM Arruda. Three-dimensional engineered bone–ligament–bone constructs for anterior cruciate ligament replacement. *Tissue engineering part A*, 18(1-2):103–116, 2011.

[92] JZ Paxton. Engineering a musculoskeletal interface to generate functional ligaments. *University of Dundee*, 2009.

[93] JZ Paxton, K Donnelly, RP Keatch, K Baar, and LM Grover. Factors affecting the longevity and strength in an *in vitro* model of the bone–ligament interface. *Annals of biomedical engineering*, 38(6):2155–2166, 2010.

[94] JZ Paxton, UNG Wudebwe, A Wang, D Woods, and LM Grover. Monitoring sinew contraction during formation of tissue-engineered fibrin-based ligament constructs. *Tissue engineering part A*, 18(15-16):1596–1607, 2012.

[95] JZ Paxton, P Hagerty, JJ Andrick, and K Baar. Optimizing an intermittent stretch paradigm using ERK1/2 phosphorylation results in increased collagen synthesis in engineered ligaments. *Tissue engineering part A*, 18(3-4):277–284, 2011.

[96] UNG Wudebwe. Factors influencing the development of a tissued engineered bone to bone ligament construct. *University of Birmingham*, 2014.

[97] UNG Wudebwe, A Bannerman, P Goldberg-Oppenheimer, JZ Paxton, RL Williams, and LM Grover. Exploiting cell–mediated contraction and adhesion to structure tissues *in vitro*. *Philosophical transactions of the royal society part B*, 370:20140200, 2015.

[98] C Lebled, LM Grover, and JZ Paxton. Combined decellularisation and dehydration improves the mechanical properties of tissue-engineered sinews. *Journal of tissue engineering*, 5:1–11, 2014.

[99] Q Ye, G Zünd, P Benedikt, S Jockenhoevel, SP Hoerstrup, S Sakyama, JA Hubbell, and M Turina. Fibrin gel as a three dimensional matrix in cardiovascular tissue engineering. *European journal of cardio-thoracic surgery*, 17(5):587–591, 2000.

[100] M Verstraete. Clinical application of inhibitors of fibrinolysis. *Drugs*, 29(3):236–261, 1985.

[101] MS Kuntamukkula, LV McIntire, JL Moake, DM Peterson, and WJ Thompson. Rheological studies of the contractile force within platelet-fibrin clots: Effects of prostaglandin E1, dibutyryl-cAMP and dibutyryl-cGMP. *Thrombosis research*, 13(6):957–969, 1978.

[102] PS Ciano, RB Colvin, AM Dvorak, J McDonagh, and HF Dvorak. Macrophage migration in fibrin gel matrices. *Laboratory investigation; a journal of technical methods and pathology*, 54(1):62–70, 1986.

[103] LF Brown, N Lanir, J McDonagh, K Tognazzi, AM Dvorak, and HF Dvorak. Fibroblast migration in fibrin gel matrices. *The American journal of pathology*, 142(1):273, 1993.

[104] S Jockenhoevel, G Zund, SP Hoerstrup, K Chalabi, JS Sachweh, L Demircan, BJ Messmer, and M Turina. Fibrin gel – Advantages of a new scaffold in cardiovascular tissue engineering. *European journal of cardio-thoracic surgery*, 19(4):424–430, 2001.

[105] JW Weisel. Fibrinogen and fibrin. *Advances in protein chemistry*, 70:247–299, 2005.

[106] PA Janmey, JP Winer, and JW Weisel. Fibrin gels and their clinical and bioengineering applications. *Journal of the royal society: interface*, 6(30):1–10, 2009.

[107] EA Ryan, LF Mockros, JW Weisel, and L Lorand. Structural origins of fibrin clot rheology. *Biophysical journal*, 77(5):2813–2826, 1999.

[108] JW Weisel. Structure of fibrin: Impact on clot stability. *Journal of thrombosis and haemostasis*, 5(s1):116–124, 2007.

[109] N Dubey, PC Letourneau, and RT Tranquillo. Neuronal contact guidance in magnetically aligned fibrin gels: Effect of variation in gel mechano-structural properties. *Biomaterials*, 22(10):1065–1075, 2001.

[110] MC McManus, ED Boland, HP Koo, CP Barnes, KJ Pawlowski, GE Wnek, DG Simpson, and GL Bowlin. Mechanical properties of electrospun fibrinogen structures. *Acta biomaterialia*, 2(1):19–28, 2006.

[111] MV Risbud and M Sittinger. Tissue engineering: Advances in *in vitro* cartilage generation. *Trends in biotechnology*, 20(8):351–356, 2002.

[112] DD Swartz, JA Russell, and ST Andreadis. Engineering of fibrin-based functional and implantable small-diameter blood vessels. *American journal of physiology-heart and circulatory physiology*, 288(3):H1451–H1460, 2005.

[113] TAE Ahmed, EV Dare, and M Hincke. Fibrin: A versatile scaffold for tissue engineering applications. *Tissue engineering part B*, 14(2):199–215, 2008.

[114] P de la Puente and D Ludeña. Cell culture in autologous fibrin scaffolds for applications in tissue engineering. *Experimental cell research*, 322(1):1–11, 2014.

[115] SV Dorozhkin. Calcium orthophosphates: Occurrence, properties, biomineralization, pathological calcification and biomimetic applications. *Biomatter*, 1(2):121–164, 2011.

[116] U Gbureck, T Hölzel, I Biermann, JE Barralet, and LM Grover. Preparation of tricalcium phosphate/calcium pyrophosphate structures via rapid prototyping. *Journal of materials science: materials in medicine*, 19(4):1559–1563, 2008.

[117] U Gbureck, JE Barralet, K Spatz, LM Grover, and R Thull. Ionic modification of calcium phosphate cement viscosity. Part I: Hypodermic injection and strength improvement of apatite cement. *Biomaterials*, 25(11):2187–2195, 2004.

[118] RJ Furlong and JF Osborn. Fixation of hip prostheses by hydroxyapatite ceramic coatings. *Journal of bone and joint surgery, British volume*, 73(5):741–745, 1991.

[119] P Habibovic, TM Sees, MA van den Doel, CA van Blitterswijk, and K de Groot. Osteoinduction by biomaterials - Physicochemical and structural influences. *Journal of biomedical materials research part A*, 77(4):747–762, 2006.

[120] M Bohner, L Galea, and N Doebelin. Calcium phosphate bone graft substitutes: Failures and hopes. *Journal of the European ceramic society*, 32(11):2663–2671, 2012.

[121] NL Davison, B ten Harkel, T Schoenmaker, X Luo, H Yuan, V Everts, F Barrère-de Groot, and JD de Bruijn. Osteoclast resorption of beta-tricalcium phosphate controlled by surface architecture. *Biomaterials*, 2014.

[122] I Odler. *Special inorganic cements*. CRC Press, London, UK, 2003.

[123] AD Wilson and JW Nicholson. *Acid-base cements: Their biomedical and industrial applications*. Cambridge University Press, Cambridge, UK, 2005.

[124] H Yuan, H Fernandes, P Habibovic, J de Boer, AMC Barradas, A de Ruiter, WR Walsh, CA van Blitterswijk, and JD de Bruijn. Osteoinductive ceramics as a synthetic alternative to autologous bone grafting. *Proceedings of the national academy of sciences*, 107(31):13614–13619, 2010.

[125] P Habibovic, H Yuan, CM van der Valk, G Meijer, CA van Blitterswijk, and K de Groot. 3D microenvironment as essential element for osteoinduction by biomaterials. *Biomaterials*, 26(17):3565–3575, 2005.

[126] LM Grover, JC Knowles, GJP Fleming, and JE Barralet. *In vitro* ageing of brushite calcium phosphate cement. *Biomaterials*, 24(23):4133–4141, 2003.

[127] LM Grover, U Gbureck, AJ Wright, M Tremayne, and JE Barralet. Biologically mediated resorption of brushite cement *in vitro*. *Biomaterials*, 27(10):2178–2185, 2006.

[128] FH Albee. Studies in bone growth: Triple calcium phosphate as a stimulus to osteogenesis. *Annals of surgery*, 71(1):32–38, 1920.

[129] WE Brown and LC Chow. A new calcium-phosphate setting cement. *Journal of dental research*, 62:672–672, 1983.

[130] P Ducheyne and K De Groot. *In vivo* surface activity of a hydroxyapatite alveolar bone substitute. *Journal of biomedical materials research*, 15(3):441–445, 1981.

[131] D Apelt, F Theiss, AO El-Warrak, K Zlinszky, R Bettschart-Wolfisberger, M Bohner, S Matter, JA Auer, and B Von Rechenberg. *In vivo* behavior of three different injectable hydraulic calcium phosphate cements. *Biomaterials*, 25(7):1439–1451, 2004.

[132] WJ Landis, KJ Hodgens, J Arena, MJ Song, and BF McEwen. Structural relations between collagen and mineral in bone as determined by high voltage electron microscopic tomography. *Microscopy research and technique*, 33(2):192–202, 1996.

[133] H Gao, B Ji, IL Jäger, E Arzt, and P Fratzl. Materials become insensitive to flaws at nanoscale: lessons from nature. *Proceedings of the national academy of sciences*, 100(10):5597–5600, 2003.

[134] W Linhart, D Briem, M Amling, JM Rueger, and J Windolf. Mechanical failure of porous hydroxyapatite ceramics 7.5 years after implantation in the proximal tibial. *Der unfallchirurg*, 107(2):154–157, 2004.

[135] JC Elliott. *Structure and chemistry of the apatites and other calcium orthophosphates*. Elsevier, Amsterdam, Netherlands, 1994.

[136] At Tas and SB Bhaduri. Chemical processing of ($CaHPO_4 \cdot 2\,H_2O$). *Journal of the American ceramic society*, 87(12):2195–2200, 2004.

[137] NA Cummings and GL Nordby. Measurement of synovial fluid pH in normal and arthritic knees. *Arthritis & Rheumatism*, 9(1):47–56, 1966.

[138] O Borkiewicz, J Rakovan, and CL Cahill. Time-resolved *in situ* studies of apatite formation in aqueous solutions. *American mineralogist*, 95(8-9):1224–1236, 2010.

[139] LM Grover, AJ Wright, U Gbureck, A Bolarinwa, J Song, Y Liu, DF Farrar, G Howling, J Rose, and JE Barralet. The effect of amorphous pyrophosphate on calcium phosphate cement resorption and bone generation. *Biomaterials*, 34(28):6631–6637, 2013.

[140] MSA Johnsson and GH Nancollas. The role of brushite and octacalcium phosphate in apatite formation. *Critical reviews in oral biology and medicine*, 3(1):61–82, 1992.

[141] S Rousseau and J Lemaitre. Long-term aging of brushite cements in physiological conditions: An *in vitro* study. *European cells and materials*, 5(Supplement 2):83, 2003.

[142] M Bohner, F Theiss, D Apelt, W Hirsiger, R Houriet, G Rizzoli, E Gnos, C Frei, JA Auer, and B Von Rechenberg. Compositional changes of a dicalcium phosphate dihydrate cement after implantation in sheep. *Biomaterials*, 24(20):3463–3474, 2003.

[143] JZ Paxton, K Donnelly, RP Keatch, and K Baar. Engineering the bone–ligament interface using polyethylene glycol diacrylate incorporated with hydroxyapatite. *Tissue engineering part A*, 15(6):1201–1209, 2008.

[144] C Vonesch, F Aguet, JL Vonesch, and M Unser. The colored revolution of bioimaging. *Signal processing magazine, IEEE*, 23(3):20–31, 2006.

[145] JC Mansfield, JS Bell, J Moger, and CP Winlove. Nonlinear optical microscopy in biomechanics. *Quantitative graph theory: mathematical foundations and applications*, pages 251–260, 2014.

[146] JJ Bozzola and LD Russell. *Electron microscopy: principles and techniques for biologists*. Jones & Bartlett Learning, 1999.

[147] T Dieing, O Hollricher, and J Toporski, editors. *Confocal Raman microscopy*. Springer, Heidelberg, Germany, first edition, 2011.

[148] EL Ritman. Micro-computed tomography – Current status and developments. *Annual review of biomedical engineering*, 6:185–208, 2004.

[149] EL Ritman. Current status of developments and applications of micro-CT. *Annual review of biomedical engineering*, 13:531–552, 2011.

[150] E Meyer. Atomic force microscopy. *Progress in surface science*, 41(1):3–49, 1992.

[151] A Bannerman, JZ Paxton, and LM Grover. Imaging the hard/soft tissue interface. *Biotechnology letters*, 36(3):1–13, 2013.

[152] R Hooke. *Micrographia: Or some physiological descriptions of minute bodies made by magnifying glasses: With observations and inquiries thereupon.* John Martyn, printer to the Royal Society, 1665.

[153] G Cox. *Optical imaging techniques in cell biology.* CRC Press, Boca Raton, FL, second edition, 2012.

[154] P Török and FJ Kao, editors. *Optical imaging and microscopy: Techniques and advanced systems.* Springer, Heidelberg, Germany, second edition, 2007.

[155] SW Paddock. Principles and practices of laser scanning confocal microscopy. *Molecular biotechnology*, 16(2):127–149, 2000.

[156] SW Paddock, editor. *Confocal microscopy: Methods and protocols.* Humana Press Inc, Totowa, NJ, 2014.

[157] J Kapuscinski. DAPI: A DNA-specific fluorescent probe. *Biotechnic and histochemistry*, 70(5):220–233, 1995.

[158] E Wulf, A Deboben, FA Bautz, H Faulstich, and TH Wieland. Fluorescent phallotoxin, a tool for the visualization of cellular actin. *Proceedings of the national academy of sciences*, 76(9):4498–4502, 1979.

[159] J Mansfield, J Yu, D Attenburrow, J Moger, U Tirlapur, J Urban, Z Cui, and CP Winlove. The elastin network: Its relationship with collagen and cells in articular cartilage as visualized by multiphoton microscopy. *Journal of anatomy*, 215(6):682–691, 2009.

[160] Aikaterini Zoumi, Alvin Yeh, and Bruce J Tromberg. Imaging cells and extracellular matrix in vivo by using second-harmonic generation and two-photon excited fluorescence. *Proceedings of the National Academy of Sciences*, 99(17):11014–11019, 2002.

[161] S Zhuo, J Chen, X Jiang, X Cheng, and S Xie. Visualizing extracellular matrix and sensing fibroblasts metabolism in human dermis by nonlinear spectral imaging. *Skin research and technology*, 13(4):406–411, 2007.

[162] RM Williams, WR Zipfel, and WW Webb. Interpreting second-harmonic generation images of collagen I fibrils. *Biophysical journal*, 88(2):1377–1386, 2005.

[163] I Gusachenko, V Tran, YG Houssen, JM Allain, and MC Schanne-Klein. Polarization-resolved second-harmonic generation in tendon upon mechanical stretching. *Biophysical journal*, 102(9):2220–2229, 2012.

[164] RM Delaine-Smith, NH Green, SJ Matcher, S MacNeil, and GC Reilly. Monitoring fibrous scaffold guidance of three-dimensional collagen organisation using minimally-invasive second harmonic generation. *PloS one*, 9(2):e89761, 2014.

[165] DB Williams and CB Carter. *The transmission electron microscope*. Springer, 1996.

[166] G Turrell and J Corset, editors. *Raman microscopy: Developments and applications*. Academic Press, San Diego, CA, first edition, 1996.

[167] WH Weber and R Merlin. *Raman scattering in materials science*, volume 42. Springer Science & Business Media, 2013.

[168] A Smekal. Zur quantentheorie der dispersion. *Naturwissenschaften*, 11(43):873–875, 1923.

[169] CV Raman and KS Krishnan. A new type of secondary radiation. *Nature*, 121(3048):501–502, 1928.

[170] I Kohl, K Winkel, M Bauer, KR Liedl, T Loerting, and E Mayer. Raman spectroscopic study of the phase transition of amorphous to crystalline β-carbonic acid. *Angewandte chemie international edition*, 48(15):2690–2694, 2009.

[171] LS Taylor and G Zografi. The quantitative analysis of crystallinity using FT-Raman spectroscopy. *Pharmaceutical research*, 15(5):755–761, 1998.

[172] M Kobayashi, F Kaneko, K Sato, and M Suzuki. Vibrational spectroscopic study on polymorphism and order-disorder phase transition in oleic acid. *The journal of physical chemistry*, 90(23):6371–6378, 1986.

[173] ACS Talari, Z Movasaghi, S Rehman, and I Rehman. Raman spectroscopy of biological tissues. *Applied spectroscopy reviews*, 50(1):46–111, 2014.

[174] Z Movasaghi, S Rehman, and IU Rehman. Raman spectroscopy of biological tissues. *Applied spectroscopy reviews*, 42(5):493–541, 2007.

[175] G Socrates. *Infrared and Raman characteristic group frequencies: Tables and charts*. John Wiley and Sons, Chichester, UK, third edition, 2004.

[176] FS Parker. *Applications of infrared, Raman, and resonance Raman spectroscopy in biochemistry*. Plenum Press, New York, NY, 1983.

[177] D Lin-Vien, NB Colthup, WG Fateley, and JG Grasselli. *The handbook of infrared and Raman characteristic frequencies of organic molecules*. Academic Press, London, UK, 1991.

[178] AG Schwartz, JD Pasteris, GM Genin, TL Daulton, and S Thomopoulos. Mineral distributions at the developing tendon enthesis. *PloS one*, 7(11):e48630, 2012.

[179] G Penel, N Leroy, P Van Landuyt, B Flautre, P Hardouin, J Lemaitre, and G Leroy. Raman microspectrometry studies of brushite cement: *In vivo* evolution in a sheep model. *Bone*, 25(2):81S–84S, 1999.

[180] G Penel, C Delfosse, M Descamps, and G Leroy. Composition of bone and apatitic biomaterials as revealed by intravital Raman microspectroscopy. *Bone*, 36(5):893–901, 2005.

[181] NJ Crane and EA Elster. Vibrational spectroscopy: A tool being developed for the noninvasive monitoring of wound healing. *Journal of biomedical optics*, 17(1):010902, 2012.

[182] CM Perlaki, Q Liu, and M Lim. Raman spectroscopy based techniques in tissue engineering – An overview. *Applied spectroscopy reviews*, 49(7):513–532, 2014.

[183] YJ Hwang and JG Lyubovitsky. The structural analysis of three-dimensional fibrous collagen hydrogels by Raman microspectroscopy. *Biopolymers*, 99(6):349–356, 2013.

[184] A Downes and A Elfick. Raman spectroscopy and related techniques in biomedicine. *Sensors*, 10(3):1871–1889, 2010.

[185] A Khmaladze, A Ganguly, S Kuo, M Raghavan, R Kainkaryam, JH Cole, K Izumi, CL Marcelo, SE Feinberg, and MD Morris. Tissue-engineered constructs of human oral mucosa examined by Raman spectroscopy. *Tissue engineering part C*, 19(4):299–306, 2012.

[186] M Leroy, JF Labbé, M Ouellet, J Jean, T Lefèvre, G Laroche, M Auger, and R Pouliot. A comparative study between human skin substitutes and normal human skin using Raman microspectroscopy. *Acta biomaterialia*, 10(6):2703–2711, 2014.

[187] NJ Everall. Modeling and measuring the effect of refraction on the depth resolution of confocal Raman microscopy. *Applied spectroscopy*, 54(6):773–782, 2000.

[188] NJ Everall. The influence of out-of-focus sample regions on the surface specificity of confocal Raman microscopy. *Applied spectroscopy*, 62(6):591–598, 2008.

[189] A Rae, R Stosch, P Klapetek, AR Hight W, and D Roy. State of the art Raman techniques for biological applications. *Methods*, 68(2):338–347, 2014.

[190] J Srajer, A Schwaighofer, and C Nowak. Surface-enhanced Raman spectroscopy for biomedical diagnostics and imaging. *Biomedical spectroscopy and imaging*, 2(1):51–71, 2013.

[191] JX Cheng and XS Xie. Coherent anti-Stokes Raman scattering microscopy: Instrumentation, theory, and applications. *The journal of physical chemistry B*, 108(3):827–840, 2004.

[192] CW Freudiger, W Min, BG Saar, S Lu, GR Holtom, C He, JC Tsai, JX Kang, and XS Xie. Label-free biomedical imaging with high sensitivity by stimulated Raman scattering microscopy. *Science*, 322(5909):1857–1861, 2008.

[193] BG Saar, CW Freudiger, J Reichman, CM Stanley, GR Holtom, and XS Xie. Video-rate molecular imaging *in vivo* with stimulated Raman scattering. *Science*, 330(6009):1368–1370, 2010.

[194] CL Evans, EO Potma, M Puoris'haag, D Côté, CP Lin, and XS Xie. Chemical imaging of tissue *in vivo* with video-rate coherent anti-Stokes Raman scattering

microscopy. *Proceedings of the national academy of sciences*, 102(46):16807–16812, 2005.

[195] BD Metscher. MicroCT for comparative morphology: simple staining methods allow high-contrast 3D imaging of diverse non-mineralized animal tissues. *BMC physiology*, 9(1):11, 2009.

[196] BD Metscher. MicroCT for developmental biology: A versatile tool for high-contrast 3D imaging at histological resolutions. *Developmental dynamics*, 238(3):632–640, 2009.

[197] NS Jeffery, RS Stephenson, JA Gallagher, JC Jarvis, and PG Cox. Micro-computed tomography with iodine staining resolves the arrangement of muscle fibres. *Journal of biomechanics*, 44(1):189–192, 2011.

[198] C Sun, F Miao, X Wang, T Wang, R Ma, D Wang, and C Liu. An initial qualitative study of dual-energy CT in the knee ligaments. *Surgical and radiologic anatomy*, 30(5):443–447, 2008.

[199] K Deng, C Sun, C Liu, and R Ma. Initial experience with visualizing hand and foot tendons by dual–energy computed tomography. *Clinical imaging*, 33(5):384–389, 2009.

[200] A Appel, MA Anastasio, and EM Brey. Potential for imaging engineered tissues with X-ray phase contrast. *Tissue engineering part B*, 17(5):321–330, 2011.

[201] EC Ismail, W Kaabar, D Garrity, O Gundogdu, O Bunk, F Pfeiffer, MJ Farquharson, and DA Bradley. X-ray phase contrast imaging of the bone–cartilage interface. *Applied radiation and isotopes*, 68(4):767–771, 2010.

[202] T Takeda, J Wu, A Yoneyama, Y Tsuchiya, TT Lwin, Y Hirai, T Kuroe, T Yuasa, K Hyodo, and FA Dilmanian. SR biomedical imaging with phase-contrast and fluorescent S-ray CT. In *Optical science and technology, the SPIE 49th annual meeting*, pages 380–391, 2004.

[203] LJ Meng, G Fu, N Li, M Newville, P Eng, and P La Rivière. X-ray fluorescence tomography using imaging detectors. In *SPIE optical engineering and applications*, pages 78041B1–B9, 2010.

[204] J Bennett, A Opie, Q Xu, H Yu, M Walsh, A Butler, P Butler, G Cao, A Mohs, and G Wang. Hybrid spectral micro-CT: system design, implementation and preliminary results. In *IEEE transactions on biomedical engineering*, volume 61, pages 246–253, 2014.

[205] JF Barrett and N Keat. Artifacts in CT: Recognition and avoidance 1. *Radiographics*, 24(6):1679–1691, 2004.

[206] EMA Anas, JG Kim, SY Lee, and MK Hasan. Comparison of ring artifact removal methods using flat panel detector based CT images. *Biomedical engineering*, 10(1):72, 2011.

[207] DE Morris, ML Mather, CG Simon, and JA Crowe. Time-optimized X-ray micro-CT imaging of polymer based scaffolds. *Journal of biomedical materials research part B*, 100(2):360–367, 2012.

[208] RS Voronov, SB VanGordon, RL Shambaugh, DV Papavassiliou, and VI Sikavitsas. 3D tissue-engineered construct analysis via conventional high-resolution microcomputed tomography without X-ray contrast. *Tissue engineering part C*, 19(5):327–335, 2012.

[209] JR Vetsch, SJ Paulsen, R Müller, and S Hofmann. Effect of fetal bovine serum on mineralization in silk fibroin scaffolds. *Acta biomaterialia*, 13:277–285, 2015.

[210] G Binnig, CF Quate, and C Gerber. Atomic force microscope. *Physical review letters*, 56(9):930, 1986.

[211] S Chowdhury and MT Laugier. The use of non-contact AFM with nanoindentation techniques for measuring mechanical properties of carbon nitride thin films. *Applied surface science*, 233(1):219–226, 2004.

[212] Y Zhu, Z Dong, UC Wejinya, S Jin, and K Ye. Determination of mechanical properties of soft tissue scaffolds by atomic force microscopy nanoindentation. *Journal of biomechanics*, 44(13):2356–2361, 2011.

[213] ZM Zhang, S Chen, and YZ Liang. Baseline correction using adaptive iteratively reweighted penalized least squares. *Analyst*, 135(5):1138–1146, 2010.

[214] F de Chaumont, S Dallongeville, N Chenouard, N Hervé, S Pop, T Provoost, V Meas-Yedid, P Pankajakshan, T Lecomte, and Y Le Montagner. Icy: An open

bioimage informatics platform for extended reproducible research. *Nature methods*, 9(7):690–696, 2012.

[215] J Clark and DJ Stechschulte. The interface between bone and tendon at an insertion site: A study of the quadriceps tendon insertion. *Journal of anatomy*, 192(04):605–616, 1998.

[216] L Zhao, A Thambyah, and ND Broom. A multi-scale structural study of the porcine anterior cruciate ligament tibial enthesis. *Journal of anatomy*, 224(6):624–633, 2014.

[217] C Rashidifard, SD Martin, N Kumar, E Azimi, B Liu, and ME Brezinski. Single detector polarization-sensitive optical coherence tomography for assessment of rotator cuff tendon integrity. *American journal of orthodontics*, 41(8):351–357, 2012.

[218] H Oguma, G Murakami, H Takahashi-Iwanaga, M Aoki, and S Ishii. Early anchoring collagen fibers at the bonetendon interface are conducted by woven bone formation: Light microscope and scanning electron microscope observation using a canine model. *Journal of orthopaedic research*, 19(5):873–880, 2001.

[219] C Wiell, M Szkudlarek, M Hasselquist, JM Møller, J Nørregaard, L Terslev, and M Østergaard. Power Doppler ultrasonography of painful Achilles tendons and entheses in patients with and without spondyloarthropathya comparison with clinical examination and contrast-enhanced MRI. *Clinical rheumatology*, 32(3):301–308, 2013.

[220] M Benjamin, S Milz, and GM Bydder. Magnetic resonance imaging of entheses. Part 1. *Clinical radiology*, 63(6):691–703, 2008.

[221] M Benjamin, S Milz, and GM Bydder. Magnetic resonance imaging of entheses. Part 2. *Clinical radiology*, 63(6):704–711, 2008.

[222] IE Chesnick, CB Fowler, JT Mason, and K Potter. Novel mineral contrast agent for magnetic resonance studies of bone implants grown on a chick chorioallantoic membrane. *Magnetic resonance imaging*, 29(9):1244–1254, 2011.

[223] M Ventura, Y Sun, V Rusu, P Laverman, P Borm, A Heerschap, E Oosterwijk, OC Boerman, JA Jansen, and XF Walboomers. Dual contrast agent for computed tomography and magnetic resonance hard tissue imaging. *Tissue engineering part C*, 19(6):405–416, 2012.

[224] M Gudur, RR Rao, Y Hsiao, AW Peterson, CX Deng, and JP Stegemann. Non-invasive, quantitative, spatiotemporal characterization of mineralization in three-dimensional collagen hydrogels using high-resolution spectral ultrasound imaging. *Tissue engineering part C*, 18(12):935–946, 2012.

[225] KP Mercado, M Helguera, D Hocking, and D Dalecki. Noninvasive quantitative imaging of collagen microstructure in three-dimensional hydrogels using high-frequency ultrasound. *Tissue engineering*, In Press, 2014.

[226] L Wang, YX Su, GS Zheng, GQ Liao, and WH Zhang. Healing masseter entheses of mandibular reconstruction with autograft – Raman spectroscopic and histological study. *International journal of oral and maxillofacial surgery*, 42(7):915–922, 2013.

[227] JP Spalazzi, AL Boskey, N Pleshko, and HH Lu. Quantitative mapping of matrix content and distribution across the ligament-to-bone insertion. *PloS one*, 8(9):e74349, 2013.

[228] SE Campbell, VL Ferguson, and DC Hurley. Nanomechanical mapping of the osteochondral interface with contact resonance force microscopy and nanoindentation. *Acta biomaterialia*, 8(12):4389–4396, 2012.

[229] JD Lin, S Aloni, V Altoe, SM Webb, MI Ryder, and SP Ho. Elastic discontinuity due to ectopic calcification in a human fibrous joint. *Acta biomaterialia*, 9(1):4787–4795, 2013.

[230] S Koutsopoulos. Synthesis and characterization of hydroxyapatite crystals: A review study on the analytical methods. *Journal of biomedical materials research*, 62(4):600–612, 2002.

[231] S Koburger, A Bannerman, LM Grover, FA Müller, J Bowen, and JZ Paxton. A novel method for monitoring mineralisation in hydrogels at the engineered hard–soft tissue interface. *Biomaterials science*, 2(1):41–51, 2014.

[232] M Keeney and A Pandit. The osteochondral junction and its repair via bi-phasic tissue engineering scaffolds. *Tissue Engineering Part B*, 15(1):55–73, 2009.

[233] SP Ho, MP Kurylo, TK Fong, SSJ Lee, HD Wagner, MI Ryder, and GW Marshall. The biomechanical characteristics of the bone-periodontal ligament-cementum complex. *Biomaterials*, 31(25):6635–6646, 2010.

[234] CP Lin, WH Douglas, and SL Erlandsen. Scanning electron microscopy of type I collagen at the dentin–enamel junction of human teeth. *Journal of histochemistry and cytochemistry*, 41(3):381–388, 1993.

[235] K Grandfield, NL Chattah, S Djomehri, N Eidelmann, FC Eichmiller, S Webb, PJ Schuck, M Nweeia, and SP Ho. The narwhal (Monodon monoceros) cementum–dentin junction: A functionally graded biointerphase. *Proceedings of the institution of mechanical engineers part H*, 228(8):754–767, 2014.

[236] Y Liu, S Thomopoulos, C Chen, V Birman, MJ Buehler, and GM Genin. Modelling the mechanics of partially mineralized collagen fibrils, fibres and tissue. *Journal of the royal society interface*, 11(92):20130835, 2014.

[237] F Grases, L Muntaner-Gimbernat, M Vilchez-Mira, A Costa-Bauzá, F Tur, RM Prieto, M Torrens-Mas, and FG Vega. Characterization of deposits in patients with calcific tendinopathy of the supraspinatus. Role of phytate and osteopontin. *Journal of orthopaedic research*, 2014.

[238] HK Uhthoff and JW Loehr. Calcific tendinopathy of the rotator cuff: Pathogenesis, diagnosis, and management. *Journal of the American academy of orthopaedic surgeons*, 5(4):183–191, 1997.

[239] O Steinbrocker. The painful shoulder. *Arthritis and allied conditions. Lea and Febiger, Philadelphia*, pages 1461–1469, 1972.

[240] JA Inzana, D Olvera, SM Fuller, JP Kelly, OA Graeve, EM Schwarz, SL Kates, and HA Awad. 3D printing of composite calcium phosphate and collagen scaffolds for bone regeneration. *Biomaterials*, 35(13):4026–4034, 2014.

[241] KA Lomashvili, S Cobbs, RA Hennigar, KI Hardcastle, and WC ONeill. Phosphate-induced vascular calcification: Role of pyrophosphate and osteopontin. *Journal of the American society of nephrology*, 15(6):1392–1401, 2004.

[242] J Rosenthal, V Mangal, D Walker, M Bennett, TJ Mohun, and CW Lo. Rapid high resolution three dimensional reconstruction of embryos with episcopic fluorescence image capture. *Birth defects research part C*, 72(3):213–223, 2004.

[243] KJ Koski and JL Yarger. Brillouin imaging. *Applied physics letters*, 87(6):061903, 2005.

[244] F Palombo, M Madami, N Stone, and D Fioretto. Mechanical mapping with chemical specificity by confocal Brillouin and Raman microscopy. *Analyst*, 139(4):729–733, 2014.

[245] Y Li, G Huang, X Zhang, L Wang, Y Du, TJ Lu, and F Xu. Engineering cell alignment *in vitro*. *Biotechnology advances*, 32(2):347–365, 2013.

[246] D Huang, TR Chang, A Aggarwal, RC Lee, and HP Ehrlich. Mechanisms and dynamics of mechanical strengthening in ligament-equivalent fibroblast-populated collagen matrices. *Annals of biomedical engineering*, 21(3):289–305, 1993.

[247] M Eastwood, VC Mudera, DA McGrouther, and RA Brown. Effect of precise mechanical loading on fibroblast populated collagen lattices: Morphological changes. *Cell motility and the cytoskeleton*, 40(1):13–21, 1998.

[248] EJ Lee, JW Holmes, and KD Costa. Remodeling of engineered tissue anisotropy in response to altered loading conditions. *Annals of biomedical engineering*, 36(8):1322–1334, 2008.

[249] F Li, B Li, QM Wang, and JHC Wang. Cell shape regulates collagen type I expression in human tendon fibroblasts. *Cell motility and the cytoskeleton*, 65(4):332–341, 2008.

[250] JHC Wang, F Jia, TW Gilbert, and SLY Woo. Cell orientation determines the alignment of cell-produced collagenous matrix. *Journal of biomechanics*, 36(1):97–102, 2003.

[251] A Kapoor, EHG Caporali, PJA Kenis, and MC Stewart. Microtopographically patterned surfaces promote the alignment of tenocytes and extracellular collagen. *Acta biomaterialia*, 6(7):2580–2589, 2010.

[252] N de Jonge, FMW Kanters, FPT Baaijens, and CVC Bouten. Strain-induced collagen organization at the micro-level in fibrin-based engineered tissue constructs. *Annals of biomedical engineering*, 41(4):763–774, 2013.

[253] Y Pang, X Wang, D Lee, and HP Greisler. Dynamic quantitative visualization of single cell alignment and migration and matrix remodeling in 3-D collagen hydrogels under mechanical force. *Biomaterials*, 32(15):3776–3783, 2011.

[254] CP Ng, B Hinz, and MA Swartz. Interstitial fluid flow induces myofibroblast differentiation and collagen alignment *in vitro*. *Journal of cell science*, 118(20):4731–4739, 2005.

[255] J Foolen, VS Deshpande, FMW Kanters, and F Baaijens. The influence of matrix integrity on stress-fiber remodeling in 3D. *Biomaterials*, 33(30):7508–7518, 2012.

[256] MF Hadi, EA Sander, JW Ruberti, and VH Barocas. Simulated remodeling of loaded collagen networks via strain-dependent enzymatic degradation and constant-rate fiber growth. *Mechanics of materials*, 44:72–82, 2012.

[257] AA Appel, MA Anastasio, JC Larson, and EM Brey. Imaging challenges in biomaterials and tissue engineering. *Biomaterials*, 34(28):6615–6630, 2013.

[258] TT Tower, MR Neidert, and RT Tranquillo. Fiber alignment imaging during mechanical testing of soft tissues. *Annals of biomedical engineering*, 30(10):1221–1233, 2002.

[259] B de Campos Vidal. Image analysis of tendon helical superstructure using interference and polarized light microscopy. *Micron*, 34(8):423–432, 2003.

[260] N Ugryumova, DP Attenburrow, CP Winlove, and SJ Matcher. The collagen structure of equine articular cartilage, characterized using polarization-sensitive optical coherence tomography. *Journal of physics D*, 38(15):2612–2619, 2005.

[261] AR Nectow, ES Gil, DL Kaplan, and ME Kilmer. A statistical algorithm for assessing cellular alignment. *Journal of biomedical materials research part A*, 101(3):884–891, 2013.

[262] AR Nectow, ME Kilmer, and DL Kaplan. Quantifying cellular alignment on anisotropic biomaterial platforms. *Journal of biomedical materials research part A*, 102(2):420–428, 2014.

[263] F Xu, T Beyazoglu, E Hefner, UA Gurkan, and U Demirci. Automated and adaptable quantification of cellular alignment from microscopic images for tissue engineering applications. *Tissue engineering part C*, 17(6):641–649, 2011.

[264] NJ Schaub, SJ Kirkpatrick, and RJ Gilbert. Automated methods to determine electrospun fiber alignment and diameter using the Radon transform. *BioNanoScience*, 3(3):329–342, 2013.

[265] CE Ayres, GL Bowlin, SC Henderson, L Taylor, J Shultz, J Alexander, TA Telemeco, and DG Simpson. Modulation of anisotropy in electrospun tissue-engineering scaffolds: analysis of fiber alignment by the fast Fourier transform. *Biomaterials*, 27(32):5524–5534, 2006.

[266] CE Ayres, BS Jha, H Meredith, JR Bowman, GL Bowlin, SC Henderson, and DG Simpson. Measuring fiber alignment in electrospun scaffolds: a user's guide to the 2D fast Fourier transform approach. *Journal of biomaterials science, polymer edition*, 19(5):603–621, 2008.

[267] JP Marquez. Fourier analysis and automated measurement of cell and fiber angular orientation distributions. *International journal of solids and structures*, 43(21):6413–6423, 2006.

[268] MS Sacks, DB Smith, and ED Hiester. A small angle light scattering device for planar connective tissue microstructural analysis. *Annals of biomedical engineering*, 25(4):678–689, 1997.

[269] MD Morris and GS Mandair. Raman assessment of bone quality. *Clinical orthopaedics and related research*, 469(8):2160–2169, 2011.

[270] J Marx, G Hudry-Clergeon, F Capet-Antonini, and L Bernard. Laser Raman spectroscopy study of bovine fibrinogen and fibrin. *Biochimica et biophysica acta*, 578(1):107–115, 1979.

[271] H Aubin, JW Nichol, CB Hutson, H Bae, AL Sieminski, DM Cropek, P Akhyari, and A Khademhosseini. Directed 3D cell alignment and elongation in microengineered hydrogels. *Biomaterials*, 31(27):6941–6951, 2010.

[272] CP Ng and MA Swartz. Mechanisms of interstitial flow-induced remodeling of fibroblast–collagen cultures. *Annals of biomedical engineering*, 34(3):446–454, 2006.

[273] VC Mudera, R Pleass, M Eastwood, R Tarnuzzer, G Schultz, P Khaw, DA McGrouther, and RA Brown. Molecular responses of human dermal fibroblasts to dual cues: Contact guidance and mechanical load. *Cell motility and the cytoskeleton*, 45(1):1–9, 2000.

[274] JHC Wang and ES Grood. The strain magnitude and contact guidance determine orientation response of fibroblasts to cyclic substrate strains. *Connective tissue research*, 41(1):29–36, 2000.

[275] TL Tuan, A Song, S Chang, S Younai, and ME Nimni. *In Vitro* fibroplasia: Matrix contraction, cell growth, and collagen production of fibroblasts cultured in fibrin gels. *Experimental cell research*, 223(1):127–134, 1996.

[276] L Zhang, BS Gardiner, DW Smith, P Pivonka, and A Grodzinsky. A fully coupled poroelastic reactive-transport model of cartilage. *Molecular and cellular biomechanics*, 5(2):133, 2008.

[277] RL Williams, I Vizcaíno-Castón, and LM Grover. Quantification of volume and size distribution of internalised calcium phosphate particles and their influence on cell fate. *Biomaterials science*, 2014.

[278] RL Williams, NM Salimi, GA Leeke, RH Bridson, and LM Grover. Intracellular tracking of fluorescently labelled calcium phosphate particles. *Bone and joint journal orthopaedic proceedings supplement*, 96(Supplement 11):294–294, 2014.

[279] BG Frushour and JL Koenig. Raman scattering of collagen, gelatin, and elastin. *Biopolymers*, 14(2):379–391, 1975.

[280] E Green, R Ellis, and P Winlove. The molecular structure and physical properties of elastin fibers as revealed by Raman microspectroscopy. *Biopolymers*, 89(11):931–940, 2008.

[281] MØ Olderøy, MB Lilledahl, MS Beckwith, JE Melvik, F Reinholt, P Sikorski, and JE Brinchmann. Biochemical and structural characterization of neocartilage formed by mesenchymal stem cells in alginate hydrogels. *PloS one*, 9(3):e91662, 2014.

[282] HA Benhardt and EM Cosgriff-Hernandez. The role of mechanical loading in ligament tissue engineering. *Tissue engineering part B*, 15(4):467–475, 2009.

[283] RI Abousleiman, Y Reyes, P McFetridge, and V Sikavitsas. Tendon tissue engineering using cell-seeded umbilical veins cultured in a mechanical stimulator. *Tissue engineering part A*, 15(4):787–795, 2008.

[284] JA Hannafin, SP Arnoczky, A Hoonjan, and PA Torzilli. Effect of stress deprivation and cyclic tensile loading on the material and morphologic properties of canine flexor digitorum profundus tendon: An *in vitro* study. *Journal of orthopaedic research*, 13(6):907–914, 1995.

[285] QM Tang, JL Chen, WL Shen, Z Yin, HH Liu, Z Fang, BC Heng, HW Ouyang, and X Chen. Fetal and adult fibroblasts display intrinsic differences in tendon tissue engineering and regeneration. *Scientific reports*, 4:5515, 2014.

[286] A Masic, L Bertinetti, R Schuetz, L Galvis, N Timofeeva, JWC Dunlop, J Seto, MA Hartmann, and P Fratzl. Observations of multiscale, stress-induced changes of collagen orientation in tendon by polarized Raman spectroscopy. *Biomacromolecules*, 12(11):3989–3996, 2011.

[287] ML Mather, SP Morgan, DE Morris, Q Zhu, J Kee, A Zoladek, JA Crowe, I Notingher, DJ Williams, and PA Johnson. Raman spectroscopy and rotating orthogonal polarization imaging for non-destructive tracking of collagen deposition in tissue engineered skin and tendon. In *Optics in tissue engineering and regenerative medicine III, SPIE photonics west, California, USA*, 2009.

[288] M Janko, P Davydovskaya, M Bauer, A Zink, and RW Stark. Anisotropic Raman scattering in collagen bundles. *Optics letters*, 35(16):2765–2767, 2010.

[289] T York, SB Powell, S Gao, L Kahan, T Charanya, D Saha, NW Roberts, T Cronin, J Marshall, and S Achilefu. Bioinspired polarization imaging sensors: From circuits and optics to signal processing algorithms and biomedical applications. *Proceedings of the IEEE*, 102(10):1450–1469, 2014.

[290] TA Planchon, L Gao, DE Milkie, MW Davidson, JA Galbraith, CG Galbraith, and E Betzig. Rapid three-dimensional isotropic imaging of living cells using bessel beam plane illumination. *Nature methods*, 8(5):417–423, 2011.

[291] J Ferrier, A Kesthely, and SL Xia. Hormone responses of *in vitro* bone nodule cells: studies on changes of intracellular calcium and membrane potential in response to parathyroid hormone and calcitonin. *Bone and mineral*, 19(2):103–116, 1992.

[292] C Campagnoli, IAG Roberts, S Kumar, PR Bennett, I Bellantuono, and NM Fisk. Identification of mesenchymal stem/progenitor cells in human first-trimester fetal blood, liver, and bone marrow. *Blood*, 98(8):2396–2402, 2001.

[293] C Laurencin, Y Khan, and SF El-Amin. Bone graft substitutes. *Expert review of medical devices*, 3(1):49–57, 2006.

[294] SWS Laurie, LB Kaban, JB Mulliken, and JE Murray. Donor-site morbidity after harvesting rib and iliac bone. *Plastic and reconstructive surgery*, 73(6):933–938, 1984.

[295] CF Lord, MC Gebhardt, WW Tomford, and HJ Mankin. Infection in bone allografts. Incidence, nature, and treatment. *The journal of bone and joint surgery*, 70(3):369–376, 1988.

[296] MH Alkhraisat, FT Marino, JR Retama, LB Jerez, and E López-Cabarcos. Beta-tricalcium phosphate release from brushite cement surface. *Journal of biomedical materials research part A*, 84(3):710–717, 2008.

[297] HB Pan and BW Darvell. Calcium phosphate solubility: The need for re-evaluation. *Crystal growth and design*, 9(2):639–645, 2008.

[298] SV Dorozhkin. A review on the dissolution models of calcium apatites. *Progress in crystal growth and characterization of materials*, 44(1):45–61, 2002.

[299] P Frayssinet, L Gineste, P Conte, J Fages, and N Rouquet. Short-term implantation effects of a DCPD-based calcium phosphate cement. *Biomaterials*, 19(11):971–977, 1998.

[300] B Flautre, C Delecourt, MC Blary, P Van Landuyt, J Lemaitre, and P Hardouin. Volume effect on biological properties of a calcium phosphate hydraulic cement: Experimental study in sheep. *Bone*, 25(2):35S–39S, 1999.

[301] Hardouin P Lemaitre J Pasquier G Flautre B Ohura K, Bohner M. Resorption of, and bone formation from, new beta-tricalcium phosphate-monocalcium phosphate cements: An *in vivo* study. *Journal of biomedical materials research*, 30(2):193–200, 1996.

[302] K Ishikawa. Bone substitute fabrication based on dissolution-precipitation reactions. *Materials*, 3(2):1138–1155, 2010.

[303] VS Komlev, M Mastrogiacomo, RC Pereira, F Peyrin, F Rustichelli, and R Cancedda. Biodegradation of porous calcium phosphate scaffolds in an ectopic bone formation model studied by X-ray computed microtomography. *European cells and materials*, 19:136–146, 2010.

[304] VS Komlev, M Mastrogiacomo, F Peyrin, R Cancedda, and F Rustichelli. X-ray synchrotron radiation pseudo-holotomography as a new imaging technique to investigate angio-and microvasculogenesis with no usage of contrast agents. *Tissue engineering part C*, 15(3):425–430, 2009.

[305] C Combes and C Rey. Amorphous calcium phosphates: synthesis, properties and uses in biomaterials. *Acta biomaterialia*, 6(9):3362–3378, 2010.

[306] Y Shanjani, D Croos, JN Amritha, RM Pilliar, RA Kandel, and E Toyserkani. Solid freeform fabrication and characterization of porous calcium polyphosphate structures for tissue engineering purposes. *Journal of biomedical materials research part B*, 93(2):510–519, 2010.

[307] GS Mandair and MD Morris. Contributions of Raman spectroscopy to the understanding of bone strength. *BoneKEy reports*, 4:620, 2015.

[308] SG Kazarian and KLA Chan. ATR-FTIR spectroscopic imaging: Recent advances and applications to biological systems. *Analyst*, 138(7):1940–1951, 2013.

[309] G Campi, A Ricci, A Guagliardi, C Giannini, S Lagomarsino, R Cancedda, M Mastrogiacomo, and A Cedola. Early stage mineralization in tissue engineering mapped by high resolution X-ray microdiffraction. *Acta biomaterialia*, 8(9):3411–3418, 2012.

[310] K Abdelkebir, S Morin-Grognet, F Gaudière, G Coquerel, B Labat, H Atmani, and G Ladam. Biomimetic layer-by-layer templates for calcium phosphate biomineralization. *Acta biomaterialia*, 8(9):3419–3428, 2012.

[311] AM Young, PYJ Ng, U Gbureck, SN Nazhat, JE Barralet, and MP Hofmann. Characterization of chlorhexidine-releasing, fast-setting, brushite bone cements. *Acta biomaterialia*, 4(4):1081–1088, 2008.

[312] NJ Crane, V Popescu, MD Morris, P Steenhuis, and MA Ignelzi Jr. Raman spectroscopic evidence for octacalcium phosphate and other transient mineral species deposited during intramembranous mineralization. *Bone*, 39(3):434–442, 2006.

[313] JH Petropoulos, K Tsimillis, C Savvakis, and V Havredaki. Simple sensitive techniques for absolute and differential helium pycnometry. *Journal of physics part E*, 16(11):1112, 1983.

[314] M Bohner, HP Merkle, and J Lemai. *In vitro* aging of a calcium phosphate cement. *Journal of materials science: materials in medicine*, 11(3):155–162, 2000.

[315] P Jamshidi, RH Bridson, AJ Wright, and LM Grover. Brushite cement additives inhibit attachment to cell culture beads. *Biotechnology and bioengineering*, 110(5):1487–1494, 2013.

[316] S Mandel and AC Tas. Brushite ($CaHPO_4 \cdot 2\,H_2O$) to octacalcium phosphate ($Ca_8H_2(PO_4)_6 \cdot 5\,H_2O$) transformation in DMEM solutions at 36.5°C. *Materials science and engineering part C*, 30(2):245–254, 2010.

[317] M Bohner and J Lemaitre. Can bioactivity be tested *in vitro* with SBF solution? *Biomaterials*, 30(12):2175–2179, 2009.

[318] D Rohanova, AR Boccaccini, D Horkavcova, and P Bozděchova. Is non-buffered DMEM solution suitable medium for *in vitro* bioactivity tests? *Journal of materials chemistry part B*, 2014.

[319] M Kazanci, P Fratzl, K Klaushofer, and EP Paschalis. Complementary information on *in vitro* conversion of amorphous (precursor) calcium phosphate to hydroxyapatite from Raman microspectroscopy and wide-angle X-ray scattering. *Calcified tissue international*, 79(5):354–359, 2006.

[320] J Christoffersen, MR Christoffersen, W Kibalczyc, and FA Andersen. A contribution to the understanding of the formation of calcium phosphates. *Journal of crystal growth*, 94(3):767–777, 1989.

[321] S Somrani, C Rey, and M Jemal. Thermal evolution of amorphous tricalcium phosphate. *Journal of materials chemistry*, 13(4):888–892, 2003.

[322] C Liu, Y Huang, W Shen, and J Cui. Kinetics of hydroxyapatite precipitation at pH 10 to 11. *Biomaterials*, 22(4):301–306, 2001.

[323] MS Tung and WE Brown. The role of octacalcium phosphate in subcutaneous heterotopic calcification. *Calcified tissue international*, 37(3):329–331, 1985.

[324] A Malsy and M Bohner. Brushite conversion into apatite. *European cells and materials*, 10(Supplement 1):28, 2005.

[325] I Mert, S Mandel, and AC Tas. Do cell culture solutions transform brushite ($CaHPO_4 \cdot 2\,H_2O$)) to octacalcium phosphate ($Ca_8(HPO_4)_2(PO_4)_4 \cdot 5\,H_2O$)? In *Advances in bioceramics and porous ceramics IV: ceramic engineering and science proceedings, volume 32*, pages 79–93, 2011.

[326] P Matousek. Deep non-invasive Raman spectroscopy of living tissue and powders. *Chemical society reviews*, 36(8):1292–1304, 2007.

[327] C Kendall, J Day, J Hutchings, B Smith, N Shepherd, H Barr, and N Stone. Evaluation of Raman probe for oesophageal cancer diagnostics. *Analyst*, 135(12):3038–3041, 2010.

[328] AP Evan, EM Worcester, FL Coe, J Williams Jr, and JE Lingeman. Mechanisms of human kidney stone formation. *Urolithiasis*, 43(1):19–32, 2015.

[329] M Vollenweider, TJ Brunner, S Knecht, RN Grass, M Zehnder, T Imfeld, and WJ Stark. Remineralization of human dentin using ultrafine bioactive glass particles. *Acta biomaterialia*, 3(6):936–943, 2007.

[330] P Fratzl, HS Gupta, EP Paschalis, and P Roschger. Structure and mechanical quality of the collagen–mineral nano-composite in bone. *Journal of materials chemistry*, 14(14):2115–2123, 2004.

[331] MJ Favus and S Christakos. *Primer on the metabolic bone diseases and disorders of mineral metabolism*. Lippincott-Raven, Philadelphia, PA, 1996.

[332] AK Nair, A Gautieri, SW Chang, and MJ Buehler. Molecular mechanics of mineralized collagen fibrils in bone. *Nature communications*, 4:1724, 2013.

[333] RJ White and M Averner. Humans in space. *Nature*, 409(6823):1115–1118, 2001.

[334] JD Sibonga, HJ Evans, HG Sung, ER Spector, TF Lang, VS Oganov, AV Bakulin, LC Shackelford, and AD LeBlanc. Recovery of spaceflight-induced bone loss: bone mineral density after long-duration missions as fitted with an exponential function. *Bone*, 41(6):973–978, 2007.

[335] DE Garland. A clinical perspective on common forms of acquired heterotopic ossification. *Clinical orthopaedics and related research*, 263:13–29, 1991.

[336] JA Forsberg, JM Pepek, S Wagner, K Wilson, J Flint, RC Andersen, D Tadaki, FA Gage, A Stojadinovic, and EA Elster. Heterotopic ossification in high-energy wartime extremity injuries: prevalence and risk factors. *The journal of bone and joint surgery*, 91(5):1084–1091, 2009.

[337] KA Alfieri, JA Forsberg, and BK Potter. Blast injuries and heterotopic ossification. *Bone and joint research*, 1(8):174–179, 2012.

[338] Y Liu, YK Kim, L Dai, N Li, SO Khan, DH Pashley, and FR Tay. Hierarchical and non-hierarchical mineralisation of collagen. *Biomaterials*, 32(5):1291–1300, 2011.

[339] Y Wang, T Azaïs, M Robin, A Vallée, C Catania, P Legriel, G Pehau-Arnaudet, F Babonneau, MM Giraud-Guille, and N Nassif. The predominant role of collagen in the nucleation, growth, structure and orientation of bone apatite. *Nature materials*, 11(8):724–733, 2012.

[340] W Zhang, SS Liao, and FZ Cui. Hierarchical self-assembly of nano-fibrils in mineralized collagen. *Chemistry of materials*, 15(16):3221–3226, 2003.

[341] F Nudelman, AJ Lausch, NAJM Sommerdijk, and ED Sone. *In vitro* models of collagen biomineralization. *Journal of structural biology*, 183(2):258–269, 2013.

[342] LN Niu, K Jiao, H Ryou, CKY Yiu, JH Chen, L Breschi, DD Arola, DH Pashley, and FR Tay. Multiphase intrafibrillar mineralization of collagen. *Angewandte chemie*, 125(22):5874–5878, 2013.

[343] SJ Omelon and MD Grynpas. Relationships between polyphosphate chemistry, biochemistry and apatite biomineralization. *Chemical reviews*, 108(11):4694–4715, 2008.

[344] AR Ten Cate. *Oral histology*. Mosby, Philadelphia, PA, fourth edition, 1994.

[345] JD Hartgerink, E Beniash, and SI Stupp. Self-assembly and mineralization of peptide-amphiphile nanofibers. *Science*, 294(5547):1684–1688, 2001.

[346] M Kikuchi, S Itoh, S Ichinose, K Shinomiya, and J Tanaka. Self-organization mechanism in a bone-like hydroxyapatite/collagen nanocomposite synthesized in vitro and its biological reaction *in vivo*. *Biomaterials*, 22(13):1705–1711, 2001.

[347] WS Hinegardner. Needle-shaped crystals of sodium chloride. *Journal of the American chemical society*, 55(4):1461–1462, 1933.

[348] X Li and J Chang. Preparation of bone-like apatite–collagen nanocomposites by a biomimetic process with phosphorylated collagen. *Journal of biomedical materials research part A*, 85(2):293–300, 2008.

[349] D Lickorish, JAM Ramshaw, JA Werkmeister, V Glattauer, and CR Howlett. Collagen–hydroxyapatite composite prepared by biomimetic process. *Journal of biomedical materials research part A*, 68(1):19–27, 2004.

[350] IL Cameron, NJ Short, and GD Fullerton. Verification of simple hydration/dehydration methods to characterize multiple water compartments on tendon type 1 collagen. *Cell biology international*, 31(6):531–539, 2007.

[351] L Gu, YK Kim, Y Liu, H Ryou, CE Wimmer, L Dai, DD Arola, SW Looney, DH Pashley, and FR Tay. Biomimetic analogs for collagen biomineralization. *Journal of dental research*, 90(1):82–87, 2011.

[352] RT Franceschi, BS Iyer, and Y Cui. Effects of ascorbic acid on collagen matrix formation and osteoblast differentiation in murine MC3T3-E1 cells. *Journal of bone and mineral research*, 9(6):843–854, 1994.

[353] MM Hurley, C Abreu, G Gronowicz, H Kawaguchi, and J Lorenzo. Expression and regulation of basic fibroblast growth factor mRNA levels in mouse osteoblastic MC3T3-E1 cells. *Journal of biological chemistry*, 269(12):9392–9396, 1994.

[354] A Matsugaki, G Aramoto, T Ninomiya, H Sawada, S Hata, and T Nakano. Abnormal arrangement of a collagen/apatite extracellular matrix orthogonal to osteoblast alignment is constructed by a nanoscale periodic surface structure. *Biomaterials*, 37:134–143, 2015.

[355] FR Tay and DH Pashley. Guided tissue remineralisation of partially demineralised human dentine. *Biomaterials*, 29(8):1127–1137, 2008.

[356] FR Tay and DH Pashley. Biomimetic remineralization of resin-bonded acid-etched dentin. *Journal of dental research*, 88(8):719–724, 2009.

[357] Z Meleti, IM Shapiro, and CS Adams. Inorganic phosphate induces apoptosis of osteoblast-like cells in culture. *Bone*, 27(3):359–366, 2000.

[358] X Wu, N Itoh, T Taniguchi, T Nakanishi, and K Tanaka. Requirement of calcium and phosphate ions in expression of sodium-dependent vitamin C transporter 2 and osteopontin in MC3T3-E1 osteoblastic cells. *Biochimica et biophysica acta - molecular cell research*, 1641(1):65–70, 2003.

[359] D Wang, K Christensen, K Chawla, G Xiao, PH Krebsbach, and RT Franceschi. Isolation and characterization of MC3T3-E1 preosteoblast subclones with distinct *in vitro* and *in vivo* differentiation/mineralization potential. *Journal of bone and mineral research*, 14(6):893–903, 1999.

[360] P Habibovic, DC Bassett, CJ Doillon, C Gerard, MD McKee, and JE Barralet. Collagen biomineralization *in vivo* by sustained release of inorganic phosphate ions. *Advanced materials*, 22(16):1858–1862, 2010.

[361] A Gourrier, W Wagermaier, M Burghammer, D Lammie, HS Gupta, P Fratzl, C Riekel, TJ Wess, and O Paris. Scanning X-ray imaging with small-angle scattering contrast. *Journal of applied crystallography*, 40(Supplement):s78–s82, 2007.

[362] N Bryan, K Andrews, M Loughran, N Rhodes, and J Hunt. Elucidating the contribution of the elemental composition of fetal calf serum to antigenic expression of primary human umbilical-vein endothelial cells *in vitro*. *Bioscience reports*, 31:199–210, 2011.

[363] G Gstraunthaler. Alternatives to the use of fetal bovine serum: Serum-free cell culture. *Altex*, 20(4):275–281, 2003.

[364] CEA Jochems, JBF van der Valk, FR Stafleu, and V Baumans. The use of fetal bovine serum: Ethical or scientific problem? *Alternatives to laboratory animals*, 30(2):219–228, 2002.